International Symposium

TOPICAL PROBLEMS OF NONLINEAR WAVE PHYSICS (NWP-2014)

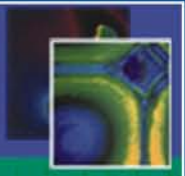

17-23 July, 2014
Nizhny Novgorod, Russia

2014 NWP

Nonlinear Dynamics on Complex Networks (NWP-1)

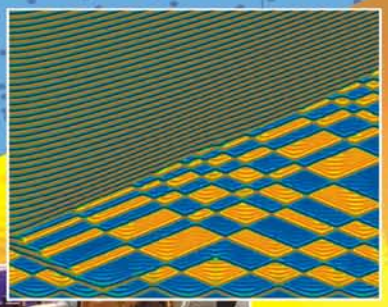

Lasers with High Peak and High Average Power (NWP-2)

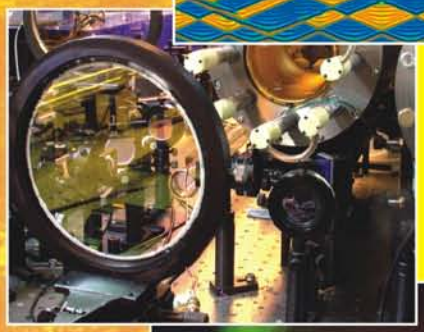

Nonlinear Phenomena in Geophysics (NWP-3)

Workshop "Ultra-high Fields in Plasmas: New Models, High Performance Simulations and Experiments

Young Scientists School

PROCEEDINGS

Russian Academy of Sciences
Institute of Applied Physics

International Symposium

TOPICAL PROBLEMS OF NONLINEAR WAVE PHYSICS

17 – 23 July, 2014

NWP-1: Nonlinear Dynamics on Complex Networks

NWP-2: Lasers with High Peak and High Average power

NWP-3: Nonlinear Phenomena in Geophysics

Workshop: Ultra-high Fields in Plasmas: New Models, High Performance Simulations and Experiments

School for Young Scientists

P R O C E E D I N G S

Nizhny Novgorod, 2014

Board of Chairs

Michael Ghil	University of California, Los Angeles, USA & Ecole Normale Supérieure, France
Sergey Gurbatov	University of Nizhny Novgorod, Russia
Efim Khazanov	Institute of Applied Physics RAS, Russia
Igor Kostyukov	Institute of Applied Physics RAS, Russia
Juergen Kurths	Potsdam Institute for Climate Impact Research, Germany; Institute of Applied Physics RAS, Russia
Evgeny Mareev	Institute of Applied Physics RAS, Russia
Vladimir Nekorkin	Institute of Applied Physics RAS, Russia
Arkady Pikovsky	Potsdam University, Germany; University of Nizhny Novgorod, Russia
Alexander Pukhov	University of Düsseldorf, Germany Institute of Applied Physics RAS, Russia
Vladimir Rakov	University of Florida, USA Institute of Applied Physics RAS, Russia
Alexander Sergeev	Institute of Applied Physics RAS, Russia
Ken-ichi Ueda	Institute for Laser Science, the University of Electro-Communications, Japan; Institute of Applied Physics RAS, Russia

ISBN 978-5-8048-0099-5

© Institute of Applied Physics RAS, 2014

Symposium Web site: http://www.nwp.sci-nnov.ru

Organized by

Institute of Applied Physics
of the Russian Academy of Sciences
www.iapras.ru

University of Nizhny Novgorod
www.unn.ru

GYCOM Ltd
www.gycom.ru

Quantron-NN Ltd

Supported by

The Government of the Russian Federation

Russian Foundation for Basic Research

Dynasty Foundation
www.dynastyfnd.ru

AMPLITUDE TECHNONOGIES
www.amplitude-technologies.com

www.corning.com

LASER Components
lasercomponents.ru

The electron version of the NWP-2014 Symposium materials was prepared
at the Institute of Applied Physics of the Russian Academy of Sciences,
46 Ulyanov Str., 603950 Nizhny Novgorod, Russia

C O N T E N T S

PLENARY TALKS

NWP-1:

NONLINEAR DYNAMICS ON COMPLEX NETWORKS

NWP-2:

LASERS WITH HIGH PEAK AND HIGH AVERAGE POWER

NWP-3:

NONLINEAR PHENOMENA IN GEOPHYSICS

WORKSHOP

"ULTRA-HIGH FIELDS IN PLASMAS: NEW MODELS, HIGH PERFORMANCE SIMULATIONS AND EXPERIMENTS"

SCHOOL FOR YOUNG SCIENTISTS

International Symposium

TOPICAL PROBLEMS OF NONLINEAR WAVE PHYSICS

PLENARY TALKS

OPTIMIZATION STUDY FOR LASER-TRIGGERED ION ACCELERATION FROM THIN TARGETS AND SOCIETAL NUCLEAR APPLICATIONS

V.Yu. Bychenkov[1, 2]

[1] P.N. Lebedev Physics Institute RAS, Moscow, Russia, bychenk@lebedev.ru
[2] Center for Fundamental and Applied Research, VNIIA, ROSATOM, Moscow, Russia

Abstract. Here the results of 3D optimization study with PIC code "Mandor" for acceleration of ions from thin targets triggered by femtosecond laser pulses are presented. For a volumetric heating of the targets with optimum thicknesses, the dependence of maximum ion energies on laser intensity shows very universal scaling ~ $I^{0.7}$ for a wide intensity range and different pulse durations and spot sizes of practical interest. More sharp dependence of maximum ion energy as compared to popular scaling ~$I^{0.5}$ is a result of absorption increase with increasing laser intensity. The proposed analytical model is consistent with numerical simulations. Several nuclear applications of societal trend are discussed for new generation lasers of high peak and averaged power.

Introduction

It is known that target thickness should be properly matched to the laser intensity [1] for obtaining maximum ion energy. Although the optimal target thickness can be estimated by the order of magnitude from 2D PIC simulations [1], 3D PIC simulations are needed to correctly quantify it for different laser intensities. The optimal target thickness was found in Ref. [1], where the square root energy scaling for the proton energy with laser intensity (energy) was also inferred. The intensity square root scaling for the maximum proton energy is also predicted by the TNSA model, which is valid for the thick targets [2]. The 3D PIC simulations to find the optimal target thickness for the laser pulse energy must also examine the dependence on different spot sizes and pulse durations. Such optimization should include the systematic study of the laser light absorption (i.e. laser to electron energy conversion efficiency) in semi-transparent targets and this will be an important part of our paper. In a comprehensive study we will quantify how all parameters of the pulse affect laser energy conversion to hot electrons and determine effectiveness of high-energy ion production. We present the results of 3D optimization study with PIC code MANDOR for acceleration of protons from thin targets triggered by femtosecond laser pulses. The main outcome here is the dependence of the maximum proton energies on the laser intensities under the conditions of volumetric heating of the optimum thickness targets.

Optimization study for ion acceleration

We have performed 3D simulations of proton acceleration by ultrashort (τ = 30 fs FWHM duration) tightly focused (FWHM of the laser spot $d = \lambda$) laser pulses with the PIC code MANDOR. As a reference we set the laser wavelength at λ = 1 μm. Laser intensity is varied from $I = 5 \times 10^{18}$ to $I = 5 \times 10^{22}$ W/cm^2 which corresponds to laser pulse energies from 0.03 J to 300 J. To examine pulse duration (τ) and spot size (d) effects on ion acceleration, three additional sets of laser pulse parameters with the same full laser energy have been used: increased laser spot size, $d = 6\lambda$, and decreased one, $d = 2\lambda$, for τ = 30 fs and for the increased pulse duration, τ = 150 fs, for the hot spot size $d = 4\lambda$. A very tight laser pulse focusing to 2λ has been implemented by using the parabolic mirror simulation technique [3]. For larger hot spots, Gaussian laser pulses have been used. The laser pulse was focused on the front side of the thin CH_2 plasma foils composed of electrons, hydrogen ions, and fully ionized carbon ions (C^{6+}). The target has an electron density of $200n_c$ (where $n_c = m_e/4\pi e^2\omega^2$ is the plasma critical density), which corresponds to a solid mass density of CH_2 (1.1 g/cm^3). The target thickness l has been varied from 3nm to 1 μm. The results of our simulations for the maximum energy of the protons (ε) from the optimum thickness targets are well approximated by the scaling $\varepsilon \propto 22E_L^{0.7}$ (see Fig. 1), which is different from the square root dependence reported earlier [1].

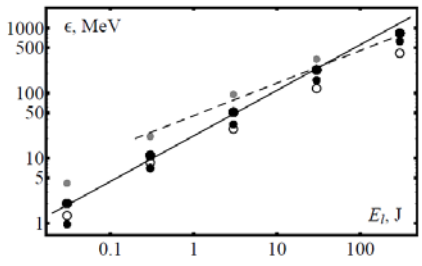

Fig. 1. Maximum proton energy for optimal target thickness vs laser energy (E_L) for τ = 30 fs and $d = 4\lambda$ (large black points), $d = 6\lambda$ (small black points), $d = 2\lambda$ (gray points) and τ = 150 fs and $d = 4\lambda$ (open circle). The black line corresponds to $\varepsilon = 22E_L^{0.7}$ and the dashed line $\varepsilon = 45E_L^{0.5}$

More sharp dependence of maximum ion energy $\varepsilon \propto E_L^{0.7}$ is a result of laser absorption increasing with intensity for semi-transparent targets. This dependence is consistent with recently proposed analytical model [4] which uses ponderomotive scaling for electron temperature vs. absorbed laser power. Given laser energies the shorter laser pulse and tighter focusing gives higher maximum proton energy. The number of energetic protons also increases with the laser energy.

Neutron and isotope production from optimized targets

We consider also some interesting examples for isotope and neutron production that makes use of protons and deuterons accelerated to multi-MeV energies from the semi-transparent targets and demonstrate that new laser technique permits production of radionuclides for SPECT (single-photon emission computed tomography) and PET (positron emission tomography), as well as for neutrons for therapy and inspection. Below (see the table) the examples of Tc-99m yield for Mo-100(p,2n)Tc-99m reaction in a thick target bombarded by laser-produced protons from CH_2 foils are given for 10J laser pulse and different focal spots: $d = 4\lambda$ (case 1), $d = 6\lambda$ (case 2), and $d = 10\lambda$ (case 3) as well as for 5J laser pulse focused into $d = 4\lambda$ hot spot (case 4). The Tc-99m activity after six hours is calculated with a laser repetition rate of 10 kHz. The ratio of long-lived Tc-99g plus Tc-98 atoms to Tc-99m atoms is a critical parameter for the formation of Tc-chelates for human application (see "Ratio" in the table). Our study is the first step aimed at establishing a list of radionuclides of interest for nuclear radionuclide therapy and emission tomography as well as the first insight into the laser-based neutron source for radiation and neutron-capture therapy.

Case N	Target thickness, μm	E_{max}, MeV	Number of protons	Number of Tc-99m	Ratio	Radiation activity, GBq	Number of Mo-99
1	0.05	70.4	1.2×10^{11}	7×10^{7}	17 %	205	5.4×10^{7}
1	0.07	73.8	1.9×10^{11}	9.2×10^{7}	18 %	269	5.8×10^{7}
1	0.1	63.5	2.3×10^{11}	1.1×10^{8}	21 %	322	5.4×10^{7}
1	0.2	45.5	2.2×10^{11}	6×10^{7}	30 %	175	1.3×10^{7}
1	0.3	38.7	1.5×10^{11}	3.3×10^{7}	33 %	97	4.9×10^{6}
2	0.03	52	9.6×10^{10}	4.8×10^{7}	20 %	140	2.5×10^{7}
2	0.05	62	1.6×10^{11}	6.6×10^{7}	21 %	193	3.1×10^{7}
2	0.1	40.5	1.7×10^{11}	4.4×10^{7}	31 %	127	8.2×10^{6}
3	0.02	47.2	8.3×10^{10}	3.3×10^{7}	23 %	97	1.2×10^{7}
3	0.05	31.8	6.7×10^{10}	1.2×10^{7}	35 %	35	1.4×10^{6}
4	0.04	49.3	5.9×10^{10}	2.6×10^{7}	21 %	76	1.2×10^{7}
4	0.05	48	7.6×10^{10}	2.9×10^{7}	24 %	85	1.1×10^{7}
4	0.07	44	$1. \times 10^{11}$	3.2×10^{7}	28 %	94	8.4×10^{6}
4	0.1	34.7	1.1×10^{11}	2.4×10^{7}	32 %	70	4×10^{6}

Acknowledgements

This research was supported by RFBR grants.

References

1. T.Z. Esirkepov, M. Yamagiwa, and T. Tajima, *Phys. Rev. Lett.*, 2006, **96**(10), 105001.
2. J. Fuchs et al., *Nature Phys.*, 2006, **2**(1), 48-54.
3. K.I. Popov et al., *Phys. Plasmas*, **15**(1), 013108.
4. E.A. Govras and V.Yu. Bychenkov, *JETP Lett.*, 2013, **98**(2), 70-75.

SIMULATION OF INTERACTING DYNAMICAL SYSTEMS IN WIRELESS SENSOR NETWORKS

A.S. Dmitriev, M.Y. Gerasimov, R.Y. Emelyanov, and **V.V. Itskov**

Institute of Radioengineering and Electronics, Russian Academy of Sciences
Moscow, Russia, chaos@cplire.ru

Abstract. Generalized wireless sensor networks – wireless active networks (WAN) – are considered as distributed multiple-unit processor platform for modeling behavior of interacting dynamical systems. During the simulation, each sensor network node represents a dynamical system. The equations of this system are solved by a special computing unit, e.g., microcontroller (MCU) placed on each node. The interaction between the dynamical systems is understood as transmission of data on the system state between the nodes of active network via radio channel. Here, this approach is investigated on an example of an ensemble of coupled logistic maps. This ensemble is implemented as a wireless network composed of ultra wideband direct chaotic transceivers PPS-43 [3] with special actuator boards attached. These actuator boards contain an MCU to iterate the maps and a display to visualize information (color LED). The modeling technique, experimental results and analysis are described.

Introduction

Usually the wireless sensor network (WSN) is described as a set of nodes equipped with sensors and combined into an ensemble by means of the interaction via radio channels [1]. However, there is an increasing number of examples of wireless sensor networks whose nodes except transceivers and sensors include actuators, i.e., devices which affect the environment; or visual information displays (LED, LCD); or information processing devices (MCU, processor) [2]. Below, for such generalized wireless sensor networks we use the term **wireless active networks** (WAN). A wide range of equipment used in nodes along with communication capabilities allows considering active wireless networks not only as a means of data acquisition on a particular area and transmission to the analysis station, but also as a powerful platform for solving wider classes of problems related to multiple-unit interacting systems.

Ultrawideband active node and actuator for simulation

An active network node consists of a wireless transceiver and a special actuator board. Ultrawideband wireless transceiver PPS-43 [3] was used as a communication part. The actuator is based on microcontroller STM32L which is used as a computing unit to solve equations of ensemble element, and a color LED as a visual indicator for one of the variables of the ensemble element state.

MCU STM32L has RISC architecture; its clock frequency can be changed in the range 1 to 32 MHz. It has good computing capabilities; it is extraordinarily small and energy efficient.

An important feature of this MCU is the ability to emulate floating point operations, so it can be used as a full functional device for modeling dynamic systems. The equations programmed in C language, and then compiled to MCU machine code.

Simulation procedure algorithm

Let us consider the procedure of simulation on the example of an ensemble of 1-d logistic maps in chaotic mode.

Simulation of collective behavior of discrete dynamic systems includes the following stages:

– Network creation: at this stage each network node declares itself and establishes connection with each other network node. For each node and for the network as a whole the process ends when each node detects all the other nodes and each node has the “knowledge” that all other nodes have received information from it.

– Synchronization of node clocks.

– Start of collective iteration and evolution.

– Brake of collective behavior in case one or more links are broken.

– Restoring collective iterations.

An important feature of the described network is its autonomy, so there is no need in control center (sink).

Experiments

The sensor network that was used in the experiment consisted of 4 nodes (fig. 1). Each node contained a direct chaotic transceiver and an actuator board on which a logistic map was iterated in accordance with the above algorithm.

The devices were arranged on a table and turned on by operator. At startup, the initial value for each dynamic system was selected using a random-number generator. According to the above rules, each device listened for the time interval T and then transmitted a packet with node ID number and state variable value information. After listening, the step was repeated. It took some time to synchronize the node clocks after turning on the last device. Time synchronization was visualized by simultaneous actuator color changes. For some time (4-5 iterations), LED colors changed chaotically and remained different on each actuator. After that, the colors were still chaotically changing with time, but the difference of node colors became visually smaller and smaller, and the collective behavior of the ensemble led to synchronous state. This state was stable and it persisted until some natural or artificial fault took place.

As an example of such a "fault," one device was turned off during the experiment. The remaining nodes started working autonomously, without using the other node state information. Three remaining powered devices worked as follows: for some time, it looked as if they were synchronous, but after several iterations the difference in the state values increased and LED colors became visually different and finally came to completely uncorrelated behavior. However, time synchronization between the devices remained, therefore color change time moments were still simultaneous.

After the node clocks lost synchronization (mistiming), the 4th device was turned on again. The clock synchronization process was repeated. It wasn't visually apparent because by this time the clock discrepancy in quartz generators wasn't large enough. Full clock synchronization was restored after the time interval about T. Then the process of restoring the synchronous state of the ensemble began. It was indicated by the process of color convergence.

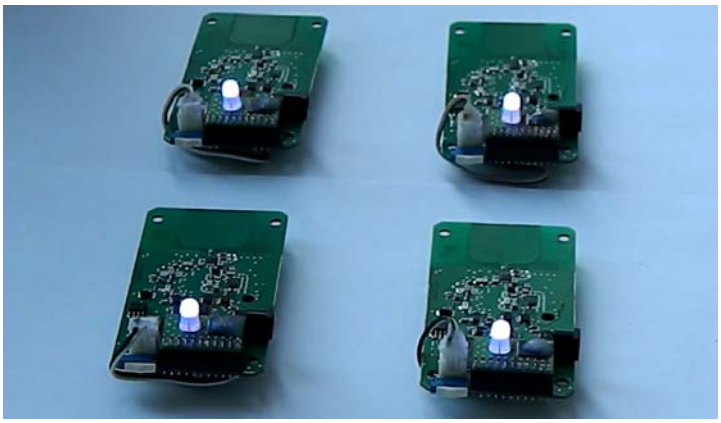

Fig. 1. Synchronous mode in the experiment

Conclusions

In this paper, the use of wireless active networks as a technique for investigation of collective behavior of dynamical systems is shown. As an example, this approach was applied in experiment to an ensemble of 1D maps, whose equations were iterated on the nodes using information on the states of the other ensemble elements, that was transmitted synchronously via ultra wideband radio channel.

References

1. http://en.wikipedia.org/wiki/Wireless_sensor_network.
2. Special Issue on Wireless Sensor and Actuator Networks, *IEEE Trans. on automatic control,* 2011, **57**(10).
3. Yu. Andreyev, A. Dmitriev, E. Efremova, and V. Lazarev, *2013 Proc. International Symposium on Nonlinear Theory and its Applications (NOLTA2013)*, Santa Fe, USA, 2013, p. 221-224.

ION ACCELERATION IN LOW DENSITY TARGETS USING ULTRA-HIGH INTENSITY LASERS

E. d'Humières[1], M. Lobet[2], A. Debayle[2], L. Gremillet[2], and **V.T. Tikhonchuk[1]**

[1] Univ. Bordeaux – CNRS - CEA, Talence, France, dhumieres@celia.u-bordeaux1.fr
[2] CEA/DAM-DIF, Arpajon, France

Abstract. Recent theoretical and experimental studies suggest the possibility of enhancing the efficiency and ease of laser acceleration of protons and ions using underdense or near critical plasmas through electrostatic shocks. Scaling shock acceleration in the low density regime to ultra high intensities is a challenge as radiation losses and electron positron pair production change the optimization of the shock process. Using large-scale Particle-In-Cell simulations, the transition to this regime in which intense beams of relativistic ions can be produced is investigated. The application of these beams to high energy laboratory astrophysics is discussed.

The intense research being conducted on sources of laser-accelerated ions and their applications, e.g. radiography and the production of warm dense matter (WDM), is motivated by the exceptional properties that have been demonstrated for proton beams accelerated from planar targets, such as high brightness, high spectral cut-off, high directionality and laminarity, and short duration (~ps at the source). In most experiments, solid density targets are used and the most energetic ions are accelerated by the so-called target normal sheath acceleration (TNSA) mechanism [1]. These ion sources are very promising for a wide range of applications [2, 3], from the production of radio-isotopes and the testing of mechanisms of extreme energy particle production in gamma-ray bursts, but also to improve prospects for the necessary gantry for proton therapy or for fast ignition of inertial confinement fusion targets with high gain.

The results in [4] suggest the possibility of enhancing the efficiency and ease of laser acceleration of protons and ions compared to what has been achieved up to now using standard TNSA. Indeed, it is not only important for applications of such ion beams that its parameters (maximum energy and total number) are enhanced, but also that it is easily usable. Regarding the second point, there are currently some issues/limitations linked to using solid targets: (1) targets need to be aligned precisely for each shot, (2) laser temporal contrast needs to be controlled, (3) debris is produced and (4) repetition rate is limited. These limitations could all be greatly alleviated if one could use gas jets as the laser interaction medium. Through simulations, we have found that shock acceleration could be used in such a low-density medium to accelerate ions [5, 6] not only very efficiently, but also with a higher number than TNSA. However, with present-day laser parameters, we find that it would require rather a thin gas jet (of the order of 100 microns), which is not readily available.

In [4], using 2D particle-in-cell simulations of exploded foils, we have shown that increasing the laser energy and intensity allows us to significantly improve the efficiency of shock acceleration versus TNSA. Using short and near-critical targets with moderately long gradients leads to a good compromise between increased maximum proton energies and the degrading of the beam characteristics. This could strongly enhance the practicality and possibilities for ion probing or WDM generation in future high-power and high repetition-rate laser facilities. Recently, important progress has been achieved in the production of short near-critical density gas jets [7]. The possibility of using high repetition gas nozzles to generate such plasmas would therefore allow us to demonstrate the efficiency of this process in a set-up which would be much more useful for applications. Scaling shock acceleration in the low density regime to ultra high intensities ($>10^{22}$ W/cm^2) is a challenge as radiation losses and electron positron pair production change the optimization of the shock process. Using large-scale Particle-In-Cell simulations including these effects, we have investigated and modeled the transition to this regime in which intense beams of relativistic ions can be produced.

Following Refs. [8, 9], the PIC code CALDER [10] has been enriched with numerical models of synchrotron radiation and Breit-Wheeler pair production [11]. In the classical case, the low-energy photon emission is treated using Sokolov's radiation friction model with a quantum-corrected radiated power [12]. In the quantum regime, Monte Carlo schemes are used to describe the discrete emission of gamma photons and their annihilation into e−e+ pairs. The physical parameters are chosen so as to reproduce laser and target conditions that could be tested with near-future laser installations like Apollon in France and the Extreme Light Infrastructure in Europe. The linearly-polarized laser pulse has a 1 μm wavelength, a 32 fs (60 ω_0^{-1}, where ω_0 is the laser frequency) FWHM duration and a peak intensity ranging from $I_0 = 10^{22}$ to 8.9×10^{23} W·cm^{-2} (i.e., a normalized field amplitude $a_0 = eE_0/m_e c\omega_0 =$

= 85 to 800). The focal spot FWHM is 10 µm. The target is taken to be a fully-ionized H plasma with a cosine squared density profile, a maximum electron density $n_e = 2\ n_c$ and a total thickness ranging from 100 to 400 µm.

For laser intensities in the range 10^{22} W·cm^{-2} to a few 10^{23} W·cm^{-2}, a clear shock signature is observed on the proton phase space (see the figure below). Maximum proton energies of around 500 MeV and 910 MeV are measured for laser intensities of 10^{22} W·cm^{-2} and 10^{23} W·cm^{-2}, respectively, for a 190 microns long target. As the laser intensity increases, the share of laser energy transferred to high energy photons also increases and the laser energy transferred to protons decreases, even if the maximum proton energy continues to increase. Laser energy absorption in protons saturates at ~50 % for a laser intensity of 10^{22} W·cm^{-2} and at ~38 % for a laser intensity of 10^{23} W·cm^{-2}, while laser energy transferred in high energy photons is around 20 % for a laser intensity of 10^{22} W·cm^{-2} and around 44 % for a laser intensity of 10^{23} W·cm^{-2}. The thickness of the target also plays an important role.

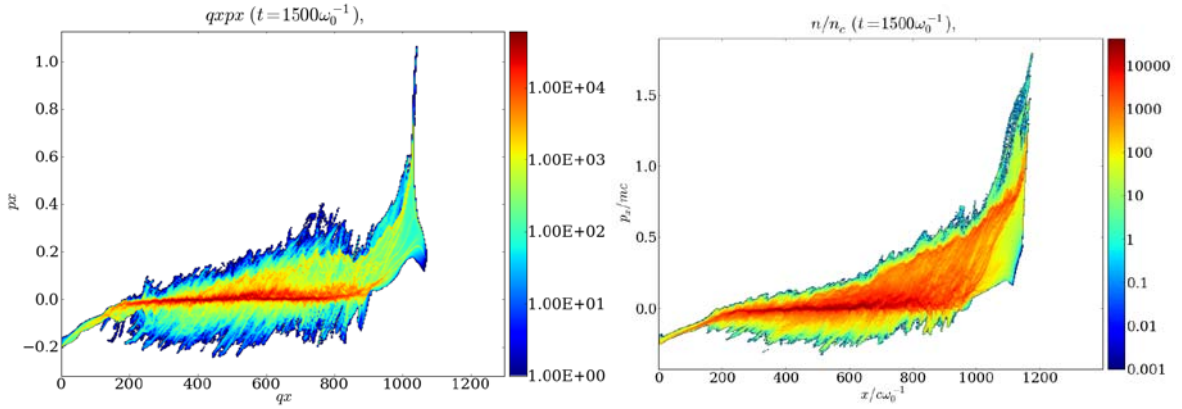

Fig. 1. Proton phase space after 1500 ω_0^{-1} for I = 10^{22} W/cm^2 (*left*) and for I = 10^{23} W/cm^2 (*right*) for a 2 n_c, 190 microns long cos^2 target. The laser comes from the left side of the simulation box

These relativistic ion beams are of great interest for high-energy laboratory astrophysics as they could be used to prepare the first relativistic collisionless shocks experiments in the laboratory using ultra high intensity laser systems like Apollon or ELI. The study of the development of relativistic collisionless shocks is crucial to test specific astrophysical scenarios (for instance for Gamma Ray Bursts models and particle acceleration models in Supernova Remnants).

Acknowledgements

The authors acknowledge support by the French Agence Nationale de la Recherche (ANR SILAMPA). The PIC simulations were performed using HPC resources at TGCC/CCRT (Grant No. 2013-052707) and at CINES under the allocation 2014-056129 made by GENCI (Grand Equipement National de Calcul Intensif).

References

1. S.C. Wilks et al., *Phys. Plasmas*, 2001, **8**, 542.
2. E. d'Humières (2012). Ion Acceleration by High Intensity Short Pulse Lasers, *Laser Pulses - Theory, Technology, and Applications*, Prof. Igor Peshko (Ed.), ISBN: 978-953-51-0796-5, InTech, DOI: 10.5772/46137.
3. A. Macchi et al., *Rev. Mod. Phys.*, 2013, **85**, 751.
4. E. d'Humières et al., *Plasma Phys. Control. Fusion*, 2013, **55,** 124025.
5. E. d'Humières et al., *J. Phys.: Conf. Ser.*, 2010, **244,** 042023.
6. E. d'Humières et al., *Phys. Plasmas*, 2013, **20,** 023103.
7. F. Sylla et al., *Rev. Sci. Instrum.* 2012, **83,** 033507**.**
8. R. Duclous, J.G. Kirk, and A.R. Bell, *Plasma Phys. Control. Fus.*, 2011, **53**, 015009.
9. N.V. Elkina, A.M. Fedotov, I.Y. Kostyukov, et al., *Phys. Rev. ST Accel. Beams*, 2011, **14**, 054401.
10. E. Lefebvre et al., *Nuclear Fusion*, 2003, **43**, 629.
11. M. Lobet, E. d'Humières, M. Grech, et al., 2013, *arXiv preprint* arXiv:1311.1107.
12. I.V. Sokolov, N.M. Naumova, J.A. Nees, et al., *Phys. Plasmas*, 2009, **16**, 093115.

THE HELMHOLTZ BEAMLINE LASER PROJECT AT THE FACILITY FOR ANTI-PROTON AND ION RESEARCH (FAIR)

Th. Kuehl

GSI-Helmhotzzentrum Darmstadt, Germany

The international accelerator Facility for Anti-Proton and Ion Research (FAIR) currently under construction at the GSI heavy ion accelerator laboratory in Darmstadt, Germany, will enable an unprecedented variety of experiments. Thereby physicists from all around the world will be able to gain new insights into the structure of matter and the evolution of the universe from the Big Bang to the present.

Besides nuclear and particle physics, plasma physics will be one main „pillar“ of the scientific program of this installation. For this part of the project, lasers are proposed for diagnostics of heavy-ion prepared plasma states, and for the preparation of interaction targets for the accelerator beam. The proposed Helmholtz Beamline will add a state-of-the-art high-energy petawatt laser to FAIR aiming at combined laser-ion experiments. The foreseen location of the laser facility enables laser-ions experiments in two experimental areas of the accelerator.

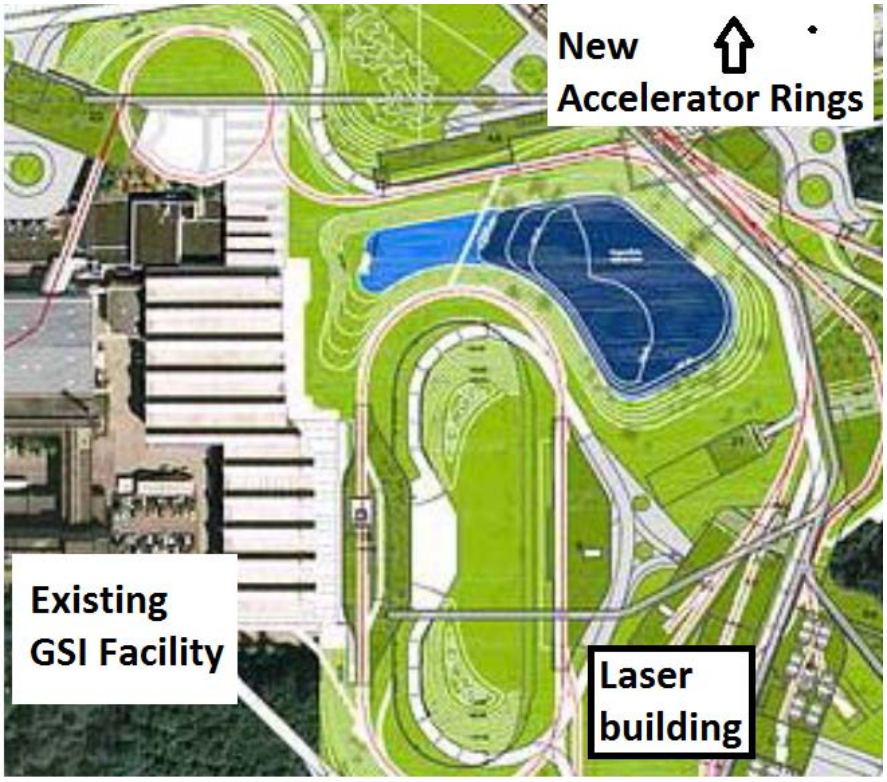

Fig. 1. View of the location of the high power laser installation in planning for FAIR. The laser is supposed to support Plasma Physics and material Science experiments in the APPA target hall and ultra-high intensity interaction in the High-Energy Storage Ring HESR. The experiments require a pulse energy above 1 kJ and an option to provide pulses above 1 PW

First, a high-energy cave, where ion beams of the highest-brilliance will turn samples into uniform macroscopic warm dense matter relevant to planetary science, will be coupled to the laser building. This fully radiation shielded environment enables multi-beam experiment setups, where the laser can be used, for instance, as a backlighter. Laser experiments are also proposed to use the High-Energy Storage Ring (HESR), that enables storing all elements, including short-lived isotopes with any ionization level at relativistic velocities. This ring will be equipped with a dedicated target station allowing for high-field experiments on exotic ions moving at highly relativistic velocities.

After a brief description of the project, the talk will focus on the technical bottlenecks and challenges of the project. In particular, some preliminary work done at the PHELIX laser facility in Darmstadt, Germany will be presented to illustrate the issues and propose some solutions.

CLIMATE NETWORKS AND EXTREME EVENTS

J. Kurths

Potsdam Institute for Climate Impact Research & Humboldt University,
Berlin & King´s College, University of Aberdeen, UK

We analyse some climate dynamics from a complex network approach. This leads to an inverse problem: Is there a backbone-like structure underlying the climate system? For this we propose a method to reconstruct and analyze a complex network from data generated by a spatio-temporal dynamical system. This approach enables us to uncover relations to global circulation patterns in oceans and atmosphere. The global scale view on climate networks offers promising new perspectives for detecting dynamical structures based on nonlinear physical processes in the climate system. Moreover, we evaluate different regional climate models from this aspect.

This concept is also applied to Monsoon data in order to characterize the regional occurrence of extreme rain events and its impact on predictability. Changing climatic conditions have led to a significant increase in magnitude and frequency of spatially extensive extreme rainfall events in the eastern Central Andes of South America. These events impose substantial natural hazards for population, economy, and ecology by floods and landslides. For example, heavy floods in Bolivia in early 2007 affected more than 133.000 households and produced estimated costs of 443 Mio. USD.

Here, we develop a general framework to predict extreme events by combining a non-linear synchronization technique with complex networks. We apply our method to real-time satellite-derived rainfall data and are able to predict a large amount of extreme rainfall events. Alongside with the societal benefits of predicting natural hazards associated with extreme rainfall, our study reveals a linkage between polar and subtropical regimes as responsible mechanism: Extreme rainfall in the eastern Central Andes is caused by the interplay of northward migrating frontal systems and a low-level wind channel from the western Amazon to the subtropics, providing additional moisture. Frontal systems from the Antarctic thus play a key role for sub-seasonal variability of the South American Monsoon System.

References

1. A. Arenas, A. Diaz-Guilera, J. Kurths, Y. Moreno, and C. Zhou, *Phys. Reports*, 2008, **469**, 93.
2. J. Donges, Y. Zou, N. Marwan, and J. Kurths, *Europhys. Lett.*, 2009, **87**, 48007.
3. R. Donner, Y. Zou, J. Donges, N. Marwan, and J. Kurths, *Phys. Rev. E*, 2010, **81**, 015101(R).
4. I.I. Mokhov, D.A. Smirnov, P.I. Nakonechny, S.S. Kozlenko, E.P. Seleznev, and J. Kurths, *Geophys. Res. Lett.*, 2011, **38**, L00F04.
5. N. Malik, B. Bookhagen, N. Marwan, and J. Kurths, *Climate Dynamics*, 2012, **39**, 971.
6. J. Donges, H. Schultz, N. Marwan, Y. Zou, J. Kurths, *Eur. J. Phys. B*, 2011, **84**, 635-651.
7. J. Donges, R. Donner, M. Trauth, N. Marwan, H.J. Schellnhuber, and J. Kurths, *PNAS*, 2011, **108**, 20422-20427.
8. K. Rehfeld, N. Marwan, S.F.M. Breitenbach, and J. Kurths, *Climate Dynamics*, 2013, **41**, 3-19.
9. J. Runge, J. Heitzig, V. Petoukhov, and J. Kurths, *Phys. Rev. Lett.*, 2012, **108**, 258701.
10. P. Menck, J. Heitzig, N. Marwan, and J. Kurths, *Nature Physics*, 2013, **9**, 89-92.
11. N. Boers, B. Bookhagen, N. Marwan, J. Kurths, and J. Marengo, *Geophys. Res. Lett.*, 2013, **40**, 4386.
12. M. Mheen, H.A. Dijkstra, A. Gozolchiani, M. Toom, Q. Feng, J. Kurths, and E. Hernandez-Garcia, *Geophys. Res. Lett.*, 2014, **40**, 2714.
13. J. Feldhoff, S. Lange, J. Volkholz, J. F. Donges, J. Kurths, and F. Gerstengarbe, *Climate Dynamics*, 2014, DOI 10.1007/s00382-014-2182-9.

COMPLEX NETWORK DYNAMICS APPROACH TO MARINE EXTERNAL FERTILIZATION

G. Martínez-Mekler[1], J. Espinal[2], and **A. Darszon[3]**

[1] Instituto de Ciencias Físicas, Universidad Nacional Autómoma de México, Cuernavaca, México, mekler@fis.unam.mx
[2] Instituto Nacional de Medicina Genómica, Distrito Federal, México
[3] Instituto de Biotecnología, UNAM, Cuernavaca, México

Abstract. In this work we study the fertilization of sea urchins by focusing on a biochemical signaling pathway of calcium concentration [Ca^{2+}], oscillations within the spermatozoa flagella, triggered by chemicals surrounding the egg, and known to control their swimming to the egg (chemotaxis). We study the discrete dynamics of a logical regulatory network model representing the pathway. With our model we predict behaviors that are corroborated by new experiments and that contribute to a better understanding of chemotaxis, membrane electrophysiology, drug operation and issues related to the development of a male contraceptive.

Complex phenomena, systems biology approach

Fertilization is one of the fundamental processes of living systems. It is a multifactorial complex phenomenon with several levels of description ranging from chemical diffusion, biochemical reactions and signaling pathways, molecular motors, wave propagation to hydrodynamics. Though here we focus on the biochemical signaling pathway level, in particular of [Ca^{2+}] in the flagellum, our findings are relevant at all other levels. Sea urchin spermatozoa swim describing cycles in a medium with chemical gradients originating at the egg position, the relation between the oscillatory space exploration process and the oscillatory biochemical fluctuations is determinant for the occurrence of chemotaxis, phase locking and synchronization come into play, and timing considerations are crucial. Many of our results are related to characteristic relaxation times, transient times, oscillation periods and so forth. For their determination, the study of properties emergent from the whole interacting biochemical network is necessary, and complex systems network research tools come into hand. It is important to stress that our work not only follows this systems biology approach, but it is also intimately related to experimental determinations undertaken within our research group.

Modeling

The logical regulatory network for the flagellum [Ca^{2+}] signaling pathway [1] mentioned in the abstract is based on Fig. 1.

The network consists of a set of N discrete variables $\{\sigma_1, \sigma_2, \ldots, \sigma_n\}$, each representing the state of a node, which take discrete values according to the figure caption. The time evolution of the state of each node σ_n given by

$$\sigma_n(t+1) = F_n(\sigma_{n1}(t), \sigma_{n2}(t), \sigma_{n3}(t), \sigma_{n4}(t) \ldots \sigma_{nk}(t)),$$

where F_n is a regulatory function, takes into account the activating/inhibiting nature of the regulators and nk is the number of nodes linked to σ_n. These regulatory functions are a type of truth table as shown in figure 1 and are based on extensive biological knowledge, mainly of an electrophysiological nature, available to us in the literature and in our own laboratory. For the [Ca^{2+}] node the regulatory table required 432 rows. The complete set of regulatory functions can be found in http://www.fis.unam.mx/research/seaurchin/discrete, as well as an interactive network evolution applet.

Results

With the dynamics of the above equation the effect of blocking or perturbing network elements (e.g., membrane channels) either individually or multiply can be explored [1, 2]. As a consequence we induced changes in the timing properties mentioned before affecting the spermatozoon motility, corroborated experimentaly. Together with statistical studies, correlation and Fourier analysis, the action of several drugs that block membrane channels was explored, leading to experimental determinations some related to chemotaxis and in cases relevant to the search of a male contraceptive. Also, argumentation for the presence and relevance of membrane channels not being considered before in the signaling pathway was advanced, setting clues for physiological experimentation [3].

In the general context of complex network dynamics, stability, redundancy and modularity issues were also addressed. The finding that the discrete network dynamics operates at criticality, where robustness and evolvability coexist is a matter for reflection. These global network considerations also appear to be of a physiological relevance [4]. We have also implemented semi-continuous and continuous formalisms for the dynamics, as well as a space-time proposal.

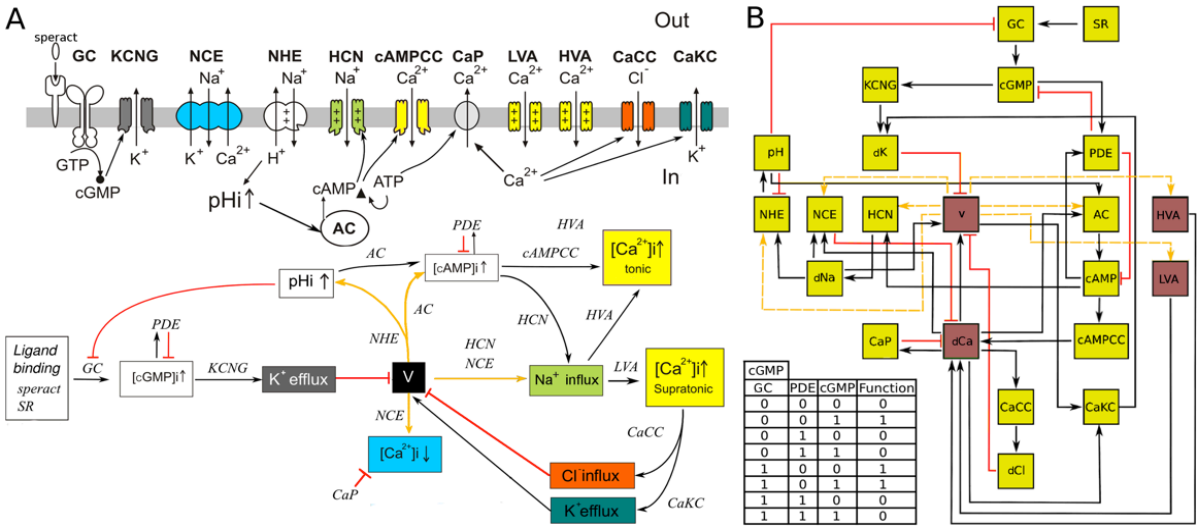

Fig. 1. A) Upper part: Schematic representaion of the components (ions, channels, molecules) of the signaling pathway triggered by speract in the sperm flagellum. Arrows traversing the membrane show ion fluxes. Arrows within the cell are indicative of causal relations. A) Bottom part: Signaling pathway operation diagram, black arrows correspond to activation, red lines to deactivation and yellow arrows can be activating or inhibitory depending on the relative state of the pathway elements being interconnected. Once speract binds to its receptor, several feedback loops are triggered according to the nature of the links involved. The concatenation of these loops leads to oscillatory stages of the whole pathway. The color code identifies the corresponding upper and lower part components. B) Network model of the signaling pathway. The network can be envisaged as a circuit where each node represents an element of the pathway and links, either in the form of arrows or lines, corresponding to connections determined in the bottom part of (A). The activating or inhibitory nature of the yellow lines depends on the value of voltage (V). Yellow nodes represent binary nodes (0, 1), and the four brown nodes are ternary nodes that can take values 0, 1 and 2. Changes in the node state are determined by the connected nodes, by means of a regulatory function (or truth table). As an illustration see the cGMP case at the bottom left of (B).

Acknowledgements

We acknowledge DGAPA-PAPIIT grant IN112514.

References

1. J. Espinal et al., "Discrete dynamics model for the speract-activated Ca^{2+} signaling network relevant to sperm motility", *PloS ONE*, 2011, **6**(8), e22619.B.
2. J. Espinal, A. Darszon, A. Guerrero, and G. Martínez-Mekler, In Silico Determination of the Effect of Multi-Target Drugs on Calcium Dynamics Signaling Network Underlying Sea Urchin Spermatozoa Motility, submitted to *Plos ONE*.
3. J. Espinal, A. Darszon, C. Beltrán, and G. Martinez-Mekler, "Network model reveals Catsper channel relevance to sea urechin sperm motility", to be submitted to *Molecular Systems Biology*.
4. J. Espinal, A. Darszon, and G. Martínez-Mekler, "Robustness and redundancy in calcium signalling network relevant to marine sperm motility", to be submitted to *Physical Biology*.

LIGHTNING: SOME NEW INSIGHTS

V.A. Rakov

Department of Electrical and Computer Engineering, University of Florida, USA
Institute of Applied Physics, Russian Academy of Science, Nizhny Novgorod, RF

Abstract. An overview of recent progress in studying the physics of cloud-to-ground lightning is given, including its initiation, propagation, and attachment to ground. Lightning electromagnetic pulse interaction with the ionosphere and production of energetic radiation (x-rays and gamma radiation) by lightning are considered. Some topics are outlined below.

Lightning leader stepping mechanism. Biagi et al. (2010), using a high-speed video camera (4.17-us frame integration time), imaged the bottom 150 m of a downward negative, dart‑stepped leader in a rocket‑and‑wire triggered flash. They observed vertically-elongated luminous formations, 1 to 4 m in length, that were separated by dark gaps, 1 to 10 m in length, from the bottom of the downward‑extending leader channel. These formations were similar to the space stems or space leaders that have been imaged in long negative laboratory sparks. Wang et al. (1999b), using a high-speed (100-ns sampling interval) digital optical imaging system (ALPS), reported observations of luminosity waves that originated at newly formed leader steps in a dart‑stepped leader and propagated toward the cloud. The spatial resolution of ALPS was about 30 m.

Lightning attachment process. Wang et al. (1999a) reported the first optical image of upward connecting leader in rocket-triggered lightning. Two dart-leader/return-stroke sequences, simultaneously recorded by the ALPS and by the electric field and current measuring systems, have been used for studying the lightning attachment process. The spatial resolution of ALPS was about 3.6 m. For one of the events the length of the upward connecting leader was estimated to be 7 to 11 m. The upward connecting leader was characterized by a light intensity about one order of magnitude lower than that of the corresponding downward leader and by a duration of several hundreds of nanoseconds. The following return stroke started at the junction point of the downward and upward leaders and then traveled in both upward and downward directions. Biagi et al. (2009), using high-speed video cameras (20-us frame integration time), recorded upward connecting leaders, ranging from 9 to 22 m in length, in eight strokes of a single rocket-triggered lightning flash.

X-rays produced by first and subsequent strokes in natural lightning. All types of negative leaders produce x-ray emissions with individual photon energies typically ranging from 30 to 250 keV (the latter being about twice the energy of a chest x-ray), although occasionally photons in the MeV range were observed. These emissions are associated with the descending leader tip and with the ground attachment process. It is likely that x-ray emissions from cloud-to-ground lightning leaders are associated with the so-called cold runaway (also known as thermal runaway) breakdown, in which very strong electric fields (>30 MV/m) cause the high-energy tail of the bulk free electron population to grow, allowing some electrons to runaway to high energies. Such very high fields may be present at streamer heads or leader tips. Mallick et al. (2012) reported that for 23 (8 first and 15 subsequent) strokes within 2 km of their observation site, the occurrence of detectable x-rays was 88 % and 47 % for first and subsequent strokes, respectively. Subsequent strokes were often more prolific producers of detectable x-rays than their corresponding first strokes. For first leaders, the maximum estimated x-ray source height did not exceed 800 m, whereas for subsequent leaders the source height distribution appeared to extend to as high as about 3.6 km. From non-detection of x-rays in association with some leaders within a flash and with some steps within the same leader, they inferred that the runaway breakdown was not a necessary feature of lightning leaders.

Acknowledgement

This work was supported in part by the U.S. National Science Foundation, the Nimbus Program, and the RF Government under Contract № 14.B25.11.0023.

References

1. C.J. Biagi, D.M. Jordan, M.A. Uman, J.D. Hill, W.H. Beasley, J. Howard, "High-speed video observations of rocket-and-wire initiated lightning", *Geophys. Res. Lett.*, 2009, **36**, L15801, doi:10.1029/2009GL038525.

2. C.J. Biagi, M.A. Uman, J.D. Hill, D.M. Jordan, V.A. Rakov, J.R. Dwyer, "Observations of stepping mechanisms in a rocket‐and‐wire triggered lightning flash", *J. Geophys. Res*., 2010, **115**, D23215, doi:10.1029/2010JD014616.
3. S. Mallick, V.A. Rakov, J.R. Dwyer, "A study of x-ray emissions from thunderstorms with emphasis on subsequent strokes in natural lightning", *J. Geophys. Res*., 2012, **117**, doi:10.1029/2012JD017555.
4. D. Wang, V.A. Rakov, M.A. Uman, N. Takagi, T. Watanabe, D.E. Crawford, K.J. Rambo, G.H. Schnetzer, R.J. Fisher, Z.-I. Kawasaki, "Attachment process in rocket-triggered lightning strokes", *J. Geophys. Res*., 1999 a, **104**, 2143–2150.
5. D. Wang, N. Takagi, T. Watanabe, V.A. Rakov, M.A. Uman, "Observed leader and return-stroke propagation characteristics in the bottom 400 m of a rocket-triggered lightning channel", *J. Geophys. Res*., 1999 b, **104**, 369–376.

CONTROL OF COMPLEX NETWORKS: INTERPLAY OF STRUCTURE AND DELAY

E. Schöll

Institut für Theoretische Physik, Technische Universität Berlin, 10623 Berlin, Germany
e-mail: schoell@physik.tu-berlin.de

Abstract. Time delayed coupling or feedback can be used to control the dynamics of complex networks. We study synchronization in delay-coupled oscillator networks, using a master stability function approach, and show that for large coupling delays synchronizability relates in a simple way to the spectral properties of the network topology, allowing for a universal classification. As illustrative examples we consider synchronization and desynchronization transitions in neural networks, in particular small-world networks with excitatory and inhibitory couplings, chimera states, and group and cluster synchronization. We show that adaptive algorithms of time-delayed feedback control can be used to find appropriate value of the control parameters, and one can even self-adaptively adjust the network topology to realize a desired cluster state.

Time delays arise naturally in many complex systems, for instance in neural networks or coupled lasers, as delayed coupling or delayed feedback due to finite signal transmission and processing times. Such time delays can either induce instabilities, multistability, and complex bifurcations, or suppress instabilities and stabilize unstable states. Thus, they can be used to control the dynamics [1, 2]. We study synchronization in delay-coupled oscillator networks, using a master stability function approach, and show that for large coupling delays synchronizability relates in a simple way to the spectral properties of the network topology, allowing for a universal classification [3]. As illustrative examples we consider synchronization and desynchronization transitions in neural networks, in particular small-world networks with excitatory and inhibitory couplings [4, 5], partial synchronization and chimera states [6, 7], and group and cluster synchronization in coupled chaotic lasers [8] and optoelectronic oscillators [9]. We show that adaptive algorithms of time-delayed feedback control can be used to find appropriate values of the control parameters [10], and one can even self-adaptively adjust the network topology to realize a desired cluster state.

An intriguing problem is the interplay of the local dynamics of the nodes with the topology of the net-work, which may have a complex structure like random, small-world, or scale-free. The master stability function is a powerful approach to the stability of synchronization in networks: It splits the linear stability problem into a local dynamical part (characterized by the largest Lyapunov exponent as a function of a complex parameter, i.e., the master stability function) and a topological part (determined by the eigenvalues of the coupling matrix). The synchronous state is stable if the master stability function is negative at all transverse eigenvalues. This approach has been generalized to include delay [3], and extended to the more general form of group synchronization, where the local dynamics on each node within a group is the same, but different for nodes in different groups. We have developed a general framework [8] for the characterization of the stability of different patterns of synchronized dynamics in networks with multiple delay times, multiple coupling functions, but also with multiple kinds of local dynamics in the network nodes. We found that the master stability function shows a discrete rotational symmetry depending on the number of groups, and illustrated our results for the example of delay-coupled semiconductor lasers and for a model for neuronal spiking dynamics. In collaboration with the group of R. Roy (University of Maryland, USA) we applied these results to a system of chaotic optoelectronic oscillators [9], and experimentally demonstrated group synchrony in a network of four nonlinear optoelectronic oscillators with time-delayed coupling.

The effect of the balance of excitatory and inhibitory couplings on synchronization in complex neuronal networks is also a topic of our investigations. Transitions between synchronization and desynchronization in networks of delay-coupled elements are studied for excitable dynamics of type I (i.e., near a saddle-node infinite period (SNIPER) bifurcation, where a saddle point and a stable node with heteroclinic connections collide and annihilate such that a limit cycle with finite amplitude and zero frequency is born.) [5], and type II (i.e., near a Hopf bifurcation) [4]. On the basis of the master stability function formalism, we demonstrate for the FitzHugh-Nagumo model (type II) that synchronization is always stable for excitatory (attractive) coupling independently of the delay and coupling strength [4]. Superimposing inhibitory (repulsive) links randomly on top of a regular ring of excitatory coupling, which creates a small-world-like network topology, we find a phase transition to desynchronization as the probability of inhibitory links exceeded a critical value. Compared to random

networks, we find that small-world topologies are more susceptible to desynchronization via inhibition. Using a generic model for type-I excitability [5], we investigate the stability of the zero-lag synchronized dynamics of the network nodes and its dependence on the coupling strength and delay time. Unlike in the FitzHugh-Nagumo model (type-II excitability), we find parameter ranges where the stability of synchronization depends on the coupling strength and delay time, with the important implication that there exist complex networks for which adding inhibitory links in a small-world fashion may not only lead to a loss of stable synchronization, but may also re-stabilize synchronization or introduce multiple transitions between synchronization and desynchronization.

An important goal with respect to the design of novel concepts of control is the combination of time-delayed feedback control with methods from the classical theory of adaptive control and optimization, which is particularly useful in case of unknown or drifting parameters. In cooperation with the group of A.L. Fradkov of St. Petersburg State University, Russia, we derived an adaptive control algorithm for cluster synchronization in delay-coupled networks of Stuart-Landau oscillators based on the speed-gradient method minimizing some cost function [10]. Following this procedure, the control parameters are no longer kept constant, but become time-dependent. Thus, one has to consider additional differential equations for the automatic tuning of these parameters. We propose cost functions based on a generalized Kuramoto order parameter, and demonstrate that the speed-gradient method allows one to find appropriate coupling phases, coupling strengths, and delay times, with which a desired state of synchrony, e.g., in-phase oscillation, splay, or various cluster states, can be selected from an otherwise multistable regime.

Acknowledgements

This work was supported by DFG in the framework of Sfb 910. I am indebted to stimulating collaboration and discussion with T. Dahms, B. Fiedler, V. Flunkert, A. Fradkov, A. Gjurchinovsky, A. Hagerstrom, P. Hövel, M. Kapeller, A. Keane, J. Lehnert, Y. Maistrenko, T. Murphy, I. Omelchenko, O. Omel'chenko, R. Roy, A. Selivanov, J. Siebert, S. Yanchuk, A. Zakharova.

References

1. E. Schöll and H.G. Schuster (Eds.), *Handbook of Chaos Control* (Wiley-VCH, 2008).
2. V. Flunkert, I. Fischer, and E. Schöll (Eds.), "Dynamics, control and information in delay-coupled systems", *Theme Issue of Phil. Trans. R. Soc. A*, 2013, **371**, 20120465.
3. V. Flunkert, S. Yanchuk, T. Dahms, and E. Schöll, "Synchronizing distant nodes: a universal classification of networks", *Phys. Rev. Lett.*, 2010, **105**, 254101.
4. J. Lehnert, T. Dahms, P. Hövel, and E. Schöll, "Loss of synchronization in complex neural networks with delay", *Europhys. Lett.*, 2011, **96**, 60013.
5. A. Keane, T. Dahms, J. Lehnert, S. A. Suryanarayana, P. Hövel, and E. Schöll, "Synchronisation in networks of delay-coupled type-I excitable systems", *Eur. Phys. J. B*, 2012, **85**, 407.
6. C. Cakan, J. Lehnert, and E. Schöll, "Heterogeneous delays in neural networks", *Eur. Phys. J. B*, 2014. **87**, 54.
7. A. Hagerstrom, T.E. Murphy, R. Roy, P. Hövel, I. Omelchenko, and E. Schöll, "Experimental observation of chimeras in coupled-map lattices", *Nature Physics*, 2012, **8**, 658; I. Omelchenko, O.E. Omel'chenko, P. Hövel, and E. Schöll, "When Nonlocal Coupling Between Oscillators Becomes Stronger: Patched Synchrony or Multichimera States", *Phys. Rev. Lett.*, 2013, **110**, 224101; A. Zakharova, M. Kapeller, and E. Schöll, "Chimera death: Symmetry breaking in dynamical networks", *Phys. Rev. Lett.*, 2014, **112**, 154101.
8. T. Dahms, J. Lehnert, and E. Schöll, "Cluster and group synchronization in delay-coupled networks", *Phys. Rev. E*, 2012, **86**, 016202.
9. C.R.S. Williams, T.E. Murphy, R. Roy, F. Sorrentino, T. Dahms, and E. Schöll, "Experimental observation of group synchrony in a system of chaotic optoelectronic oscillators", *Phys. Rev. Lett.*, 2013, **110**, 064104.
10. A.A. Selivanov, J. Lehnert, T. Dahms, P. Hövel, A.L. Fradkov, and E. Schöll, "Adaptive synchronization in delay-coupled networks of Stuart-Landau oscillators", *Phys. Rev. E*, 2012, **85**, 016201.

STATE ESTIMATION AND UNCERTAINTY QUANTIFICATION IN THE ATMOSPHERE AND THE OCEAN

O. Talagrand[1], M. Jardak[1], G. Candille[1], and **L. Descamps[2]**

[1]Laboratoire de Météorologie Dynamique, École Normale Supérieure
Paris, France, talagrand@lmd.ens.fr
[2] Météo-France, Toulouse, France

Abstract. Estimation of the state of the atmospheric or oceanic flow, as well as of the associated uncertainty, is crucial for many applications. We present and discuss the methods that are used at present for assimilation of observations, in which an appropriate description of the propagation of uncertainty in the dynamical evolution of the flow is absolutely necessary. Similar questions arise in the context of the prediction of the future state of the flow. Emphasis is put on the Bayesian character (or otherwise) of the methods, and on their possible limitations.

Uncertainty is ubiquitous in science and technology, and often needs to be accurately quantified. This is particularly true of geophysical systems such as the atmosphere or the ocean. In view of the very broad spectrum of spatial and temporal scales over which they evolve, both systems are very difficult (and costly) to observe. They are in addition nonlinear, and actually chaotic, making it particularly difficult to predict their future evolution.

Assimilation of observations

Assimilation of observations, which originated from the need to define initial conditions to numerical weather predictions, is the process by which observations of the atmospheric or oceanic flow are combined together with a numerical model of the dynamics of the flow. The numerical dimension of the problem (the state vector of a model for numerical weather prediction can have dimension as large as 10^9), together with the complexity of the underlying dynamics (not to mention the need for the forecast to be ready in time…), make assimilation a particularly challenging problem.

In view of the significant uncertainty affecting both the observations and our knowledge of the underlying dynamics, assimilation of observations is best expressed as a problem in *Bayesian estimation*. Namely, determine the probability distribution for the state of the system under observation, conditioned to the available information. The main difficulty is actually to describe in a practically useful way the evolution of the uncertainty on the state of the system. The main two present types of assimilation algorithms, *Variational Assimilation* (VA) on the one hand, and *Ensemble Kalman Filter* (*EnKF*) on the other, are both empirical extensions, to weakly nonlinear situations, of Best Linear Unbiased Estimation (BLUE), which achieves Bayesian estimation in linear and Gaussian cases. Variational Assimilation globally adjusts a model solution to observations distributed over a period of time. Ensemble Kalman Filter evolves in time an ensemble of estimates of the system state, meant to span at any time the uncertainty of the state of the flow. It updates those estimates, following a basically Gaussian scheme, as new observations become available.

Particle Filters, like EnKF, evolve an ensemble of state estimates, but use an exactly Bayesian updating scheme. However, their cost has so far been too high for use for large dimension systems. Their performance and possible future evolution are discussed.

Assimilation is closely linked to the instabilities in the observed system, and essentially consists in a sense in monitoring and controlling those instabilities. The links between assimilation and instabilities are discussed, and two specific algorithmic procedures are presented in this context: *Quasi-Static Variational Assimilation* (*QSVA*) and *Assimilation in the Unstable Subspace* (*AUS*).

Ensemble Kalman Filter and Particle Filters, which both produce an ensemble of estimates of the system state, are explicitly probabilistic. Results are presented of the performance of an ensemble probabilistic form of Variational Assimilation.

Prediction

Similar questions arise in the context of prediction. Ensemble methods have been developed for Numerical Weather Prediction. These methods are discussed, and their performance described. They have led to significant progress, in particular as to the confidence that can be granted to numerical forecasts.

Probabiistic Estimation

Objective evaluation of the performance of probabilistic evaluation systems is discussed as a question in itself. The two properties that make the quality of such systems are *reliability* and *resolution*. The former is statistical consistency between predicted probabilities and observed frequencies of occurrence. The latter is the capacity of *a priori* distinguishing between different occurrences. A number of objective scores measure the degree to which a probabilistic estimation system possesses those two properties. In the case of atmospheric applications, scores saturate for ensemble dimension in the range of a few tens. This is shown to result from the fact that the validation sample in such applications will always in some sense be very small, thus imposing strong limits as to what can be expected from probabilistic estimation methods.

Acknowledgements

This research has been done in part on the occasion of the *Prevassemble* projet, funded by the French Agence Nationale pour la Recherche.

THE CLASSICAL LIMIT OF RADIATION REACTION EFFECTS IN ULTRAINTENSE LASER FIELDS

M. Tamburini, A. Di Piazza and **Ch.H. Keitel**

Max-Planck-Institut für Kernphysik, Heidelberg, Germany
Matteo.Tamburini@mpi-hd.mpg.de

Abstract. The dynamics of an electron in a strong laser field can be significantly altered by radiation reaction (RR) effects. Here the features and the implications of RR effects in the classical limit are discussed. In particular, the influence of RR effects on laser-driven ion acceleration in the radiation pressure acceleration regime is examined. In addition, a novel route to the control of the electron dynamics via the nonlinear interplay between the Lorentz and RR forces is presented.

Introduction

Next-generation 10-PW optical laser systems are expected to achieve intensities beyond 10^{23} W/cm^2 [1, 2], and laser pulses with power beyond 100-PW and intensity up to 10^{25} W/cm^2 are envisaged at the Extreme Light Infrastructure (ELI) [3] and at the eXawatt Center for Extreme Light Studies (XCELS) [4]. At such ultrahigh intensities, an electron becomes relativistic in a fraction of the laser period and its dynamics is dominated by radiation reaction (RR) effects, i.e., by the back reaction on the electron's motion of the radiation emitted by the electron itself while being accelerated by the laser field [2]. Hence, a deep understanding of RR effects is crucial for the design and the interpretation of future laser-matter experiments in the ultrarelativistic regime.

In the first part of the talk the main features of RR effects and their description in terms of a RR force are briefly discussed. In particular, it is stressed that the presence of the RR force leads to a qualitatively different collective plasma dynamics, which is accounted for by a generalized Vlasov equation [5]. Some new effects induced by the RR force such as the contraction of the electron phase space [5], the formation of attractors [6] , the noticeable enhancement in the growth rate of parametric instabilities [7] , and RR induced electron trapping [8] are mentioned.

RR effects on radiation pressure acceleration

In the second part of the talk, RR effects on ion acceleration in superintense laser foil interaction are examined. On the one hand, no significant RR effect is present for circularly polarized laser pulses whenever the laser pulse breaks through the foil [9, 10]. On the other hand, the RR force strongly affects the dynamics for a linearly polarized laser pulse, reducing the maximum ion energy and also the width of the spectrum [9, 10]. This is explained by the strong longitudinal motion driven by the oscillating component of the **J×B** force, which noticeably increases the penetration of the laser pulse inside the plasma [9], and is suppressed for a circularly polarized laser pulse. However, in the relativistic nonlinear transparency regime, RR effects become important both for linearly and circularly polarized laser pulse and enhance the ion energy gain [9–11].

Novel perspectives: electron dynamics control via self-interaction

To date, the research has focused on revealing RR effects and understanding their fundamental features rather than exploiting them in a possibly beneficial and controlled way. In the third part of the talk we show that RR effects can even provide a route to the control of the electron dynamics via the nonlinear interplay between the Lorentz and RR forces. This is achieved in a setup where an ultrarelativistic electron is exposed to a strong either few-cycle [12] or bichromatic laser pulse. Our exact analytical calculations for a plane-wave pulse and our more realistic numerical simulations for a focused laser pulse show that, already at the intensities achievable with state-of-the-art laser systems, an ultrarelativistic electron colliding head-on with a bichromatic laser pulse can be deflected in an ultrafast and controlled way within a cone of about 8° aperture independently of the initial electron energy [13]. At still higher intensities, the interplay between the RR and the Lorentz force can even overcome the radiation losses themselves, resulting in a RR assisted electron acceleration instead of damping [13].

References

1. A.V. Korzhimanov, A.A. Gonoskov, E.A. Khazanov, and A. M. Sergeev, *Phys. Usp*., 2011, **54**, 9.
2. A. Di Piazza, C. Müller, K.Z. Hatsagortsyan, and C.H. Keitel, *Rev. Mod. Phys*., 2012, **84**, 1177.

3. http://www.eli-laser.eu/
4. http://www.xcels.iapras.ru
5. M. Tamburini, F. Pegoraro, A. Di Piazza, C.H. Keitel, T.V. Liseykina, A. Macchi, *Nucl. Instrum. Meth. Phys. Res. A*, 2011, **653**, 181.
6. G. Lehmann, K.H. Spatschek, *Phys. Rev. E*, 2012, **85**, 056412.
7. N. Kumar, K.Z. Hatsagortsyan, and C.H. Keitel, *Phys. Rev. Lett.*, 2013, **111**, 105001.
8. L.L. Ji, A. Pukhov, I.Yu. Kostyukov, B.F. Shen, and K. Akli, Phys. Rev. Lett., 2014, **112**, 145003.
9. M. Tamburini, F. Pegoraro, A. Di Piazza, C.H. Keitel, and A. Macchi, *New J. Phys*., 2010, **12**, 123005.
10. M. Tamburini, T.V. Liseykina, F. Pegoraro, and A. Macchi, *Phys. Rev. E*, 2012, **85**, 016407.
11. M. Chen, A. Pukhov, T.-P. Yu, and Z.-M. Sheng, *Plasma Phys. Control. Fusion*, 2011, **53**, 014004.
12. M. Tamburini, A. Di Piazza, T.V. Liseykina, and C.H. Keitel, *Phys. Rev. Lett.*, *in press*; arXiv:1208.0794.
13. M. Tamburini, C.H. Keitel, and A. Di Piazza, *Phys. Rev. E*, 2014, **89**, 021201(R).

PROGRESS OF CERAMIC LASERS AND THERMAL-LENS FREE COOLING

Ken-ichi Ueda

Inst. for Laser Science, Univ. Electro-Communications, Tokyo, Japan
Inst. of Laser Engineering, Osaka Univ. Suita, Osaka
Hamamatsu Photonics, Hamamatsu, Hamamatsu, Japan
Toyota Physical and Chemical Institute, Nagakute, Aichi Japan
Mega Grant Russia, Inst. Applied Physics, Nizhny Novgorod, Russia
ueda@ils.uec.ac.jp

1. Introduction

Until today, the major scaling technique to generate high output is an aperture scaling because the output power is limited by the damage threshold. We need a large aperture amplifier for high power output. LLNL (Lawrence Livermore National Laboratory) developed 40×40 cm power glass amplifiers for NIF (National Ignition Facility) to achieve the ignition of laser fusion. The NIF laser is a largest laser system in the human history. A scalable glass laser system was only one possibility to generate MJ, EW power output. However, such type of scaling law is not so available any more because the new frontiers of science request high peak & high average power all together. We need a paradigm shifting technology in laser materials and power scaling technique. Ceramic laser and coherent beam combining are the keys to break the bottleneck.

2. Recent progress of Ceramic Laser

Among the solid state lasers, a crystalline laser has better spectroscopic, mechanical and physical, and thermo-optical properties than a glass laser. The only one disadvantage is the mass production and possible cost. Ceramic laser solves most of these problems, because it is a glass-like fabricated polycrystalline material. There were many demostrations of high power and high efficiency operation in the last 15 years. Today we have several plans to develop 10–100 J ceramic lasers which operate more than 10 Hz by LD pumping.

We organize LCS meetings to stimulate and encourage the ceramic laser technology every year. In 2013 we had significant progress in ceramic techniques, such as "single crystal quality ceramic" laser by not only wet chemical method but also reactive sintering method, "ceramic fiber", "nano-imprinting on the ceramic surface", and "solid state single crystal growing (SSCG)" (Fig. 1). We understood SSCG has a big potential for our future, because the growing speed of SSCG is as fast as 10 cm/h to m/h. This is quite surprising for us, and we need new crystal growing physics in this field. Please remind that most important key technology on semiconductor technology is an epitaxial crystal growing technique. Without this epitaxial growth, we can not get any high quality semiconductor wafers with high quality. We discuss the future of the single crystal growing by SSCG method in the paper.

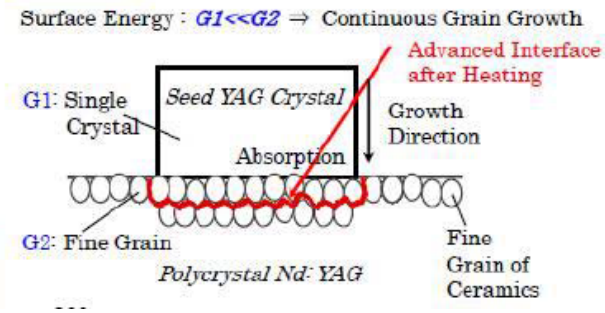

Fig. 1. Solid State Crystal Growing

3. Cooling efficiency to flat temperature profile

How to develop a thermal-lens-free solid state laser? This is a big issue because the cooling mechanism of a solid state laser is thermal conduction. The calculation of the temperature profile of an end-cooled rod (disk) was carried out as a function of aspect ratio (L/D). The temperature profiles of end-cooled disk/rod under the center-half pumping are shown in Fig. 2. We calculated the integrated thermal lens effect along the rod axis under the constant deposited energy as shown in Fig. 3. The

thermal-lens-decay curves are linear (slope = 2) in log-log plot for the thin disk regime (L/D < 0.1) and are saturated at 10 ms for the rod regime (L/D > 1). These are analyzed as a cooling dominant case and a thermal diffusion dominant case. The cooling time constant for 1/10 decay is $T_{1/10} = kL^2$ for thin disk lasers and the lateral diffusion time constant for 1 cm rod is 10 ms. L^2 property is a result of high thermal gradient, that is a product of deposition density and thickness.

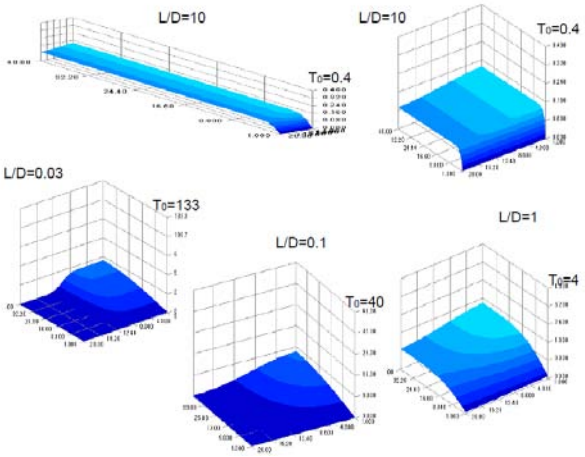

Fig. 2. Cooling profiles of end-cooled rod/disk lasers

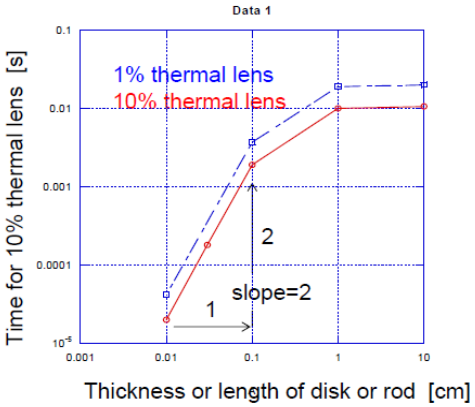

Fig. 3. Decay time of thermal lens vs aspect ratio

4. HDD laser for high efficiency cooling

What is the most efficient cooling technique in the laser history? It should be exhaustion technique. High speed flow in gas and liquid lasers is an efficient way to remove heat from lasing volume. Fast flow gas laser systems were developed for industrial applications and even for IFE driver ELECTRA, NRL. For the next generation beam combining technique, smaller is always better in wavefront distortion. How about the moving solid state lasers? The high density solid material means the large heat capacity. It is a big advantage for moving solid state lasers. From our calculation the heat removal power is more than 1600 times larger than KrF gas laser as shown in Fig. 4. When the major cooling mechanism is collisional gas cooling from the surface, the solid state laser has no optical distortion. The possibility of high speed moving solid state gain medium should be considered seriously again.

Solid state laser vs Gas laser

	YAG		KrF	Ratio
density [g/cc]	4.55	>>	0.00498	914
Specific heat [J/g/K]	0.59	>	0.33	1.79
Specific heat [J/cc/K]	2.68	>>	0.00164	1634
Moving speed [m/s]	14 m/s	>	7.8 ms	comparable
	for 3.5"" HD drive @7200 rpm		in ELECTRA @ 5 Hz operation	

Fig. 4. Cooling power: solid state laser vs gas laser

There have been proposals on the moving solid state lasers, moving slab, rotary tube and rotary disk. For the stable operation the rotary disk regime should be better than the others because the driving power is smaller and technical matching to the LD pumping is good.

A hard disk drive (HDD) shown in Fig. 5 is widely used in PC technology and video players. Typical HDD has four platters with 3.5 inches in diameter. A HDD of less than $50 can be converted to the rotary thin disk amplifier with four transmission-type thin disks. The rotating speed is 7200 rpm, it means 120 Hz by only 2.4 W power dissipation. The thickness of ceramic disk platter in the typical HDD is 0.63 mm. This corresponds to the optimum thickness of thin disk laser in the transmission geometry. The cooling power scaling is dependent on the ratio of cooling area to heating area as shown in Fig. 6. According to the cooling scaling for 5 mm pumping area, the cooling power is 1600 times larger than the static thin disk scheme. More than 1600-times larger cooling power is powerful enough to develop thermal-lens-free ceramic lasers. In addition, a transmission optics is always better

from the point of wavefront distortion. This is another fundamental advantage of high speed rotary disk amplifier.

When we use transmitting rotating thin disk amplifiers, the amplifier system looks like in Fig. 5. A high speed rotary transmission thin disk is a possible future for us to realize thermal-lens-free and scalable solid state lasers for coherent beam combining technology.

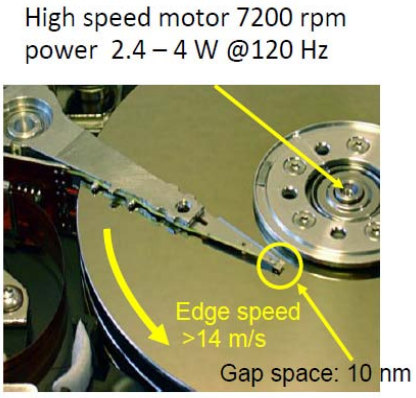

Fig. 5. High speed rotary disks in HDD

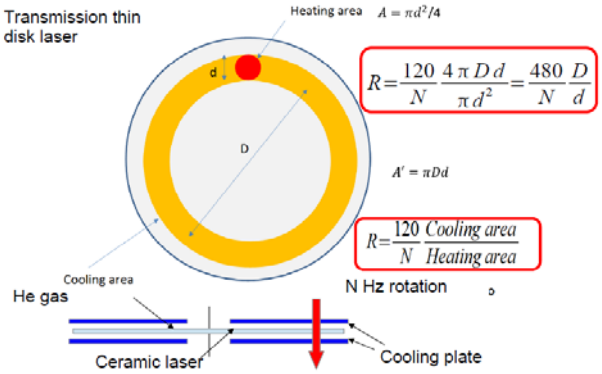

Fig. 6. Cooling enhancement in rotary disk geometry

5. Summary

For the next generation of solid state laser technology, we proposed several key ideas, ultra-low loss ceramic fabrication, solid state single crystal growth, end-cooled rod/disk geometry for flat temperature profile, high speed rotary disk using HDD technology. We need much more effort to develop robust and mass productive module for the thermal-lens-free solid state laser unit for coherent beam combination.

International Symposium

TOPICAL PROBLEMS OF NONLINEAR WAVE PHYSICS

NWP-1:

NONLINEAR DYNAMICS ON COMPLEX NETWORKS

Invited

SYNCHRONIZATION OF COUPLED NEARLY IDENTICAL DYNAMICAL SYSTEMS

S. Acharyya[1] and **R.E. Amritkar**[2]

[1] Physical Research Laboratory, Ahmedabad, India, suman@prl.res.in
[2] Institute of Infrastructure, Technology, Research and Management, Ahmedabad, India
ravin012@gmail.com

Abstract. We study the stability of generalized synchronization by obtaining an approximate master stability function (MSF) in a network of coupled nearly identical dynamical systems. We show that in the star network of coupled Rössler systems, the critical size beyond which synchronization is unstable can be increased by having a larger frequency for the central node. For the ring network, the critical size is not significantly affected. Next we use the MSF to construct optimized networks which show better synchronizability. Optimized network shows interesting structural properties, e.g. in the optimized network, nodes with higher frequencies, have higher degrees and are chosen as hubs.

Master stability function for nearly identical oscillators

An important tool for the study of stability of complete synchronization of coupled identical oscillators is the master stability function (MSF), introduced by Pecora and Carroll [1]. In practical world, most of the interacting dynamical systems are nonidentical in nature and instead of complete synchronization they show generalized synchronization, i.e. a functional relationship between the variables. Thus, to better understand synchronization processes of natural systems we construct a master stability function for generalized synchronization [2].

Consider a network of N coupled nearly identical chaotic oscillators with dynamics

$$\dot{x}_i = f(x_i, r_i) + \varepsilon \sum_{j=1}^{N} g_{ij} h(x_j), \quad i = 1, \ldots, N, \tag{1}$$

where $x \in R^m$ is m dimensional state variable and $f, g : R^m \to R^m$ define the dynamics of the isolated oscillator and their coupling, ε is scalar coupling strength, G is coupling matrix. r_i is some parameter of the dynamics that depends on oscillator i and we call it a node dependent parameter (NDP). Master stability equation for this system is given by [2]

$$\dot{\eta} = [D_x f + \alpha D_x h + \nu_r D_r D_x f]\eta. \tag{2}$$

We call α a network parameter and ν_r a mismatch parameter.

The master stability function (MSF) is defined as the largest Lyapunov exponent calculated from Eq. (2). For a given network, we determine the eigenvalues and eigenvectors $\gamma_i, \phi_i, i = 1, \ldots, N$ of the coupling matrix G arranged in decreasing order. Next we determine $\nu_i = \phi^T R \phi$, where $R = diag(\delta r_1, \ldots, \delta r_N)$. If the MSF is negative for all $\alpha = \varepsilon\gamma_i$ and $\nu_r = \nu_i, i = 2, \ldots, N$, i.e. the transverse components, then the synchronization is stable.

We consider an example of x–coupled nearly identical Rössler oscillators

$$(\dot{x}_i, \dot{y}_i, \dot{z}_i) = \left(-\omega_i y_i - z_i + \varepsilon \sum_j^N g_{ij} x_j, \omega_i x_i + a y_i, b + z_i (x_i - c)\right),$$

where the frequency parameter ω is the NDP. The MSF for nearly identical Rössler oscillators is shown in Fig. 1(a). From Fig. 1(a) we can see that the negative region of the MSF increases as the mismatch parameter ν_ω increases.

Size instability

By size instability one refers to a critical number of oscillators that can be coupled in a well structured network to obtain synchronization and beyond this critical number no stable synchronization can be seen.

For a star network of x–coupled identical Rössler oscillators, we have $N_c = 32$. For nearly identical oscillators, if one chooses the frequency of the central node to be 1.05 and the average frequency 1.0, then $N_c = 35$. Thus, we see that the non-identical nature of the oscillators can be put to good use by judicious choice of the frequencies for different nodes to increase N_c.

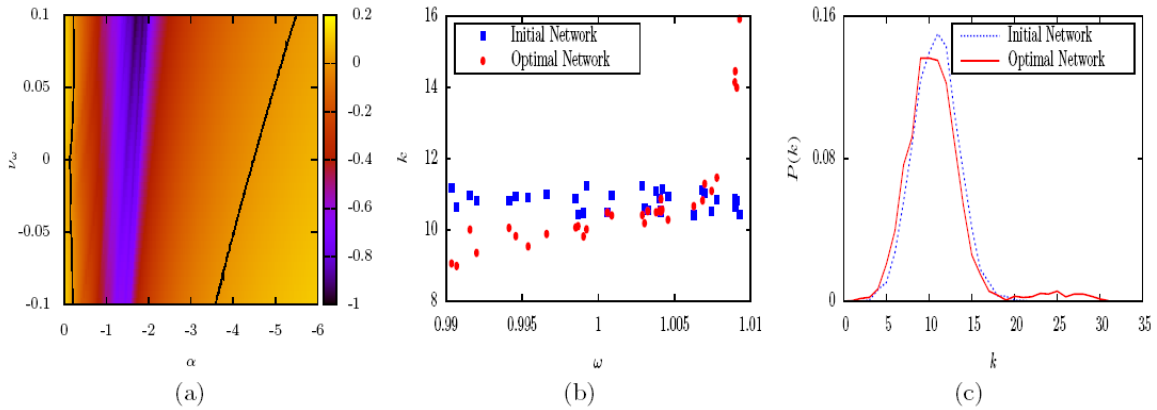

Fig. 1. (a) The color map of the MSF for coupled nearly identical Rössler systems with the frequency ω_i as the NDP is shown on the α–ν_ω plane. Here, we take the coupling matrix to be symmetric so that α and ν_ω are real. The zero values of the MSF are shown by two curves. We can see that the stability of MSF increases as ν_ω increases. The other Rössler parameters are $a = b = 0.2$; $c = 7.0$. (b) The degree k of the nodes of the initial network (blue squares) and optimized network (red circles) are plotted as a function of the NDP ω for 32 coupled Rössler oscillators. The nodes with higher ω value have higher degree. (c) The degree distribution $P(k)$ of the initial network (blue dotted line) and the optimal network (red solid line) are shown as a function of k. For the degree distribution of optimal network a very small peak at higher degree value is seen. These results are averaged over 100 runs.

In a ring network, for x–coupled identical Rössler oscillators $N_c = 17$. For nearly identical oscillators, N_c does not change significantly.

Synchronization optimized networks

Now, we address the problem of constructing optimized networks with better synchronizability for coupled nearly identical oscillators. Let l_ε be the range of ε values for which synchronization is stable. By better synchronizability we mean that l_ε is maximum for the optimal networks. We start with a random network of N number of nodes, M number of edges and carry out the optimisation using Metropolis algorithm and by rewiring the network with N and M fixed.

Figure 1(b) and (c) compares the degree distribution of the random and optimised networks. We see that in the optimised network, the degree of nodes with larger frequency is larger compared to other nodes. We have investigated several other structural properties of optimised networks. In the optimised network compared to random network, some important results are as follows. (i) The nodes with larger frequency have larger degree, i.e. these nodes act as hubs. (ii) The edges are preferably between nodes which have large frequency differences. (iii) There is an overall increase in the clustering coefficients with the increase being smaller for nodes with larger and smaller frequencies. (iv) The betweenness centrality of nodes with larger frequencies is larger. (v) The closeness centrality of nodes with larger frequencies is larger. (vi) The optimized network is disassortative.

To conclude, we have investigated the stability of synchronization of nearly identical oscillators. The nearly identical nature can be judiciously used to increase the critical size of the network in size instability. We construct optimised networks with better synchronizability. We find that the non-identical nature of the oscillators has an important bearing on the structural properties of optimised networks.

References

1. L.M. Pecora and T.L. Carroll, *Phys. Rev. Lett.*, 1998, **80**, 2109-2112.
2. S. Acharyya and R.E. Amritkar, *EPL*, 2012, **99**, 40005-1-6.

Invited

POINCARÉ RECURRENCES IN THE STROBOSCOPIC SECTION OF A NONAUTONOMOUS VAN DER POL OSCILLATOR

N.I. Semenova and **V.S. Anishchenko**

Saratov State University, Saratov, Russia, wadim@info.sgu.ru

Abstract. In the present work we analyze the statistics of a set which is obtained by calculating a stroboscopic section of phase trajectories in a harmonically driven van der Pol oscillator. It is shown that this set is similar to the linear shift on a circle with an irrational rotation number which is defined as the detuning between the external and natural frequencies. The dependence of minimal return times on the size ε of the return interval is studied numerically for the golden ratio. Furthermore, it is also found that in this case, the value of the Afraimovich-Pesin dimension is $\alpha_C = 1$.

In recent years a new approach arises in the classical problem of Poincaré recurrences in Poisson-stable systems [1–3]. This fact is related to the problem of statistics of recurrences in a whole set of phase trajectories of a system (the global approach) [4, 5]. In the present work we analyze the shifts on the circle with irrational rotation numbers ρ in the global approach:

$$x_{n+1} = x_n + \Delta, \ \mathrm{mod}\, 2\pi, \ \Delta = 2\pi\rho. \tag{1}$$

The set $\{x_n, \mathrm{mod}\, 2\pi\}$ produced by the map (1) exemplifies a simple minimal set with irrational ρ. The recurrence theory has been developed for this set [5] and the following results are used in this work. The irrational rotation number ρ in (1) can be approximated by the ratio of two integers m_i and n_i (i=1,2,…). In this case the rate of rational approximations for $i\to\infty$ is defined by the measure of irrationality μ

$$\left|\rho - \frac{m}{n}\right| < \frac{C}{n^{\mu}}. \tag{2}$$

It has been proven in [5] that for the circle map (1)

$$\ln\left\langle \tau_{\inf}(\varepsilon)\right\rangle \sim -d \ln\varepsilon / \nu(\rho), \ \varepsilon << 1, \ \mathrm{d} = 1. \tag{3}$$

Here $\langle\tau_{\inf}(\varepsilon)\rangle$ is a mean minimal return time which is defined by covering the whole set of (1) with elements ε. $\nu(\rho)$ is the maximal rate of Diophantine approximations of an irrational number ρ over all possible pairs of m and n in (2), d is a fractal dimension of the set which is equal to unity for (1). It has been proved in [4, 5] that in the general case for ergodic sets with zero topological entropy, the following expression is valid:

$$\ln\left\langle \tau_{\inf}(\varepsilon)\right\rangle \sim -d \ln\varepsilon / \alpha_C, \quad \varepsilon << 1, \tag{4}$$

where α_C is the Afraimovich-Pesin dimension. When (3) is compared with (4), it is apparent that $\alpha_C = \nu(\rho)$ for the shifts on the circle (1). In this case the AP dimension coincides with the rate $\nu(\rho)$ of Diophantine approximations. Since $\nu(\rho) = \mu - 1$ for Diophantine approximations, we have $\alpha_C = 1$ [4].

The theoretical results for the circle map (1) have been confirmed numerically in [6]. The universal dependence $\tau_{\inf}(\varepsilon)$, the so-called "Fibonacci stairs", has been obtained for this system. This dependence is depicted in Fig. 1,a for $\rho = (5^{1/2} - 1)/2$ which is often called the golden ratio. The Fibonacci stairs has several properties, which are as follows.

1. When ε decreases, the sequence of $\tau_{\inf}(\varepsilon)$ strictly corresponds to the basic Fibonacci series (Fig. 1, a).
2. When ε changes within any stairs step, three return times $\tau_1 < \tau_2 < \tau_3$ exist and $\tau_3 = \tau_1 + \tau_2$, and $\tau_1 = \tau_{\inf}$.
3. Lengths and heights of the stairs in Fig. 1,a are defined by the rotation number, i.e., $\Delta = -\ln\rho$.

We consider a nonautonomous van der Pol oscillator which is described by the system of equations:

$$\begin{cases} \dot{x} = y, \\ \dot{y} = \alpha(1 - x^2)y - \omega_0^2 x + A\sin\Omega t, \end{cases} \tag{5}$$

where $\alpha > 0$ is the excitation parameter, ω_0 is the basic frequency of the self-sustained oscillations, A and Ω are the amplitude and the frequency of the external force. The set which we are interested in can be formed by using the polar coordinate system in (5). Doing this we can turn from (5) to the set of equations for the amplitude and phase:

$$\dot{a} = (1 - a^2\cos^2\psi)\alpha a\sin^2\psi - \frac{\Omega^2 - \omega_0^2}{2\Omega}a\sin 2\psi - \frac{A}{\Omega}\sin\psi\sin\Theta$$
$$\dot{\psi} = \Omega + (1 - a^2\cos^2\psi)\frac{\alpha\sin 2\psi}{2} - \frac{\Omega^2 - \omega_0^2}{2\Omega}(\cos 2\psi - 1) - \frac{A}{\Omega}\cos\psi\sin\Theta \qquad (6)$$
$$\dot{\Theta} = \Omega$$

where a and ψ are the amplitude and phase of the van der Pol oscillator (5) in the polar system of coordinates, Θ is the phase of the external force ($\Theta = \Omega t$).

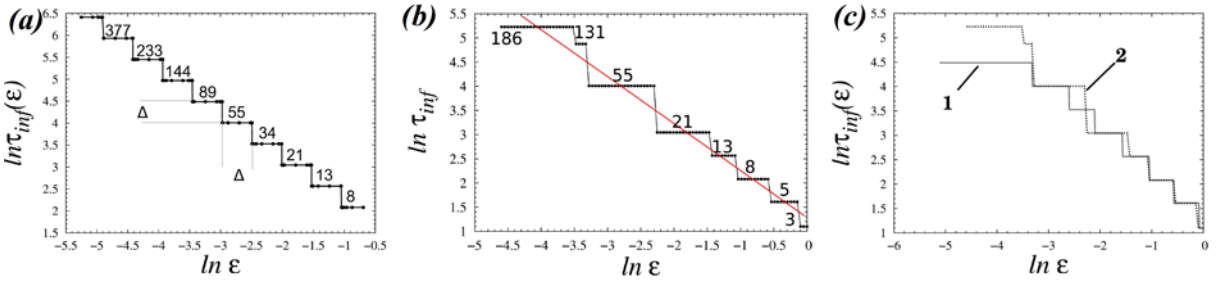

Fig. 1

We now consider a stroboscopic section by calculating a and ψ through the period of the external force $T = 2\pi/\Omega$. The phase of each subsequent point is changed following the law (1). The set of points in the stroboscopic section of the system (6) is similar to the circle map with $a = 2 = \text{const}$.

The rotation number ρ is the mean increment of the angle over one iteration of the map with respect to the total angle. The dependence of the rotation number on Ω for the fixed parameters $\alpha = 0.1$, $\omega_0 = 1$ and $A = 0.1$ conforms to the dependence $\rho = \omega_0/\Omega$.

We are interested in the case of the golden ratio ($\rho = 0.5(5^{1/2} - 1)$) which agrees with the external force frequency $\Omega = 1.61637276$. Let us calculate the dependence $\langle\tau_{\text{inf}}(\varepsilon)\rangle$ in the stroboscopic section of the system (6) for $\omega_0 = 1$ and $\Omega = 1.61637276$. The results are shown in Fig. 1,b. In the region of relatively large values $-2.5 < \ln\varepsilon < 0$ there is a sufficiently good agreement with the universal properties which have been established for the linear circle map. The universality of the Fibonacci stairs for the numerical data shown in Fig. 1, b is violated in the range of small values $\ln\varepsilon < -2.5$. Our calculations have shown that as ε decreases, the error of calculation of τ_{inf} increases. This is related to the fact that the parameters of the differential system (6) are difficult to select so that ρ is equal exactly to the golden ratio. The influence of this accuracy can be estimated numerically by considering the map (1) in the presence of Gaussian noise: $x_{n+1} = x_n + \Delta + \sqrt{2D}\xi(n)$, where D is the intensity of Gaussian noise. Taking into account the fact that the dependence in Fig. 1, b is calculated for the rotation number given with the accuracy $\approx 10^{-8}$, the noise intensity in (7) is set to be $D = 5\cdot 10^{-7}$. The calculation results are shown in Fig. 1, c. It can be seen that the dependence $\ln\tau_{\text{inf}}(\varepsilon)$ for the noisy system (Fig. 1, c, curve 1) is similar to that shown in Fig. 1, b (Fig 1, c, curve 2). The slope of the experimental data in Fig. 1, b over the range of ε variation ($-2.5 \le \ln\varepsilon < 0$) is $|k| = 1.02$. This means that $\alpha_C = \nu(\rho) = 1$ and there is a full correspondence between the theoretical results and the numerical data. If we average over the whole interval of ε, we will have $\alpha_C = \nu(\rho) = 0.954338$. This result is close to the theoretical one with the error 4.57 %. The result of averaging of $\langle\tau_{\text{inf}}(\varepsilon)\rangle$ is shown in Fig. 1, b by a dashed line.

Acknowledgements

The reported study was partially supported by RFBR, research project No. 13-02-00216a. N.I. Semenova gratefully acknowledges the Dynasty Foundation.

References

1. V.V. Nemytsky, V.V. Stepanov, *Qualitative Theory of Differential Equations*, Moscow, 1947.
2. A. Poincaré, *Izbrannye Trudy*, M.: Nauka, 1972, **2**.
3. M. Hirata, B. Saussol, S. Valenti, *Commun. Math. Phys.*, 1999, **206**(1), 33-55.
4. V. Afraimovich, E. Ugalde, J. Urias, *Fractal Dimension for Poincaré recurrences*, Elsevier, 2006.
5. V. Afraimovich, *Chaos*, 1997, **7**(1), 12-20.
6. N.I. Biryukova, T.E. Vadivasova, V.S. Anishchenko *Perculiarities of Poincaré recurrences in a circle map with different irrational rotation numbers*, 2014, submitted to *Phys. Let. A.*
7. S.P. Kusnetsov, *Dynamical chaos*, M.: Fizmatlit, 2001, p. 266.

POINCARÉ RECURRENCES IN THE PHASE-FREQUENCY SYNCHRONIZATION REGIME IN THE RÖSSLER OSCILLATOR

Y. Boev, T. Vadivasova, and **V. Anishchenko**

Department of Physics, Saratov State University, Saratov, Russia
boev.yaroslav@gmail.com, vadivasovate@yandex.ru, wadim@info.sgu.ru

In our work we investigate Poincaré recurrence time statistics [1–3] in a Rössler oscillator. Analysis of the statistics of Poincaré recurrence times to a finite size region has shown that a spiral attractor mode of an autonomous system has the return time distribution, which is characterized by a «line structure» with clearly visible equidistant maxima. The distance between the peaks is determined by the mean oscillation period, and the envelope of this distribution (except an initial distribution segment) obeys an exponential law. This distribution structure is observed at any attractor point when return times are studied both in a three-dimensional region and in a two-dimensional area in the XY projection, and does not depend on the size ε of the return vicinity. Numerical experiments have corroborated the relationship between the mean return time $\langle\tau_r\rangle$ and the fractal dimension of the attractor, which is observed in the limit of small ε. It has been shown that to calculate the dimension one needs to examine the trajectory returns to a small region in the full phase space but not in a projection of the attractor.

When a system with a spiral attractor is subjected to an external harmonic force, the return time distribution in the vicinity of an attractor point either in the space of dynamical variables x, y, z or in the XY -plane has the same structure as in the autonomous case. This means that equidistant peaks are observed in the distribution and the envelope decays exponentially. However, the external force affects the position of the peaks and thus, the mean time changes. The calculations have shown that for an appropriately chosen size of the return vicinity, the dependence of $\omega_r = \frac{2\pi}{\langle\tau_r\rangle}$ on the external force parameters (for example, external frequency) enables determining the boundaries of the synchronization region. A good accuracy in determining the frequency locking boundaries is achieved by selecting the return region with a sufficiently large size. When we consider a small return vicinity, we cannot define precisely the boundaries of the synchronization region but can diagnose confidently the existence of the synchronization effect.

Acknowledgements

The reported study was partially supported by the RFBR, research project No. 13-02-00216a and by the Russian Ministry of Education and Science (project code 1008).

References

1. H. Poincaré, *Acta Mathematica*, 1890, **13**, A3–A270.
2. J. Gao, *Physical Review Letters*, 1999, **83**, 3178–3181.
3. M. Hirata, B. Saussol, and S. Vaienti, *Communications in Mathematical Physics*, 1999, **206**, 33–55.

Invited

A NONLINEAR DYNAMICS-BASED APPROACH TO CONTROL COMPLEX NETWORKS

S.P. Cornelius[1,2], **W.L. Kath**[2], and **A.E. Motter**[2]

[1]Center for Complex Network Research, Boston, USA, spcornelius@gmail.com
[2]Northwestern University, Evanston, USA

Abstract. The control of complex networks is of paramount importance in areas as diverse as ecosystem management, emergency response, and cell reprogramming. A fundamental property of networks is that perturbations to one node can affect other nodes, potentially causing the entire system to change behavior or fail. Here, I will show that it is possible to exploit this same principle to control network behavior. The approach is based on exploiting the nonlinear dynamics inherent to real systems, and allows bringing the system to a desired target state even when this state is not directly accessible due to constraints that limit the allowed interventions. Applications show that this framework permits both reprogramming a network to a desired task as well as rescuing networks from the brink of failure—which I will illustrate through the mitigation of cascading failures in a power-grid network and the identification of potential drug targets in a signaling network of human cancer.

A fundamental property of networks is that initially localized perturbations can propagate in the form of a cascade, potentially cause the system as a whole to fail or change behavior. From a dynamical point of view, this is fundamentally a consequence of the nonlinearity inherent to the dynamics of most real networks [1]. It is this nonlinearity that permits the coexistence of multiple stable states (some desirable, others not), which correspond to different possible modes of operation of a real network. As such, when a network is perturbed, it can spontaneously go to a "bad" state even if there are "good" ones available. Here, I will show that this principle can be a blessing in disguise, being exploited in reverse as a new strategy to control network behavior [2]. In particular, I will show how one can perturb a network that is in (or will approach) a "bad" state in such a way that it spontaneously evolves to a target state with more desirable properties.

This research was motivated by recent case studies that have shown how networks damaged by an external perturbation can, counter-intuitively, be healed by intentionally applying additional, compensatory perturbations. For example, bacterial strains left unable to grow in the wake of genetic mutations can be made viable again by the further knockout of specific genes [3], while extinction cascades in ecological networks perturbed by the loss of one species can often be mitigated by the targeted suppression of additional species [4]. However, a systematic extension of such a strategy to general networks has remained an open problem, partly due to system-specific constraints that restrict the interventions that can feasibly be implemented in real networks. As an example, in food-web networks, it may only be possible to suppress (but not increase) the populations of certain species (e.g., via hunting, fishing, culling, or non-lethal removals), while some endangered species can't be manipulated at all. Similarly, one can easily knock down one or more genes in a genetic network, but coordinating the upregulation of entire genetic pathways is comparatively difficult. Such constraints generally preclude bringing the system directly to a given target, or even to a similar state. This is particularly true in the common case where the eligible modifications to the network state span a subspace of measure zero in the full phase space of the network dynamics, as in the example of an endangered species above.

The critical insight underlying the solution to this problem is that even when a desired stable "target" state of a dynamical system cannot be reached directly, there will exist a set of other states that eventually do evolve to the target—the so-called *basin of attraction* of that state. If we could only bring the system to one of those states through an eligible perturbation, the system would subsequently reach the target on its own, without any further intervention. A core component of this research is thus the introduction of a scalable algorithm that can locate basins of attraction in a general dynamical system [2] (for a freely-available software implementation of the algorithm, see Ref. [5]). This algorithm is based on casting the problem as a series of constrained nonlinear optimization problems, which enables systematic construction of compensatory perturbations via small imaginary changes to the state of the network.

Prior to the introduction of this technique there were no systematic, efficient, and general purpose methods for locating specific portions of attraction basins in high-dimensional dynamical systems, short of conservative estimates and brute-force sampling. The latter requires an amount of computation time exponential in the number of dynamical variables of the system, which is notoriously large for complex networks of interest. In contrast, the running time of our approach scales only as the number of variables to the power 2.5. Another remarkable aspect of this approach is its robustness;

even if the target state cannot be reached by any eligible perturbation, I will show it may nonetheless be possible to drive the network to a similar state using this control procedure. This would not be possible if the dynamics were linear, since in that case the nonlocal nature of the control trajectories may prevent numerical convergence to the desired target even when the initial state is already close to the target [6]. Moreover, only nonlinear dynamics allows for the existence of multiple stable behaviors observed in real systems.

There are numerous potential applications for the above control approach. Aside from the possibility of network reprogramming illustrated in the example above—i.e., driving a system from an undesirable state to a desirable state—the idea of control via compensatory perturbations is a natural framework for rescuing networks from impending (or pre-existing) failure. As a stylized example, we consider a simple model power system, which can be rescued in real time from desynchronization instabilities in the generators that can be the prelude to large blackouts. This is possible despite constraints that forbid the direct modification of certain dynamical variables in the grid. Indeed, the network nonlinearity that is exploited by our control approach is what allows controlling the fate of the entire network through perturbations to only a subset of its components. This concept of indirect targeting can be relevant to large-scale failures like traffic jams, genetic diseases, and financial panics, which can be caused by abnormal activity in small crucial components (roads, genes, or financial institutions) that are nonetheless unamenable to direct control. As an example, I will consider the case of model food web systems suffering from invasive species, which might be restored to their pristine state through control actions on only the native species in the network. This is possible because the control approach introduced here takes explicit advantage of the interconnectedness of the network vis-a-vis how a given node is ultimately affected by changes to the state of the rest of the system.

This work illustrates how interconnectedness and nonlinearity—unavoidable features of real systems commonly thought to be impediments to their control—can actually be turned to our advantage. Our approach is based on the systematic construction of compensatory perturbations to the network, and, as illustrated in the above applications, can account for both rather general constraints on the admissible interventions and the nonlinear dynamics inherent to most real complex networks. These results provide a new foundation for the control and rescue of network dynamics and for the related problems of cascade control, network reprogramming, and transient stability. In particular, I will discuss potential applications for controlling urban networks, such as smart traffic and power grids and other forms of self-healing infrastructure. For more information, see the original publications, Refs. [2, 5].

Acknowledgements

This work was supported by NSF under Grant DMS-1057128, NCI under Grant 1U54CA143869 and a Northwestern-Argonne Early Career Investigator Award to A.E.M.

References

1. A.E. Motter and R. Albert, *Physics Today*, 2012, **65**(4), 43.
2. S.P. Cornelius, W.L. Kath, and A.E. Motter, *Nat. Commun*., 2013, **4**, 1942.
3. A.E Motter, N. Gulbahce, E. Almaas, and A-L. Barabási, *Mol. Syst. Biol*., 2008, **4**, 1942.
4. S. Sahasrabudhe and A.E. Motter, *Nat. Commun*., 2011, **2**, 170.
5. S.P. Cornelius and A.E. Motter, *Nat. Protoc. Exch*., 2013, doi:10.1038/protex.2013.063.
6. J. Sun and A.E. Motter, *Phys. Rev. Lett*., 2013, **110**, 208701.

WAVE PATTERNS IN A RING OF ELECTRICALLY COUPLED OSCILLATORY NEURONS WITH EXTRA CHEMICAL COUPLINGS

A.S. Dmitrichev and **V.I. Nekorkin**

Institute of Applied Physics RAS, Nizhny Novgorod, Russia
admitry@neuron.appl.sci-nnov.ru

Abstract. We study spatial-temporal dynamics of a network of oscillatory cells, whose architecture has two components – regular and irregular ones. The regular component is represented by a ring of electrical couplings. As the irregular component we consider both a pair and a random set of mutual chemical couplings. The laws of evolution of wave activity in such a network are investigated depending on coupling strengths and statistical characteristics of the irregular component.

It has become clear that many real network systems from various fields of modern science have complex enough, irregular architecture of interelement couplings. Although there exists a large number of studies on collective dynamics of such systems [1–5], most of them are devoted to processes of partial (formation of phase coherent clusters of oscillatory activity) and full synchronization. Wave processes in irregular systems are not so well studied.

Recently, we considered the ring of electrically coupled Morris-Lecar neurons [6]. It is shown that the system is capable of producing the so-called "anti-phase wave patterns" looking like the envelope solitons. They have the form of spatio-temporal oscillations with a smooth localized envelope which propagates along the system preserving its shape and velocity. Here we consider the same system but with additional irregular component represented by pairs of mutual chemical couplings with identical properties. To model the component we add the term $I_i^{chem} = -d_2 \sum_j a_{ji} H(\bar{v}_j - \theta)(\bar{v}_i - \bar{v}_{rev})$ on the right-hand side of the first Eq. (1) (see [6]). The parameters d_2, $\bar{v}_{rev}$, and θ of this term characterize respectively the strengths, the reversal potentials and the activation thresholds of chemical couplings, the matrix $\boldsymbol{A}=\{a_{ij}\}$ describes the architecture of the couplings.

We assume that the parameters of the system in the absence of irregular component ($d_2 = 0$) belong to the region of existence of "anti-phase wave patterns" (namely, $\varepsilon = 3.28$, $\bar{I} = 48$, $d = 0.05$) and study how the patterns are transformed when irregular couplings are applied. For classification of emerging collective activity, by analogy with the Kuramoto order parameter (denote it by R) [7], we introduce wave order parameter, R_w, as follows

$$R_w e^{i\Psi_w} = \frac{1}{N} \sum_{j=1}^{N} e^{i(\varphi_j - \varphi_{j-1})}, \qquad (1)$$

where the phases, φ_j, are determined in accordance with (7) of [6]. A wave order parameter indicates how close the regime is to wave activity.

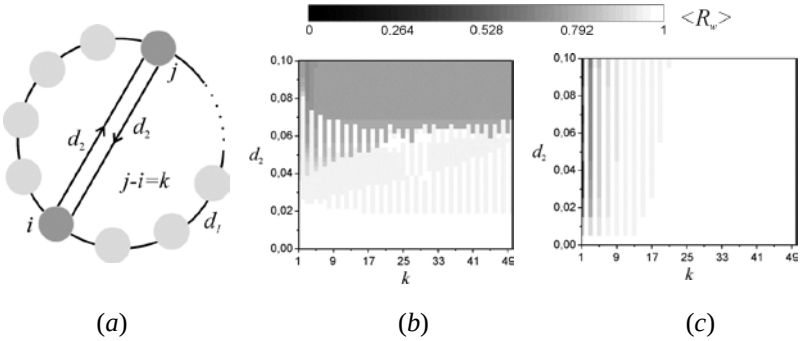

Fig. 1. Architecture of a ring network with extra pair of mutual couplings (*a*). Dependences of averaged wave order parameter, <*R*w>, on the strength of extra chemical couplings, d_2, and interelement distance, *k*, for excitatory (*b*) and inhibitory (*c*) couplings. Parameter values: $\theta = 0$, (*a*) $\bar{v}_{rev} = 25$, (*b*) $\bar{v}_{rev} = -31$

Firstly, we consider the case when the irregular component is represented by a pair of mutual chemical couplings. Suppose, for example, that the pair is between the *i*-th and *j*-th elements. The architecture of such network system is shown in Fig. 1*a*. Note that the regular component of the system has the dihedral symmetry. Consequently, the collective dynamics of the system depends only on the distance between the elements of the irregular component, $k = |j–i|$, but is independent of the relative positions of the elements. Therefore, to study collective effects emerging in such a system we carry out numerical simulation of the system for a one-parameter family of matrices $\boldsymbol{A}(k)$ with non-zero elements of the form $a_{1,k+1} = a_{k+1,1} = 1$. Figures 1*b*, *c* on the (k, d_2) parameter planes depict the

time-averaged wave order parameter for modes emerging when either excitatory or inhibitory couplings are applied. For excitatory couplings, there exists a critical value d_2^c of their strength that depends on k. Note that the dependence $d_2^c(k)$ is not monotonic. It has the form of damped oscillations relatively $d_2 \approx d = 0.5$. For d_2 less than the critical value, the wave activity is set in the system. In this region $R_w \approx 1$, $R \approx 0$. Otherwise, the chaotic oscillatory activity is set in the system (here $R_w < 0.8$, $R \approx 0$). The chaotic nature of oscillations is confirmed by the presence of positive Lyapunov exponents in the spectrum of the corresponding chaotic attractor. When inhibitory couplings are applied, wave activity is mostly observed. The chaotic regime is observed in a narrow region masked by odd values of $k < 9$.

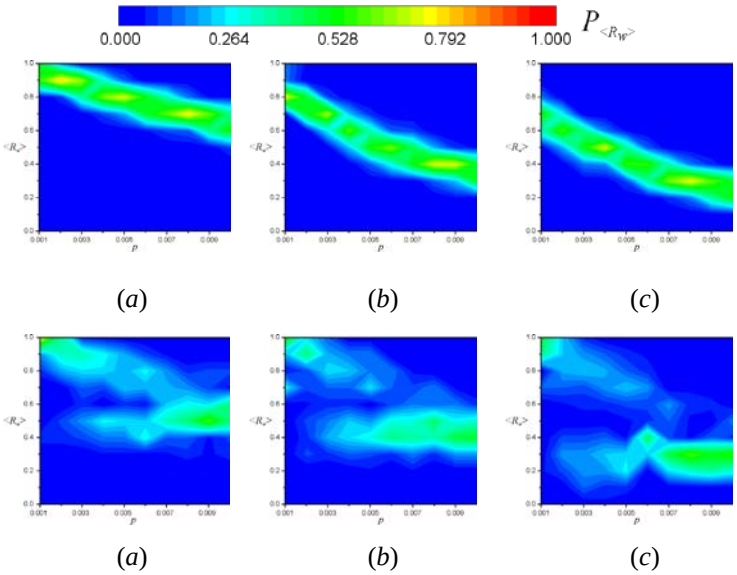

Fig. 2. Dependences of the probability density function for averaged wave order parameter, $P_{<Rw>}$, on the probability of formation of extra excitatory chemical couplings, p, and their strengths, d_2. Parameter values: $\theta = 0$, $\bar{v}_{rev} = 25$, (*a*) $d_2 = 0.025$, (*b*) $d_2 = 0.05$, (*c*) $d_2 = 0.075$

Fig. 3. Dependences of $P_{<Rw>}$ for extra inhibitory chemical couplings. Parameter values: $\theta = 0$, $\bar{v}_{rev} = -31$, (*a*) $d_2 = 0.025$, (*b*) $d_2 = 0.05$, (*c*) $d_2 = = 0.075$

Now, let us consider the case when the irregular component represented by a random set of mutual chemical couplings. To generate the set, i.e. the matrix $\boldsymbol{A}$, we use the Erdos Renyi model. In that model, coupling between any pair of elements is formed with equal predefined probability, p, independently of the other couplings. Obviously, for $0 < p < 1$, there are at least $N(N-1)/2$ different sets (or matrices $\boldsymbol{A}(p)$). Therefore, to study collective effects emerging in such a system we analyze the behavior of probability density function for $<R_w>$ (denote it by $P_{<Rw>}$), rather than $<R_w>$ itself. Figures 2 and 3 show the dependence of $P_{<Rw>}$ on the probability of formation of chemical couplings, p, and their strength, d_2. Figure 2 corresponds to the excitatory couplings, while figure 3 to inhibitory ones. Analysis of $P_{<Rw>}$ dependences shows that they have Gaussian-like distributions. For excitatory couplings, the expectation of $<R_w>$ decreases monotonically when either p or d_2 increases. At the same time its variance remains constant. Thus, wave activity in this case is observed only for small values of p and d_2. Absolutely different laws are observed when the irregular component is formed by inhibitory couplings. For any value of d_2 there is a set of critical values of probability, $p_i^c(d_2)$, where the expectation of $<R_w>$ undergoes jumps. At the same time between the critical values, the expectation of $<R_w>$ remains unchanged. Here wave activity is observed for any value of d_2, but small values of p.

Acknowledgements

This research was supported by the Russian Foundation for Basic Research (grants №№ 12-02-00526, 13-02-00858, 14-02-00042, 14-02-31873)

References

1. Q. Wang, G. Chen, M. Perc, *Plos One*, 2011, **6**(1), e15851.
2. C. Li, Q. Zheng, *Phys. Biol*., 2010, **7**, 036010.
3. M. Muller-Linow, C.C. Hilgetag, M.-T. Hutt, *PLoS Comput. Biol*., 2008, **4**(9), e1000190.
4. K. Park, Y.-C. Lai, S. Gupte, and J.-W. Kim, *Chaos*, 2006, **16**(1), 015105.
5. I. Leyva, et al., *Phys. Rev. E*, 2011, **84**, 065101(R).
6. A.S. Dmitrichev, et al., Eur. Phys. *J. Special Topics*, 2013, **222**, 2633-2646.
7. J.A. Acebrón, L.L. Bonilla, C.J. Pérez Vicente, F. Ritort, R. Spigler, *Rev. Mod. Phys*., 2005, **77**, 137.

Invited

EXTREME EVENTS IN EXCITABLE SYSTEMS

G. Ansmann[1], R. Karnatak[2], K. Lehnertz[1], and **U. Feudel[2]**

[1] Department of Epileptology, University Bonn, Bonn, Germany
[2] Institute for Chemistry and Biology of the Marine Environment, Carl von Ossietzky University Oldenburg, Oldenburg, Germany

We consider the dynamics of rare events at which an observable of a complex dynamical system is extreme in amplitude. Since our goal is to contribute to the understanding of the emergence and the termination of epileptic seizures and of harmful algal blooms, we focus on excitable systems, which are useful models to describe those two phenomena. Therefore, we study deterministic networks of excitable elements of FitzHugh–Nagumo type. We demonstrate that these networks are capable of self-generating such events at irregular times, i.e., without a change of control parameters or without an input to the system. To get a better understanding of this behavior, we study a reduced system consisting of two coupled FitzHugh–Nagumo oscillators, which mimics the extreme-event dynamics observed for the networks. We discuss the properties of the networks as well as of the reduced system that may be involved in the generation and termination of such extreme events.

PHASE LOCKING WITH ARBITRARY PHASE SHIFT OF TWO SYNAPTICALLY COUPLED NEURONS

S.Yu. Gordleeva[1,2], **A.Yu. Simonov**[2], **A.N. Pisarchik**[3], and **V.B. Kazantsev**[2]

[1] Institute of Applied Physics RAS, Nizhny Novgorod, Russia, gordleeva@neuro.nnov.ru
[2] Nizhny Novgorod State University, Nizhny Novgorod, Russia
[3] Centro de Tecnologia Biomedica, Universidad Politecnica de Madrid, Madrid, Spain

Abstract. The phase dynamics of a pair of spiking neural oscillators coupled by a unidirectional nonlinear connection has been studied. The synchronization effect with the controlled relative phase of spikes has been obtained for various coupling strengths and depolarization parameters. It has been found that the phase value is determined by the difference between the depolarization levels of neurons and is independent of the synaptic coupling strength. The synchronization mechanism has been studied by means of the construction and analysis of one-dimensional phase maps. The phase locking effect for spikes has been interpreted in application to the synaptic plasticity in neurobiology.

Phase synchronization of two neurons with an arbitrary phase shift can play an important role in the generation and propagation of information signals in living neuronal networks of the brain. In particular, two pacemakers can establish both negative (anticipated synchronization) and positive (synchronization with phase delay) phase shift. This phenomenon is of potential importance for large networks with numerous synchronized pairs controlling switching between signal propagation paths through the initiation of synaptic rearrangements owing to the adjustment of their depolarization levels. We have presented a model of a pair of spiking Hodgkin–Huxley neuronal oscillators coupled by a unidirectional spiking chemical connection which simulates synaptic input:

$$\begin{aligned} C\frac{dV_1}{dt} &= -\sum I_{ion,1} - I_{app,1}, \\ C\frac{dV_2}{dt} &= -\sum I_{ion,2} - I_{app,2} - I_{syn}, \\ I_{syn} &= \frac{g_{syn}(V_2 - V_{syn})}{1+\exp-(V_1-\theta_{syn})/k_{syn}}. \end{aligned} \tag{1}$$

Here, the subscripts 1 and 2 mark the master (presynaptic) and slave (postsynaptic) neurons, respectively; C is the specific membrane capacitance; V_1 and V_2 are the membrane potentials; and t is the time. The dynamics of the membrane potential of each neuron is determined by three ion currents I_{ion}, sodium, potassium, and ohmic leakage, as well as by direct depolarizing current. The instantaneous active ion currents depend on the state of gate variables whose dynamical equations are not presented here for the sake of brevity. The action of the master neuron on the slave one is described by the synaptic current I_{syn} in the equation for the potential of the slave neuron. The applied currents $I_{\text{app},i}$ are constant and determine the depolarization level of the neurons, as well as the dynamical regime (excitable, oscillatory, or bistable). The relative phase in the case of coupled spiking oscillators is defined as the difference between the timings of spike generation by two oscillators divided by the period:

$$\varphi(n) = \frac{t_2^{ap}(n) - t_1^{sp}(n)}{T_1}. \tag{2}$$

Figure 1 shows examples of (left panels) traces of the membrane potentials of the system specified by Eqs. (1) and (middle panels) the corresponding dynamics of the phase calculated by Eq. (2). It can be seen that both the anti-phase synchronization regime (Fig. 1a) and in-phase oscillations (Fig. 1b) occur in the model depending on the parameters. Furthermore, the steady-state phase can be close to unity (Fig. 1c), which can be treated as anticipated synchronization.

The mechanisms of spike phase locking of the slave neuron have been analyzed by the method of point maps [1]. The right panels in Fig. 1 exemplify the phase maps corresponding to the in-phase and anti-phase synchronization regimes. The intersections of the phase map curve with the diagonal specify the fixed points whose stability depends on the multiplier. It can be seen that one stable fixed point corresponding to the steady relative phase exists in each case.

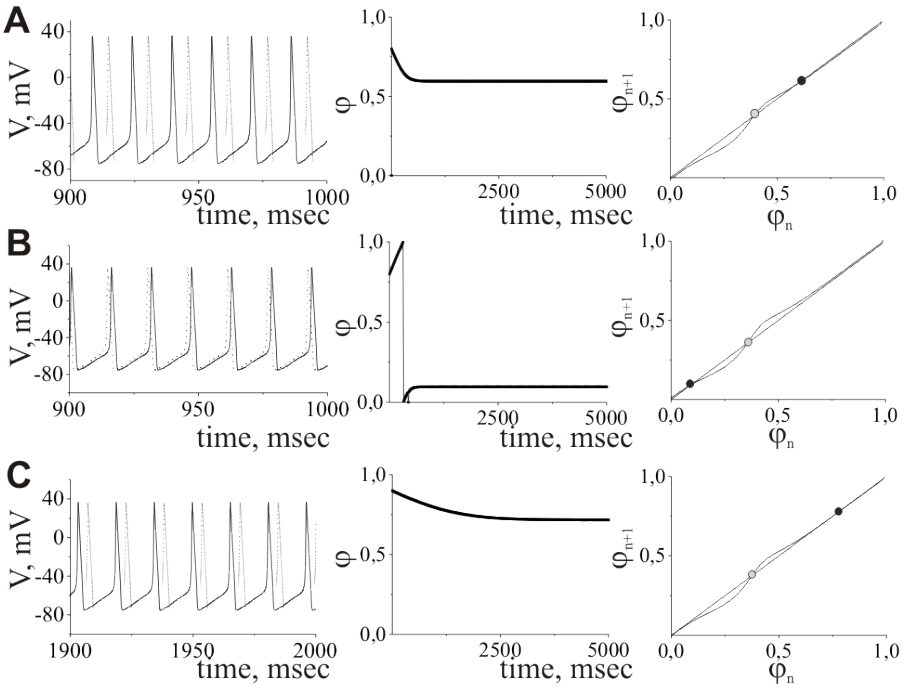

Fig. 1. Examples of the synchronization regimes in the model of a pair of synaptically coupled spiking neural oscillators specified by Eqs. (1): (a) anti-phase regime, (b) in-phase regime with delay, and (c) in-phase anticipated regime. The left panels are the traces of the membrane potentials after transient processes for the (dashed lines) master neuron and (solid lines) slave neuron. The middle panels show the time dependence of the relative phase. The right panels are the phase maps, where the closed and open circles are the stable and unstable fixed points, respectively

It has been shown analytically and numerically that, at weak interaction, a stable locking regime is established with various relative phases depending on the frequency detuning of the oscillators, which is specified by the external applied current (Fig. 2). The steady state relative phase in this case is independent of the coupling strength, which is an additional control parameter expanding the allowed phase range. The result obtained in this work confirms the hypothesis of the possible effect of the active extracellular medium of the brain on the signal transmission process.

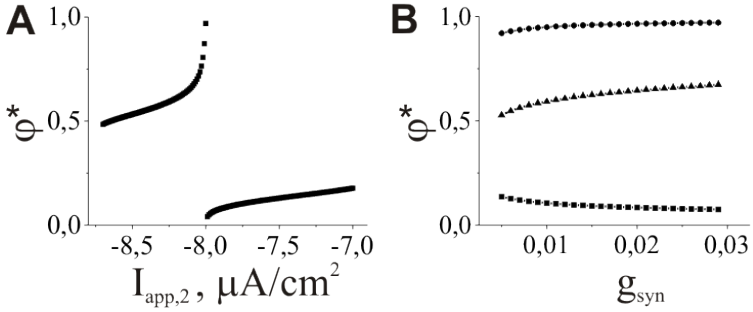

Fig. 2. Coordinate of the stable fixed point versus (a) the depolarization level and (b) the coupling strength at various depolarization levels $I_{app,2}$

Acknowledgements

The work was supported by the Council of the President of the Russian Federation for Support of Young Scientists and Leading Scientific Schools (No. SP-991.2012.4, SP-1668.2013.4), by the Russian Foundation for Basic Research #14-04-32211 мол_а, by the Russian President Grant No MK-4602.2013.4, and by the Russian Foundation for Basic Research grants # 13-02-01223, 13-04-12041.

References

1. A.Yu. Simonov, S.Yu. Gordleeva, A.N. Pisarchik, V.B. Kazantsev, *JETP Letters*, January 2014, **98**(10), DOI 10.1134/S0021364013230136.

Invited

ON THE DYNAMICAL BEHAVIOR OF LARGE DYNAMICAL NETWORKS

M. Hasler

School of Computer and Communication Sciences
Ecole Polytechnique Fédérale de Lausanne (EPFL)
Lausanne, Switzerland, martin.hasler@epfl.ch

Abstract. Networks of N interconnected dynamical systems are considered, where N is supposed to be large. Often, their collective dynamical behavior is studied by analyzing the infinite network as $N \to \infty$. It is then tacitly assumed that the qualitative behavior of the network for sufficiently large, but finite N is the same as for infinite N. We make the point that this has to be rigorously proved, by giving a counter-example. We also show for a network of identical phase oscillators, how to establish such a proof for multistable, synchronously rotating behavior. We believe that the method is widely applicable.

Dynamical networks are (usually large) dynamical systems with the structure of a graph. On each of the N vertices of the graph a (usually small) dynamical system is located. It interacts only with the dynamical systems on neighboring vertices. Two vertices are neighbors if they are linked with an edge in the graph [1].

What are the salient features of network dynamics that are generated by the local dynamics and their interactions? This is, of course, an extremely difficult question, but in a number of cases an answer can be given. It is often formulated with the help of some sort of a limit dynamical system when the network grows to infinite size, i.e. when $N \to \infty$ [2–4]. This limit system is, on the one hand, usually much simpler to analyze and, on the other hand, it is concluded that for sufficiently large finite systems the dynamical behavior is the same as for the infinite system.

This conclusion should be made with care. We give as a counter-example a network of interacting identical phase oscillators with a large number of coexisting synchronously rotating solutions, both in the finite and in the infinite system. Some of them are stable in the infinite system but the corresponding solutions in the finite system are unstable for large N. In view of this counter-example, there is a need to make the infinite limit mathematically rigorous and to investigate which dynamical features are the same in the infinite system and in the finite system with sufficiently large N.

In order to make the limit $N \to \infty$ rigorous, we reformulate the equations of the finite system in such a way that is has the same structure as the infinite system and consequently the finite and the infinite systems are just two different dynamics in the same space. Then we estimate the difference between the time derivatives of linear perturbations of the same synchronously rotating solutions. If this difference vanishes when $N \to \infty$ and if the perturbation in the infinite system dynamics decays exponentially fast, then both in the infinite system and in the finite system for large enough N the considered synchronously rotating solution is stable [4].

We specifically considered here networks of interacting phase oscillators, but we believe that the method can be extended to many other dynamical networks.

Acknowledgements

Thanks are due to Yuri Maistrenko and Taras Girnyck for many fruitful discussions.

References

1. A. Ajdari Rad, A. Khadivi, M. Hasler, “Information processing in complex networks”, *IEEE Circuits and Systems Magazine*, 2010, **10**(3), 26-37.
2. D.A. Wiley, S. Strogatz, M. Girvan, “The size of the sync basin”, *Chaos*, 2006, **16**, 015103.
3. E. Ott, T.M. Antonsen, “Low-dimensional behavior of large systems of globally coupled oscillators”, *Chaos*, 2008, **18**, 037113.
4. T. Girnyk, M. Hasler, Y. Maistrenko, “Multistability of twisted states in non-locally coupled Kuramoto-type models”, *Chaos*, 2013, **22**, 013114.

SYNCHRONIZATION PHENOMENA IN COMPLEX NETWORKS OF DYNAMICALLY COUPLED PHASE OSCILLATORS

D.V. Kasatkin

Institute of Applied Physics RAS, Nizhny Novgorod, Russia, e-mail: kasatkin@neuron.appl.sci-nnov.ru

Abstract. The processes of synchronization and phase cluster formation are investigated in complex networks of dynamically coupled phase oscillators. Coupling weights evolve dynamically depending on the relative phases between the oscillators. It is shown that a network exhibits several types of behavior: two-cluster mode, synchronized, partially synchronized and desynchronized modes. We find the occurrence of multi-stable states depending on initial distribution of coupling weights.

Networks of coupled phase oscillators have been extensively studied recently as a mathematical model for understanding the collective behavior of a wide variety of physical, biological and chemical systems. Such models are widely used in the study of the effects of synchronization in networks of self-oscillating elements. Most of studies in this field are devoted to analyzing the dynamics of networks, where couplings between the different oscillators in the network are fixed. In this work, we consider the case when couplings are dynamic and depend on the state of interacting oscillators.

We consider the dynamics of networks of coupled phase oscillators described by the following equations:

$$\frac{d\phi_i}{dt} = \omega_i - \frac{1}{N}\sum_j k_{ij} f(\phi_i - \phi_j), \quad i = 1, 2, ..., N . \tag{1}$$

Here ϕ_i is the phase of the i-th oscillator, ω_i are natural frequencies of the oscillators, $f(\phi)$ is 2π-periodic coupling function and k_{ij} denotes the coupling weight of the connection from the j-th to the i-th oscillator. We consider the coupling weights k_{ij} to be dynamic and represented by the following dynamical equation:

$$\frac{dk_{ij}}{dt} = -\varepsilon(g(\phi_i - \phi_j) + k_{ij}), \tag{2}$$

where $g(\phi)$ is 2π-periodic plasticity function [1], which determines how the coupling weight depends on the relative timing of the oscillators. We assume that the evolution of the couplings is slower than the evolution of the oscillators, i.e., $\varepsilon << 1$. Unlike the works [1–2], we implemented the limitation condition for coupling growth by adding a linear term in equation (2). We choose the coupling and plasticity functions in the simplest form $f(\phi) = \sin(\phi+\alpha)$ and $g(\phi) = \sin(\phi+\beta)$, where parameter α can be regarded as the phase difference induced by a short transmission delay of the coupling and parameter β controls the characteristic of plasticity function.

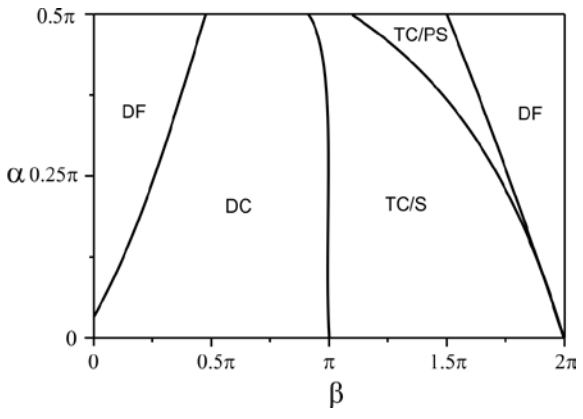

Fig. 1. Diagram of dynamical modes of system (1)-(2) for N = 200: (S) – synchronized mode, (TC) – two-cluster mode, (PS) – partially synchronized mode, (DF) – desynchronized mode with fixed phase relationship between oscillators, (DC) – desynchronized mode with time-varying phase relationships between oscillators

In numerical simulations we consider a network consisting of $N = 200$ oscillators with identical natural frequencies ω_i = 1. Figure 1 presents the diagram illustrating a distribution the domains with different dynamic behavior of the network in the region of parameters $\alpha \in [0, \pi/2]$ and $\beta \in [0, 2\pi)$. This diagram is constructed on the basis of the analysis of several two-parametric diagrams of the time averaged value of the order parameters R_m, m = 1, 2, calculated for different initial conditions. We analyzed the order parameters during 10^3 time steps after 10^6 initial time steps were discarded as transient.

It has been established that the network exhibits the following dynamical modes:

- Synchronous mode (*S*), when all oscillators of the network are synchronized after a transition process (Fig. 2, *a*, *b*). This mode is realized in the parameter domain *S* (see Fig. 1) when the initial values of coupling weights are distributed predominantly in the range $k_{ij} > 0$.
- Two-cluster mode (*TC*), in which two groups of synchronized oscillators are organized (Fig. 2, *c*, *d*). The clusters are in anti-phase relationship with each other. In figure 2, *d* the second order parameter R_2 converges to 1 and R_1 takes a value close to 0. The ratio of the number of elements forming clusters depends on the initial conditions.
- Partially synchronized mode (*PS*), when the network is divided into two parts. The oscillators of the first part form several synchronized groups. The second part includes oscillators whose phase will continue to change in time in the relative phases of oscillators of the synchronized groups (Fig. 2 *e*, *f*). Synchronized groups form pairs that are in anti-phase relative to each other. The frequencies of different pairs of the synchronized groups differ.
- Desynchronized mode with a fixed phase relationship (*DF*) between oscillators (Fig. 2, *g*, *h*). In this mode the oscillator phases are distributed over the entire range $(0, 2\pi)$ (Fig. 2, *h*). In [1] this mode is referred to as coherent.
- The network can also show another type of desynchronized mode (*DC*). In this mode, the relative phase relationships between oscillators continuously change in time.

Furthermore we found the occurrence of multi-stable states of network depending on initial conditions.

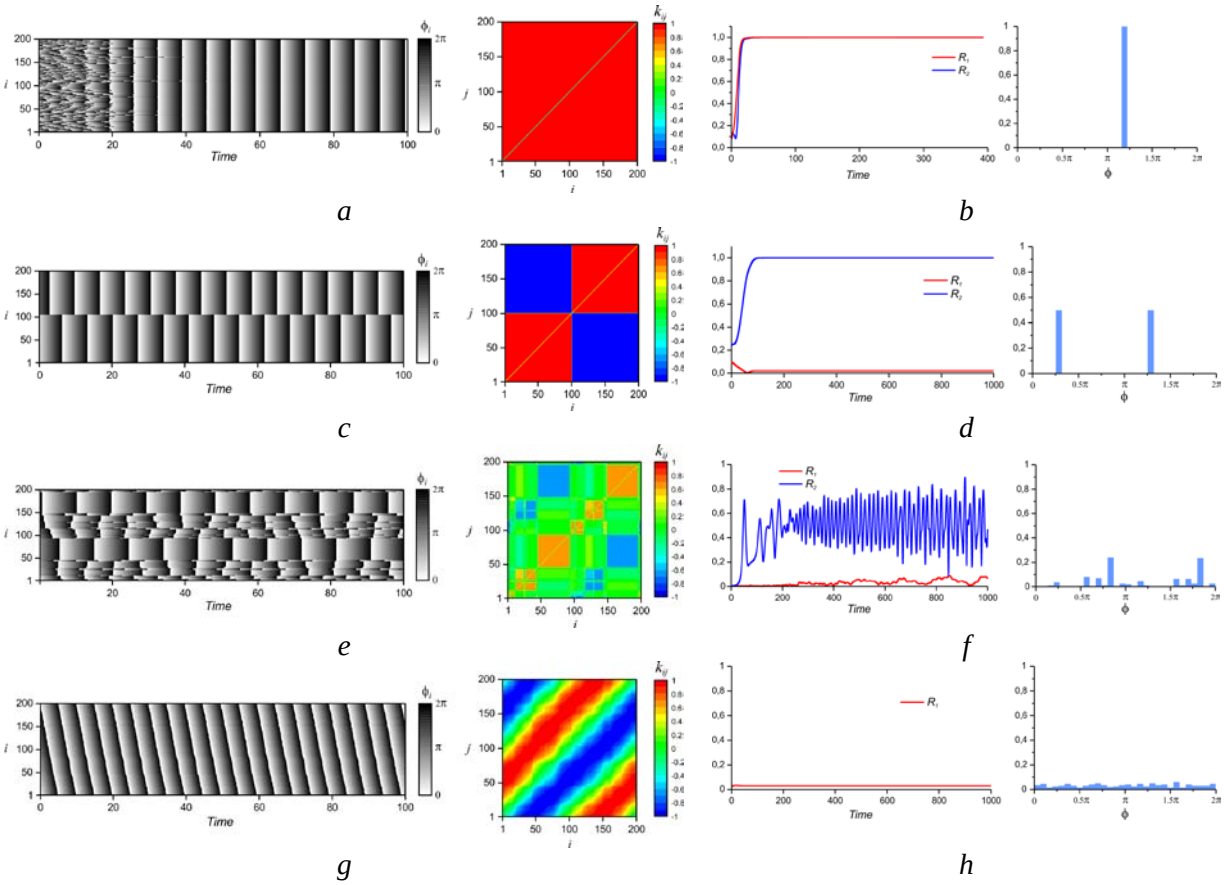

Fig. 2. Dynamical modes of the network (1)–(2). Time evolution of the oscillator phases and matrix of coupling weights at a moment of time $t = 10000$ (*a*, *c*, *e*, *g*); time evolution of order parameters and phase distribution at a moment of time $t = 10000$ (*b*, *d*, *f*, *h*). Parameter values: $\alpha = 0.2$, $\beta = 5$ (*a*–*d*), $\alpha = 1.5$, $\beta = 3.9$ (*e*–*f*), $\alpha = 1.2$, $\beta = 0.2$ (*g*–*h*)

Acknowledgements

This research was supported by the Russian Foundation for Basic Research (grant 13-02-00858).

References

1. T. Aoki and T. Aoyagi, *Phys. Rev. E*, 2011, **84**(6), 066109.
2. V.K. Chandrasekar, J. Sheeba, B. Subash, M. Lakshmanan, J. Kurths, *Physica D*, 2014, **267**, 36-48.

DELAY OF THE SPIKE OSCILLATION SUPPRESSION IN THE NONAUTONOMOUS MODEL OF NEURON FIRING

S.Yu. Kirillov and **V.I. Nekorkin**

Institute of Applied Physics RAS, Nizhny Novgorod, Russia, e-mail: skirillov@neuron.appl.sci-nnov.ru

Abstract. The spike response to a slowly varying synaptic current has been investigated in the modified FitzHugh-Nagumo model of neuron firing. It was shown that the spike oscillations disappear when the synaptic current value greatly exceeds the value predicted by the classical bifurcation theory. It was found that the dynamic double limit cycle bifurcation and nonlocal oscillation properties underlie the delay phenomenon.

The metastability and the transients are a major challenge in neurodynamics. The mechanisms of generation and suppression of the spike sequences (the action potential series) in a neuron are very important for explaining the principles of the information processing and transmission in the brain.

Neurons communicate via special contacts (synapses). In many natural experiments the synaptic currents were slowly varying compared with the period of the inherent oscillations in neurons. One of the methods for studying such slowly driven systems is based on the dynamic bifurcation theory [1–3].

Here we report the delay of the spike oscillation suppression explored theoretically. We employ the nonautonomous model of neuron firing. The model dynamics is described by the modified FitzHugh-Nagumo model that takes into account the nonlinear character of the ionic recovery currents [4]

$$\begin{aligned} \dot{u} &= f(u) - v + I_{syn}(t), \\ \dot{v} &= \varepsilon\big(g(u) - v\big), \end{aligned} \tag{1}$$

where $f(u) = u - u^3/3$ is the nonlinear cubic function, the function $g(u)$ has the piece-wise linear form given by $g(u) = \alpha u$, for $u \le 0$ and $g(u) = \beta u$, for $u > 0$, $I_{syn}(t)$ is the time-varying synaptic current.

In equation (1) the variable u describes the membrane potential dynamics, while the variable v defines common features of the membrane ion currents. The positive parameter ε defines the ion currents rate of change, the positive parameters α and β describe the ion currents nonlinear properties.

We consider the case when the synaptic current decreases linearly with time:

$$I_{syn}(t) = I_0 - \mu t, \tag{2}$$

where the parameter I_0 controls the membrane depolarization level at the initial moment of time, the small positive parameter $0<\mu<<1$ determines the synaptic current rate of decrease.

There are two quasi-stable modes of activity in model (1), (2): the slowly varying spike oscillation mode and the slowly varying steady state. If at the initial moment of time the system is in the spike oscillation mode, the slowly varying synaptic current leads it to the steady state. The phase space analysis is used to explore this phenomenon further.

Since the parameter μ is small enough, the phase space of the nonautonomous model (1), (2) can be analyzed using the relaxation oscillation method [5]. According to this method the study of (1), (2) reduces to separate investigation of the slow and fast subsystems that can be obtained from (1), (2) in the limit case $\mu \to 0$.

When $\mu = 0$, the neuron dynamics for each $I_{syn} = \text{const}$ is determined by a two-dimensional autonomous system. The bifurcation analysis of (1) in the autonomous case was presented in [4]. Here, we fix the parameters $\alpha = 0.5$, $\beta = 2$, $\varepsilon = 0.35$ and vary the control parameter $I_{syn} = I_0$. The corresponding bifurcation diagram and the structurally stable phase portraits are presented in Fig. 1a. Of particular interest for our consideration is location of the bifurcation point in the vicinity of the double limit cycle. System (1) has three equilibrium states: O_1 is a stable focus, O_2 is a saddle state, and O_3 is an unstable focus. There are also other limit sets in the phase space of model (1). For the parameter value $I_{syn} = I_0^T$, a double limit cycle bifurcation occurs. As a result, for the parameter values $I_{syn} > I_0^T$ two limit cycles appear: a stable limit cycle C^S and an unstable limit cycle C^U.

When $\mu \to 0$, the synaptic current changes quasi-statically. Then the limit cycles C^S and C^U form two-dimensional invariant manifolds in the phase space of (1), (2). Similarly, the equilibrium states O_1, O_2 and O_3 form one-dimensional invariant manifolds and the saddle point separatrices form two-dimensional invariant manifolds.

When $0 < \mu << 1$ and the synaptic current rate is not infinitesimal, the invariant manifolds deform in comparison with the quasi-static case. The motion of the representative point in the local vicinity of the invariant manifold that was born from C^S determines the spike oscillation mode. The time of this motion is basically defined by the dynamic double limit cycle bifurcation. This time is sufficiently

long compared with the period of the spike oscillations. The slowly varying steady state is determined by the motion of the representative point in the local vicinity of one-dimensional invariant manifold which is close to the manifold formed by O_1. The transition from the spike oscillation mode to the steady state is determined by the properties of the threshold manifold. This two-dimensional invariant manifold is born from the «static» separatrix manifold formed in the phase space of (1), (2) by the incoming separatrix W_1^S of the saddle O_2. The threshold manifold significantly differs from the «static» manifold even for a very small values of μ.

The disappearance of the spike oscillations is shown in Fig. 1b. It can be seen from the figure that the spikes disappear with considerable delay after the control parameter passes the double limit cycle bifurcation point. The delay value roughly monotonically decreases with increasing value of the parameter μ. It is shown in Fig. 1c. The local jumps in this figure are influenced by the properties of the threshold manifold. The jump value correlates with the value of μ and may by significant compared with the delay time. Consequently, the important feature of the system dynamics is that the moment of spike disappearance depends on the phase of the oscillation at the initial moment of time. It determines the memory effect in the model.

To conclude, we demonstrated that an arbitrarily slow drift of the synaptic current significantly changes response characteristics of the neuron as compared to the quasi-static case. We have shown that the dynamic double limit cycle bifurcation and nonlocal oscillation properties of the model underlie the delay phenomenon and the memory effect.

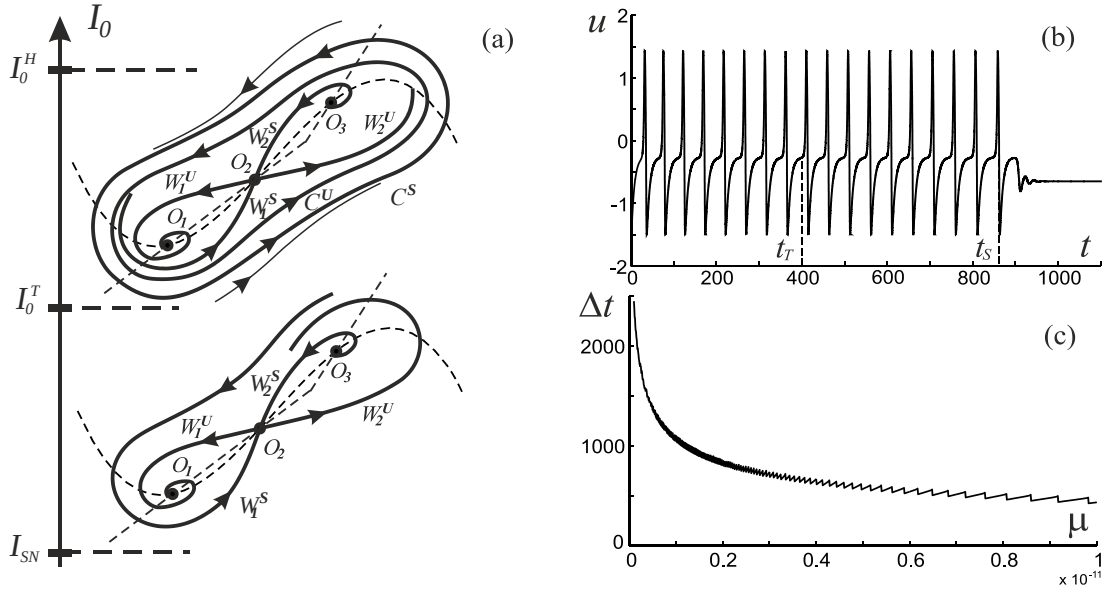

Fig. 1. (a) Bifurcation diagram and quality structurally stable phase portraits of (1), (2) for μ = 0. I_0^T denotes the double limit cycle bifurcation point, I_{SN} – the saddle-node bifurcation, I_H – the homoclinic orbit bifurcation.
(b) Spike oscillation disappearance; t_T is the time of the passage through a double limit cycle bifurcation point and t_S is the spike oscillation disappearance time. Parameters: $\mu=1\times10^{-11}$, I_0 = 0.2100951289.
(c) The delay time Δt depending on the synaptic current rate of decrease μ

Acknowledgements

This research was supported by the Russian Foundation for Basic Research (grants Nos.14-02-31622, 14-02-00042, 14-02-00916, and 14-02-31873).

References

1. E. Benoit (Ed.), *Dynamic bifurcations*. Springer, Lecture Notes in Mathematics, 1991, **1493**, 219 p.
2. S.Yu. Kirillov, V.I. Nekorkin, *Radiophys. Quant. El.*, 2013, **56**(1), 36-50.
3. C. Kuehn, *Physica D*, 2011, **240**, 1020-1035.
4. V.I. Nekorkin, A.S. Dmitrichev, D.S. Shapin, V.B. Kazantsev, *Math. Model*., 2005, **17**(6), 75-91 (in Russian).
5. V.I. Arnold, V.S. Afraimovich, Yu.S. Ilyashenko, L.P. Shilnikov, *Bifurcation theory*, in: Dynamical Systems. Encyclopaedia of Mathematical Sciences, vol. V, Springer, 1994, 283 p.

NEURON CLUSTERING CONTROLS PERSISTENT ACTIVITY IN CORTEX

V.V. Klinshov and **V.I. Nekorkin**

Institute of Applied Physics, Nizhny Novgorod, Russia
vladimir.klinshov@gmail.com

Abstract. We derive connectivity rules from experimental data observed in layer 5 of rat neocortex to generate a model of neural connectivity in cortical microcircuits. Our model predicts that microcircuits of about 100 μm contain groups of densely connected neurons which we call clusters. We show that such clusters contain comparatively large groups of excitatory neurons which are almost all-to-all connected with stronger than average synapses. We demonstrate that a small network of about a hundred of cortical neurons embedding such a cluster creates a bistable neural spiking with distinct high and low firing rates. Furthermore, interactions among hundreds of such minimal clusters and surrounding neurons are sufficient for generating both spontaneous network activity and persistent activity representing several simultaneously stored memories in a large-scale network.

The flow of information in neural circuits and their function depend crucially on the organization of neuronal wiring. A number of recent studies reveal nonrandom features of neuronal wiring in cortical circuits [1–3]. The statistics of cortical circuit connectivity have been shown to strongly differ from that of random networks on both local and global scales. In particular, there is evidence that a small number of cortical neurons chosen randomly from local cortical circuits exhibit certain connection patterns, or network motifs, significantly more often than expected by chance. Moreover, the overrepresentation of the motifs is positively correlated with connection strength. These features suggest that local cortical circuits involve multiple clusters of highly and strongly connected neurons.

Clustering in synaptic connections creates additional complexity in the structure and dynamics of neural networks. It is, however, difficult to measure all the statistical properties of neuronal wiring experimentally, therefore the precise connectivity structure of cortical circuits remains unclear. For example, the typical size of a clustered neural ensemble in local cortical networks, or the number of clusters of neurons that exist in a given local volume of cortex remain ambiguous. To shed light on these questions, we derived a computational model of network connectivity from the recently discovered non-random features of cortical circuits [1, 3]. Furthermore, we explored the role of the resultant clusters of synaptic connections in the dynamics of cortical networks.

Our model is defined as a network of N neurons that contains K clusters with M neurons per cluster. Note that KM can be smaller than N, i.e. some neurons of the network may not belong to any of the clusters. The probability of two units being connected equals c_2 if they belong to the same cluster and c_1 otherwise (if they belong to different clusters, or one of them or both do not belong to any cluster). We also assume that the distributions of synaptic weights are different between the inside and outside the clusters, where "inside" means a connection linking two neurons belonging to the same cluster, and "outside" means any other connection. Rigorous mathematical analysis shows that only a single set of the network parameters fits the experimentally observed statistical characteristics of cortical microcircuits satisfactorily. Namely, this parameter set describes a network with a single ($K = 1$) cluster of about one fifth ($\beta \approx 0.22$) neurons which are connected very densely ($c_2 \approx 1$). The neurons in the cluster also have stronger connections with a long-tailed distribution.

We investigated implications of the synaptic clustering for the network dynamics. To this end, we compared the dynamics of the networks with different levels of clustering which is characterized by the intra-cluster connectivity c_2. The maximal value of $c_2 = 1$ means ultimate clustering, and the minimal value of $c_2 = c_1$ means no clustering at all. We showed that for strong clustering, even quite small networks ($N \approx 50$) with clustering demonstrate bistabile spontaneous dynamics with two distinct types of activity: the low state and the high state (Fig. 1). In the latter regime, the clustered neurons produce irregular spikes with a high firing rate of ($f \sim 50$ Hz). In contrast to that, the network with low clustering becomes bistable only when it is very large ($N \sim 1000$). In the high state such a large network produces spikes quite regularly and with unnaturally high firing rate ($f > 100$ Hz).

Thus, the immediate consequence of synaptic clustering is capability of small cortical microcircuits to create bistable dynamics with physiologically relevant types of activity. It is noteworthy that the minimal size required for bistability roughly corresponds to the number of cells in a “minicolumn” [4], which may be a minimal functional module of neocortex. Moreover, synaptic clustering on local scales may play an important role in the dynamics of large-scale neural networks. To reveal this role

we simulated a large network of about 10 000 neurons into which we incorporated local clustering. We started from random connectivity, then partitioned the network into a number of local subnetworks and reorganized the connections inside each subnetwork according to our model. In the resultant network, novel dynamical features emerge. Similarly to the network with no clustering, sparse non-clustered connections generate a low-frequency spontaneous activity [5]. On the background of this low-rate activity, clustered connections create local spots displaying high-rate activity, and the network becomes multistable.

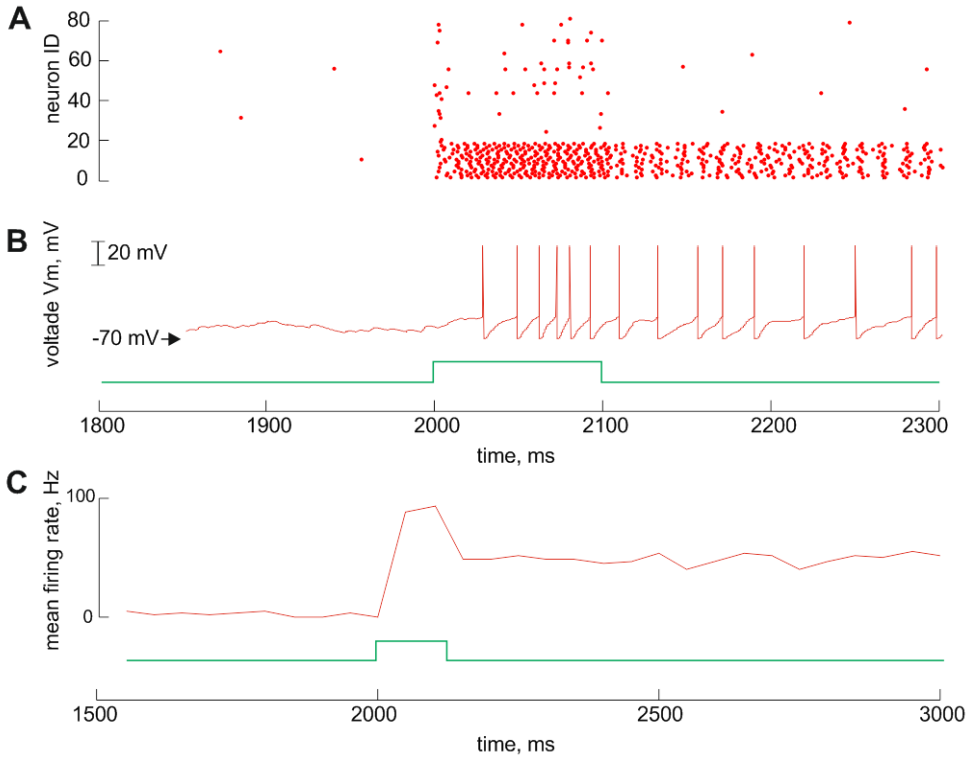

Fig. 1. The bistable dynamics of the network with clustering. An external input applied at t = 2000 ms for 100 ms switches the network from the low to the high state. A: Spike raster, dots represent spikes of the individual neurons. B: The membrane potential of one of the clustered neurons (red) and the external input (green). C: The mean firing rate of the clustered neurons (red) and the external input (green). Note that the time scale is the same for A and B but different for C

Multistable behavior is considered to play an important role for various neural computation tasks [6], such as temporal integration in decision making and interval timing and working memory. Here, we have demonstrated this phenomenon in a network with a biologically relevant connectivity structure. Thus, our results may bridge a gap between anatomical structure and persistent activity observed during working memory and other cognitive processes.

References

1. S. Song, P.J. Sjostrom, M. Reigl, S. Nelson, and D.B. Chklovskii, *PLoS. Biol*., 2005, **3**, e68, doi:10.1371/journal.pbio.0030068.
2. R.J. Prill, P.A. Iglesias, and A. Levchenko, *PLoS. Biol*., 2005, **3**, e343, doi:10.1371/journal.pbio.0030343
3. R. Perin, T.K. Berger, and H. Markram, *Proc. Natl. Acad. Sci. USA*, 2011, **108**, 5419-5424.
4. V.B. Mountcastle, *Cereb. Cortex*, 2003, **13**, 2-4.
5. J. Teramae, Y. Tsubo, and T. Fukai, *Scientific Reports*, 2012, **2**, doi:10.1038/srep00485.
6. H.R. Wilson and J.D. Cowan, *Biophys. J*., 1972, **12**, 1-24.

ENERGY LOCALIZATION TO ENERGY TRANSPORT IN THE SYSTEM OF N WEAKLY COUPLED GRANULAR CHAINS

M.A. Kovaleva[1] and **Yu. Starosvetsky**[2]

[1] N.N. Semenov Institute of Chemical Physics, Moscow, Russia, makovaleva@chph.ras.ru
[2] Technion – Israel Institute of Technology, Haifa, Israel

Abstract. Regimes of nonlinear, resonant energy transport in the system of three weakly coupled, non-linear oscillators and oscillatory chains are considered. A special analytical method based on the limiting phase trajectories and saw-tooth transformations has been developed to obtain the analytical criterion of formation of a highly non-stationary regime manifested by irregular energy transport from the first to the third oscillator. The results are extended for the case of larger numbers of oscillators (chains).

The concept of limiting phase trajectories (LPTs) introduced by Manevitch [1] is a natural approach for a rather comprehensive description of intensive energy exchange between two weakly coupled, non-linear oscillators as well as oscillatory chains [2–6]. The term LPT refers to the trajectory corresponding to the oscillations of weakly coupled oscillators or, alternatively, an oscillator and an external source of energy undergoing maximum possible energy exchange. As shown in [2–6], the transition from the regimes of complete energy exchange between the two coupled oscillators, the oscillatory chains to energy localization on one of them can be completely understood in terms of LPT transformations. In the present work we study the mechanism of formation of non-stationary regimes manifested by the recurrent energy transport in the system of three weakly coupled, non-linear oscillators

$$\begin{aligned}
&\frac{d^2x_1}{dt^2} + x_1 = \varepsilon[(-x_1)^{3/2}_{+} - (x_1)^{3/2}_{+}] - \beta_1\varepsilon(x_1 - x_2);\\
&\frac{d^2x_2}{dt^2} + x_2 = \varepsilon[(-x_2)^{3/2}_{+} - (x_2)^{3/2}_{+}] - \beta_1\varepsilon(x_2 - x_1) - \beta_2\varepsilon(x_2 - x_3);\\
&\frac{d^2x_3}{dt^2} + x_3 = \varepsilon[(-x_3)^{3/2}_{+} - (x_3)^{3/2}_{+}] - \beta_2\varepsilon(x_3 - x_2);
\end{aligned} \tag{1}$$

where $\varepsilon << 1$ characterizes weak coupling and weak nonlinearity (due to smallness of the amplitudes), β_1 and β_2 are the parameters of coupling.

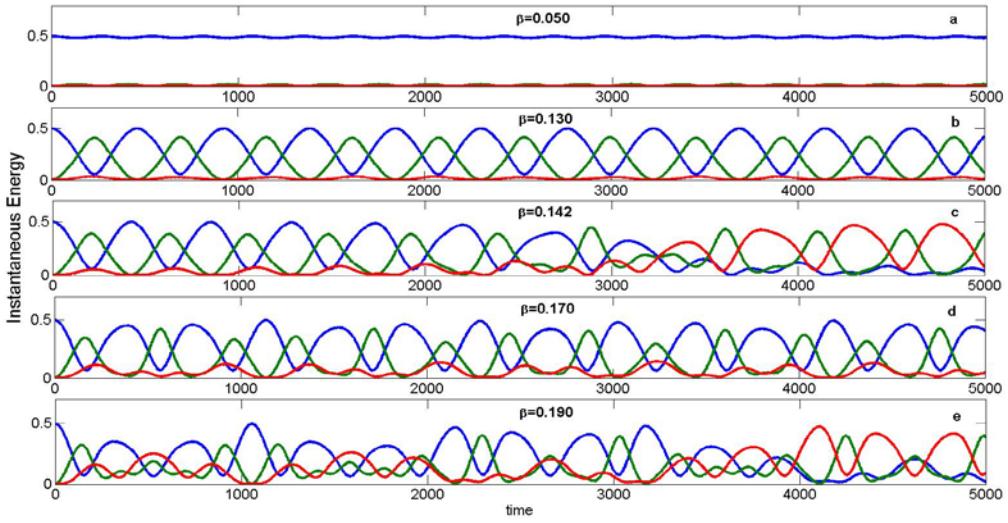

Fig. 1. Instant energies on each oscillator (the blue curve refers to the 1st oscillator, the green curve to the 2nd and the red curve to the 3rd oscillator) for different values of coupling parameter

In Figure 1 we show that gradual variation of the parameter of coupling leads to two peculiar global bifurcations of the system response excited by the pulse excitation provided to the first oscillator. In Figures 1(*a–e*) we plot instant energies recorded on each oscillator. Here, we show that gradual variation of the parameter of coupling leads to two peculiar global bifurcations of the system response.

Introducing the complex variables $v_j = \frac{du_j}{dt}$; $v_j = \frac{1}{2}\left(\psi_j + \psi_j^*\right)$; $u_j = -\frac{i}{2}\left(\psi_j - \psi_j^*\right)$; $\psi_j = (v_j + iu_j)$; $\psi_j^* = (v_j - iu_j)$, separating "fast" $\tau_0 = t$ and "slow" $\tau_1 = \varepsilon\tau_0$ time-scales and seeking the solutions in the form $\psi_j = \varphi_j e^{i\tau_0}$, $j = 1,2$ we use the multiple–scale procedure $\varphi_j(\tau_0,\tau_1) = \varphi_{j,0}(\tau_0,\tau_1) + \varepsilon\varphi_{j,1}(\tau_0,\tau_1)$, $j = 1,2,3$, $\frac{d}{d\tau} = \frac{\partial}{\partial\tau_0} + \varepsilon\frac{\partial}{\partial\tau_1}$ to obtain a system in the main asymptotic approximation:

$$\begin{aligned}
&\frac{d\varphi_{10}}{d\tau_1} = i\gamma|\varphi_{10}|^{1/2}\varphi_{10} + \frac{i\beta_1}{2}(\varphi_{10} - \varphi_{20}),\\
&\frac{d\varphi_{20}}{d\tau_1} = i\gamma|\varphi_{20}|^{1/2}\varphi_{20} + \frac{i\beta_1}{2}(\varphi_{20} - \varphi_{10}) - \frac{i\beta_2}{2}(\varphi_{20} - \varphi_{30}),\\
&\frac{d\varphi_{10}}{d\tau_1} = i\gamma|\varphi_{30}|^{1/2}\varphi_{30} + \frac{i\beta_2}{2}(\varphi_{30} - \varphi_{20}).
\end{aligned} \tag{2}$$

Since only the resonant term of Hertzian potential should be included in this approximation, we obtain the coefficient γ as the corresponding amplitude of the Fourier-spectrum.

Based on the theory of limiting phase trajectories [7] one can easily deduce the first transition criterion (β_{CR1}) predicting the breakdown of energy localization on the first oscillator and the formation of the recurrent energy transport between the two coupled oscillators. The second criterion (β_{CR2}) predicting the breakdown of energy localization on the first two oscillators succeeded by the irregular energy wandering between all the three oscillators is somewhat more complicated. To derive this criterion analytically we formulate the special resonant conditions between the limiting phase trajectory recorded on the first two oscillators and the response of the third one. Limiting phase trajectory is approximated (to the leading order) by the saw-tooth functions [7]. This enables the derivation of the second criterion analytically in the closed form. The analytical prediction – β_{CR2} = = 0.138; breakdown of LPT in the original system (1) β_{CR2} = 0.140.

The derived analytical approximation is further extended to the system of three (and more) weakly coupled chains (i.e. granular chains) where the transport of localized excitations (breathers) between the two and three chains is predicted analytically. It is worth emphasizing that the first and second criteria can be hardly obtained by the conventional bifurcation analysis of stationary regimes, which provides very crude, unsatisfactory predictions.

Acknowledgements

This research is supported by the grant 14-01-00284 A of the Russian Foundation for Basic Research. The second author is grateful to the Israel Science Foundation (Grant 484 /12) for financial support.

References

1. L.I. Manevitch, *Arch. Appl. Mech*., 2007, **77**, 301.
2. L.I. Manevitch and A.I. Musienko, *Nonlin. Dyn*., 2009, **58**, 633.
3. L.I. Manevitch and V.V. Smirnov, *Phys. Rev. E*, 2010, **82**, 036602.
4. L.I. Manevitch, A.S. Kovaleva, and D.S. Shepelev, *Physica D*, 2011, **240**, 1.
5. L.I. Manevitch, A.S. Kovaleva, and E.L. Manevitch, *Math. Prob. Eng*., 2010, **760479**, 518.
6. Y. Starosvetsky, Y. Ben-Meir, *Phys. Rev. E*, 2013, **87**, 062919.
7. V.N. Pilipchuk, *J. Sound Vib*., 1996, **192**(1), 43.

EFFICIENCY OF LEADER´S STRATEGY TO GAIN PUBLIC OPINION: MODELING AND COMPUTER SIMULATION IN A SOCIAL NETWORK

E.V. Kurmyshev[1] and **H.A. Juarez**[1]

[1] Centro Universitario de los Lagos, Universidad de Guadalajara, Lagos de Moreno, México,
ekurmyshev@culagos.udg.mx; hjuarez@culagos.udg.mx

Abstract. Public opinion is formed by means of self-organization of agents' opinion influenced by a leader, the latter uses a strategy to gain as many followers as possible. Efficiency of straightforward, zigzag and staircase strategies of a single leader in the opinion formation in a social network is studied in the frame of C/PA bounded confidence model. Results of simulation show complex bifurcation patterns of opinion dynamics; a decrease or even the total loss of control of the leader over the society is observed. Comparative analysis of the efficiency of the three strategies of a dictator and democratic leader is presented.

C/PA model of opinion dynamics

Social groups are constituted of persons of different psychological types [1]. In order to capture this important feature, a model of opinion dynamics in a mixed C/PA society was proposed in [2]. It consists of agents of two psychological types, concord (C-) and partial antagonism (PA-) agents. The interval $S = [-1, 1]$ is a continuous opinion space. Each agent i is characterized by his/her opinion, x_i, and uncertainty or tolerance, $u_i \in (0, 0.7)$. An opinion segment $s_i = [x_i - u_i, x_i + u_i]$ is assigned to each agent i. For two agents, i and j, their opinion segments overlap if and only if the opinion overlap $h_{ij} = \min(x_i + u_i, x_j + u_j) - \max(x_i - u_i, x_j - u_j) > 0$. The C/PA society of N agents consists of two subpopulations, M_C and M_{PA} of pN and $(1 - p)N$ size respectively, where a fraction of C-agents, $0 \le p \le 1$, is a parameter of the model. When an active agent i, either C- or PA-type, interacts with a passive one j, agent j changes its opinion and uncertainty following the updating rules for the C-agents, Eqs. (1), if $j \in M_C$ or those for the PA-agents, Eqs. (2), if $j \in M_{PA}$. The opinion and uncertainty of passive (receptive) agent j are changed when $0 \le h_{ij}$. The updating rule for the opinion and uncertainty of a passive C-agent j is as follows:

$$x_j := x_j + \mu_1(h_{ij} / 2u_i)(x_i - x_j); \quad u_j := u_j + \mu_2(h_{ij} / 2u_i)(u_i - u_j) \tag{1}$$

The interaction of C-agents is always attractive, which gives the name to the concord agents. Real life interaction between persons is usually repulsive-attractive, so the updating rule for the opinion and uncertainty of a passive PA-agent j is given by the following equations:

$$x_j := x_j + \mu_1(h_{ij} / 2u_i)(h_{ij} / u_i - 1)(x_i - x_j); \; u_j := u_j + \mu_2(h_{ij} / 2u_i)(h_{ij} / u_i - 1)(u_i - u_j) \tag{2}$$

The relative agreement $(h_{ij}/ 2u_i)(h_{ij}/ u_i - 1) \in [-0.125, 1]$, thus the opinions of PA-agents can diverge from that of active agents when $(h_{ij} / u_i - 1) \le 0$.

Model leader in the mixed C/PA-society

A leader must be able to communicate ideas to agents and convince them [3]. Communication implies direct or implicit interaction of the leader with a relatively large portion of population. To convince implies having some kind of "power" of opinion manipulation. This "power" can be either natural (charismatic leaders), given by some degree of reputation or experience, or implemented by some means such as a reward or even coercion. We consider as a leader an agent connected with a significant part of population; his/her degree of connectivity d_l runs through 0.2 to 1. A leader has a goal and strong conviction to reach it, so his/her opinion x_l is considered to be unaffected by other agents; he/she is always an active agent. The "democracy level" of the leader is represented by his/her opinion uncertainty or tolerance, u_l. We assume that a "dictator" (authoritarian leader) has invariable low tolerance, $u_l = 0.2$, whereas the tolerance of "democratic leader" equals the average tolerance of population, $u_l = U$.

Experiment design and results of computer simulation

Given a leader of certain type, what strategy is favorable to gain maximum number of followers? To answer this question, the efficiency of the straightforward, zigzag and staircase leader´s strategies

implemented by leaders of democratic and dictator type is assessed. The inverse problem is formulated as follows: Given the goal and strategy, a "leader" (coordinator) of what type is preferable? We study numerically the steady state patterns of opinion distribution on the Small World (SW) networks of 600 PA- and 400 C-agents, in function of the average initial tolerance of population, *U* ranging from 0.2 through 0.7. The system evolves 500 time steps to reach steady state distributions of opinion. Each time step, $N = 1000$ pairs of linked agents are selected randomly, and one agent of each pair is taken to be a passive agent; if $h_{lj} \geq 0$, then the passive agent updates his/her opinion according to Eqs. (1) or (2).Uniform initial conditions for the opinion and tolerance of agents are used. We consider the following strategies: **Straightforward** (leader´s opinion and tolerance are invariable all time); **Staircase** (leader´s opinion and tolerance are not affected any time, but his/her opinion changes linearly in time from an initial to target value) and **Zigzag** (leader´s opinion and tolerance are not influenced any time, but his/her opinion changes in time in zigzag in a such way that the initial opinion is equal to the target one). Agents, whose opinion $x_j \in (x_l - 0.1; x_l + 0.1)$, are considered to be followers of the leader with the target opinion x_l. Examples of leader´s efficiency versus *U* are given in Fig. 1. The plots represent the average over 30 simulations for each value of *U*.

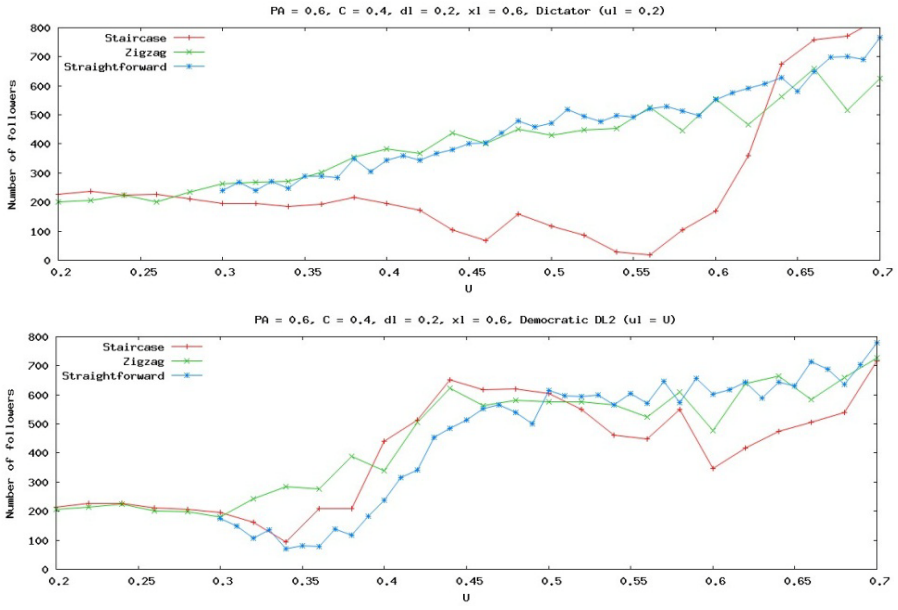

Fig. 1. Number of followers of dictator (A) and democratic leader (B) for each of the three strategies

Conclusions

1. Leader´s efficiency depends strongly on the C/PA composition [4] and public tolerance, *U*. None of the three strategies can be considered preferable in all range of the parameter *U*.
2. In the low tolerance society ($U \in (0.2, 0.3)$), the efficiency of the dictator is almost equal to that of the democratic leader for each strategy.
3. Strong variations in the number of followers and low efficiency of leader, up to the total loss of control over public opinion are observed as a function of public tolerance *U*.
4. In order to give practical recommendations, detailed analysis of the opinion dynamics should be done in the following parametric space: social C/PA composition of the society, average tolerance of agents *U*, type of leader and his/her social power, leader´s connectivity to the network d_l, leader´s strategy and target opinion, topology of the network along with the initial conditions of the society.

References

1. H.-X. Yang, Z.-X. Wu, C. Zhou, T. Zhou, B.-H. Wang, *Phys. Rev. E*, 2009, **80,** 046108.
2. E. Kurmyshev, H.A. Juárez, and R.A. González-Silva, *Physica A*, 2011, **390**(16), 2945-2955.
3. B.M. Bass and R. Bass, *The Bass handbook of leadership*, 4th ed, Free Press, 2008.
4. E. Kurmyshev and H. A. Juárez, **arXiv:1305.4677** (May 2013).

Invited

EXAMPLES OF MECHANICAL SYSTEMS MANIFESTING CHAOTIC HYPERBOLIC ATTRACTORS OF SMALE-WILLIAMS TYPE

S.P. Kuznetsov

Kotel'nikov Institute of Radio-Engineering and Electronics of RAS, Saratov Division, Russia
spkuz@yandex.ru

An interesting kind of dynamical behavior is structurally stable chaotic dynamics associated with uniformly hyperbolic attractors, such as the Smale – Williams solenoid [1]. As we try developing clear and transparent examples [2], the preference surely should be given to mechanical systems. Indeed, it is the mechanical motions that are easily perceived and interpreted due to our everyday experience [3]. I report here on three simple mechanical systems with chaotic attractors of Smale – Williams type.

1. Consider a particle of unit mass on a plane in a stationary potential field possessing rotational symmetry about the origin, with minimum on the unit circle (Fig. 1). An additional potential force field is applied, being switched on and off periodically, with time interval T and producing short-time kicks of magnitude and direction depending on the instantaneous position of the particle. The model equations are

$$\begin{aligned} \ddot{x} &= \mu x(1-x^2-y^2)+(-x+x^2-y^2)\sum_{n=-\infty}^{\infty}\delta(t-nT)-\alpha\dot{x} \\ \ddot{y} &= \mu y(1-x^2-y^2)+(-y-2xy)\sum_{n=-\infty}^{\infty}\delta(t-nT)-\alpha\dot{y}. \end{aligned} \qquad (1)$$

In practice, a pulsed potential field can be produced using six electromagnets (the hexapole) and an additional magnet G that creates a centrally symmetric part of the potential. All these magnets are switched on periodically by current pulses (Fig. 1a). The particle should be a permanent magnet, one pole of which is involved in the interaction, and the other one is removed outside the interaction region. Panel (b) depicts the trajectory of the particle, and panel (c) shows the attractor in the stroboscopic section in a two-dimensional projection. The attractor is a kind of Smale – Williams solenoid, with distinguishable Cantor-like transversal structure. As checked, the angular coordinate behaves in accordance with the expanding circle map (one bypass for the pre-image implies two detours for the image in the opposite direction).

2. Consider two disks arranged horizontally, one above the other, which rotate about the common axis alternately (while one is rotating, the other is at rest and vice versa) with angular velocity ω (Fig. 2a). On each disk a particle is placed, capable to slide with the friction force proportional to its relative velocity. Suppose that there is a potential field symmetric about the axis, with potential minimum at the center and strongly growing to the edges of the disks. In addition, assume that the two particles interact via the appropriately chosen potential $V(\mathbf{r}_1-\mathbf{r}_2)$, where $\mathbf{r}_1$ and $\mathbf{r}_2$ are the position vectors. Model equations are

$$\begin{aligned} \ddot{x}_1 &= x_1(k+x_1^2+y_1^2)+\alpha(-\omega_1 y_1-\dot{x}_1)-\varepsilon[(x_1-x_2)^2-(y_1-y_2)^2], \\ \ddot{y}_1 &= y_1(k+x_1^2+y_1^2)+\alpha(\omega_1 x_1-\dot{y}_1)+2\varepsilon(x_1-x_2)(y_1-y_2), \\ \ddot{x}_2 &= x_2(k+x_2^2+y_2^2)+\alpha(-\omega_2 y_2-\dot{x}_2)+\varepsilon[(x_1-x_2)^2-(y_1-y_2)^2], \\ \ddot{y}_2 &= y_2(k+x_2^2+y_2^2)+\alpha(\omega_2 x_2-\dot{y}_2)-2\varepsilon(x_1-x_2)(y_1-y_2), \end{aligned} \qquad (2.5)$$

where

$$\omega_1(t)=\begin{cases}\omega_0, & nT\le t<nT+T/2\\ 0, & nT+T/2\le t<nT,\end{cases} \qquad \omega_2(t)=\begin{cases}0, & nT\le t<nT+T/2\\ \omega_0, & nT+T/2\le t<nT.\end{cases} \qquad (2.6)$$

With appropriate parameters, the chaotic dynamics in the map for the state transformation in successive periods of switching corresponds to the attractor of the Smale – Williams type.

3. The third example is related to a simplified model for parametric oscillations of a string. In the classic wave equation $\rho y_{tt}=Gy_{xx}$ with periodic boundary conditions we assume the tension force to depend on time as $G(t)=1+a_2^0\sin^2\pi(t/T-1/4)\sin 2\omega_0 t+a_6^0\cos^2\pi(t/T-1/4)\sin 6\omega_0 t$, wheread the density depends on the spatial coordinate as $\rho(x)=1+\varepsilon\sin 4k_0 x$ [4]. Next, we introduce dissipation by the terms $-(\alpha+\beta u^2)y_t$ and $-\gamma y$ added to the right-hand side of the equation. Nonlinear dissipation is needed to stabilize the parametric instability; moreover, it is also important that the cubic

nonlinearity provides generation of the third harmonic in the wave-oscillatory motion. Taking into consideration that the parametric excitation alternates at k_0 and $3k_0$, we use the ansatz $y = u_1 \cos k_0 x + v_1 \sin k_0 x + u_3 \cos 3k_0 x + v_3 \sin 3k_0 x$ to compose the low-dimensional model as a set of second-order ordinary differential equations for the variables $u_{1,3}$ and $v_{1,3}$ [3]. Figure 3 illustrates results of the numerical simulation for the finite-dimensional model which agree well with those relating to the partial-differential equations [4].

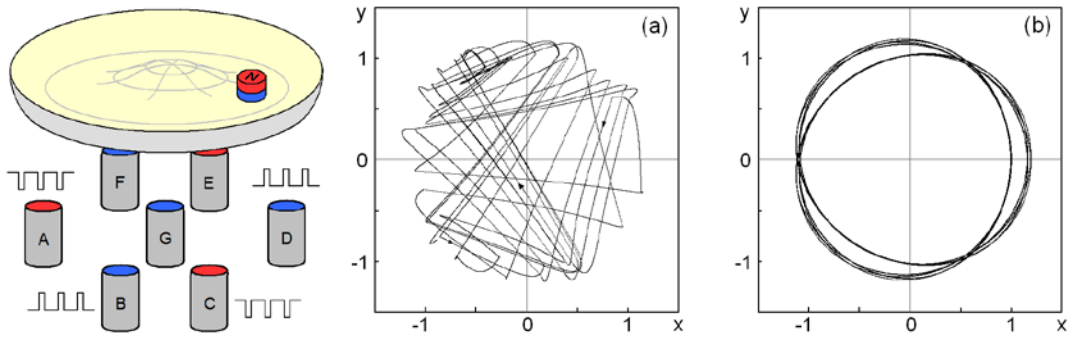

Fig. 1. Schematic setup (a), trajectory for the particle motion under periodic kicks (b) and stroboscopic portrait of the attractor (c). Parameters in equations (1): μ = 0.3, T = 4

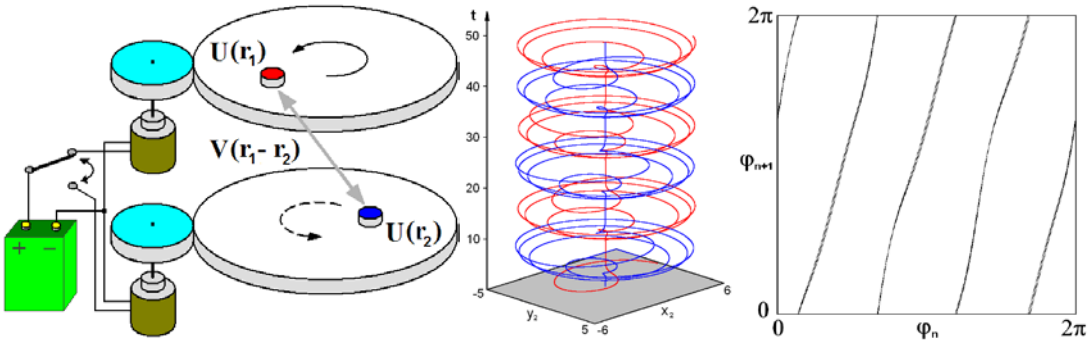

Fig. 2. Schematic setup (a), trajectories for the particles moving on the discs (b) and diagram for the angular variable of one particle (c). Parameters in equations (2): $k = 3$, $\alpha = 3$, $\varepsilon = 0.03$, $T = 16$, $\omega_0 = 2\pi$

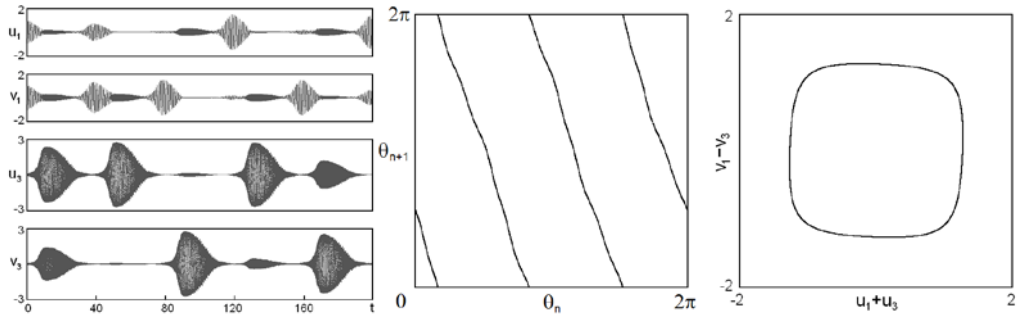

Fig. 3. Plots of the amplitude coefficients versus time (a), diagram for the angular variable for the amplitude ratio for cosine and sine components (b) and stroboscopic portrait of attractor in projection on the plane (c)

at $\omega_0 = k_0 = 2\pi$, $T = 40$, $L = 1$, $a_2^0 = 0.4$, $a_6^0 = 0.2$, $\varepsilon = 0.2, \alpha = 0.4, \gamma = 0.03$

Acknowledgements

The work is supported by the RFBR grant No. 12-02-00342 and by the grant of the President of the Russian Federation for Leading Research Schools NSh-1726.2014.2.

References

1. L. Shilnikov, *Int. J. of Bifurcation and Chaos*, 1997, **7**(9), 1353-2001.
2. S.P. Kuznetsov, *Physics-Uspekhi*, 2011, **54**(2), 119-144.
3. S.P. Kuznetsov, *Nonlinear Dynamics and Mobile Robotics*, 2013, **1**(1), 3–22.
4. O.B. Isaeva, A.S. Kuznetsov, S.P. Kuznetsov, *Phys. Rev. E*, 2013, **87**, 040901.

Invited

ENERGY EXCHANGE AND LOCALIZATION IN FINITE NONLINEAR OSCILLATORY CHAINS

L.I. Manevitch

Semenov Institute of Chemical Physics of the Russian Academy of Science, Moscow, Russia
manevitchleonid3@gmail.com

Abstract. We discuss a recently developed concept of limiting phase trajectories (LPT) allowing a unified description of resonance non-stationary processes for a wide range of classical and quantum dynamical systems. This concept provides the far going extension of the linear beating phenomenon to a diverse variety of nonlinear systems. The non-stationary processes are characterized by intense energy exchange between different parts of the system or by strong energy localization. They include, e.g., targeted energy transfer, non-stationary vibrations of carbon nanotubes, quantum tunneling, auto-resonance and non-conventional synchronization. In such processes, LPTs play the key role, similar to that of normal modes in a stationary case.

A comprehensive theory of *nonlinear normal modes (NNMs)* was developed for the analysis of stationary processes, their stability and bifurcations [1–3]. Besides, the combinations of non-resonant NNMs in quasi-linear systems can be used for an asymptotic description of non-stationary processes with account of the amplitude dependence of the frequencies [4]. However, energy exchange and transport under the condition of resonance are characterized by the complicated non-stationary behavior, for which any analytical investigation is prohibitively difficult.

We discuss a new concept and methods of analysis, which provide the answers to the following open questions relating to the resonance non-stationary processes:

1) What is an adequate description of nonlinear beating?

2) How to extend the concept of beats to multi-particle linear and non-linear systems? What is the relationship between beats and stationary excitations of the equilibrium ground state?

3) What are the conditions of the transition from intense energy exchange to energy localization in finite discrete systems and carbon nanotubes?

4) What conditions provide irreversible energy transfer in classical and quantum systems?

5) What are the conditions of transition from irreversible energy transfer to autoresonance in the systems with slowly varying frequency of external excitation?

6) Can non-conventional synchronization of weakly coupled auto-generators exist?

Recent studies [5–14] have proved that the answers to the above-listed questions can be obtained in the framework of the *LPT concept*. It was shown that along with NNMs, the fundamental oscillations of another type can exist in the systems of weakly coupled oscillators. The solutions of this type which are referred to as LPTs describe non-stationary processes with the strongest modulation. They are characterized by the maximum possible energy exchange between the oscillators or clusters of the oscillators (effective particles), or the maximum energy transfer from the external source of energy.

The development and use of the analytical framework based on the LPT concept are motivated by the fact that non-stationary processes occurring in a broad variety of finite dimensional physical models are beyond the paradigm of nonlinear normal modes, fully justified only for quasi-stationary processes and non-stationary processes in a non-resonant case. While the NNMs approach was proved to be an effective tool for the analysis of existence, instability and bifurcations of stationary regimes, the use of the LPTs concept provides adequate procedures for studying the strongly modulated regimes as well as the transition to energy localization.

From the beginning, the systems with constant parameters are discussed. It is shown that the LPT approach allows one to distinguish the non-stationary motions related to quasi-linear, moderately and strongly nonlinear regimes and to define the parametric boundaries for their existence and stability. Unique analytical approximations based on reduced order models describing non-stationary dynamics are presented as well. The obtained approximations reveal a series of unexpected phenomena in various nonlinear, classical and quantum systems, such as externally driven nonlinear oscillators, systems of weakly coupled nonlinear oscillators and oscillatory chains, as well as systems of two-level quantum models. Moreover, the same concept enables prediction of non-conventional LPT-synchronization in the system of weakly coupled autogenerators, and this is in contrast to the conventional NNM-synchronization. A special attention is paid to non-stationary nonlinear dynamics of single walled carbon nanotubes, in which the significant phenomenon of weak energy localization has been revealed.

Along with the well-known asymptotic methods, the investigation of the new phenomena has required application of a special technique of non-smooth temporal transformations providing a simple description of strongly modulated and transient regimes.

The applications of the LPT concept to the systems with slowly-varying parameters relates to two significant problems. One of them is prediction of the necessary conditions for the emergence of autoresonance in the nonlinear systems with time-dependent frequency detuning. The second problem is the targeted energy transfer in nonlinear systems with time-varying parameters. The latter problem in the conservative limit is mathematically similar to that for nonlinear quantum tunneling.

The presented results allow making some general conclusions.

The conventional classification of the problems of mathematical physics (in the oscillation and wave theory) draws first of all a sharp distinction between linear and nonlinear models. Such a distinction is caused by understandable mathematical reasons, including the inapplicability of the superposition principle in the nonlinear case. However, in-depth physical analysis allows us to introduce an alternative basis for the classification of oscillation problems, focusing on the difference between the stationary (or non-stationary, but non-resonance) and resonance non-stationary processes. In the latter case, the difference between the linear and nonlinear problems is not so fundamental, and a specific technique, efficient in the same degree for description of both linear and nonlinear resonance non-stationary processes, can be developed. The existence of an alternative approach in the framework of the linear theory seems unexpected. Really, the superposition principle allows us to find a solution describing arbitrary non-stationary oscillations as a combination of linear normal modes, which correspond to stationary processes. However, in the systems of weakly coupled oscillators, in which resonant non-stationary oscillations are possible, the LPT as another type of fundamental solution can exist. It describes the strongly modulated non-stationary oscillations with using a specific mathematical tool. We demonstrate that the LPT concept suggests a unified approach to the study of such physically different processes as strongly non-stationary energy transfer in a wide range of classical oscillatory systems and quantum dynamical systems with constant and time-varying parameters. Furthermore, this analogy paves the way for simple mechanical simulation of complicated quantum effects.

Acknowledgements

The work was supported by the RFBR, Project No. 14-01-00284.

References

1. M. Rosenberg, *Adv. Apple. Mech*., 1966, **9**, 155-242.
3. L. Manevitch, Yu. Mikhlin, and V. Pilipchuk, *The Normal Vibrations Method for Essentially Nonlinear Systems*, Nauka Publ., Moscow, 1989 (in Russian).
4. A. Vakakis, L. Manevitch, Yu. Mikhlin, V. Pilipchuk, and A. Zevin, *Normal Modes and Localization in Nonlinear Systems*, Wiley, New York, 1996.
5. A. Nayfeh and D. Mook, *Nonlinear oscillations*, J. Wiley & Sons, New York, 1979.
6. L. Manevitch, *Arch. Appl. Mech*. 2007, **77**(5), 301-312.
7. L. Manevitch, A. Kovaleva, and D. Shepelev, *Physica D*, 2011, **240**(1), 1-12.
8. L. Manevitch and A. Kovaleva, Nonlinear energy transfer in classical and quantum systems, *Phys. Rev. E*, 2013, **87**(2), 022904.
9. L. Manevitch, Y. Kosevich, M. Mane, G. Sigalov, L. Bergman, and A. Vakakis, *Int. J. Nonlinear Mech*., 2011, **46**(1), 247-252.
10. A. Kovaleva and L. Manevitch, *Phys. Rev. E*, 2013, **88**(2), 24901.
11. L. Manevitch, M. Kovaleva, and V. Pilipchuk, *Europh. Lett.*, 2013, **101**(5), 50002.
12. M. Kovaleva, L. Manevitch, and V. Pilipchuk, *JETP*, 2013, **117**(2), 369-377.
13. L. Manevitch and V. Smirnov, *Physical Review E*, 2010, **82**(3), 036602.
14. V. Smirnov, D. Shepelev, and L. Manevitch, *Phys. Rev. Let.*, 2014, in press.
15. L.I. Manevitch and O.V. Gendelman, *Tractable Models of Solid Mechanics. Formulation, Analysis and Interpretation*, Springer, Heidelberg Dordrecht London New York, 2011.

Invited

RECURRENCE PLOTS AND COMPLEX NETWORKS FOR TIME SERIES ANALYSIS

N. Marwan, J. Donges, R. Donner, and **J. Kurths**

Potsdam Institute for Climate Impact Research, Potsdam, Germany, marwan@pik-potsdam.de

Abstract. Recurrence plots and derived techniques are powerful and modern time series analysis tools with a wide applicability. Recent developments have linked recurrence plots with complex networks analysis, thus, providing new and complementary measures of complexity for time series analysis. The complex network measures are related to geometrical and topological properties of the phase space representation of the dynamics. Recent applications have demonstrated the potential for data classification (e.g., for medical diagnosis), transition analysis (e.g., for detecting paleoclimatic regime transitions), or coupling analysis (e.g., for identifying coupling directions or indirect couplings).

Introduction

In the last two decades, the method of recurrence plots has been developed as a powerful approach to investigate complex dynamics [1, 2]. A recurrence plot (RP) is the graphical representation of a binary symmetric square matrix that encodes the times when two states $\mathbf{x}(i)$ and $\mathbf{x}(j)$ are in close proximity (i.e., neighbours in phase space)

$$R_{i,j} = \Theta(\varepsilon - \|\mathbf{x}(i) - \mathbf{x}(j)\|)$$

Based on such a recurrence matrix **R**, a large and diverse amount of information on the dynamics of the system can be extracted and statistically quantified (using recurrence quantification analysis, dynamical invariants, etc.) in order to study dynamical properties, complexity, dynamical transitions, synchronization, or indirect couplings. The potential of the RP based time series analysis has been shown by numerous applications in various disciplines, such as cardiophysics [3], ecology [4], econophysics [5, 6], engineering [7, 8], etc. RP based techniques often provide useful results even when applied to short and non-stationary data, which is often a critical issue when studying real world data.

Complex network based time series analysis

During the last years, increasing efforts have been spent on applying network-based concepts also for the analysis of dynamically relevant statistical properties of time series (e.g., cycle networks, correlation networks, visibility graphs [9]). A widely used approach is to identify the recurrence matrix **R** as the adjacency matrix of a complex network. The time points of the states are, thus, the nodes of the network. Links in the network correspond to close states in the phase. This procedure allows us to apply new quantitative characteristics (such as average path length, clustering coefficient, or centrality measures of the recurrence network) providing complementary information about the topological properties of the attractor of the dynamical system.

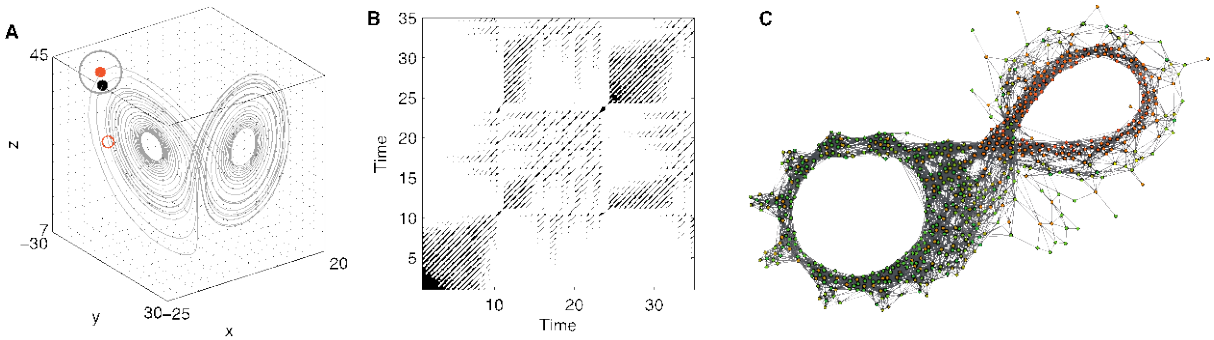

Fig. 1. (A) Phase space trajectory of the Lorenz system, the corresponding (B) recurrence plot, and (C) complex network as derived from the recurrence plot

The probably most interesting complex network measure for this purpose is the transitivity coefficient *T*

$$T = \frac{\sum_{ijk=1}^{N} A_{jk} A_{ij} A_{ik}}{\sum_{ijk=1}^{N} A_{ij} A_{ik} (1 - \delta_{jk})}$$

measuring the probability that two neighbours of a node are also linked. Such probability will be high for phase space trajectories evolving parallel for a long time, but low for quickly diverging phase space trajectories. Therefore, roughly speaking, this measure can be interpreted in the sense of regularity of the dynamics. In fact, it can be shown that T is related to the dimension of the attractor in phase space [10] and that it can be used for studying coupling directions [11].

Application example

Long-term variations in aeolian dust deposits are related to changes in terrestrial vegetation and are often used as a proxy for changing climate regimes in the past. In the presented example, marine terrigenous dust flux records from the Ocean Drilling Programme (ODP) surrounding Africa are used to infer changes in African climate during the last 5 Ma. The complex network measures applied to these time series enable us to identify three epochs with transitions between qualitatively different types of environmental variability in North and East Africa [12, 13]. These environmental regime shifts coincide statistically significantly with major steps in hominid evolution, suggesting that the observed shifts between more regular and more erratic environmental variability may have acted as a trigger for rapid change in the development of human kind in Africa.

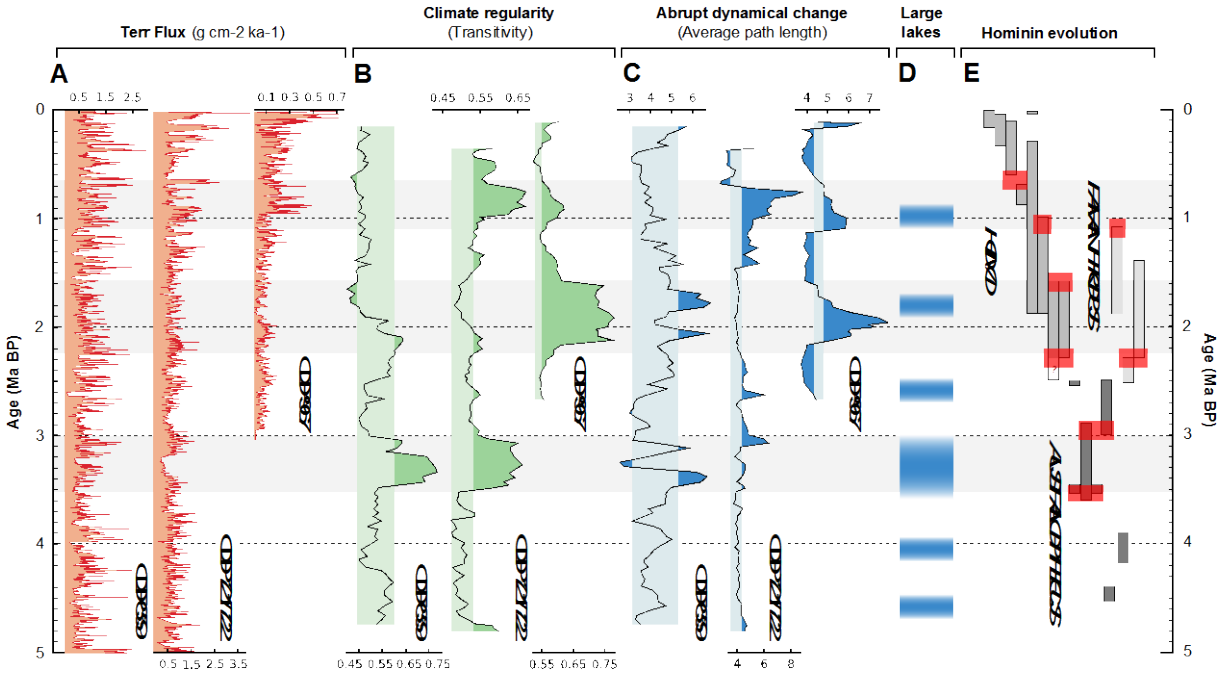

Fig. 2. (A) Dust flux records from surrounding Africa analysed by complex network measures (B) transitivity and (C) average path length. Environmental regime transitions coincide with (D) lake high stands and (E) hominin evolution steps

References

1. N. Marwan, M.C. Romano, M. Thiel, and J. Kurths, *Phys. Rep.*, 2007, **438**, 237–329.
2. N. Marwan, Eur. Phys. J. – Spec. Top., 2008, **164**, 3–12.
3. G.M. Ramírez Ávila, A. Gapelyuk, N. Marwan, et al., *Philos. Trans. A*, 2013, **371**, 20110623.
4. A. Facchini, C. Mocenni, N. Marwan, et al., *Ecol. Modell.*, 2007, **203**, 339–348.
5. P.M. Crowley and A. Schultz, *Int. J. Bifurc. Chaos.*, 2011, **21**, 1215–1231.
6. C. Kyrtsou and C.E. Vorlow, *N. Trends Macroecon.*, 2005, 223–238.
7. A.K. Sen, R. Longwic, G. Litak, K. Górski, *Mech. Syst. Signal Process*, 2008, **22**, 362–373.
8. G. Litak, A. Syta, B.F. Yao, C.X. Li, *J. Theor. Appl. Mech.*, 2009, **47**, 55–67.
9. R.V. Donner, M. Small, J.F. Donges, N. Marwan, et al., *Int. J. Bifurc. Chaos*, 2011 **21**, 1019–1046.
10. R.V. Donner, J. Heitzig, J.F. Donges, Y. Zou, et al., *Eur. Phys. J. B*, 2011, **84**, 653–672.
11. J.H. Feldhoff, R.V. Donner, J.F. Donges, N. Marwan, J. Kurths, *Phys. Lett. A*, 2012, **376**, 3513–3504 .
12. N. Marwan, J. Donges, Y. Zou, R. Donner, J. Kurths, *Phys. Lett. A*, **372**, 4246–4254.
13. J.F. Donges, R.V. Donner, M.H. Trauth, N. Marwan, H.-J. Schellnhuber, J. Kurths, *Proc. Natl. Acad. Sci. U. S. A.*, 2011, **108**, 20422–7.

COLLECTIVE DYNAMICS OF SPIKING NEURAL NETWORKS WITH MODULAR STRUCTURE AND DELAYED COUPLING

O.V. Maslennikov* and **V.I. Nekorkin**

Institute of Applied Physics, Nizhny Novgorod, Russia
* olmaov@neuron.appl.sci-nnov.ru

Abstract. We consider the impact of the delayed coupling on the collective dynamics of modular neural networks. Each module with complex topology contains excitatory and inhibitory neurons displaying irregular spiking sequences. Different modules are connected by relatively sparse excitatory delayed coupling. We found a dual role of the inter-module coupling delay in the collective network dynamics. First, with increasing time delay, in-phase and anti-phase regimes of the modular activity alternate. Second, the average frequency of the collective oscillations in each of these regimes decreases with increasing inter-module coupling delay.

Many natural systems are generally organized as complex networks of interconnected units. Interesting results were obtained relating to topological features of networks, for instance the fact that a number of networked systems – from neural and gene to social networks and the Internet – exhibit the same characteristics (e.g., the small world phenomenon). Recently, a more realistic and complicated class of networks began to be explored – dynamical networks. In this case not only complex topology is taken into account but also dynamics of nodes and links. The topical problem is the interplay between network complexity and individual nodal dynamics: what is the influence of both of them on collective network dynamics? The problem considered in this paper is the influence of structure modularity and delayed coupling on the collective behavior of spiking neural networks [1].

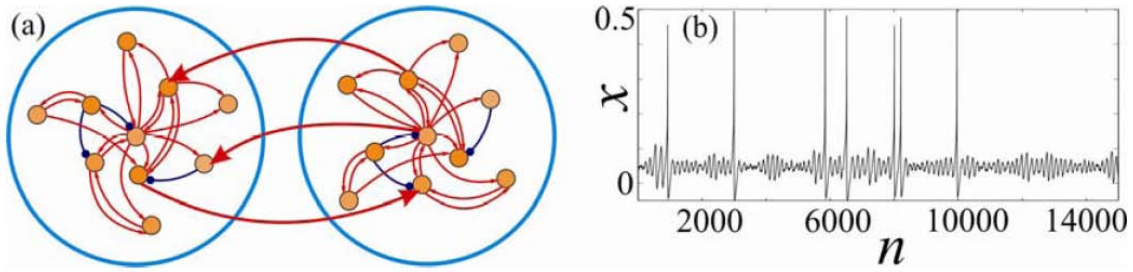

Fig. 1. (a) Schematic structure of a modular network consisting of two interacting subnetworks. (b) Example of the waveform of individual nodes

An example of a modular network is shown schematically in Fig. 1a. Such a model reflects the property of cortical networks that are spatially remote from each other and thus they interact with time delay. Each module consists of $N = 100$ active nodes coupled with each other by directed links which model the chemical synapses. Following the experimental observations, we set 80 % of the total number of neurons sending excitatory connections, and the rest 20 % of neurons inhibitory ones. We consider three different algorithms for generating an intra-module connection topology – a random Erdös-Rényi, small-world Watts-Strogatz, and scale-free Barabási-Albert network (the latter is shown schematically in Fig. 1a) – each of them more or less reproduces structural properties of real neural networks. The connections between the modules are random and relatively sparse: 5 % of nodes in one module send directed excitatory links to random nodes of another module.

Dynamics of the nodes is described by the following two-dimensional discrete-time system (a map) [2]:

$$x_{n+1} = x_n + F(x_n) - \beta H(x_n - d) - y_n,$$
$$y_{n+1} = y_n + \varepsilon(x_n - J).$$

Here the variable x describes qualitatively the membrane potential dynamics of a nerve cell, and y is responsible for the total effect of all ionic currents. $F(x)$ is a cubic function, $H(x)$ is a Heaviside step function, and ε, β, d, and J are control parameters. We chose the parameters so that the system should generate irregular spike sequences shown in Fig. 1b.

Consider the collective dynamics when the modules are coupled with delayed excitatory links. We gradually increase the delay τ starting from zero keeping constant the coupling strength and other parameters. For small spiking, the events depicted in Fig. 2a occur in a rather regular manner, although

at the individual level the rastrograms are stochastic. Synchronous behavior appears at the modular level shown in Fig. 2b where the waveforms of the average modular activity are shown. With a further increase of delay, we first observe incoherent spiking behavior and then another type of regularization – asynchronous modular oscillations (Fig. 2c, d).

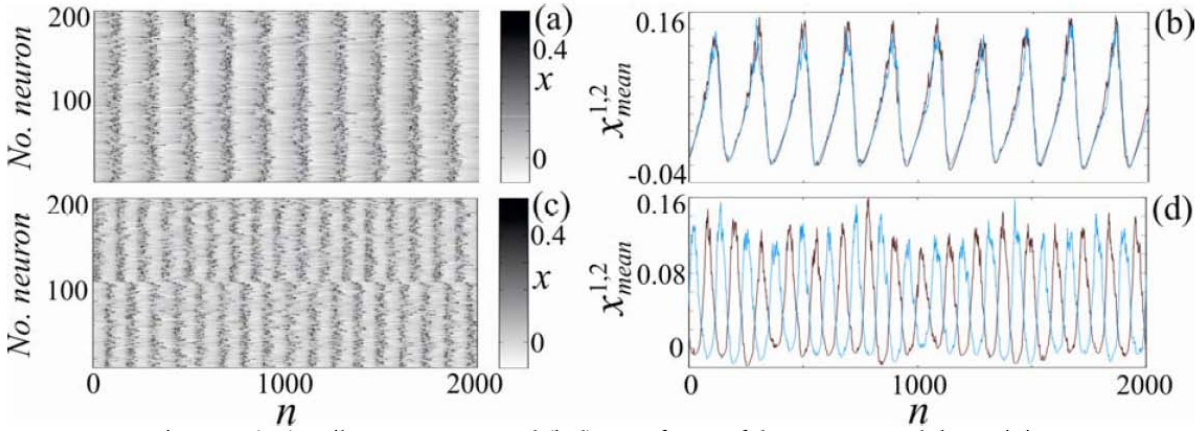

Fig. 2. (a, c) Spike rastrograms and (b, d) waveforms of the average modular activity for time delay (a, b) $\tau = 10$ and (c, d) $\tau = 50$

To characterize numerically the phenomena observed we use a simple synchronization parameter σ and plot spectra of average modular activity. The value of σ is equal to 1, if two burst-like modular oscillations are in-phase and σ is equal to 0 if they are anti-phase. Figure 3a shows the alternation of in-phase and anti-phase regimes as the delay increases. Another counterintuitive result shown in Fig. 3b is that within each of the regimes the average modular frequency decreases. This effect is observed for all three types of network topology considered.

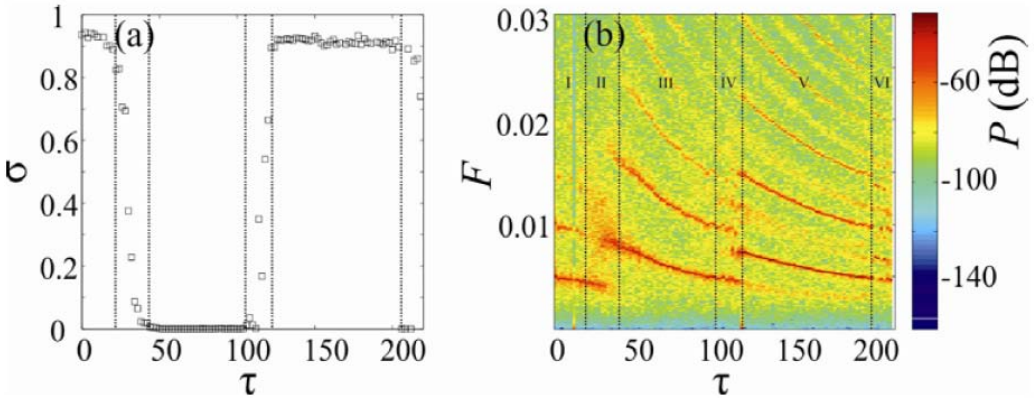

Fig. 3. (a) Modular synchronization parameter and (b) spectrogram of the average modular activity versus coupling delay τ

Thus, we found a dual role of the inter-module coupling delay in the collective network dynamics. First, with increasing time delay, in-phase and anti-phase regimes, where individual spikes form rhythmic modular burst-like oscillations, alternate with each other. Second, the average frequency of the collective oscillations in each of these regimes decreases with increasing inter-module coupling delay.

Acknowledgments

This work was supported by the Russian Foundation for Basic Research (Projects № 12-02-00526, 13-02-97050, 13-02-00858, 14-02-31622, 14-02-31873, and 14-02-00042).

References

1. O.V. Maslennikov, V.I. Nekorkin, *Phys. Rev. E*, 2014 (accepted 13/06/2014).
2. M. Courbage, V.I. Nekorkin, L.V. Vdovin, *Chaos*, 2007, **17**, 043109.

Invited

SYNCHRONIZATION IN MULTIFREQUENCY OSCILLATOR COMMUNITIES

A. Pikovsky[1,2] and **M. Komarov**[1,2]

[1]Department of Physics and Astronomy, University of Potsdam, Potsdam, Germany, pikovsky@uni-potsdam.de
[2] Department of Control Theory, Nizhny Novgorod State University, Nizhny Novgorod, Russia

Abstract. Typically in considerations of globally coupled oscillator populations one considers narrow frequency distributions. In this talk results for heterogeneous populations consisting of subpopulations at different natural frequencies are discussed.

Kuramoto model and its numereous generalizations describe the dynamics of the phases of self-sustained oscillators with close frequencies and global sinusoidal coupling. In contrast to previous works, we consider the case of multifrequency oscillator communities, where natural frequencies of interacting groups differ significantly. In this setup we cannot use a standard method of averaging since communities have strongly diverse periods of oscillations. In our work we extend the theory for two different cases of multifrequency populations in the phase approximation:

(i) in the first part we focused on the non-resonant interaction. In this case we assume that there are several groups of oscillators and that the frequencies within each group are close to each other but are strongly different between the groups. In this situation, the coupling within the group is resonant, like in usual Kuramoto-type models, but the coupling between the groups can be only non-resonant. We employed the Ott-Antonsen theory and demonstrated a variety of possible nontrivial regimes due to nonresonant interaction: coexistence and bistability of synchronous states as well as periodic oscillations. For a large number of interacting groups, more complex states appear: a stable heteroclinic cycle and a chaotic regime.

(ii) In the second part of the work we have considered the case of resonant interaction, where basic population frequencies strongly diverse from each other, but are in a combinational resonance. We focused in this work on a detailed description of the most elementary three-community “triplet” resonance. This is accomplished by using the Ott-Antonsen ansatz allowing one to write a closed system for complex order parameters for certain cases. Remarkably, for the triplet of populations the inter-community interaction not only shifts relative phases of the communities mean fields, but influences internal synchrony within communities.

Acknowledgements

M.K. thanks the RSCF (grant 14-12-00811) for partial support.

References

1. M. Komarov and A. Pikovsky, "Dynamics of Multifrequency Oscillator Communities", *Phys. Rev. Lett.*, 2013, **110**, 134101.
2. M. Komarov and A. Pikovsky, "Effects of non-resonant interaction in ensembles of phase oscillators", *Phys. Rev. E*, 2011, **84**, 016210.

Invited

SEGMENTED PATTERNS AND MECHANISMS OF THEIR FORMATION

A.A. Polezhaev

P.N. Lebedev Physical Institute of the Russian Academy of Sciences, Russia
e-mail address: apol@lpi.ru

Abstract. Segmented patterns are formed in different systems: physical, chemical, biological. First we give examples of segmented patterns observed in living systems and discuss possible mechanisms of their formation. Then we suggest three possible mechanisms for formation of segmented waves and spirals observed in the Belousov-Zhabotinsky reaction dispersed in a water-in-oil microemulsion. The first mechanism is caused by interaction of two coupled subsystems, one of which is excitable, and the other one has Turing instability. For the second mechanism we suggest "splitting" of the traveling wave in the vicinity of the bifurcation point of codimension-2, where the boundaries of the Turing and wave instabilities intersect. Finally we show that segmented waves can emerge in some simple two-component reaction-diffusion models with more than one steady state.

Segmentation is characteristic for systems of different nature. A great variety of segmented patterns is demonstrated by living systems. For instance, one can mention insects, flowers, seashells, various species of seaweed, pigmentation of the animal skin. Nice examples of segmented patterns are presented by growing colonies of some microorganisms – bacteria and amoebae. A very important example is vertebrate somitic segmentation in higher animals. Mechanisms of segmentation may be quite different. Nowadays some of them are well established while others need clarifying. It is assumed that segmented patterns on animal coats are caused by Turing instability. Patterns formed by aggregating cells of bacteria *Escherichia coli* are due to chemotaxis. Somites in the course of vertebrate segmentation are formed sequentially in space and time as a result of bulk oscillations in the presumptive mesoderm.

Segmented patterns are observed also in chemical systems. An interesting example of such patterns are segmented or dashed traveling waves first observed in the Belousov-Zhabotinsky reaction dispersed in a water-in-oil aerosol OT microemulsion, the so called BZ-AOT system. This system was developed by a group of V. Vanag and co-workers [1]. It demonstrates a remarkable variety of pattern formation phenomena, many of them previously unobserved in other reaction-diffusion systems. In particular for the first time the waves were obtained which in the course of propagation split into segments of certain scale – the so-called dashed and segmented waves. They were observed in the freshly made microemulsion and disappeared after 2–3 hours [2, 3]. Segmented waves were also discovered in a chlorine dioxide-iodine-malonic acid reaction [4] and in a reaction-diffusion-convection system [5].

Below we analyze possible mechanisms for segmented wave formation [6].

Interaction of excitability and Turing instability

We consider the case of a spatially-distributed system which is a combination of two subsystems: one corresponding to the excitable medium and the other potentially (for corresponding parameters) having Turing instability. The first subsystem parametrically influences the second one transferring it into unstable state. For the first subsystem we have chosen the FitzHugh-Nagumo model with the single excitable steady state which for appropriate initial conditions generates a spiral wave. For the second subsystem we explored either Brusselator (as is shown in Eq. 1) or another FitzHugh-Nagumo model with one of the parameters depending on the variables of the first subsystem.

$$\begin{cases} \dfrac{du}{dt} = u - \frac{u^3}{3} - v + D_F \nabla^2 u, \\ \dfrac{dv}{dt} = (u - \gamma v + \delta)\varepsilon, \\ \dfrac{dx}{dt} = a - (b(u) + 1)x + x^2 y + \nabla^2 x, \\ \dfrac{dy}{dt} = b(u)x - x^2 y + D_B \nabla^2 y, \end{cases} \tag{1}$$

where $b(u) = \begin{cases} b_c + \Delta \cdot u, & u \geq 0 \\ b_c, & u < 0 \end{cases}$, b_c is the value of the parameter b corresponding to the Turing bifurcation.

Numerical simulations demonstrate that depending on the properties of the interacting subsystems and values of the parameters used this mechanism is able to produce a variety of segmented waves differing in shape and size of segments.

Traveling wave segmentation near the Turing and wave bifurcations codimension-2 point

In the vicinity of the point of intersection in parametric space of the boundaries of Turing and wave bifurcations a wave can be presented in the form of superposition of corresponding modes: $u(r,t) = A_T e^{ik_T r} + A_L e^{i(wt+k_W r)} + A_R e^{i(wt-k_W r)} + c.c.$ Here A_T is the complex amplitude of the mode corresponding to the wave vector k_T, which became unstable due to the Turing bifurcation; A_R, A_L are complex amplitudes of modes corresponding to equal in magnitude but opposite in direction wave vectors $\pm k_W$ and frequency w, which became unstable due to the wave bifurcation.

Assuming that both bifurcations are supercritical, we can describe the dynamics of interacting modes by amplitude equations. Depending on the parameters these equations have several stable stationary solutions corresponding to different regimes: stationary Turing patterns, propagating waves and a mixed regime, when both a stationary pattern and a traveling wave coexist. The latter is just the case when a Turing pattern is superimposed on a traveling wave resulting in its "splitting" into segments.

Segmented waves in two-component reaction-diffusion models with multiple steady states

This mechanism was suggested in [2]. The authors explain segmentation of the wave by interaction of the excitable state and the state which demonstrates the so-called pseudo-Turing instability. (The interval of unstable modes includes the zero mode corresponding to uniform oscillations.) In numeric experiments they obtained segmented waves in the Gray-Scott model and in Oregonator [2, 3]. We obtained a segmented wave in the FitzHugh-Nagumo model in the case when it has three stationary states:

$$\begin{cases} \dfrac{du}{dt} = u - \frac{u^3}{3} - v + \nabla^2 u, \\ \dfrac{dv}{dt} = (\rho u - v + \delta)\varepsilon + D\nabla^2 v. \end{cases} \qquad (2)$$

Analysis of these equations has shown that in the case of constant values of parameters it is impossible to meet the conditions of both excitability (small ε), on the one side, and pseudo-Turing instability, on the other side. It becomes possible if one of the parameters, say ρ, is not constant: $\rho(u) = \begin{cases} \rho_1, u \geq 0 \\ \rho_2, u < 0 \end{cases}$. However, the range of parameters enabling segmented wave formation for this mechanism appears to be very narrow.

Acknowledgements

This work was partly supported by grants from the RFBR No. 14-01-00196 and 12-02-00529.

References

1. V.K. Vanag and I.R. Epstein, *Phys. Rev. Lett*., 2001, **87**, 228301.
2. V.K. Vanag and I.R. Epstein, *Phys. Rev. Lett.*, 2003, **90**, 098301.
3. V.K. Vanag and I.R. Epstein, *Proc. Natl. Acad. Sci. USA*, 2003, **100**, 14635–14638.
4. L. Yang, I. Berenstein and I.R. Epstein, *Phys. Rev. Lett.*, 2005, **95**, 038303.
5. F. Rossi and M.L.T. Liveri, *Ecological Modelling*, 2009, **220**, 1857–1864.
6. M.Yu. Borina and A.A. Polezhaev, *Kompjuternye Issledovanija i Modelirovanie*, 2013, **4**, 533–542 (in Russian).

Invited

SYNCHRONIZATION AND CONTROL IN NETWORKS OF STOCHASTICALLY COUPLED OSCILLATORS

M. Porfiri

New York University Polytechnic School of Engineering, Brooklyn, NY 11201

Abstract. The study of synchronization has attracted the interest of researchers from different fields of science and engineering for its pervasiveness across natural and technological settings. While most of the existing research has focused on static networks, in many instances, the coupling strength or the network topology may vary in time. In this presentation, we focus on stochastic networks, and we specifically address mean square synchronization of networks of chaotic maps. We demonstrate the possibility of formulating a master stability function for a class of stochastic networks and we offer a toolbox of close-form results to study blinking networks and stochastic pinning control.

Introduction

Synchronization is ubiquitous in both natural and technological settings. Synchronization has been observed in a large range of phenomena, spanning from biological systems, including animal grouping, fireflies' blinking, animal gaits, heart stimulation, epidemiology, and neural activity, to secure communications, chemistry, meteorology, and optoelectronics [1, 2]. Despite the vast technical literature on synchronization, the large majority of available studies has focused on dynamical systems that are coupled via static networks, whose topology and coupling strengths do not vary in time [1, 2].

Understanding synchronization over time-varying networks is a relatively untapped research question, with potential impact in improving our capacity of modeling complex systems and engineering adaptive networks [3]. For example, chaos synchronization over time-varying deterministic network topologies has been considered in [4], while stochastic networks have been examined in [5]. These studies have remarkably contributed to our understanding of synchronization over time-varying networks, by establishing a set of conditions for synchronization based on the node and the network dynamics.

However, many research questions are yet to be addressed, including the role of the time scale of the network dynamics on synchronization as well as the possibility of controlling the synchronized state of the system. Here, we seek to offer some answers to these questions by summarizing recent work at New York University [6–11]. We focus on the synchronization of N chaotic maps, whose individual dynamics is governed by $x(k + 1) = F(x(k))$ where $x \in \mathrm{R}^m$ is the oscillator state, F is a nonlinear function describing the system dynamics, and k is the time variable. The oscillators are coupled through a stochastically switching network described at time k by the graph Laplacian $L(k) = = [L_{ij}(k)] \in \mathrm{R}^{N\times N}$ with $i, j = 1,\ldots, N$. The equations of motion read

$$x_i(k+1) = F(x_i(k)) - \varepsilon \sum_{j=1}^{N} L_{ij}(k) H(x_j(k)) \qquad (1)$$

where $i = 1, \ldots, N$, H is the coupling function, and ε is the positive coupling strength.

Approach

Our analysis is based on the linear stability of the synchronization manifold in the mean square sense, whereby we linearize the system dynamics in the neighborhood of a synchronized trajectory and then study the mean square stability of the error dynamics. For switching networks characterized by independent identically distributed graph Laplacians, mean square stability of the error dynamics corresponds to the stability analysis of a time-varying deterministic system for the evolution of the error autocorrelation. Importantly, the error autocorrelation is a vector in $\mathrm{R}^{mN\times mN}$, which results into the analysis of a far larger system. While the analysis of such a system is generally very challenging, closed-form analytical results can be established in a few important scenarios.

Results

First, we consider networks of so-called conspecific agents [9], for which: i) the cardinality of an agent's neighbor set and the weights assigned to its neighbors are given by two jointly distributed random variables; and ii) the neighbors of an agent are selected with equal probability. The fact that each dynamical system is virtually not able to distinguish among others is the reason why we have selected the name "conspecific agents." Such networks include classical Erdos-Renyi random networks and numerosity-constrained networks, which we have proposed to investigate the role of perceptual nume-

rosity on collective behavior of animal groups [6]. For networks of conspecifics agents, we extend the master stability function [12] to a stochastic setting. Similar to the classical MSF for static networks, our stochastic MSF allows for assessing synchronization in terms of network spectral properties. Computation of the MSF involves the estimate of the Lyapunov exponents for an auxiliary dynamical system as a function of two independent parameters that are related to the spectral properties of the expectation and autocorrelation of the coupling matrix. We illustrate the results through simulations on chaotic Henon maps coupled through a numerosity-constrained network.

As a second case study, we consider blinking networks consisting of an undirected and unweighted pristine static network and stochastic on-off couplings between any pair of nodes. These intermittent couplings have probability p to be switched on at any instant in time and they are independent of each other. The blinking model was originally introduced in [5] for a pristine network consisting of a regular lattice of cells with constant 2K-nearest neighbor couplings. Therein, sufficient conditions for global chaos synchronization in a continuous-time setting are proposed based on Lyapunov stability theory. Focusing on the linear stability of the synchronization manifold in a mean square sense and assuming that the inner coupling H equals the node dynamics F, we establish tractable necessary and sufficient conditions for synchronization. Specifically, by projecting the variational equations on the eigenvectors of a higher order state matrix, we establish a necessary and sufficient condition for synchronization based on the largest Lyapunov exponent of the map and the spectral radius of such matrix. By leveraging classical eigenvalue bounds, we finally establish tractable conditions that can be used for dissecting the role of p on synchronizability as a function of the pristine network topology. Such conditions are tested on chaotic Henon maps, with a lattice as the pristine network.

Finally, we investigate the controllability of static networks of coupled maps through stochastic pinning. In this node-to-node control scheme [13, 14], the network dynamics are tamed onto a desired trajectory through a feedback control input that is applied stochastically to the network nodes. The problem is similar to the blinking model, whereby the time-varying network is composed of a pristine static network and stochastic on-off coupling. The pristine network is associated with the target network, while on-off coupling corresponds to one-directional links between the pinner and pinned nodes. The network controllability is investigated by analyzing the local mean square stability of the error dynamics with respect to the desired trajectory. Through the analysis of the spectral properties of relevant matrices, a toolbox of conditions for controllability is obtained, involving the individual maps, spectral properties of the target network, and the probability distribution of the pinning control. With reference to networks of Chirikov standard maps, we demonstrate the use of these conditions in the design of stochastic pinning control strategies.

Acknowledgements

This work was primarily supported by the National Science Foundation under CAREER Grant No. CMMI-0745753.

References

1. A. Arenas, A. Diaz-Guilera, J. Kurths, Y. Moreno, and C.S. Zhou, *Phys. Rep.*, 2008, **469**(3), 93-153.
2. A. Pikovsky, M. Rosenblum, and J. Kurths, "Synchronization", *A Universal Concept in Nonlinear Sciences*, Cambridge University Press, Cambridge, 2001.
3. I. Belykh, M. di Bernardo, J. Kurths, M. Porfiri, *Physica D*, 2014, **267**, 1-6.
4. W. Lu, F.M. Atay, and J. Jost, *SIAM J. Math. Anal.*, 2007, **39**(4), 1231-1259.
5. I.V. Belykh, V.N. Belykh, and M. Hasler, *Physica. D*, **195**(1-2), 188-206.
6. N. Abaid, M. Porfiri, *IEEE Trans. Autom. Control*, 2011, **56**(3), 649-654.
7. M. Porfiri, *Europhysics Letters*, 2011, **96**(4), 40014.
8. N. Abaid, M. Porfiri, *Automatica*, 2012, **48**(8), 1845-1851.
9. N. Abaid, I. Igel, M. Porfiri, *Linear Algebra Appl.*, 2012, **437**(1), 221-235.
10. M. Porfiri, *Phys. Rev. E*, 2012, **85**(5), 056114.
11. V. Mwaffo, P. De Lellis, M. Porfiri, *Chaos*, 2014, **24**(1), 013101.
12. L.M. Pecora, T.L. Carroll, *Phys. Rev. Lett.*, 1998, **80**(10), 2109-2112.
13. M. Porfiri, F. Fiorilli, *Chaos*, 2009, **19**(1), 013122.
14. M. Porfiri, F. Fiorilli, *Physica D*, 2010, 239(8), 454-464.

Invited

ON HYPERSTABLE INTERCONNECTIONS (FROM THE LEGACY OF V.M. POPOV)

V. Rasvan

University of Craiova, Craiova, Romania, vrasvan@automation.ucv.ro

Abstract. The role of the interconnections in analysis of complex systems is emphasized in the context of hyperstability theory (hyperstable interconnections) and dissipativeness theory (neutral interconnections). It is conjectured that neutral/hyperstable interconnections are preserving individual properties in various structures of oscillators connected through a graph – as considered within the synchronization theory.

Hyperstability and hyperstable interconnections

V.M. Popov has achieved a worldwide fame due to his frequency domain inequality ensuring absolute stability of the nonlinear systems with sector restricted nonlinearities (Lurie type systems) with all its extensions (several nonlinear functions, several equilibria, time delay, distributed parameters) and additional applications (forced and self-sustained oscillations, dissipativeness). Less known is his pioneering, almost unique introduction and development of the concept and of the theory of the hyperstability blocks and systems. As pointed out in the Preface of his book [1], he "starts from the usual point of view of the control engineer who likes to have at his disposal a wide range of elements capable of being combined in various ways to form control systems as complex as desired but who does not like to burden his creative imagination with instability problem". These desired elements might be the hyperstable blocks. The block interconnections preserving the stability that have been pointed out by Popov himself are the feedforward and feedback interconnections. In a rather uncirculated paper [2] he introduced a third kind of interconnections – the triplet (which connects three blocks unlike the other ones connecting two blocks). For blocks with a single input and output these interconnections are independent and may be viewed as "bricks" for describing/building more complex interconnections.

Dissipativeness and neutral interconnections

Dissipativeness theory appears to be in close connection with hyperstability theory. In fact there exist at least three concepts of dissipativeness [3] but we refer here to that introduced in [4] and developed further by subsequent authors with particular reference to control engineering. In fact the so called "supply rate" of the dissipativeness theory is nothing more than the integrand of the integral (cumulative, if discrete time systems are considered) index of the hyperstability theory. Among the concepts of [4] one may find the "neutral interconnections" for which the sum along the blocks of the structure of the supply rates is zero, exactly as in the case of the hyperstable interconnections. The class of neutral interconnections appears however as a broader class of interconnections that not only integrates the elementary hyperstable interconnections but may incorporate interconnections defined by nonlinear relations between variables.

Synchronization theory and its interconnections

The more recent and independently developed theory of synchronization relies on considering complex structures as underlined by a connection graph whose vertices are "oscillators" (e.g. [5]), i.e. dynamical systems, more or less identical, whose properties may be established by standard methods. It is then required to check preservation of individual properties in the global structure. The natural conjecture unifying the aforementioned types of interconnections would be that neutral/hyperstable connections are preserving the individual properties of the oscillators. A quite straightforward while classical example is the stability of the nuclear reactors with coupled active zones considered in [6]; interesting enough, such an instrument as the rearrangement inequalities can suggest new types of interconnections that preserve stability. It thus appears that, at the conceptual as well as at the instrumental level it is important to unify synchronization theory with hyperstability and dissipativeness (which as stated, contain the "bricks" of structure building). On the other hand, there is a contradiction between the aims of the control engineer who is interested in regular behavior such as stable equilibria, stable oscillatory regimes a.s.o. and other requirements which are oriented to more complex phenomena (we mention but the Turing instability which may account for pattern generation). Hyperstable and neutral interconnections seem oriented to the first class of problems but they give only sufficient con-

ditions for stability and/or stable oscillations. Other phenomena are characterized by using bifurcation theory. The presumable gap between the two kinds of behavior may suggest new development.

References

1. V.M. Popov, "Hyperstability of control systems", *Springer Verlag, Berlin-Heidelberg-New York*, 1973.
2. V.M. Popov, "An analogue of electrical circuit synthesis in hyperstability" (in Romanian), *Proceedings of the National Symposium on Electrical networks analysis and synthesis*, Bucharest, Romania, 1967, paper 9.1.
3. V. Rasvan, "Three lectures on dissipativeness", *Proceedings of International Conference on Automation, Quality and Testings*, Robotics AQTR 2006, May 2006, Cluj Napoca Romania, IEEE paper 1-4244-0361-8/06, IEEE catalogue number 06EX1370.
4. J.C. Willems, "Dissipative Dynamical Systems I, II", *Archive for Rational Mechanics and Analysis*, 1972, **45**, 321-393.
5. J.K. Hale, "Diffusive Coupling, Dissipation and Synchronization", *Journ. of Dynamics and Differential Equations*, 1997, **9**(1), 1-52.
6. V.D. Gorjacenko, "Research methods for the stability of nuclear reactors" (Russian), *Atomizdat*, Moscow, 1977.

THE EFFECT OF COHERENCE RESONANCE IN DIFFERENT TIME-DELAYED SYSTEMS

V.V. Semenov, A.V. Feoktistov, and **T.E. Vadivasova**

Saratov State University, Saratov, Russia, semenov_v_v@list.ru

Abstract. The effect of coherence resonance is studied in different time-delayed systems. The possibility to control the coherence resonance by changing time-delayed feedback parameters is shown in numerical and full-scale (physical) experiments. The observed effects are exemplified for the excitable FitzHugh-Nagumo oscillator and the van der Pol oscillator with subcritical Andronov-Hopf bifurcation, which is not an excitable system. The behavior of these systems is analyzed in terms of stochastic bifurcations. The numerical and experimental results are in a good correspondence, and this gives evidence of their reliability.

Control of unstable or irregular states of nonlinear dynamical systems is one of the main problems of applied nonlinear dynamics and a central issue of current research. Particularly simple and efficient control scheme is time-delayed feedback control, introduced by Pyragas [1], which is also known as time-delayed autosynchronization (TDAS). This method is robust and universal to apply, easy to implement experimentally, and it has been used in a large variety of systems in physics, chemistry, biology, medicine and engineering [2–6].

The possibility to control the coherence resonance by time-delayed feedback was numerically shown in [7] by using the FitzHugh-Nagumo model (1) with colored noise:

$$\begin{cases} \varepsilon\dot{x} = x - x^3/3 - y, \\ \dot{y} = x + a + \eta(t) + K\left[y(t-t) - y(t)\right], \\ \tau_c\dot{\eta} = -\eta + \sqrt{2\sigma^2\tau_c}\,\xi(t), \end{cases} \qquad (1)$$

where $\xi(t)$ is a normalized source of white Gaussian noise and $\eta(t)$ is a colored noise acting the Fitz-Hugh-Nagumo oscillator. We have created the analog model of the system (1) for experimental verification of the results which are presented in [7]. The results obtained in the full-scale experiments are very similar to the numerical results in [7]. Changing the time delay one can control the correlation time of the oscillations of the FitzHugh-Nagumo system in the regime of coherence resonance. This effect is detected from the observation of power spectrum evolution and dependence of correlation time on the delay. Time delayed feedback can make the oscillations more correlated or less correlated. The same result was obtained in the case of FitzHugh-Nagumo system driven by white Gaussian noise.

The presented results correspond to the coherence resonance control in excitable systems. It will be interesting to carry out similar experiments for non-excitable systems which demonstrate the regime of coherence resonance. The van der Pol oscillator with subcritical Andronov-Hopf bifurcation is an example of such system. This oscillator with time-delayed feedback was studied both in numerical and in full-scale (real) experiments. The equations of the system under study are the following:

$$\begin{cases} \dot{x} = y, \\ \dot{y} = (\varepsilon + \gamma x^2 - x^4)y - x + K\left[x(t-\tau) - x(t)\right] + \sqrt{2D}\,\xi(t). \end{cases} \qquad (2)$$

The carried out numerical and full-scale experiments show that changing of time delay can control the correlation time of the oscillations of van der Pol oscillator with subcritical Andronov-Hopf bifurcation in the regime of coherence resonance.

The obtained results show that time-delayed feedback permits controlling the correlation of oscillations in the regime of coherence resonance. This effect has a general character and is observed both in excitable and non-excitable systems.

Acknowledgements

The work is partly supported by the Russian Ministry of Education and Science (project code 1008)

References

1. K. Pyragas, *Phys. Let*. A, 1992, **170**, 421-428.
2. E. Scho¨ll, "Nonlinear Spatio-Temporal Dynamics and Chaos in Semiconductors Nonlinear Science Series", *Cambridge University Press, Cambridge*, 2001, **10**, 420.
3. E. Schöll, "Pattern formation and time-delayed feedback control at the nano-scale", In *Nonlinear dynamics of nanosystems* (eds G. Radons, B. Rumpf & H. G. Schuster). Weinheim, Germany: Wiley-VCH, 2009, p. 455.
4. K. Pyragas, *Phil. Trans. R. Soc. A*, 2006, **364**, 2309-2334.
5. L. Schimansky-Geier, B. Fiedler, J. Kurths, and E. Schöll, (eds), *Analysis and control of complex nonlinear processes in physics, chemistry and biology*. Singapore: World Scientific, 2007, 135-183.
6. E. Schöll, P. Hövel, V. Flunkert, and M.A. Dahlem, "Time-delayed feedback control: from simple models to lasers and neural systems", In *Complex time-delay systems* (ed. F. M. Atay). Berlin, Germany: Springer, 2009, 1-71.
7. S.A. Brandstetter, M. A. Dahlem, and E. Schöll, *Phil. Trans. R. Soc. A*, 2010, **368**, 391-421.

THE AFRAIMOVICH-PESIN DIMENSION OF POINCARE RECURRENCES IN A CIRCLE MAP

N.I. Semenova, T.E. Vadivasova, and **V.S. Anishchenko**

Saratov State University, Saratov, Russia, harbour2006@mail.ru

Abstract. It is first established that the dependence of the minimal return time on the vicinity size is universal for the golden and silver sections in a circle map and can be referred to as "Fibonacci's stairs". The theoretical result for the Afraimovich-Pesin dimension equality $\alpha_C = 1$ is confirmed for irrational rotation numbers with the measure of irrationality $\mu = 2$. It is shown that some transcendental numbers ($\omega = e$, $ln2$, π) are Diophantine and have the measure $\mu = 2$. It is also confirmed that the calibration function $1/t$ cannot be applied for Liouvillian numbers. All the obtained features hold for both the linear and nonlinear circle map.

The analysis of Poisson-stable systems is one of the classical problems of dynamical systems. The recurrence of phase trajectories in the neighborhood of a selected initial state has been proved for this kind of systems and the term “Poincaré recurrences” has been introduced [1]. The theory of Poincaré recurrences describes the statistics of return times both in the neighborhood of a given initial state [2, 3] (the so-called local approach) and in the whole set of the phase trajectories of the system [4–6] (the so-called global approach). In the latter case, Poincaré recurrences are characterized by dimension of return times (Afraimovich-Pesin dimension) [6]. In the framework of the global approach the return time statistics depends on the topological entropy h_T. In the global approach, the whole set of phase trajectories of a dynamical system is covered with cubes (or balls) having size $\varepsilon \ll 1$. A minimal return time to the u_i-neighborhood $\tau_{\inf}(u_i)$ is defined for each covering element u_i ($i = 1, 2, \ldots, m$). Then the mean minimal return time is calculated over the whole set of covering elements u_i [7–9].

It was established in [4] that

$$\left\langle \tau_{\inf}(\varepsilon) \right\rangle \sim \phi^{-1}(\varepsilon^{d/\alpha_C}), \tag{1}$$

where d is the fractal dimension of the set, α_C is the AP dimension of the sequence of return times, ϕ is the gauge function whose form depends on the topological entropy h_T and can be defined by one of the following forms:

$$\phi(t) \sim 1/t, \quad \phi(t) \sim \exp(-t), \quad \phi(t) \sim \exp(-t^2)... \tag{2}$$

It was shown in [4, 6] that for $h_T = 0$ the gauge function is $\phi(t) \sim 1/t$. Then the following law is valid

$$\left\langle \tau_{\inf}(\varepsilon) \right\rangle \sim \varepsilon^{-d/\alpha_C}, \quad \varepsilon << 1. \tag{3}$$

We consider a particular example of a minimal set that is produced by the circle map

$$\Theta_{n+1} = \Theta_n + \Delta + K \sin \Theta_n, \quad \mod 2\pi, \tag{4}$$

where Δ and K are the parameters of the map. The circle map of type (4) is a reference model of a wide class of dynamical systems with quasiperiodic behavior. The trajectories of (4) are characterized by a rotation number.

In the case $K = 0$ the trajectory is rotated by a constant angle Δ per iteration. Thus, the rotation number can be defined as $\omega = \Delta/2\pi$. An irrational value of ω is associated with quasiperiodic trajectories which are everywhere dense on a circle, and the distribution $p(\Theta)$ is uniform on the interval $0 \le \Theta \le 2\pi$. Therefore, we do not need to calculate the mean value of $\tau_{\inf}$. For $K = 0$, the ergodic set $\{\Theta_n\}$ is characterized by $h_T = 0$, i.e., it is an ergodic set without mixing.

All irrational numbers can be divided into transcendental and algebraic numbers. The latter can be exampled by $n^{1/k}$, where n and k are natural numbers. The numbers that are not algebraic are said to be transcendental (π, e, ln2, and others). Irrational values of ω can be approximated by the ratio of two integers m_i/n_i. This method is said to be the method of rational approximations and the ratio is called the ith convergent of a continued fraction. An irrational rotation number ω is said to be Diophantine if the approximation error obeys the inequality

$$\omega - m/n < C/n^{\mu}, \tag{5}$$

where m/n is a convergent from a set of pairs of integers m_i and n_i, $2 \le \mu < \infty$ is the measure of irrationality, C is a constant. Otherwise, ω is Liouvillian number. For the circle map

$$\ln\left\langle \tau_{\inf}(\varepsilon) \right\rangle \sim -d/\nu(\omega) \ln\varepsilon, \quad \varepsilon << 1, \quad \mathrm{d} = 1. \tag{6}$$

Here $\nu(\omega)$ is the maximal rate of Diophantine approximations of an irrational rotation number. Comparing (3) and (6) we obtain that $\nu(\omega) = \alpha_C$ in the considered set.

We calculate the dependence $\langle\tau_{inf}(\varepsilon)\rangle$ on the set $\{\Theta_n\}$ of the map (4) for $K = 0$ and ω which is equal to the golden ratio, i.e. $\omega = (5^{1/2} - 1)/2$. The numerical results for $\tau_{inf}(\varepsilon)$ are shown in Fig. 1. As can be seen from the figure, this dependence looks like a step function, which can be referred to as the "Fibonacci stairs". We have found that it has several features, including:

1. When ε decreases, the sequence of $\tau_{inf}(\varepsilon)$ strictly corresponds to the basic Fibonacci series.
2. When ε changes within any stairs step, three return times $\tau_1 < \tau_2 < \tau_3$ exist $\tau_3 = \tau_1 + \tau_2$, and $\tau_1 = \tau_{inf}$.
3. The lengths and heights of the stairs in Fig. 1 are universal and equal to $-ln\omega$.

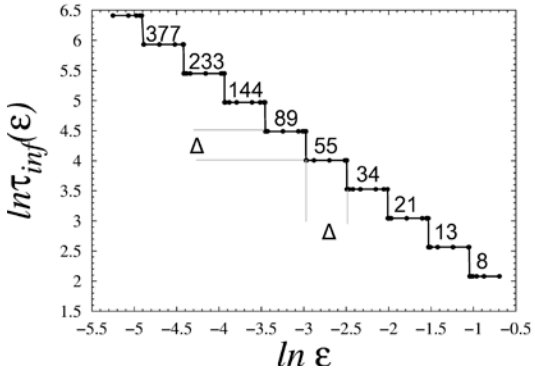

Fig. 1. "Fibonacci stairs" for the circle map in the case of the golden ratio

Similar results were obtained for the silver ratio $\omega = 2^{1/2} + 1$. The differences are that for the silver ratio the sequence of minimal return times obeys the Pell law. The golden and silver ratios are algebraic Diophantine numbers with the measure of irrationality $\mu = 2$. For the other algebraic Diophantine numbers $\omega = 2^{1/3}$, $\omega = 7^{1/3}$ the universal geometry of the Fibonacci stairs is not valid. However, the other conclusions are still valid. It has been shown numerically that for Diophantine numbers with the measure of irrationality $\mu = 2$, the AP dimension α_C coincides with the rate of Diophantine approximations $\nu(\omega)$ equal to 1. This conclusion is valid for the circle map (4) in both the linear ($K = 0$) and the nonlinear ($K > 0$) case. For transcendental Diophantine numbers e, π, $\pi/100$ and ln2 the situation is similar. Calculating the slope of Fibonacci stairs both by averaging and theoretically gives $\alpha_C = \nu(\omega) = 1.0$. This implies that π and e are Diophantine numbers with measure of irrationality $\mu = 2$. Numerical results for transcendental Liouvillian number $\omega = \sum_{i=0}^{\infty} 10^{-i!}$ attest that $\mu \to \infty$. In this case $\phi(t) \sim 1/t$ cannot be considered as a gauge function. We only know that (6) does not hold for Liouvillian numbers and this fact corroborates the theoretical results [4, 6]. In addition, we have studied the Poincaré recurrence statistics for a stroboscopic section of a nonautonomous van der Pol oscillator. The results show a complete analogy with the properties of recurrences in the linear circle map.

Acknowledgements

The reported study was partially supported by RFBR, research project No. 13-02-00216a. N.I. Semenova gratefully acknowledges the Dynasty Foundation.

References

1. V.V. Nemytsky, V.V. Stepanov, *Qualitative Theory of Differential Equations*, Moscow, 1947.
2. M. Kac, *Bull. of the American Math. Soc*., 1947, **53**(10), 1002-1010.
3. M. Hirata, B. Saussol, S. Valenti, *Commun. Math. Phys*., 1999, **206**(1), 33-55.
4. V. Afraimovich, *Chaos*, 1997, **7**(1), 12-20.
5. V. Afraimovich, G.M. Zaslavsky, Phys. Rev. E, 1997, **55**, 5418-5426.
6. V. Afraimovich, E. Ugalde, J. Urias, *Fractal Dimension for Poincaré recurrences*, Elsevier, 2006.
7. V.S. Anishchenko, S.V. Astakhov, *Usp.Fis. Nauk.*, 2013, **56**(10), 955-972.
8. V. Afraimovich, W.W. Lin, N.F. Rulkov, *Int. J. Bifurc. Chaos*, 2000, **10**(10), 2323-2337.
9. V. Anishchenko, M. Khairulin, G. Strelkova, J. Kurths, Eur. Phys. J. B, 2011, **82**, 219-225.

Invited

DYNAMICS IN CLUSTERED NEURONAL CULTURES: A VERSATILE EXPERIMENTAL SYSTEM FOR COMPLEX NETWORKS

S. Teller and **J. Soriano**

Department ECM, Physics Faculty, University of Barcelona, Barcelona, Spain
teller.sara@gmail.com
jordi.soriano@ub.edu

Abstract. We study spontaneous activity in networks formed by interconnected aggregates of neurons ('clustered neuronal cultures'). We monitor spontaneous activity using high-resolution fluorescence imaging. Network's dynamics is characterized by collective episodes of activity in which groups of clusters fire sequentially in a short time window. The functional connectivity of the network is drawn from the observed dynamics, picturing a circuitry that is both directed and weighted. These functional networks have distinct topological properties, in particular the existence of assortativity traits and a 'rich-club' core. Our work illustrates the attractiveness of a relatively simple experimental system to explore complexity in neuronal networks.

Introduction

Activity in a neuronal network is governed by the interplay between the intrinsic neuronal dynamics and the neuronal interconnectivity. The wiring of the network not only shapes the collective activity of the network, but delineates a number of traits that are essential for the functioning of the circuit, from information processing to resilience to perturbations and damage. The analysis of all these aspects has been tackled in the last years with the assistance of network theory, which has provided a number of *network measures* that describe the major topological traits of the neuronal system under study. The distribution of connections in a network, clustering coefficients, the existence of hubs, assortativity traits, or the 'rich club' phenomena are some of the network measures that have elegantly described systems as diverse as the human brain, genetic networks or social friendship.

To further understand the importance of these measures to describe and predict the behavior of neuronal systems, more accessible systems in the form of *neuronal cultures* have gained substantial interest in the last decades. Indeed, neurons from the cortex or other brain areas can be dissociated, seeded over a substrate, and cultured along several weeks. Neurons self-organize, connecting to one another to create a *de novo* neuronal network with rich spontaneous activity patterns. Here we show how a particular configuration of a neuronal culture can be used as a model system to investigate functional connectivity in neuronal circuits and its interrelation with the underpinned structural one, and to probe the resilience of the network to damage.

Experiments

Our neuronal cultures are formed by aggregates of tightly packed neurons termed *clusters* (Fig. 1A), which connect to one another to shape a web of easily identifiable nodes. The cultures are confined within 3 mm diameter wells to access the entire network and monitor all the clusters simultaneously. Clustered networks form quickly, and by 4–5 days after the seeding of the neurons the network shows a rich spontaneous activity. We record this activity using high-speed calcium imaging (Fig. 1B), a technique that reveals the activation of neurons (or clusters in our case) as an intense increase in their brightness. A typical experiment contains on the order of 40 clusters. We typically record spontaneous activity along 1 h, and with 10 ms temporal resolution.

Spontaneous activity is characterized by episodes of collective activity in which a group of clusters fire sequentially in a short time window. Figure 1C depicts the variations in fluorescence amplitude for 5 clusters along 3 min of recording. The clusters' activations are revealed by sharp peaks in the signal. We denote by *bursts* these sequences of activation (yellow box in the figure). The clusters that participate in a given sequence, and even the order of the cascade of activations, vary along the recording, although some sequences have a tendency to appear more often than others. In the depicted example, clusters 2-3-4 shape the first burst, and clusters 1-5 the second. Clusters 2-3-4 participate in other sequences, revealing the existence of persistent functional couplings between clusters.

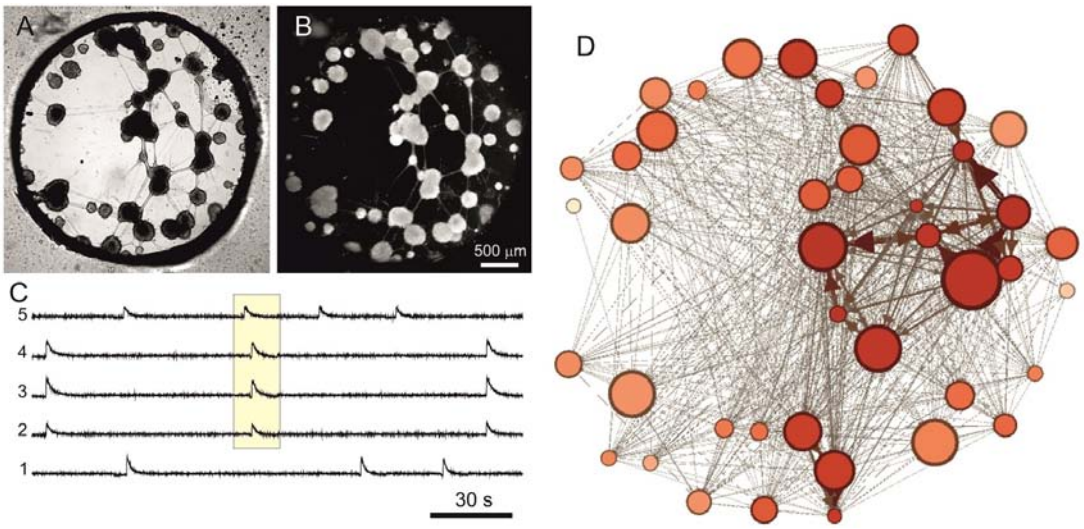

Fig. 1. Clustered neuronal culture. (A) Bright-field image of a typical culture prepared within a 3 mm diameter well. The aggregates of neurons or *clusters* appear as dark circular objects. Connections between clusters are visible as straight filaments. (B) Corresponding fluorescence image. Firing episodes are revealed by a strong increase in the brightness of the clusters. (C) Representative fluorescence traces for five clusters (labeled 1 to 5), and along 3 min of spontaneous activity. Sharp increases in the fluorescence amplitude reveal the ignition of a cluster. The yellow box highlights a *burst*, i.e. a group of clusters that fire sequentially in a short time window. (D) Resulting functional network, built from the analysis of time delays between consecutive clusters' activations. Statistics is based on 135 bursts. The size of the nodes is proportional to their actual size for easier comparison. The lines (functional links between clusters) are thickness coded according to their weight

Functional networks, 'rich club' and resilience to damage

The time delays between clusters' activations in a sequence can be used to construct a functional map of cluster-to-cluster interactions in the network. As can be observed in the yellow box of Fig. 1C, cluster #5 fires first, followed by 2-3-4, which get activated very closely in time. It is plausible to assume that cluster #2 was strongly influenced by clusters #3 and #4 given their temporal proximity, but weakly influenced by #5 given the relatively long time delay. More formally, in our construction we assign a functional link to all pairs of clusters within a sequence, and weighting each link according to a function that sharply decreases with the time spanned between clusters' activations. The obtained values are finally averaged over all the sequences. Figure 1D shows the final functional network, which is directed and weighted. Note that those clusters that persistently fire together are coupled through very strong functional links. The details of the construction of the functional networks are described in Ref. [1].

The analysis of the topological traits of the functional network reveals that the network is assortative, i.e. nodes preferentially connect to others with similar degree, providing weighted Pearson correlation coefficients around 0.47 for 15 different network realizations [1]. We also observed that these networks exhibit the 'rich club' property [1], i.e. the interconnectivity of the nodes with the highest degree, which shapes a 'connectivity backbone' in the network that confers it resilient characteristics. Indeed, we observed that the clustered networks are more resistant to damage compared to other configurations. The modular dynamics exhibited by the clustered networks, as well as their resilience to attack, suggests that this configuration enhances survival while maintaining a high flexibility and adaptability.

Acknowledgements

The research was supported by the Ministerio de Ciencia e Innovación (Spain) under projects FIS2010-21924-C02-02, FIS2011-28820-C02-01, FIS2012-38266-C02-01, and FIS2010-09832-E. We also acknowledge the Generalitat de Catalunya under projects 2009-SGR-00014.

References

1. S. Teller, C. Granell, M. De Domenico, J. Soriano, S. Gómez, A. Arenas, *PLoS Comput. Biol*., in press (arXiv:1402.4824).

ABOUT LANDAU-HOPF SCENARIO IN ENSEMBLES OF REGULAR AND CHAOTIC OSCILLATORS

A.P. Kuznetsov, L.V. Turukina, and **I.R. Sataev**

Kotel'nikov Institute of Radio-Engineering and Electronics of RAS, Saratov Branch

Introduction

As is known, the Landau-Hopf scenario implies that the oscillatory modes with incommensurable frequencies emerge subsequently, which leads to increasingly more complicated oscillatory regimes [1, 2]. In this case, we can speak about a cascade of quasi-periodic Hopf bifurcations [3] responsible for the soft birth of the tori of increasingly higher dimension. The possibility of such a scenario remains largely debated for several decades. In this paper we discuss the conditions and situations, in which such a scenario can actually occur.

When choosing a model to analyze, we have to take into account several important physical aspects. First, the oscillatory modes responsible for the dynamics must be characterized by different degrees of activation. For example, if we consider an ensemble of coupled van der Pol oscillators, we must introduce a set of parameters λ_i controlling the negative friction and select them appropriately to ensure conditions for gradual involving of the modes in the motion in the course of decreasing dissipation level. (In the context of the hydrodynamic problems it just corresponds to increasing Reynolds number.) Second, all the oscillatory modes have to be separated in frequency in sufficient degree. Otherwise, essential interaction of the modes will occur, which can destroy the Landau-Hopf picture. Third and finally, it is desirable to have a situation, where the coupled oscillators are arranged in such way that they all are involved essentially in the interaction; it means that no preferable interaction of each concrete partial oscillator should occur, say, with spatially close neighbors, or with a different number of neighbors. If these three conditions are met, the control parameter of each single oscillator λ_i will regulate a certain quasi-periodic bifurcation. Otherwise, it might happen that due to the different number of interacting neighbors the elements with a close level of activation would have essentially different influence on the picture of the multi-frequency dynamics.

Network of five coupled van der Pol oscillators

Let us consider a model satisfying the above requirements. It will be a kind of network of five oscillators with global coupling and equidistant spectrum [4]:

$$\begin{aligned}
&\ddot{x}-(\lambda_1-x^2)\dot{x}+x+\frac{\mu}{4}(4\dot{x}-\dot{y}-\dot{z}-\dot{w}-\dot{v})=0,\\
&\ddot{y}-(\lambda_2-y^2)\dot{y}+(1+\frac{\Delta}{4})y+\frac{\mu}{4}(4\dot{y}-\dot{x}-\dot{z}-\dot{w}-\dot{v})=0,\\
&\ddot{z}-(\lambda_3-z^2)\dot{z}+(1+\frac{\Delta}{2})z+\frac{\mu}{4}(4\dot{z}-\dot{y}-\dot{x}-\dot{w}-\dot{v})=0,\\
&\ddot{w}-(\lambda_4-w^2)\dot{w}+(1+\frac{3\Delta}{4})w+\frac{\mu}{4}(4\dot{w}-\dot{y}-\dot{x}-\dot{z}-\dot{v})=0,\\
&\ddot{v}-(\lambda_5-v^2)\dot{v}+(1+\Delta)v+\frac{\mu}{4}(4\dot{v}-\dot{y}-\dot{x}-\dot{z}-\dot{w})=0
\end{aligned} \qquad (1)$$

Here λ_i are control parameters responsible for excitation of the partial oscillators, Δ determines the frequency detuning of the oscillators, and the frequency of the first oscillator is unity. We set hereafter $\lambda_1=0.1$, $\lambda_2=0.2$, $\lambda_3=0.3$, $\lambda_4=0.4$, $\lambda_5=0.5$.

Figure 1 shows the Lyapunov chart obtained for the model (1) on the parameter plane (Δ,μ). Because of the structure of the system, the main resonance effects are actually excluded. In particular, no tongues of resonant tori of different dimensions similar to those mentioned, e.g., in Ref. [5] are observed. The only pronounced tongue corresponding to a resonant two-frequency torus may be seen in the region $\Delta\le 0.5$ between the domains of the five-frequency tori and of the complete synchronization. Interestingly, it is immersed in the region of chaos that occurs at small coupling. Here the three-frequency, four-frequency, and partially the five-frequency tori are destroyed, although the chaos is weak. On the other hand, in the case of large detuning of the oscillators, $\Delta\ge 1$, with decreasing dissipation parameter μ one can observe the appearance of all the tori of higher dimensions. Boundaries of

the relevant areas in the asymptotic $\Delta \to \infty$ correspond to the values of the control parameters $\mu = \lambda_i$. Thus, a decrease in the parameter of dissipative coupling qualitatively corresponds to the pattern expected for the Landau-Hopf scenario.

Network of five coupled chaotic Rössler oscillators

Now let us consider a network of five coupled Rössler oscillators:

$$\begin{aligned} \dot{x}_n &= -(1+\frac{n-1}{4}\Delta)y_n - z_n, \\ \dot{y}_n &= (1+\frac{n-1}{4}\Delta)x_n + py_n + \frac{\mu}{4}\sum_{i=1}^{5}(y_i - y_n), \\ \dot{z}_n &= q + (x_n - r_n)z_n. \end{aligned} \qquad (2)$$

Here the parameter Δ is responsible for the frequency detuning of the oscillators. Parameter n varies from 1 to 5.Values of the parameters $p = 0.15$, $q = 0.4$, $r = 8.5$ correspond to the chaotic regime in individual subsystems [6]. Lyapunov exponents chart for the system (2) is shown in Figure 2. At low coupling the hyperchaotic mode HC5 dominates with five positive Lyapunov exponents. With the increasing of coupling the number of positive exponents gradually decreases, and after the transition via HC4, HC3 and HC2 regimes usual chaos C arises. For even stronger coupling a complicated picture of alternating modes of different types may be observed, and tori of different dimensions are quite typical. At high frequency detuning, a cascade of quasiperiodic Hopf bifurcation is observed. It corresponds to the Landau-Hopf scenario [1, 2, 4]. But now the bifurcations follow quickly one after another, so that the scenario develops in a narrow range of coupling parameter. Nevertheless, we note the fact of possible Landau-Hopf scenario and a cascade of quasiperiodic bifurcations of invariant tori in coupled chaotic oscillators.

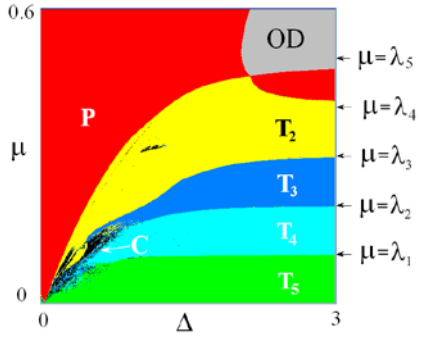

Fig. 1. Chart of Lyapunov exponents for the network of five globally coupled non-identical van der Pol oscillators (1), where $\lambda_1 = 0.1$, $\lambda_2 = 0.2$, $\lambda_3 = 0.3$, $\lambda_4 = 0.4$, $\lambda_5 = 0.5$

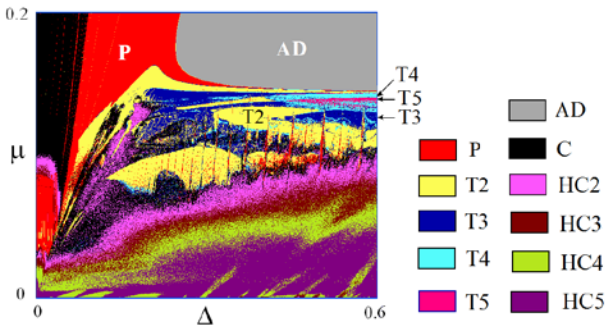

Fig. 2. Chart of Lyapunov exponents for the network of five chaotic oscillators (2). $p = 0.15$, $q = 0.4$, $r_1 = 7.3$, $r_2 = 7.6$, $r_3 = 7.9$, $r_4 = 8.2$, $r_5 = 8.5$

Conclusion

Thus, under certain conditions, e.g. in the case of non-identical parameters of the active modes and of detuning for the modes in an ensemble of self-oscillating elements, one can observe a sequential cascade of soft quasi-periodic bifurcations involving tori of increasing dimension that can be regarded as occurrence of the Landau-Hopf scenario. At the same time, high-dimensional quasiperiodicity is typical not only for ensembles of oscillators with regular behavior, but also for dissipatively coupled chaotic oscillators.

Acknowledgements. The work was supported by RFBR grant No. 12-02-00342.

References

1. L.D. Landau, *Akad. Nauk Dok.*,1944, **44**, 339.
2. E. Hopf, *Communications on Pure and Applied Mathematics*, 1948, **1,** 303-322.
3. Broer H., Simó C., Vitolo R., *Regular and Chaotic Dynamics*, 2011, **16** (1-2), 154-184.
4. A.P. Kuznetsov, S.P. Kuznetsov, I.R. Sataev, L.V. Turukina, *Physics Letters A*, 2013, **377**, 3291-3295.
5. A.P. Kuznetsov, I.R. Sataev, L.V. Turukina, *Нелинейная динамика*, 2011, 7 (3), 411-425. (in Russian).
6. M.G. Rosenblum, A.S. Pikovsky, J. Kurths, *Phys. Rev. Lett.*, 1996, **76,** 1804.

SYNCHRONIZATION OF OSCILLATORS IN A KURAMOTO-TYPE MODEL WITH GENERIC COUPLING

V. Vlasov[1], **E.E.N. Macau**[2], and **A. Pikovsky**[1,3]

[1]Department of Physics and Astronomy, Potsdam University, 14476 Potsdam, Germany, mr.voov@gmail.com
[2] National Institute for Space Research -INPE, 12227-010 Sao Jose dos Campos, SP, Brazil
[3]Department of Control Theory, Nizhny Novgorod State University, Nizhny Novgorod, Russia

Abstract. We study synchronization properties of coupled oscillators on networks that allow description in terms of global mean field coupling. These models generalize the standard Kuramoto-Sakaguchi model, allowing for different contributions of oscillators to the mean field and to different forces from the mean field on oscillators. We present the explicit solutions of self-consistency equations for the amplitude and frequency of the mean field in a parametric form, valid for noise-free and noise-driven oscillators. As an example we consider spatially spread oscillators, for which the coupling properties are determined by finite velocity of signal propagation.

Synchronization of large ensembles of oscillators is an ubiquitous phenomenon in physics, engineering, and life sciences. The most simple setup pioneered by Winfree and Kuramoto is that of global coupling, where all the oscillators equally contribute to a mean field which acts equally on all oscillators [1, 2]. In this study we consider a generalized Kuramoto-type model of mean field coupled oscillators with different parameters for all elements. In our setup there is still a unique mean field $H(t)$, but oscillators differently contribute to it with their own phase shifts βj and coupling factors Bj, and also the mean field acts on each oscillator with different phase shifts α_i and coupling coefficients A_i. Additionally, the noise term is included in the consideration:

$$\dot{\theta}_i = \omega_i + A_i \,\mathrm{Im}\left(H(t)e^{-\mathrm{i}(\theta_i-\alpha_i)}\right) + \sqrt{D}\xi_i(t),$$

$$H(t) = \frac{\varepsilon e^{-\mathrm{i}\delta}}{N}\sum_{j=1}^{N} B_j e^{\mathrm{i}(\theta_j-\beta_j)}.$$

Such a situation appears, e.g., if the oscillators are spatially arranged and the phase shift and the attenuation due to propagation of their signals cannot be neglected. A regime, where the mean field rotates uniformly, is the most important one. For this case the solution of the self-consistency equation for an arbitrary distribution of frequencies and coupling parameters is found analytically in the parametric form, both for noise-free and noisy oscillators. First, we consider independent distributions for the coupling parameters when self-consistency equations can be greatly simplified. Secondly, as one of the examples we considered a situation, where contributions to the mean field and its action on oscillators are prescribed by a geometric configuration of the oscillators; phase shifts and the contribution factors result from the propagation of the signals as waves having certain velocity. The general formulation we developed can be used for any such configuration. It appears that the method above may be useful also in more general network setups, where there is no global mean field, but such a field can be introduced as approximation (cf. [3, 4]).

Acknowledgements

V. V. thanks the IRTG 1740/TRP 2011/50151-0, funded by the DFG /FAPESP.

References

1. Y. Kuramoto, *Chemical Oscillations*, Waves and Turbulence (Springer, Berlin, 1984)
2. J.A. Acebrón, L.L. Bonilla, C.J.P. Vicente, F. Ritort, and R. Spigler, *Rev. Mod. Phys*., 2005, **77**, 137.
3. P.S. Skardal and J.G. Restrepo, *Phys. Rev. E*, 2012, **85**, 016208.
4. R. Burioni, M. Casartelli, M. di Volo, R. Livi, and A. Vezzani, "From global synaptic activity to neural networks topology: a dynamical inverse problem," 2013, arXiv:1310.0985v2 [cond-mat.dis-nn].

Invited

DETERMINISTIC AND STOCHASTIC DYNAMICS IN MULTISTABLE NON-ADIABATIC GENETIC REPRESSILATOR

I. Potapov[1], B. Zhurov[2], and **E. Volkov[2]**

[1]Department of Mathematics, Tampere University of TechnologyTampere, Finland
[2]Dept. of Theoretical Physics, Lebedev Physical Inst., Moscow, Russia

Abstract. The dynamics of the simplest ring genetic oscillator – Repressilator – is investigated by extensive bifurcation analysis and stochastic simulations of intrinsic noise. A full deterministic model demonstrates the emergence of an unusual genetic switch between a stable steady state and a limit cycle, if realistic in vivo values of parameters are taken into account. Stochastic simulations for small copy numbers of Repressilators in one plasmid confirm the existence of the switch and point out how to control the effects of intrinsic noise.

Living cells are multi-stable and multi-rhythmic dynamical systems. Coexisting multiple stable dynamic behaviors underlie biological diversity and cell differentiation. However, our knowledge of how cells sustain their diverse dynamic behaviors, especially in the presence of molecular noise, is still limited. In the 1970-1980s there were many studies of cell variability in cell biochemistry and in cell surface processes. Now the focus has changed and variability is mainly addressed in genetics, with synthetic genetic circuits being the basic source of models for study.

Here, we use a genetic oscillator known as Repressilator – a three-element gene ring network in which each of the element unidirectionally represses the next one. The figure below shows the scheme and the set of reactions for the Repressilator network. Gene G_1 is a source of mRNA M_1 (transcription) codes for monomer protein activity P_1 produced by the translation process. Transcription rate α corresponds to RNApolymerase activity and translation rate g is determined by ribosome function. We assume that the presence of all the biochemical components of these subprocesses are not limiting factors for the whole process of cycling.

Then proteins P_1 participate in reversible homodimerization producing dimers D_1, which are repressing transcription factors (TFs) for the next gene G_2 and so on. Dimers Di are repressors of the transcription of G_{i+1} gene because they compete with RNApolymerase for binding with the promoter preventing transcription initiation.

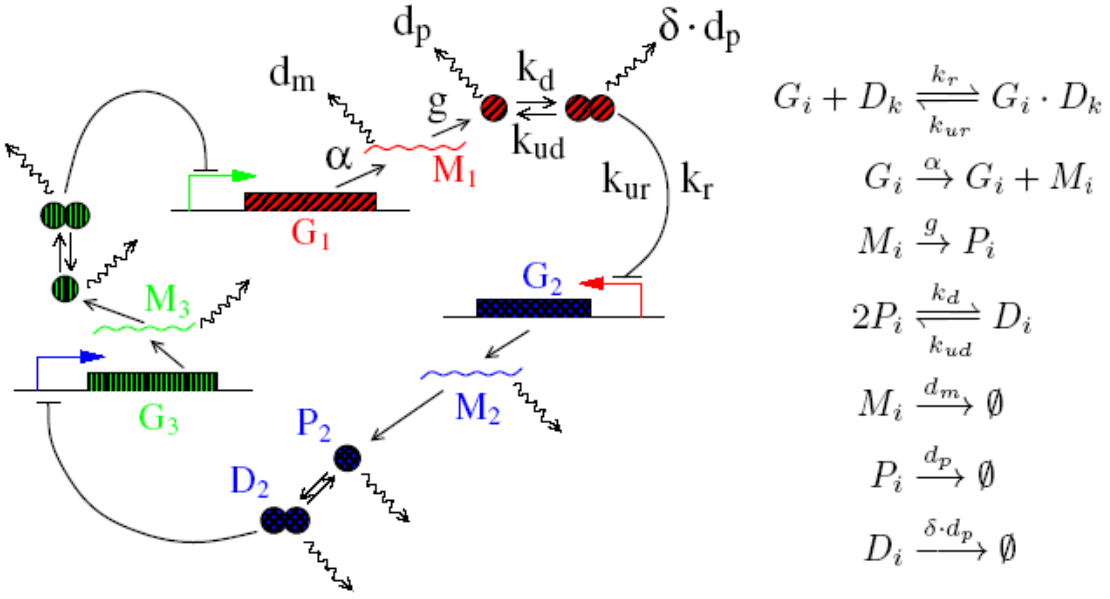

$$G_i + D_k \underset{k_{ur}}{\overset{k_r}{\rightleftharpoons}} G_i \cdot D_k$$
$$G_i \xrightarrow{\alpha} G_i + M_i$$
$$M_i \xrightarrow{g} P_i$$
$$2P_i \underset{k_{ud}}{\overset{k_d}{\rightleftharpoons}} D_i$$
$$M_i \xrightarrow{d_m} \emptyset$$
$$P_i \xrightarrow{d_p} \emptyset$$
$$D_i \xrightarrow{\delta \cdot d_p} \emptyset$$

The idea of Repressilator is old (1967) but it was realized experimentally in live bacterial cells and was modeled as the system of ODE as well as via stochastic simulation in 2000 [1] only.

For many years the standard assumption for deterministic modeling in genetics was the use of the quasi-steady state approximation (QSSA) for multimerization of transcription factors and for regulatory reactions of TFs on the promoter sites [2, 3]. This approach, sometimes called “adiabatic” [4], results in important simplification of the models via reducing the model dimension and the appearance

of nonlinear Hill function describing the regulation of transcription. In this approach Repressilator was formulated as a 6-dim system of ODE which exhibits sustained oscillations emerging via the supercritical Andronov-Hopf bifurcation (AHB) [1].

The number of molecules participating in the functioning of genetic circuits is small, which prescribes using stochastic simulations for the study of their dynamics. These calculations are very time consuming, which stimulates many authors to use reduced models and the QSSA approximation. The usage of Hill and Michaelis-Menten functions for compact description of enzymatic activities is the well accepted approximation that has been applied to many types of genetic circuits demonstrating correct results for steady state characteristics of these circuits. However, when fluctuations are allowed, the models with Hill function as transcription rate fail to produce correct results [5]. Moreover, it has been shown that the model of reduced Repressilator leads to great quantitative distortions in the values of oscillation period and amplitude [6].

In this work we investigate the dynamics of Repressilator without using the QSSA assumption bearing in mind the recent experimental results about the complex way along which the TF (LacI dimer) is searching its cognate site on DNA [7]. The in vivo searching times estimated to be several minutes are comparable with the mRNA and TF degradation times that are around 5 and 15 min, respectively. Recently, the specific-site searching times for all the 180 known E. Coli TFs were analyzed and the times between 160 s and 1550s were computed [8]. We explore the minimal but detailed model of Repressilator with 7 elementary reactions explicitly described as a 12-dim ODE system to discover deterministic regimes and use stochastic simulation to examine the role of internal noise. We find that the non-adiabatic character of the oscillating regime, which contains a more or less slow subsystem for TF-DNA interaction, open the possibility for emergence of the oscillation through the subcritical AHB. Parametric analysis reveals this bifurcation in a broad interval of control parameters especially if degradation of TF dimers is taken into account. Unlike the QSS approximation, our straightforward approach shows the oscillatory dynamics of Repressilator to be very sensitive to even a small TFs dimer degradation rate that has not been investigated previously in the literature.

The subcritical AHB reveals the hysteretic properties of the model, that is, two stable dynamic regimes, a stable steady state and a limit cycle co-exist in the parameter space opening an essential possibility for noise-induced switching. The hysteresis is further conformed to the stochastic simulation, where we have shown the existence of two distinct dynamical behaviors for a single parameter set. Though the ultimate coexistence of the two dynamical attractors has been shown, the means for switching and control of the behaviors requires further investigation.

We study the effect of TF dimerization and dimer degradation on the noise levels in the oscillatory signal of this genetic circuit. We show that degradation of the proteins in the dimer form can lead to a significant reduction in the noise levels as judged by the shape of the return time (period) distribution. However, in the hysteresis region of the parameter values the return time distribution can be significantly distorted by the presence of the stationary dynamical attractor. Furthermore, we hypothesize that the distribution can be bimodal due to the small frequency oscillations at the stationary dynamical attractor.

Acknowledgements

This work is partially supported by RFBR grants 12-02-00529, 14-01-00196.

References

1. M.B. Elowitz and S. Leibler, *Nature*, 2000, **403**, 335.
2. C.V. Rao, A.P. Arkin, *J. Chem. Phys.*, 2003, **118**(11).
3. J. Hasty et al., *Chaos*, 2001, **11**(1).
4. D. Schultz, J.N. Onuchic, and P.G. Wolynes, *J. Chem. Phys.*, 2007, **126**, 245102.
5. R. Bundschuch, F. Hayot, and C. Jayaprakash, *Biophys. J.*, 2003, **84**, 1606-1615.
6. M.R. Bennett, D. Volfson, L. Tsimring, and J. Hasty, *Biophys. J.*, 2007, **92**, 3501-3512.
7. J. Elf, G.W. Li, and X.S. Xie, *Science*, 2007, **316**, 1191-1194.
8. M. Tabaka, T. Kalwarczyk, and R. Holyst, *Nuclear Acid Research*, 2013, **42**(2), 727-738.

NEUROBIOLOGY OF ALTERNANS ARRHYTHMIA: A SIMULATION STUDY OF THE HEART OF ANIMAL MODELS

T. Yazawa[1] and **H. Kitajima**[2]

[1] Tokyo Metropolitan University, Tokyo, Japan, yazawa-tohru@tmu.ac.jp
[2] Kagawa University, Takamatsu, Japan

Abstract. Alternans is an arrhythmia exhibiting alternating amplitude/interval from beat to beat on heartbeat recordings, such as the finger pulse. Alternans is well known since Traube's document in 1872 and is called harbinger of death, but the mechanisms for its generation is not fully defined and much work still remains. We studied this abnormal state of the heart, in animal models (electrophysiology) and with a numerical model (computer simulation). We focused our attention on a causal association between the pace-making cells and ventricular cells. We revealed that one of the main causalities in generating alternates was a potassium ionic abnormality.

Introduction

The cardiac alternans (CA) is an intriguing period-2 phenomenon. Since Traube's publication (1872), CA has remained an electrocardiographic curiosity for more than three quarters of a century [1, 2]. Nowadays, researchers believe that CA is the harbinger for sudden death [1, 3]. Indeed, in the worst case scenario with human hearts, CA triggers a cardiac instability (e.g. ventricular arrhythmias) and causes a sudden cardiac death [1]. Reducing the risk of sudden death is a goal of research in physiology and technology, but mechanisms for the generation of alternas have not been fully understood. In our physiological experiments on the crustaceans, CA was frequently observable with the "isolated" hearts. This animal model may contribute to the advance in management of the dysfunction of a complex cardiovascular disease. Genetics has revealed that the cardiovascular system of us and those of invertebrates resemble each other because of evolution (e.g., a homologous gene, Nkx-2.5, for making the heart). The invertebrate cardiac physiology has an over 100 years of history. We thus tried to study CA, using animal models and a newly assembled mathematical model [4]. A computer simulation regarding to CA rhythm based on the real-world crustacean data has not been conducted before.

Methods. Ethics: Specimens were treated as per the ethical regulations of the Tokyo Metropolitan University. Animal Heartbeat: The electrocardiogram (EKG) from model animals by implanted metal electrodes connected to an amplifier (usually x10,000 magnification, DAM50, WPA, USA) and a Power Lab System (AD Instruments, Australia) that digitized EKGs at 1 kHz.

Results. EKG: Figure 1 shows crustacean dying-EKGs of a specimen (Ligia exotica). Time from the start of recording is shown. Regular beatings at about 200 beat-per-min (BPM) were observable (8:50-1:04:50). Then, the "death-rhythm" i.e., CA appeared (1:06:15-1:12:55). Then, heart rate increased significantly up to over 300 BPM before dying. A significant rate-increase gives evidence for significant depolarization of membrane potential of cardiac cells. Insects, lobsters, and crayfish exhibited the same phenomena before dying, i.e., regular rhythm, CA, then mortal moment.

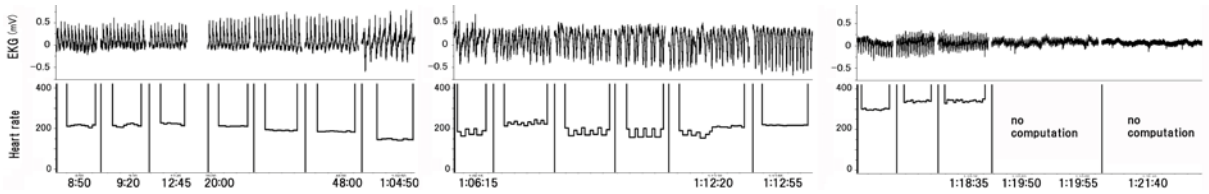

Fig. 1. Ligia EKG

Simulation. The heart network structure is known. Pacemaker cells (L) excite heart muscle cells (M). Human ventricular muscle cells (M) receive signal from the pacemaker cells (L). Shape of the signal from L is characterized by a unique potential shape. However, in the previous modeling studies, the shape was a rectangular wave. The coupling scheme from L to M was not incorporated into this modeling. We (Fig. 2A) used a real synaptic-potential-shape for modeling [4]. Where does CA arise? At L, or at M, or L-M interactions? A model can solve this question. The L-to-M signal is the target in the present study. In the present paper, we used a simpler model than the one used before [4]. By numerical analysis of our model we found that two parameters (the conductance of the sodium ion and concentration of the potassium ion in the extracellular space) play key roles of generating CA (Fig. 2B). For M, we used the Luo-Rudy I model [5]. Considering the synaptic current from L to M, the dynamics of the pacemaker cells does

not affect that of the muscle cells. Thus, in this study we only consider the muscle cell with a periodic force. The period of the external force (usually called BCL: basic cycle length) is assumed to be 380 [msec]. The membrane potential V of the Luo-Rudy I model with the synaptic input is described by

$$C\frac{dV}{dt} = -\left(I_{Na} + I_{Ca} + I_K + I_{K_1} + I_{Kp} + I_b + I_{syn}\right). \quad (1)$$

The synaptic current I_{syn} from L to M is given by

$$I_{syn} = G_{syn}\left(V - V_{syn}\right)s(t^*), \quad (2)$$

where G_{syn} is the maximum synaptic conductance, V_{syn} is the reversal potential and $s(t^*)$ is given by

$$s(t^*) = \frac{\tau_1}{\tau_2 - \tau_1}\left(-\exp\left(-\frac{t^*}{\tau_1}\right) + \exp\left(-\frac{t^*}{\tau_2}\right)\right), \quad (3)$$

where τ_1 and τ_2 are the rise and the decay time of the synapse, respectively. We identified these values as 18 ms and 288 ms, respectively, from the experimental data (Fig. 2A). We adjusted this crustacean values to a mouse model. In this mouse model, BCL is 380 ms. Crustacean BCL was 1200 ms in the experiment. Thus, our two values for τ_1 and τ_2 are now 5.5 and 90, respectively. t^* is the time which is reset at every nT (n is integer and T is BCL).

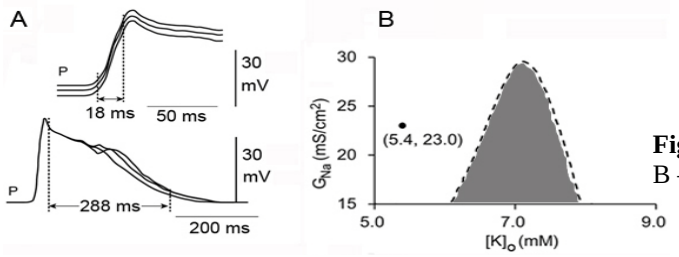

Fig. 2. A – configuration of the synaptic potential. B – simulation, $[K]_o$ vs. G_{Na}

Discussion

We studied bifurcation phenomena correlated to CA in the model. The values of the parameters related to the synapse are fixed to be G_{syn} = 4.0, V_{syn} = –29. Figure 2B shows a two-parameter bifurcation diagram on the parameter plane $[K]_o$ (extracellular concentrations of potassium ions) and G_{Na} (conductance for the sodium current). In this parameter region we observed the period-doubling bifurcation. The period-doubling bifurcation was alternans (Fig. 2B in the gray region). The closed circle (5.4, 23.0) indicates normal blood condition, i.e., the original values of the parameters. These simulation results indicate that alternans can be generated within a certain range of extracellular potassium concentration, from 6 to 8, if G_{Na} is fixed to 15. With a normal G_{Na} (23.0), alternans can be induced at around 7 mM$[K]_o$.

Conclusion

Cardiac cell puncture, e.g., owing to ischemia, resulting in a great increase of $[K]_o$, which induce depolarization, is a major cause for alternans. Genetic K-channel malfunction can lead to CA sickness. Overall K ion concentration in blood is a key issue.

Acknowledgements

This work was supported by JSPS Grants, No. 23500524 (TY) and No. 23500367 (HK). We thank DVX Inc. Tokyo, Japan, for financial support, research No. 4DQ404.

References

1. D.S. Rosenbaum et al., “Electrical alternans and vulnerability to ventricular arrhythmias”, *The New England J. of Medicine*, 1994, **330**, 235-241.
2. B. Surawicz, and C. Fisch, “Cardiac alternans: diverse mechanisms and clinical manifestations”, *Journal of American College of Cardiology*, 1992, **20**, 483-99.
3. B. Pieske, and J. Kockskämper, “Alternans goes subcellular. A “disease” of the ryanodine receptor?” *Circulation Research*, 2002, **91**, 553-555.
4. H. Kitajima, and T. Yazawa, “Modified Luo-Rudy model and its bifurcation analysis for suppressing alternans”, *Proceedings. NOLTA*, 2011, 390-393.
5. C.H. Luo, and Y. Rudy, “A model of the ventricular cardiac action potential. Demoralization, repolarization, and their interaction.” *Circ. Res.*, 1991, **68**, 1501–1526.

Invited

QUANTIFICATION OF STRESS BY DETRENDED FLUCTUATION ANALYSIS OF HEARTBEATS, BOTH IN THE LOBSTERS AND HUMANS

T. Yazawa

Tokyo Metropolitan University, Tokyo, Japan, yazawa-tohru@tmu.ac.jpe-mail

Abstract. The aim of this study is to develop a method to quantify stress. Electrocardiograms of both animal models and humans were analyzed by the Detrended Fluctuation Analysis (DFA) that calculates the scaling exponent (SI) from the beat-interval time series. I found that SI numerically distinguishes between normal hearts and abnormal hearts. SI ranges across various heart conditions: healthy basal condition and stressful condition. This study suggests that DFA is a practical method to make a gadget for health management.

Introduction

The involuntary cardiac nerves, the acceleratory nerves (CA) and the inhibitory nerves (CI), govern the heart. These autonomic nerves (ANS) carry psychological message to the heart, indeed ANS modulates heart rate every moment. Thus, the heart is a window of mind. However, ANS is not clearly understood because recording ANS-activities is difficult. But in crustaceans, I have recorded them. Both CA and CI were active during the heart pumped. Interestingly, CI often excited at a high-rate, and concomitantly CA became quiet, for a second [1]. During that period, the heartbeat disappeared, although a quick restitution occurred in a minute. The brief cessation of heartbeat intermittently and regularly occurred if an animal could spend a “stress free” time, for example, hiding in a shelter. The stress free behavior never happened if a human got close to the lobster. Crustaceans are a miraculous specimen, because we can recognize animal’s stress simply by electrocardiograms.

Crustacean hearts and human hearts strongly resemble each other in structure and function. In the developing heart, it is known that homologous genes function to form the heart in any animal, e.g., Nkx2-5 (NK2 homeobox gene) [2]. In both crustaceans and humans, both CA and CI nerves are connected with the cardiac pacemaker cells, but CA further proceeds to the ventricular muscles beyond the pacemaker cells. Why does CA govern entire heart muscles? The answer is: CA-muscle-connection can substantialize a direct modulation of force of contractions, but CI merely needs suppression of rhythm [3]. The resemblance between crustacean hearts and human hearts guarantee that some knowledge obtained from crustacean hearts is applicable to human hearts.

I studied electrocardiograms of both animal models and humans. I used a modified Detrended Fluctuation Analysis (mDFA) that calculates the scaling exponent (originally, Peng et al., [4]). As a result, SI numerically distinguished between normal hearts and abnormal hearts. I here show that the mDFA is a potential method for health checking.

Materials and Methods

A Power Lab System (AD Instruments, Australia) was used for heartbeat recordings. For EKG electrodes, a set of ready-made three AgAgCl electrodes (Vitrode V, Nihonkoden Co. Ltd. Tokyo) were used. EKG signals were transferred to a Power Lab System. Finger pulse recordings were also used with a Power Lab System. Permanently mounted metal electrodes were glued on the carapace for crustacean EKG recordings. All subjects were treated as per the ethical regulations of Tokyo Metropolitan University.

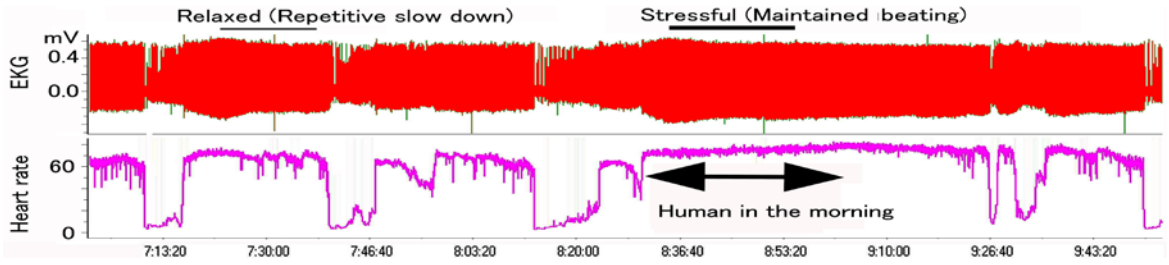

Fig. 1. Lobster EKG. Black bars show “relaxed” condition (a thin bar) and the stressful condition (a thick bar). Arrows: Human visited the room for feeding lobster. Note, a steady beating continued at stressful condition. This was the consequence of discharge of cardio-regulatory nerves, i.e., an increased cardio-accelerator and concomitant cessation of the inhibitor. This autonomic response is the lobster’s expression of stress/fear/anxiety

Results

Animal models. Figure 1 shows an example of crustacean heartbeat recording. The spiny lobster (*Panulirus japonicus*) exhibited the periodic slowdown of heart rate when the specimen was at rest, i.e., without the frightening stimuli from the environment. Crabs in a relaxed condition also exhibited this on/off switching patterns, i.e., alternating appearance of a maintained high rate (50–70 beat per min (BPM)) and of extremely low rates (5–15 BPM) (Fig. 1). I analyzed both conditions in various period lengths (Fig. 2). I assumed that mDFA is also practically useful for human hearts.

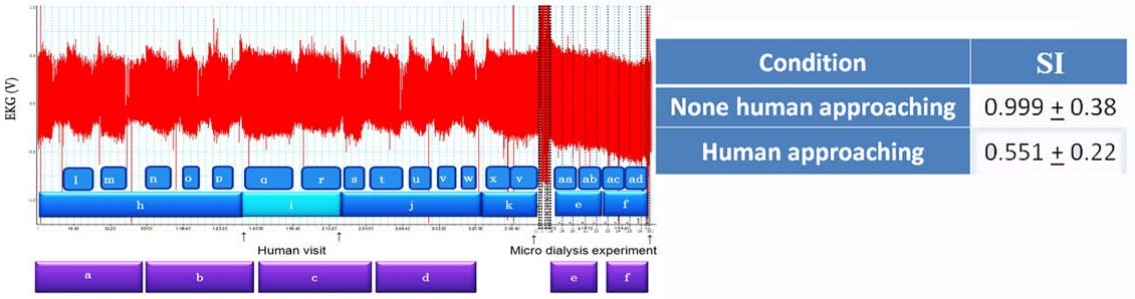

Fig. 2. Scaling exponent (SI) computed from EKGs, at relaxed conditions and stressful conditions

Human subjects. Human EKGs were analyzed by mDAF. Table 1 shows that there is a difference in SIs between stressful individuals and non-stressful individuals. Appendix in Table 1 shows that cardiac muscle injury can be detectable by mDFA.

Table 1. Comparison: Stress level and exponent value (Indonesia, 2012, working with Prof. A. Hutapea)

Categories	Subjects	Stress level (Interview)	Scaling exponent (SI)
Business owner (a company)	No. 1	Fairly Low	1.03
Business owner (a company)	No. 2	High	0.72
Top management (President of a Univ.)	No. 1	High	0.84
Top management (Vice president)	No. 2	High	0.84
Middle management (Dean)	No. 1	High	0.72
Middle management (Secretary of president)	No. 2	High	0.76
Ordinary employee (Teaching Only professor)	No. 1	Fairly Low	1
Ordinary employee (Teaching Only professor)	No. 2	Fairly Low	0.98

Table 1. Apendix: Cardiac disease	Age	Daily life	Scaling exponent (SI)
Patient with stent-placement	60 ♂	OK	1.26
Patient with bypass-surgery	45 ♂	OK	1.38
Patient with inplantable cardioverter	53 ♂	OK	1.22
Ventricular septal defect (20 y ago operation)	48 ♀	OK	1.41
Healthy Representative (Hosewife)	46 ♀	OK	1.03

Conclusion

mDFA and SI are usable. mDFA will be incorporated in a gadget for checking health and stress.

Acknowledgements

This work was supported by JSPS Grant, No. 23500524. I thank DVX Inc. Tokyo, Japan, for financial support for research, No. 4DQ404.

References

1. T. Yazawa and K. Kuwasawa, “Intrinsic and extrinsic neural and neurohumoral control of the decapod heart”, *Experientia*, 1992, **48**, 834-840.
2. http://ghr.nlm.nih.gov/gene/NKX2-5.
3. T. Yazawa and K. Kuwasawa, “The cardio-regulator nerves of the hermit crabs: anatomical and electrophysiological identification of their distribution inside the heart”, *J. Comp. Physiol. A.*, 1984, **154**, 871-881.
4. C.-K. Peng, S. Havlin, H.E. Stanley, and A.L. Goldberger, "Quantification of scaling exponents and crossover phenomena in nonstationary heartbeat time series," *Chaos*, 1995, **5**, 82-87.

CHIMERA-LIKE STATES IN AN ENSEMBLE OF GLOBALLY COUPLED OSCILLATORS

A. Yeldesbay, A. Pikovsky, and **M. Rosenblum**

Institute for Physics and Astronomy, University of Potsdam
Karl-Libknecht-Strasse 24/25, 14476 Potsdam-Golm, Germany
azayeld@gmail.com

Abstract. We demonstrate the emergence of a complex state in a homogeneous ensemble of globally coupled identical oscillators, reminiscent of chimera states in nonlocally coupled oscillator lattices. In this regime some part of the ensemble forms a regularly evolving cluster, while all other units irregularly oscillate and remain asynchronous. We argue that the chimera emerges because of effective bistability, which dynamically appears in the originally monostable system due to internal delayed feedback in individual units. Additionally, we present two examples of chimeras in bistable systems with frequency-dependent phase shift in the global coupling.

Recently, a lot of attention has been attracted to the regimes of the coexistence of coherence and incoherence in oscillators lattices, which is also known as “chimeras” [1]. These states have been investigated in numerous theoretical studies [2] and demonstrated in an experiment [3]. Also, it has been shown that for some initial conditions two interacting populations of globally coupled identical oscillators can exhibit symmetry-breaking of synchrony, so that one population synchronizes whereas the other remains asynchronous [4]; the existence of such chimeras has been also confirmed experimentally [5]. A natural question, addressed in our work, is under which conditions can such a symmetry-breaking into synchronous and asynchronous groups be observed in a completely homogeneous globally coupled population of identical oscillators.

In case of global coupling, one may expect that all oscillators should evolve similarly, since they are subject to the same force. This expectation is rather natural and is indeed true for simple systems like the standard Kuramoto model as well as for many other examples from the literature. However, a state with one large synchronized cluster and a cloud of scattered units, reminiscent of chimera state, was observed by K. Kaneko in a system of identical globally coupled chaotic maps [6]. For periodic units such a state has been reported by Daido and Nakanishi [7] and Schmidt et al. [8], who studied the cases of linear and nonlinear global coupling, respectively, see also [9]. These observations of identical nonlinear elements behaving differently, in spite of being driven by the same force, indicate presence of bi- or multistability. In our work [10] we have demonstrated that chimera-like states naturally appear for a minimal generalization of the popular Kuramoto-Sakaguchi phase model to the case of globally coupled identical phase oscillators with internal delayed feedback, and discuss the underlying mechanism of dynamically sustained bistability.

Globally coupled self-sustained oscillators can be quite generally treated in the phase approximation [11]. In the simplest case of identical sine-coupled units such an ensemble of N units is described by the Kuramoto-Sakaguchi model [12]. We have considered a similar setup for oscillators with an internal delayed feedback loop. The latter is a natural ingredient, e.g, of lasers with external optical feedback [13] and of numerous biological systems where signal transmission in the feedback pathway may be rather slow [14]. Assuming the global coupling to be of the Kuramoto-Sakaguchi type, we wrote our basic model as

$$\dot{\varphi}_k = \omega + \alpha \sin(\varphi_{\tau,k} - \varphi_k) + \varepsilon\, Im\left(e^{i\beta} Z e^{-i\varphi_k}\right), \qquad k = 1, \dots, N, \tag{1}$$

where φ is oscillators' phase, $\varphi_\tau \equiv \varphi(t-\tau)$, τ is the delay, $\varepsilon > 0$ is the coupling strength, β is the phase shift in the coupling, $Z = Re^{i\theta} = N^{-1}\sum_{k=1}^{N} e^{i\varphi_k}$ is the complex Kuramoto order parameter (complex mean field), and α is the feedback strength. We choose the parameter of the system so that every individual oscillator without coupling is in monostable mode.

Numerical simulations reveal that the model (1) in finite parameter domain demonstrates a chimera-like state, where the ensemble splits into two domains: a synchronized cluster of oscillators and an asynchronous cloud. For the elements in the cluster the phase dynamics is highly regular with a nearly constant instantaneous frequency, while oscillators in the cloud are chaotic and their instantaneous frequencies strongly fluctuate. Moreover, individual frequencies in the cloud are only weakly correlated, so that the phase differences demonstrate many phase slips and are unbounded. This irregularity

is also reflected in the strong fluctuations of the cloud contribution to the mean field, to be compared with nearly constant contribution from the cluster. For different initial conditions the size of the cluster grows relatively fast at the beginning, and after transients in the dynamics tend to some fixed range, thereby, a fully synchronized state is never reached because of the instability of the latter.

In our work we demonstrated numerically and explained semi-quantitatively the emergence of chimera states in ensembles of identical globally coupled oscillators. We have outlined a mechanism of dynamically sustained bistability: the ensemble splits into two parts with completely different dynamics, and these parts together create a mean field that allows such a bistability. This mechanism is nontrivial, because for the chosen parameters the uncoupled systems are monostable. However, due to interaction, the oscillators become effectively bistable: being forced by the same field they exhibit two very different dynamical patterns. The oscillators in one group are regular and are therefore easily synchronized with each other, while the others are highly irregular and remain in different asynchronous, although correlated, states. The global field that leads to the bistability is dynamically sustained in a self-consistent way.

Finally, we discussed two less nontrivial setups, where it was demonstrated that chimera-like states are also possible without this mechanism, if the individual units are naturally bistable. In the first example, in contradiction to our basic model (1), not only individual oscillators possess a delayed feedback loop, but the global coupling is also delayed, with a different delay time. If the coupling is organized in a way that it acts repulsively on the oscillators in one state and attractively on those which are in the other state, the system exhibits a chimera-like state. A similar scenario has been realized in the second example, with bistable identical Stuart-Landau oscillators without delays, having two stable limit cycles and globally coupled via an additional linear circuit.

Acknowledgements

This work was supported by DFG, Grant No. PI-2020/17.

References

1. D. Battogtokh and Y. Kuramoto, *Phys. Rev. E*, 2000, **61**, 3227; Y. Kuramoto and D. Battogtokh, *Nonlinear Phenom. Complex Syst.*, 2002, **5**, 380.
2. D.M. Abrams and S.H. Strogatz, *Phys. Rev. Lett.*, 2004, **93**, 174102; O.E. Omel'chenko, Y.L. Maistrenko, and P.A. Tass, *Phys. Rev. Lett.*, 2008, **100**, 044105; G.C. Sethia, A. Sen, and F.M. Atay, *Phys. Rev. Lett.*, 2008, **100**, 144102; G. Bordyugov, A. Pikovsky, and M. Rosenblum, *Phys. Rev. E*, 2010, **82**, 035205; C.R. Laing, *Physica D: Nonlinear Phenomena*, 2009, **238**, 1569; E.A. Martens, C.R. Laing, and S.H. Strogatz, *Phys. Rev. Lett.*, 2010, **104**, 044101; M. Wolfrum, O.E. Omelchenko, S. Yanchuk, and Y.L. Maistrenko, *Chaos*, 2011, **21**, 013112; C.R. Laing, K. Rajendran, and I.G. Kevrekidis, *Chaos*, 2012, **22**, 013132; Y. Zhu, Y. Li, M. Zhang, and J. Yang, *Europhys. Lett.*, 2012, **97**, 10009; M.J. Panaggio and D.M. Abrams, *Phys. Rev. Lett.*, 2013, **110**, 094102.
3. S. Nkomo, M.R. Tinsley, and K. Showalter, *Phys. Rev. Lett.*, 2013, **110**, 244102.
4. D.M. Abrams, R. Mirollo, S.H. Strogatz, and D.A. Wiley, *Phys. Rev. Lett.*, 2008, **101**, 084103 (2008); A. Pikovsky and M. Rosenblum, *Phys. Rev. Lett.*, 2008, **101**, 264103.
5. M.R. Tinsley, S. Nkomo, and K. Showalter, *Nature Physics*, 2012, **8**, 662; E.A. Martens, S. Thutupalli, A. Fourriere, and O. Hallatschek, *Proc. Natl. Acad. Sci. U.S.A.*, 2013, **110**, 10563.
6. K. Kaneko, *Physica D*, 1990, **41**, 137.
7. H. Daido and K. Nakanishi, *Phys. Rev. Lett.*, 2006, **96**, 054101.
8. L. Schmidt, K. Schönleber, K. Krischer, and V. García-Morales, *Chaos*, 2014, **24**, 013102.
9. G.C. Sethia and A. Sen, *Phys. Rev. Lett.*, 2014, **112**, 144101.
10. A. Yeldesbay, A. Pikovsky, and M.G. Rosenblum, *Phys. Rev. Lett.*, 2014, **112**, 144103.
11. Y. Kuramoto, *International Symposium on Mathematical Problems in Theoretical Physics*, Springer Lecture Notes Phys., **39**, H. Araki (Ed.), New York, 1975, p. 420; Y. Kuramoto, *Chemical Oscillations, Waves and Turbulence*, Springer, Berlin, 1984.
12. H. Sakaguchi and Y. Kuramoto, *Prog. Theor. Phys.*, 1986, **76**, 576.
13. C. Masoller, *Phys. Rev. Lett.*, 2002, **88**, 034102.
14. L. Glass and M.C. Mackey, *From Clocks to Chaos: The Rhythms of Life.*, Princeton Univ. Press, Princeton, NJ, 1988; A. Takamatsu, T. Fujii, and I. Endo, *Phys. Rev. Lett.*, 2000, **85**, 2026; J. Batzel and F. Kappel, *Math. Biosci.*, 2011, **234**, 61.

SIMULTANEOUS ACTION OF AMPA AND NMDA SYNAPTIC CURRENTS ON THE MODEL OF DOPAMINERGIC NEURON

D.G. Zakharov

Institute of Applied Physics RAS, Nizhny Novgorod, Russia
Nizhny Novgorod State University, Nizhny Novgorod, Russia

Abstract. Dopaminergic neurons are unique neurons due to the response differentiation to the action of the typical excitatory stimuli. It means that only NMDA synaptic current can significantly increase generation frequency (more than 5-fold in comparison with tonic activity frequency), whereas AMPA current usually suppresses neuron activity. Here we consider the simultaneous action of these synaptic currents. It is shown that in the case of stimuli steps, either frequency growth or activity suppression is demonstrated, depending on the strength of AMPA and NMDA receptors. The highest frequency is obtained for the case of simultaneous action of these synaptic currents.

Dopaminergic (DA) neurons, generating a periodic spike train with frequencies from 1 to 4 Hz in tonic mode, have a unique response (in comparison with other types of neurons) to the typical excitatory stimuli. They produce the high frequency generation (frequency can exceed 20 Hz) [1, 2] under the action of the NMDA synaptic current, whereas the applied current, as well as the stimulation of AMPA receptors, does not initiate an significant increase in the generation frequency. Moreover, the neuron activity is often suppressed [3, 4]. Earlier we introduced a phenomenological model of DA neurons constructed in the framework of modified FitzHugh-Nagumo (FHN) equations [5, 6] which reproduces response differentiation inherent in dopaminergic neurons:

$$\begin{aligned} \dot{u} &= f(u) - j_{KCa} + j_{sti}, \\ \dot{v} &= \varepsilon\, g(u,v), \end{aligned} \tag{1}$$

where $f(u) = a_1(u^3 + a_2u^2 + a_3u + a_4)$ is a cubic function, and $g(u,v) = \begin{cases} u - c, & u \le c, \\ 0.01(u-c) - v, & u < c \end{cases}$ is a piece-wise linear function. The main difference in comparison with typical FHN equations is the change of the linear term "$-v$" by the nonlinear term $j_{Kca}(u,v) = g_{KCa}(E_{KCa} - u)\dfrac{v^4}{v^4 + k}$. The latter is an SK-type Ca^{2+}-dependent K^+-current. Parameter g_{Kca} is its maximal current density, E_K is the reversal potential, and k is half activation of the current. The substitution results in a new shape of u-nullcline – it becomes symmetrical with respect to u-axis, and we choose the function $g(u,v)$ to be piece-wise to avoid nullcline intersection (and thus to avoid existence of steady states) at the negative half plane of the phase space (see Fig. 1).

Hear we consider two types of external stimulation – AMPA and NMDA synaptic currents:

$$\begin{aligned} \mathrm{j_{sti}} &= \mathrm{g_{NMDA}(u)(E_{NMDA} - u) + g_{AMPA}(E_{AMPA} - u)}, \\ \mathrm{g_{NMDA}(u)} &= \frac{\overline{\mathrm{g}}_{\mathrm{NMDA}}}{1 + 0.28[\mathrm{Mg}]\mathrm{e}^{-0.08\mathrm{u_d}}}, \end{aligned} \tag{2}$$

where g_{AMPA} and g_{NMDA} are the maximum conductivities of AMPA and NMDA receptors, respectively; E_{AMPA} and E_{NMDA} are the respective reversal potentials; $[Mg]$ is a Magnesium concentration. Let us fix the model parameters $a_1 = -50.5$, $a_2 = 1.35$, $a_3 = 0.54$, $a_4 = 0.0472$, $c = -0.585$, $[Mg] = 2$, and $E_N = E_A = 0$ so that a stable limit cycle exists on the phase plane. It was shown earlier [5, 6] that in the framework of model (1) in the case of separate action of the external stimuli, the AMPA-current results in activity suppression, even for the small values of parameter g_{AMPA}, whereas the NMDA synaptic current causes frequency growth (by a factor of 5–7) in the wide range of g_{NMDA} values. What happens with neuron activity in the case of simultaneous action of these synaptic currents? Actually, it depends on the strength of the maximum conductivities g_{AMPA} and g_{NMDA}. The related two-parametric bifurcation diagram is shown in Fig. 2. The curve labeled "A-H" corresponds to the supercritical Andronov-Hopf bifurcation. Below this curve there exists a stable steady state corresponding to the neuron rest state. When we pass through the bifurcation curve, a stable limit cycle appears and the neuron starts to generate spikes periodically (Fig. 3). The spike frequency grows with increasing g_{NMDA} values up to the

frequency peak (approximately 7-fold more than the frequency of tonic activity) and then starts to decrease (Fig. 4). So we can conclude that

1. Different types of neuron activity may be observed under the simultaneous action of AMPA and NMDA synaptic currents, i.e. rest state, low frequency or high frequency activity.
2. The type of activity is determined by the ratio of maximal activities of AMPA and NMDA synaptic currents.
3. The highest frequency is achieved for the case of the simultaneous action of synaptic currents for small values of the maximum conductivity of AMPA receptors (see Fig. 4).
4. For the strong AMPA current (for example, see the curves corresponding to g_{AMPA} = 0.075 or g_{AMPA} = 0.01 in Fig. 4) the frequency maximum decreases substantially.

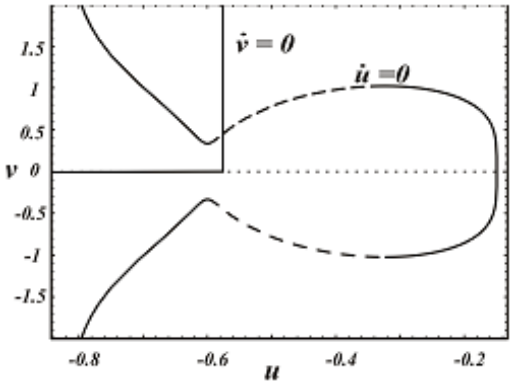

Fig. 1. Nullclines of the model (1)

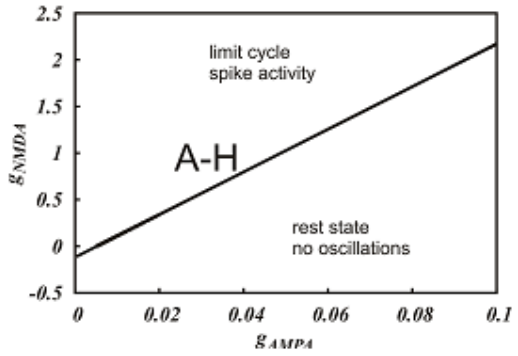

Fig. 2. Two-parametrical bifurcation diagram

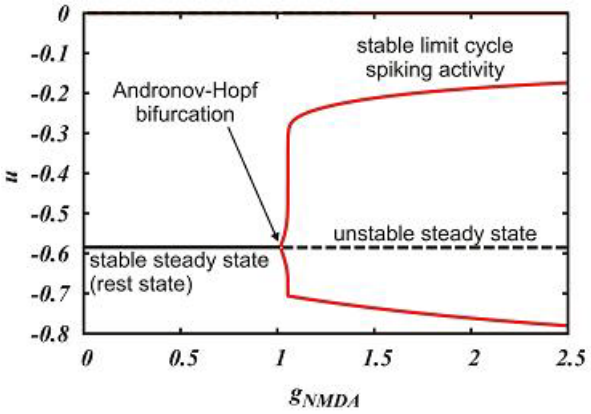

Fig. 3. One-parametric bifurcation diagram for g_{AMPA} = 0.05

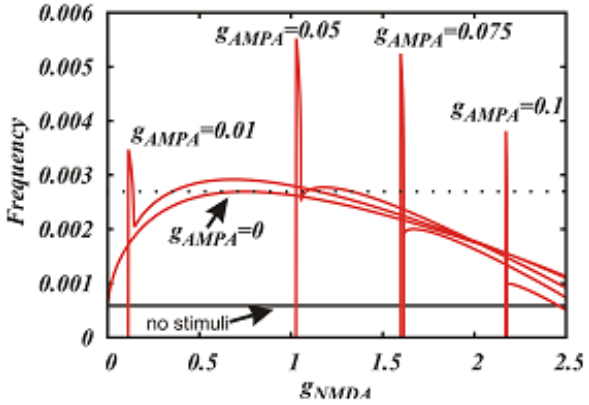

Fig. 4. Dependence of frequency on the maximum conductivity of NMDA receptors for different values of maximum conductivity of AMPA receptors. Note that the first strong peak in the curves corresponds to the small amplitude limit cycle which observed in the small neighborhood of the supercritical Andronov-Hopf bifurcation

Acknowledgements

This work was supported by the Russian Foundation for Basic Research (project 14-02-00916-a).

References

1. B.I. Hyland, J.N.J. Reynoldsa, J. Hay, et al., *Neuroscience*, 2002, **114**, 475-492.
2. Y.-X. Li, R. Bertram, and J. Rinzel, *Neuroscience*, 1996, **71**, 397-410.
3. C.L. Christoffersen and L.T. Meltzer, *Neuroscience*, 1995, **67**, 373-381.
4. M. Hajos, T. Sharp, and N.R. Newberry, *Brain Res.*, 1996, **737**, 308-312.
5. D.G. Zakharov and A.S. Kuznetsov, *Chaos, Solitons & Fractals*, 2012, **45**, 640-644.
6. D.G. Zakharov and A.S. Kuznetsov, *JETP Letters*, 2012, **95**, 598-602.

AMPLITUDE CHIMERAS AND CHIMERA DEATH IN DYNAMICAL NETWORKS

A. Zakharova[*], **M. Kapeller,** and **E. Schöll**

Technische Universität Berlin, Germany
[*]e-mail: anna.zakharova@tu-berlin.de

Abstract. We find chimera states with respect to amplitude dynamics in a network of Stuart-Landau oscillators. They appear due to the interplay of nonlocal network topology and symmetry-breaking coupling. As the coupling range is increased, the oscillations die out, amplitude chimeras disappear and the network enters a symmetry breaking stationary state. This particular regime is a novel pattern which we call *chimera death*. It is characterized by the coexistence of spatially coherent and incoherent inhomogeneous steady states and therefore combines the features of chimera state and oscillation death. Additionally, we show two different transition scenarios from amplitude chimera to chimera death.

We investigate the paradigmatic model of Stuart-Landau oscillators

$$\dot{z} = f(z) \equiv \left(\lambda + i\omega - |z|^2\right) z \,, \tag{1}$$

where $z = re^{i\phi} = x + iy \in \mathbb{C}$, $\lambda, \omega \in \mathbb{R}$. For $\lambda > 0$ the uncoupled systems demonstrate limit cycle oscillations with radius $r_0 = \sqrt{\lambda}$ and frequency ω. The Stuart-Landau system is therefore a model for nonlinear oscillations close to a Hopf bifurcation. Here we study a ring of N nonlocally coupled Stuart-Landau oscillators:

$$\dot{z}_j = f(z_j)\frac{\sigma}{2P}\sum_{k=j-P}^{j+P}\left(\mathrm{Re}\, z_k - \mathrm{Re}\, z_j\right), \tag{2}$$

where $j = 1, 2, \ldots, N$. The coupling parameters which are identical for all links are the coupling strength $\sigma \in \mathbb{R}$ and the coupling range P/N, where P corresponds to the number of nearest neighbors in each direction on a ring. The particular coupling through the real variable which we introduce here breaks the rotational symmetry of the system. This is a necessary condition for the existence of nontrivial steady states and therefore for oscillation death [1]. While tuning the coupling range P for the fixed value of coupling strength σ we uncover a variety of dynamic regimes in Eq. (2) which are shown as space-time plots color-coded by the variable y and snapshots in Fig. 1. In particular, we find chimera behavior with respect to the amplitude, i.e., *amplitude chimeras*, where one part of the network is oscillating with spatially coherent amplitude, while the other displays oscillations with spatially incoherent amplitudes [Fig. 1(a),(f)]. The increase of coupling range induces a transition from amplitude chimeras to an in-phase synchronized state [Fig. 1(b),(g)]. By rising the coupling range even further we detect a novel pattern which provides bridging between chimera states and oscillation death. Therefore, we call it *chimera death* [Fig. 1(c)–(e), (h)–(j)]. In this regime the oscillations die out in a peculiar way. In more detail, the population of identical oscillators breaks up into two domains: (i) spatially coherent oscillation death, where the neighboring elements of the network populate the same branch of the inhomogeneous steady state, and (ii) spatially incoherent oscillation death, where the sequence of populated branches of neighboring nodes is completely random. Interestingly, the increase of the coupling range for the fixed coupling strength also induces structural changes of chimera death pattern: the number of clusters in the coherent domain is decreased [Fig. 1(c)–(e), (h)–(j)].

To provide an overall view on the network behavior for the wide range of coupling parameters we plot the map of regimes in the plane of coupling range and coupling strength. The oscillatory behavior of Eq. (2) is represented by amplitude chimera (blue region in Fig. 2), which is observed for small coupling range, and by in-phase synchronized oscillations (light green region in Fig. 2). The steady state solutions occur for larger values of coupling parameters and are manifested by chimera death (red region in Fig. 2). The existence of two distinct transition scenarios from the oscillatory to the steady state regime becomes evident from Fig. 2. For a small value of coupling strength $\sigma = 10$, the chimera death state is born from amplitude chimera by passing through in-phase synchronized oscillations when the coupling range is increased (diamonds in Fig. 2). In contrast, for a large value of the coupling strength, for example, $\sigma = 26$, a slight increase of the coupling range from $P/N = 0.04$ to $P/N = 0.05$ destroys amplitude chimeras and directly leads to chimera death.

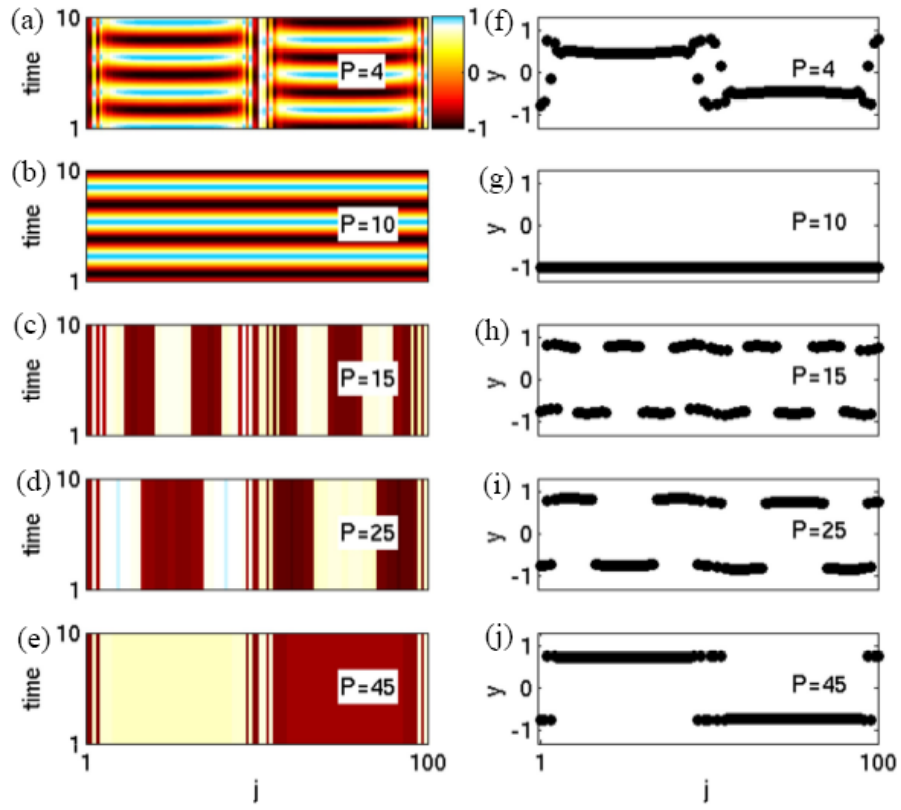

Fig. 1. Space-time plots (*left panel*) and snapshots for the variable y (*right panel*) in a network of Stuart-Landau oscillators for coupling strength $\sigma = 10$ and varying nearest neighbors number P. $P = 4$: amplitude chimera; $P = 10$: in-phase synchronization; $P = 15$: multi-cluster (> 3) chimera death; $P = 25$: 3-cluster chimera death; $P = 45$: 1-cluster chimera death. Other parameters: $N = 100$, $\lambda = 1$, $\omega = 2$

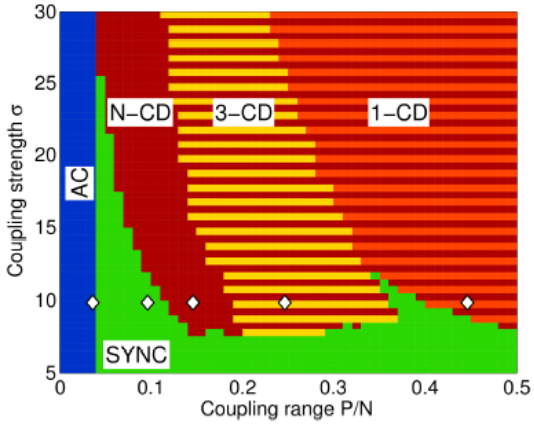

Fig. 2. Map of dynamic regimes for $N = 100$, $\lambda = 1$, $\omega = 2$ in the plane of coupling range P/N and coupling strength σ. 1-CD: 1-cluster chimera death; 3-CD: 3-cluster chimera death; N-CD: multi-cluster (> 3) chimera death. AC: amplitude chimera; SYNC: in-phase synchronized oscillations. Diamonds mark the parameter values chosen in Fig. 1

Acknowledgements

This work was supported by DFG in the framework of SFB 910.

References

1. A. Zakharova, I. Schneider, Y.N. Kyrychko, K.B. Blyuss, A. Koseska, B. Fiedler, and E. Schцll, *Europhys. Lett.*, 2013, **104**, 50004.
2. A. Zakharova, M. Kapeller, and E. Schöll, *Phys. Rev. Lett.*, 2014, 112, 154101.

International Symposium

TOPICAL PROBLEMS OF NONLINEAR WAVE PHYSICS

NWP-2:

LASERS WITH HIGH PEAK AND HIGH AVERAGE POWER

GENERATION AND CHARACTERIZATION WITH FROG TECHNIQUE OF FEMTOSECOND OPTICAL PULSES TUNABLE IN THE RANGE OF 2 TO 3 μm FROM SILICA-BASED ALL-FIBER LASER SYSTEM

E.A. Anashkina, A.V. Andrianov, M.Yu. Koptev, S.V. Muravyev, and **A.V. Kim**

Institute of Applied Physics, Russian Academy of Sciences, Nizhny Novgorod, Russia,
elena.anashkina@gmail.com

Introduction

Coherent optical sources in the mid-IR range are attractive for a variety of applications. Typically, mid-IR light is generated by using optical parametric oscillators, solid-state lasers based on Cr^{2+} and Fe^{2+} doped II-VI crystals or quantum cascade lasers [1]. However, an all-fiber, mid-IR light source using nonlinear optical conversion in a fiber with special composition can provide significant advantages over existing laser sources [2]. Passive GeO_2-doped core fibers attract researchers' attention for operation in the "molecular fingerprint" mid-IR (2–3 μm) spectral range [3–6].

Here we report a simple technique of routine generation of femtosecond optical pulses tunable in the range of 2–3 μm in an all-fiber scheme starting from an Er-doped laser setup based on telecom components. We demonstrate Raman-shifted solitons with durations of the order of one hundred fs in a passive silica-based GeO_2-doped core fiber.

Experimental setup

The experimental setup is shown in Fig. 1(a). It is based on a passive mode-locked Er-doped fiber oscillator, fiber amplifiers and pieces of different nonlinear fibers. The oscillator with passive mode locking via nonlinear polarization rotation delivers femtosecond pulses with a 30 nm spectral bandwidth centered at 1.57 μm at a fundamental frequency of 49 MHz. Then the pulses pass through a polarization controller (PC), are amplified in the diode-pumped Er:fiber amplifier up to a maximum average power of 150 mW and propagate through a 2-m piece of standard telecom fiber SMF-28.

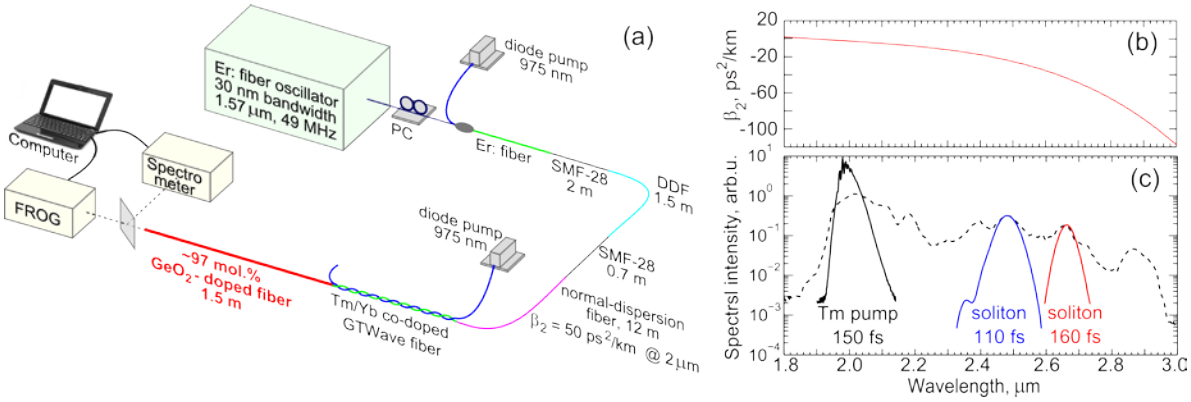

Fig. 1. (a) Experimental setup. (b) Calculated group velocity dispersion of the GeO_2-doped fiber. (c) Supercontinuum spectrum (dash line) generated in the GeO_2-doped fiber with the pump pulses from the output of the Tm:fiber amplifier (black, solid line). Spectra of FROG-retrieved solitons (blue and red, solid lines)

Next, we use a 1.5-m long dispersion-decreasing fiber (DDF) to convert the pulse wavelength from 1.6 μm up to 2 μm due to Raman soliton self-frequency shift and a 0.7-m long piece of SMF-28 as a mode field adapter to fiber stretcher. Then the pulses propagate through a 12-m long fiber stretcher with normal dispersion (β_2 = 50 ps^2/km at 2 μm) and are amplified in an 8-m long GTWave Tm/Yb co-doped fiber. The calculated active fiber parameters at 2 μm are β_2 = –90 ps^2/km, the effective mode area A_{eff} = 60 μm^2 and the nonlinear coefficient γ = 1 (W km)$^{-1}$. After that, the amplified pulses with the spectrum shown in Fig. 1(c) having energy of 3 nJ and duration of 150 fs at full width at half maximum (FWHM) are coupled into the 1.5 m-long fiber with 97 mol.% GeO_2 content in the core. The calculated dispersion profile is shown in Fig. 1(b). The calculated cutoff is 1.9 μm, but the effective mode area A_{eff} is smoothly changing from 6 μm^2 at a wavelength of 2 μm up to 11 μm^2 at 3 μm. The losses at the splicing of the Tm:fiber and the germanate-core fiber are about 70% mainly due to a large difference between their fundamental mode areas.

Experimental results

The optical pulses in the GeO_2-doped fiber undergo high-order soliton compression with corresponding spectral broadening at the initial stage of supercontinuum generation [5, 6]. Estimated solition number is $N \approx 10$. After a transient stage when the maximum pulse compression occurs, the pulses decay into solitons in the anomalous dispersion range and dispersion waves at shorter wavelengths in the normal dispersion range as well. At the GeO_2-doped fiber output we observe supercontinuum generation up to 3 μm that contains Raman solitons as shown in Fig. 1(c). The SHG-FROG (second-harmonic generation frequency-resolved optical gating) home built apparatus is used to characterize optical pulses. We measure two different FROG-traces presented in Fig. 2(a, d).

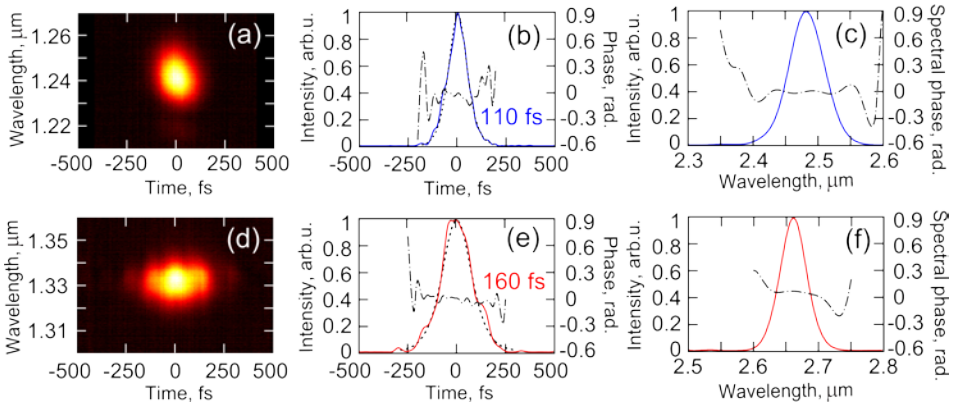

Fig. 2. (a, d) FROG-traces and corresponding retrieved intensity profiles (solid lines), their sech-shape approximations (dot lines), and reconstructed phases (dash-dot lines) of the pulses centered at 2.48 μm (b) and at 2.66 μm (e). (c, f) Spectra and spectral phases of FROG-pulses

The retrieved pulse at 2.48 μm has a duration of 110 fs and a time-bandwidth product (TBP) of 0.34. FROG-error is 0.006. The retrieved pulse at 2.66 μm has a duration of 160 fs, TBF of 0.327, and FROG-error of 0.007. Their shapes are fitted very well by sech-shaped functions (see Fig. 2(d, e)). The reconstructed pulses in the frequency domain are shown in Fig. 2(c, f). The fluctuations of the reconstructed spectral phases from the flat ones are not more than 0.1 rad. So we state that these pulses are actually solitons.

Conclusion

Femtosecond optical pulses with broad tunability in the range of 2–3 μm are demonstrated in a germanate-glass core silica-glass cladding fiber with a driving pulse at 2 μm produced by an all-fiber laser system consisting of Er:fiber source at 1.6 μm, Raman fiber shifter, and Tm:fiber amplifier. FROG measurements have confirmed that tunable pulses are Raman solitons with a duration of 110 fs at 2.48 μm and with a duration of 160 fs at 2.66 μm.

Acknowledgements

This work was partly supported by the Russian Foundation for Basic Research through grants 13-02-97125 and 14-02-00537. E.A.A. acknowledges the Dynasty Foundation support.

References

1. M. Ebrahim-Zadeh and I.T. Sorokina, *Mid-infrared coherent sources and applications*, Springer, 2008.
2. G.S. Qin, X. Yan, C. Kito, M.S. Liao, C. Chaudhari, T. Suzuki, Y. Ohishi, *Opt. Letters*, 2009, **34**, 2015-2017.
3. M. Zhang, E.J.R. Kelleher, T.H. Runcorn, V.M. Mashinsky, O.I. Medvedkov, E.M. Dianov, D. Popa, S. Milana, T. Hasan, Z. Sun, F. Bonaccorso, Z. Jiang, E. Flahaut, B.H. Chapman, A.C. Ferrari, S.V. Popov, and J.R. Taylor, *Opt. Express*, 2013, **21**, 23261-23271.
4. V.A. Kamynin, A.S. Kurkov, and V.M. Mashinsky, *Laser Phys. Lett.*, 2012, **9**, 219-222.
5. E.A. Anashkina, A.V. Andrianov, M.Yu. Koptev, S.V. Muravyev, and A.V. Kim, *Optics Express*, 2012, **20**, 27102-27107.
6. E.A. Anashkina, A.V. Andrianov, M.Yu. Koptev, S.V. Muravyev, and A.V. Kim, "*Towards Mid-Infrared Supercontinuum Generation with Germano-Silicate Fibers*," IEEE Journal of Selected Topics in Quantum Electronics, 2014, **5**(20), accepted.

MULTIMILLIJOULE CHIRPED PULSE TAPERED FIBER AMPLIFIERS FOR COHERENTLY COMBINED LASER SYSTEMS

A.V. Andrianov[1,2], **E.A. Anashkina**[1,2], **A.V. Kim**[1,2], **I.B. Meyerov**[2], **S.A. Lebedev**[2], **A.M. Sergeev**[1,2], and **G. Mourou**[3]

[1] Institute of Applied Physics, Russian Academy of Sciences, Nizhny Novgorod, Russia,
[2] Nizhny Novgorod State University, Nizhny Novgorod, Russia
[3] DGAR-IZEST, Ecole Polytechnique, Route de Saclay, F-91128 Palaiseau Cedex, France

Abstract. We numerically investigated amplification of high energy chirped pulses in Large Mode Area tapered fiber amplifiers and their coherent combining. We developed a three-dimensional model of strongly chirped nanosecond pulse amplification and compression back to femtosecond duration fully taking into account transverse and longitudinal variations of refractive index profile and distribution of active ions in the fiber, wavelength dependence of emission and absorption cross sections, gain saturation and Kerr nonlinearity. About 3 mJ of output energy can be extracted in 1 ns pulse from the tapered amplifier with single-mode beam quality. We also numerically investigated possibilities of compression and coherent combining of up to 36 perturbed amplifying channels.

In this work we investigated applications of tapered fiber amplifiers for high energy coherently combined laser systems. Such a system utilizing thousands of chirped pulse fiber amplifiers which would finally deliver Joule level pulses at several kilohertz repetition rate compressed down to 200-300 fs duration is currently developed under ICAN project (International Coherent Amplification Network) [1]. Tapered (conical) active fibers have a strictly single mode core at the input that gradually expands up to several tens of microns and may be operated in effectively single mode regime, despite imperfect launching [2]. A three-dimensional numerical model of amplification of broadband nanosecond pulses with subpicosecond resolution in tapered fibers was developed on the basis of unidirectional wave propagation equation which includes diffraction, inhomogeneous refractive index distribution and third-order nonlinearity. The model of gain is based on phenomenological extension of semi-classical Maxwell-Bloch equations allowing inclusion of emission and absorption cross sections of real ions.

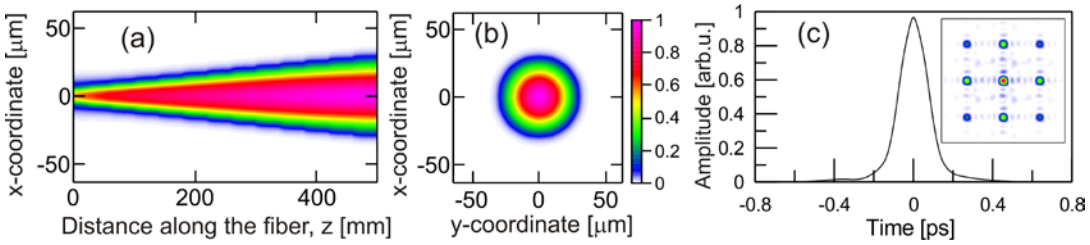

Fig. 1. Field distributions in the tapered amplifier: along the fiber (a), at the fiber output (b), temporal profile after combining and compression (c), far-field combined pattern (c, inset)

Amplification of 250 fs Gaussian pulses stretched to 1 ns in Yb-doped active fiber tapered from 10 μm to 60 μm is shown in Fig. 1(a, b). Modeling shows that single-mode propagation is maintained along the taper even in the presence of strong Kerr nonlinearity and saturated gain. Maximum output pulse energy with single mode quality obtained in the modeling is 1.7 mJ, and it can be further scaled up to 3 mJ by using 10–110 μm taper. Coherent combining of up to 36 amplifiers (arranged in 6x6 square grid) with random core perturbations leading to excitation of high-order modes was also modeled showing 88 % efficiency with respect to unperturbed amplifiers. The far-field pattern of combined beams is shown in Fig. 1(c) along with temporal field distribution of 380 fs compressed pulse. Despite noticeable high-order modes excitation in each individual channel, high quality of the combined output pulse is maintained.

References

1. G. Mourou, T. Tajima, B. Brocklesby, and J. Limpert, *Nature Photonics*, 2013, **7**(4), 258-261.
2. V. Filippov, Yu. Chamorovskii, J. Kerttula, K. Golant, M. Pessa, and O. G. Okhotnikov, 2008, *Optics express*, **16**(3), 1929-1944.

UPGRADE OF Nd:GLASS PUMP LASER FOR PETAWATT LEVEL PEARL FACILITY

K.F. Burdonov, A.P. Fokin, A.A. Shaykin, and **A.A. Soloviev**

Institute of Applied Physics of the Russian Academy of Science,
Nizhny Novgorod, Russia, kfb.iap@gmail.com

Abstract. This paper presents experimental study of an extremely-short spatial filter for multistage nanosecond pump laser of OPCPA-based petawatt-class PEARL laser facility. The degradation of pump radiation parameters associated with the filter induced spherical aberrations was investigated. The experiments showed that the spherical lenses based spatial filter does not lead to pump beam quality degradation paving the way to increase the energy of Nd:glass pump laser.

In modern petawatt level OPCPA laser facilities [1, 2] multistage neodymium glass amplifiers are typically used as a pump for final stages of parametric amplification and actually determine the output power of all facility. Thus, the objective of increasing the output laser pulse power is, in particular, an increase of the energy of neodymium pump amplifier. A typical Nd:glass amplifier consists of a line of active elements and spatial filters between them. The system of spatial filters (SF) is crucial in the pump laser with high intensity. Spatial filters perform filtering of the spatial spectrum high frequency components, block glares and take part in beam scaling during amplification to reduce the nonlinear effects in the active elements.

For 100 mm aperture radiation, the length of a nonaberrational spatial filter is about 4 meters. Shortening of the spherical lenses based telescope increases the aberration, especially spherical, this adversely affects the subsequent doubling ratio of the second-harmonic pulse amplitude distribution.

Since the number of filters in one channel can be more than ten, with an aperture of radiation greater than 100 mm, they actually determine the size of the entire laser system. Therefore, the problem of determining the minimum length of the spatial filter while maintaining the quality of the phase front and efficiency of frequency doubling is critical.

This paper presents an experimental study of the laser radiation parameters at the output of the 300 J multistage nanosecond pulse amplifier and the quality of subsequent frequency doubling in a KD*P-crystal depending on the length of the output spatial filter. Two spherical lenses based spatial filters with the lengths of 9 and 2 meters, with the same input and output apertures of 100 and 130 mm respectively, were compared. The longer telescope provided the diffraction quality of the transmitted radiation, the short one introduces significant spherical aberration of amplitude deviations up to 1.5 λ.

We investigated the influence of spatial filter spherical lenses aberrations on the transmission factor, radiation phase distribution, and the second harmonic conversion efficiency.

Optical scheme of the experimental setup is shown in Figure 1.

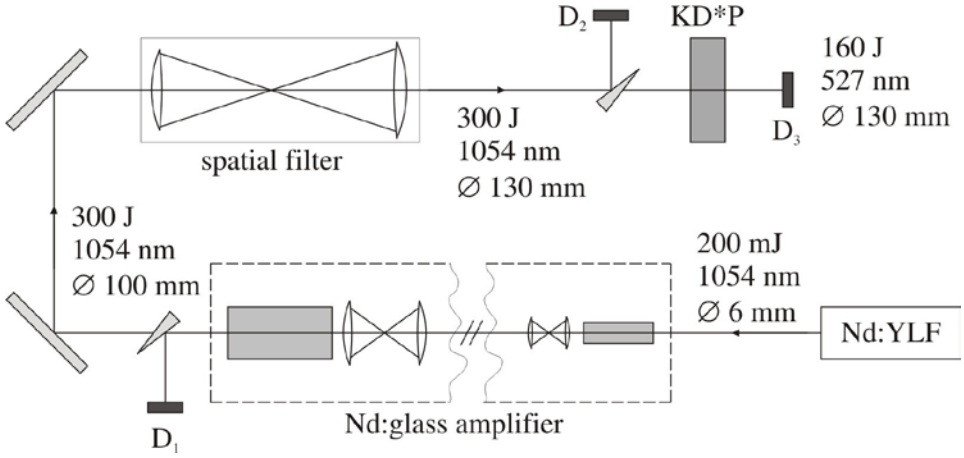

Fig. 1. Optical scheme of experimental facility

The Nd:YLF laser generates seed pulses with a duration of 1 ns and an energy of 200 mJ at a wavelength of 1054 nm [3]. Then a seed pulse enters a multistage amplifier consisting of the beam spatial structure formation system [4], and seven consecutive active elements made of neodymium

phosphate glass with diffraction-limited spatial filters between the elements. The active elements are pumped by broadband discharge lamps. The amplifier operates in one "shot" per 15 minutes. At the exit of the last active element of the amplifier, the laser pulse with a cross-section diameter of 95 mm acquires the energy of 300 Joules. The output spatial filter of the multistage amplifier increases the transverse beam diameter up to 122 mm. After the laser pulse amplifier, there is a nonlinear KD*P-crystal with a thickness of 25.5 mm for second harmonic generation. The facility is equipped with a laser beam diagnostic system before and after the output spatial filter and after the doubling crystal (D1, D2 and D3) for control of the radiation quality.

In order to take into account all the effects related to the ionization of the diaphragm, the spatial filters were studied at the best possible laser energy of 300 J.

Figure 2 shows the dependence of the frequency doubling efficiency on the incident pump energy in a DKDP-crystal. The accuracy of energy measurement is 7%.

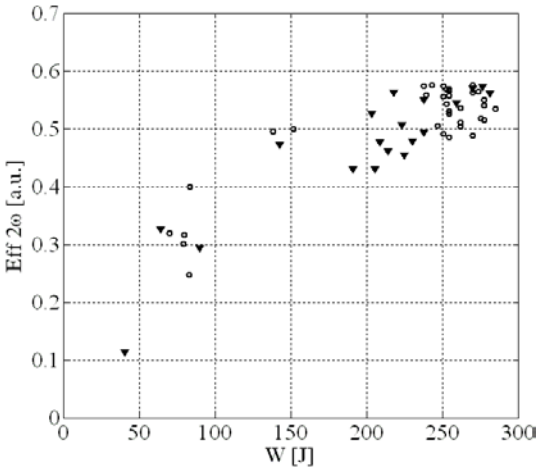

Fig. 2. The conversion efficiency of the output radiation of the second harmonic in the KD*P crystal for the diffractional SF (circles) and the aberrational SF (triangles)

We have also performed experimental study of a unique wide aperture 150 mm Nd:glass active element [5]. It has been shown that using this active element in the scheme of the pump laser can increase the energy of 300 joule pump laser beam of PEARL system up to 500 J and more.

The experiments showed that the use of a short aberrational spatial filter does not affect the frequency doubling coefficient compared to the case of long diffractional spatial filter, and also does not degrade the amplitude and phase quality of the second harmonic pulse. The space occupied by long diffractive spatial filters allows placing more short spatial filters. Thus, the use of short spatial filters with wide aperture active elements in multistage pump lasers will be able to significantly increase their energy and in the near future obtain the multipetawatt output power of OPCPA systems.

Acknowledgement

This work was supported in part by the Ministry of Education and Science of the Russian Federation under Contract No.14.Z50.31.0007.

References

1. V. Lozhkarev et al., *Laser Physics Letters*, 2007, **4**, 421-427.
2. A. Korzhimanov et al., *Phys. Usp.*, 2011, **54**, 9-28.
3. A. Poteomkin et al., *Quantum Electronics*, 2005, **35**, 10.
4. M. Martyanov et al., *Quantum Electronics*, 2008, **38**(4), 354-358.
5. A. Shaykin et al., *Quantum Electronics*, 2014, **44**(5), 426-430.

WIDE-APERTURE ROD LASER AMPLIFIER ON NEODYMIUM GLASS

A.P. Fokin, A.A. Soloviev, K.F. Burdonov, and **A.A. Shaykin**

Institute of Applied Physics of the Russian Academy of Sciences, Nizhny Novgorod, Russia
ap.fokin@mail.ru

Abstract. We present the test of the unique big-aperture rod laser amplifier with 150 mm diameter made of neodymium glass. The main results are the distribution of low-signal gain with mean value of 2.3, calculations of stored energy and pulse distortion.

Introduction

Wide-aperture rod amplifiers made of neodymium glass are widely used in high-power lasers [1]. Availability of active elements with a large aperture, high optical quality and high stored energy are the main advantages of Nd:glass. Large aperture optics allows one to amplify nanosecond pulses up to energies of a few kJ while keeping intensity of the laser beam below the breakdown value.

In high-power neodymium glass amplifiers, there are two types of active elements geometries - slabs and rods. This paper describes the test results of the unique rod amplifier made of neodymium glass with a diameter of 150 mm.

Amplifier

Laser amplifier is a cylinder of phosphate glass doped with neodymium ions placed in a pump chamber providing optical pumping of the active medium with flash lamps.

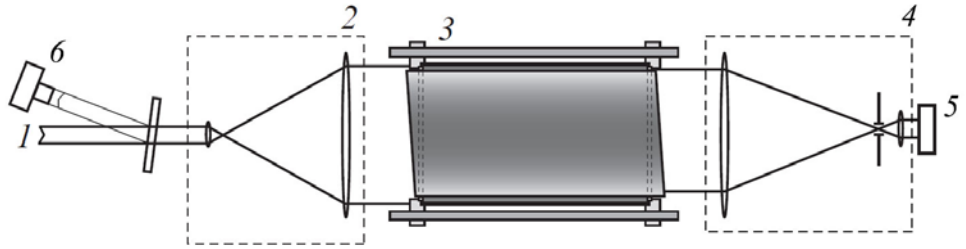

Fig. 1. Experiment scheme

Measurements of the gain have been performed according to the scheme shown in Fig. 1. Pulse energy at the entrance of the active element (3) was 2mJ with a duration of one ns and a quasi-homogeneous spatial intensity distribution. The amplified pulse was transferred to the camera (5) by the telescope; the spontaneous emission was filtered by the iris. The experimental distribution of the small-signal gain is shown in Fig. 2.

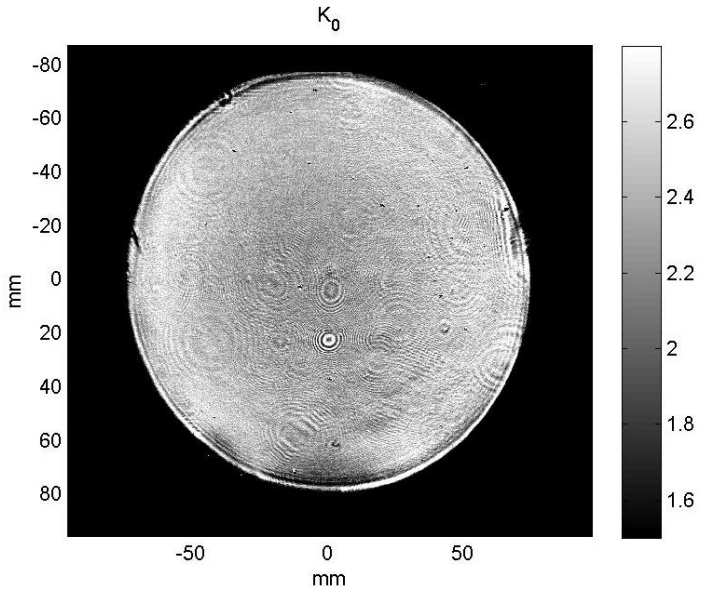

Fig. 2. Gain distribution

To estimate the effectiveness of practical application of the 150-mm laser amplifier we made numerical simulations of eight-stage pump laser of the petawatt OPCPA complex PEARL [2]. A 150-mm laser amplifier has been used as a final stage of the pump laser. In the simulations we used the experimental gain distributions. The model is based on solutions of balance equations obtained by Franz and Nodvik [3]. To calculate the absorption, the element was divided into layers with absorbing elements between them; the diffraction effects were not taken into account. Using the 150-mm laser amplifier, we could increase the pump pulse energy up to 540 J. Inhomogeneity of the pulse intensity will not exceed 10 % and the shift of the pulse maximum is not more than 5 %.

Conclusion

The unique 150-mm neodymium glass rod active element has been tested. It has been shown that using this active element in the scheme of the pump laser can increase the energy of the pump laser beam of PEARL system up to 540 J. It has been shown that pulse distortions will not affect the efficiency of parametric amplification.

References

1. A.K. Poteomkin et al., *IEEE J. Quantum Electron*., 2009, **45**, 854-863.
2. V.V. Lozhkarev et al., *Laser Phys. Lett.*, 2007, **4**, 421-427.
3. L.M. Frantz and J.S. Nodvik, *J. Appl. Phys.*, 1963, **34**(8), p. 2346.

OPTIMIZATION OF TEMPORAL PARAMETERS OF PETAWATT FEMTOSECOND PULSES BY XPW AND SPM TECHNIQUES

V.N. Ginzburg, E.A. Khazanov, A.A. Kochetkov and **S.Yu. Mironov**

IAP RAS, Nizhny Novgorod, Russia, vlgin@rambler.ru

Abstract. The investigation of linear and nonlinear optical properties of industrially produced thin plastic plates demonstrates good perspectives for implementation of this material for PW power pulse shortening by SPM and compression on chirped mirrors. The calculations show that the XPW technique can also be used for this purpose.

Self-phase modulation (SPM) and cross polarized wave generation (XPW) processes based on cubic nonlinearity in isotropic medium can be used for enhancing temporal parameters of high peak power lasers. SMP can be used for additional pulse compression on chirped mirrors of high peak power pulses after their spectrum broadening in nonlinear medium. XWP is widely used for temporal contrast clearing in double CPA schemes.

For SPM of high power pulses, thin plates of large aperture are needed. We have investigated optical properties of industrially produced thin plastic plates. It was shown that these elements have good linear optical quality. The study of nonlinearity was based on intense-pulse spectrum modification in plastic plates and its comparison with spectrum modifications in glass plates. The set of experiments demonstrated that for different values of B-integral, spectrum modifications in a 0.7 mm plastic plate qualitatively correspond to spectrum modifications in a 1.7 mm glass plate. In these experiments we have not observed any damage of plastic plates. So, this extremely cheap material is very promising for implementation of the SPM technique for high power pulse shortening.

The spectra observed in this set of experiments (both for plastic and glass) have a specific structure – narrow peaks and no broadening unlike the classical SPM of gaussian pulses. Our calculations have shown that such structure can be explained by the existence of noncompensated spectral phase terms of third order and higher due to the imperfect stretcher-compressor tuning. Nevertheless, after quadratic phase subtraction the power ratio increase with respect to the initial pulse weakly depends on the value of high-order spectral dispersion (see fig.1 curves 1 and 2).

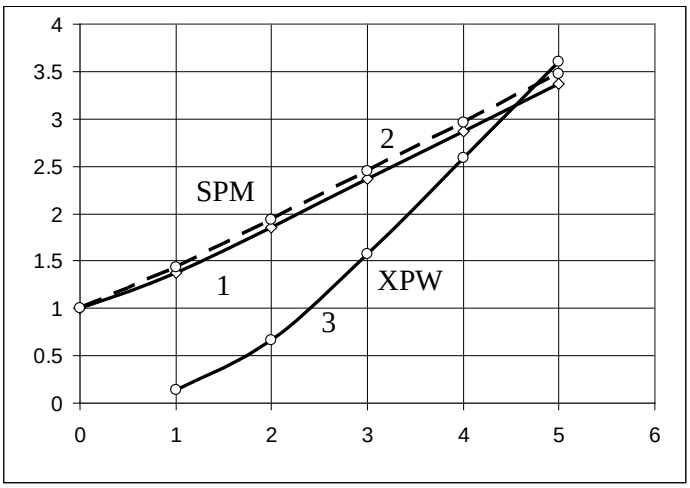

Fig. 1. Power ratio increase *versus* B-integral:
1. SPM of gaussian pulse, 2. SPM of non-FT limited pulse, 3. XPW of gaussian pulse in BaF2

The XPW technique was used, as a rule, for contrast filtering between amplification stages in double CPA schemes because of its rather low energy conversion efficiency (typically about 15 %) originating from space and time radiation heterogeneity. We propose to use the XPW process together with quadratic phase subtraction at the output of high power lasers, where space intensity distribution is quasi-uniform and intensity rather than energy is important for applications. Our calculations demonstrate that for a BaF2 crystal used for XPW generation after quadratic phase subtraction, the power ratio increase reached the same value of ~3.5 as for the SPM technique at B-integral value of 5 (see fig. 1 curve 3), keeping the contrast clearing property.

Invited

LUCIA LOW TEMPERATURE AMPLIFIER HEAD PERFORMANCE

T. Gonçalvès-Novo, B. Vincent, and **J.-C. Chanteloup**

LULI, Ecole Polytechnique, CNRS, CEA, UPMC ; Route de Saclay, 91128 Palaiseau, France
thierry.novo@polytechnique.edu

Abstract. Within the framework of LULI's Lucia DPSSL program, a low temperature amplifier head was developed to ramp up the energy to 30 J. This amplifier takes advantage of the benefits of the laser properties of Yb^{3+}: YAG at low temperature (around 100–200 K) for efficiency and thermal management. We will detail the prototype with particular emphasis on the laser gain medium cooling approach and present the latest performances achieved.

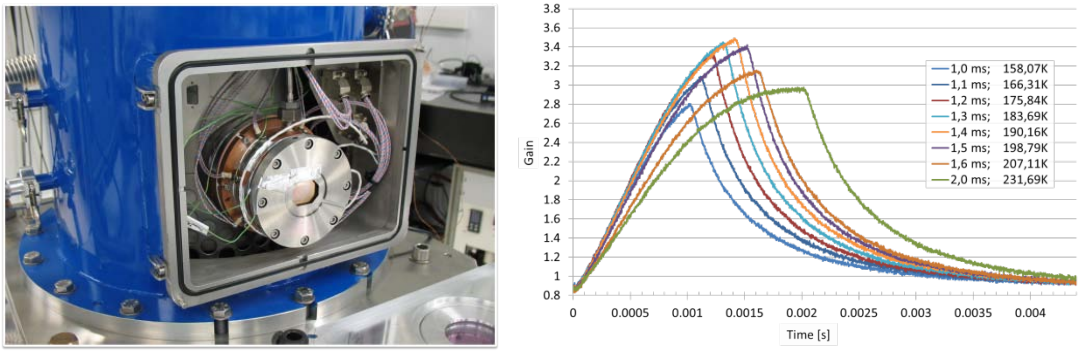

Fig. 1. The left picture displays a view of the low temperature laser head. The right sketch shows the single pass laser gain as a function of time for different pump pulse durations

THE PULSE CONTRAST OF THE MULTI-TW PHOSPHATE ND:GLASS LASER FACILTY

D.S. Gavrilov, A.G. Kakshin, and **E.A. Loboda**

Russian Federal Nuclear Center – Institute of Technical Physics,
Snezhinsk, Russia, dep5@vniitf.ru e-mail

Abstract. We report on the results of the phosphate Nd:glass laser facility pulse contrast investigation. All types of radiation before the main pulse arrival, having various geneses and the degree of influence on the target surface, are thoroughly studied. The measurements were carried out in all time intervals of interest with necessary resolution and dynamic range. A set of ultrashort prepulses in the chirp duration time interval (~ 1 ns), originating from the optical elements with parallel surfaces in the optical system, have been detected.

The facility is a CPA all phosphate Nd:glass laser. It delivers up to 20 J of on-target energy in a single-shot @ 1054 nm. In the time domain of recompressed pulses several types of pre-pulses are observed:

1. long-scale ASE (Amplified Spontaneous Emission);
2. short-scale ASE ($\tau \sim 10$ ns);
3. ultrashort ($\tau \sim 1$ ps) pre-pulse coming from a multipass regenerative amplifier;
4. ultrashort pre-pulses ($\tau \sim 1$ ps) generated by the self phase modulation from post-pulses;
5. leading edge of the recompressed pulse.

The first type of parasitic lasing is the output flash-lamp pumped rod amplifiers ASE, not isolated from the target by optical switches. It lasts up to 700 μs and contains substantial amount of energy that can pre-heat target surface or even destroy thin foils [1]. The main features of the long ASE pedestal are measured with Coherent Ultima Labmaster LM-P2 calorimeter and CCD camera. The detected ASE energy ≤ 10 μJ in a ∅130 μ spot resulted in $F_{ASE} \sim 0.07$ J/cm^2 of on-target fluence; the long ASE energy contrast ratio is $\geq 2 \cdot 10^6$. The minimum target thickness t may be estimated as

$$t \geq \frac{1}{T_M} \cdot \frac{\eta \cdot F_{ASE}}{c \cdot \rho},$$

where η is low energy absorption, T_M is melting point, c is thermal capacity, ρ is target density. For aluminum limited by long ASE, the target thickness is ~ 100 nm.

The short-scale ASE is part of ASE pedestal near the main pulse that cannot be cut by optical switches having ~ 4 ns rise time. It originates from the regenerative amplifier (RA) and its spatial parameters and small-signal gain are equal to the main pulse. The short ASE intensity level was measured by means of 1 GHz Tektronix oscilloscope and p-I-n photodiode (PD) with ≈ 0.5 ns time resolution. A plasma shutter prevented the PD damage. The intensity contrast ratio for this kind of prepulse ($\geq 3 \cdot 10^{13}$) is high due to the relatively large energy of the master oscillator picked pulse and small losses in the stretcher and RA.

The ultrashort pre-pulse coming from the regenerative amplifier 12 ns prior to the main pulse, has the intensity contrast ratio $\geq 2 \cdot 10^{11}$. It may be easily improved (if necessary) by introducing additional fast optical switches.

Ultrashort pre-pulses within chirped pulse duration time interval may be generated due to self-phase modulation (SPM) from post-pulses [2]. The sources of the post-pulses are optics with parallel surfaces in the laser channel. If a collinear stretched pulse and its replica overlap in time, their interference leads to temporal intensity modulations. The subsequent SPM of the modulated chirp in a nonlinear medium results in spectral phase aberrations. After recompression, a set of pre- and post-pulses appears with time intervals equal to the optical delay between the main pulse and its replica. The intensity of the pre-pulses is determined by the break-up integral (B-integral) and initial contrast ratio. Since the laser facility operates in a single-shot regime, scanning cross-correlator is not suitable for contrast measurements. We used a ~ 2 ps time resolution streak camera with a plasma shutter to record temporal history with enhanced dynamic range (~ 10^5). A number of pre-pulses have been detected in the temporal interval -1000…0 ps, all of them give rise to plasma formation. These prepulses may be completely eliminated: all plane-parallel optics is to be replaced by wedged-like elements. The post-pulses are cut after spatial filtering.

One of the most important features of a recompressed pulse is its leading edge that can significantly affect the state of plasma at the moment of arrival of the main pulse. The intensity and contrast ratio are degraded by spectral and spatial amplitude and phase aberrations arising from spectral clipping, misalignment in the stretcher and compressor, B-integral. Measurements of the leading edge profile were carried out by a third-order cross-correlator at a low energy level (~ 1 mJ) and a streak camera with a plasma shutter under nominal experimental conditions (~ 20 J). The intensity contrast ratios of 10^5 and 10^8 correspond to –20 ps and –60 ps time delays respectively.

References

1. K.B. Wharton, C.D. Boley, A.M. Komashko, et al., *Phys. Rev. E*, 2001, **64**, 025401.
2. N.V. Didenko, A.V. Konyashchenko, A.P. Lutsenko, et al., *Optics Express*, 2008, **16** (5), 3178-3190.

STUDY OF XPW-FILTER FOR TEMPORAL CONTRAST IMPROVEMENT OF PEARL LASER

A.A. Kochetkov and **V.N. Ginzburg**

IAP RAS, Nizhny Novgorod, Russia
antkoch2012@gmail.com

Abstract. We investigated the effect of generation of a cross-polarized wave (XPW) in relation to terawatt femtosecond laser pulses. On the basis of the written software code which simulates the process of XPW, a theoretical study in the temporal and spatial dimensions was performed. The generation efficiency in the laser system PEARL was estimated. It was shown experimentally that the efficiency of the XPW-process based on the front end of the complex can achieve 20%. We studied the modulation of the signal spectrum, the dependence of efficiency on the crystal's angle of rotation, and made more accurate estimates of the loss of efficiency in case of the off-axis crystal clipping. Also, different variants of schemes of installing the XPW-filter in the laser complex PEARL were developed.

With the development of lasers with petawatt power level, wide horizons for new research and applications are opened. Along with peak power, modern laser systems have strict requirements to temporal characteristics, such as duration and contrast.

This work is devoted to developing a method for improving the temporal contrast of the laser complex PEARL [1] constructed at the Institute of Applied Physics of the Russian Academy of Science (IAP RAS). Nowadays, there are several ways to improve the contrast of high-power laser pulses. The most common ones are the plasma mirror [2] and the method of the cross-polarized wave generation (XPW) [3]. One of the drawbacks of the plasma mirror is the fact that it is not reusable. This is associated with difficulties in applications because the element interacting with a high-power pulse should be under vacuum. That's why the XPW-method was chosen for contrast clearing in PEARL. XPW is based on a degenerate four-wave mixing process governed by the anisotropy of the real part of crystal's third-order nonlinearity tensor $\chi^{(3)}$, in which a new wave polarized in the orthogonal direction can be generated efficiently. Implementation of the XPW-method is quite straightforward: a linearly polarized laser pulse is focused into a crystal positioned between two crossed polarizers. Efficient conversion with XPW only occurs at high intensities. Weaker, unconverted pre- and post-pulses are thus rejected by the second polarizer, thereby improving the temporal contrast of the pulse.

In this work, using the software code simulating the process of generation we estimated the efficiency of XPW in relation to PEARL, analyzed the dependence of generation efficiency on crystal's angle of rotation and on B-integral. Also, losses associated with off-axis crystal cutting and presence of ellipticity of the input signal polarization were estimated. The experimental part was performed based on the front end of the laser system PEARL. The results correspond to the data of numerical calculations; maximum efficiency achieved with the use of a BaF_2 crystal [6] was about 20%, which is an acceptable value for the XPW-filter installation in the complex. Based on the results obtained in experiments we proposed installation schemes for the XPW-filter in the complex.

References

1. V. Lozhkarev, G. Freidman,V. Ginzburg, E. Katin, E. Khazanov, A.Kirsanov, G. Luchinin, A. Mal'shakov, M. Martyanov, O. Palashov, A. Poteomkin, A. Sergeev, A. Shaykin, and I. Yakovlev, *Laser Physics Letters*, 2007, **4**(6), 421-427.
2. G. Doumy, F. Quere, O. Gobert, M. Perdrix, P. Martin, P. Audebert, J.C. Gauthier, J.-P. Geindre, and T. Wittmann, *Phys. Rev. E*, 2004, **69**, 026402.
3. L. Canova, S. Kourtev, N. Minkovski, A. Jullien, R. Lopez- Martens, O. Albert, and S. M. Saltiel, *Appl. Phys. Lett.*, 2008, **92**, 231102.
4. V. Gordienko, P. Mikheev, and S. Syrtsov, *Bull. Russ. Acad. Sci.: Phys*, 2007, **71**, 122–125.

Invited

CRYOGENIC DISK YB:YAG LASER: STATUS QUO AND PERSPECTIVES

I.B. Mukhin, E.A. Perevezentsev, O.L. Vadimova, I.I. Kuznetsov, and **O.V. Palashov**

Institute of Applied Physics of the Russian Academy of Science,
Nizhny Novgorod, Russia, mib_1982@mail.ru

Abstract. A ytterbium doped, disk shaped "active mirror" is a most perspective design for high average and peak power lasers and advantages of disk lasers may be improved by cooling active elements to cryogenic temperatures. A high power cryogenic disk laser is currently under development at IAP RAS. Composite Yb:YAG/YAG disks with undoped cup are used to suppress amplified spontaneous emission and thermal distortions. The developed laser system emits more than 100 mJ of output energy in a 7 ns laser pulse at a repetition rate up to 1 kHz with ~1kW of pump power. The next amplification stage with 3 kW of pump is planned to increase the output energy to 1 Joule.

The increase of repetition rate is one of main topics of modern pulsed lasers. Due to effective heat removal, weak self-focusing and high optical efficiency, thin disk lasers may be excellent high average and peak power sources [1]. At present, output parameters of thin disk lasers have been reached multi-kW of average power or hundreds mJ of pulse energy at reduced duty circle of the pump [2, 3]. But a high pulse energy and, at the same time, a high repetition rate have not been demonstrated yet. One of perspective ways to solve this problem is cryogenic cooling of disk shaped active elements, which strongly improves their laser and thermooptical characteristics and allows increasing output energy to a multi-J range at a repetition rate near 1 kHz [4]. We report current results of cryogenic disk laser development at IAP RAS (Nizhny Novgorod, Russia). The main goal of this research is the demonstration of the advantages of cryogenic cooling for high capacity and high power sources.

The theoretical model of amplification in disk shaped active elements has been developed taking into account strongly nonuniform heat release, amplified spontaneous emission (ASE) and a multi-pass scheme of amplification. We have shown experimentally and theoretically that the ASE effect may be strongly reduced in composite active elements with undoped cup and cladding [5] and a new technique of thermal diffusion bonding has been developed to fabricate composite active elements with undoped cup [6]. Another difficulty in cryogenic lasers is boiling of liquid nitrogen at high pump power. Based on technologies of room temperature disk lasers, we are developing a cryogenic disk laser head with active micro channel cooling by liquid nitrogen (fig. 1). It has already generated more than 1 kW of pump power with negligible thermal distortions of the laser beam.

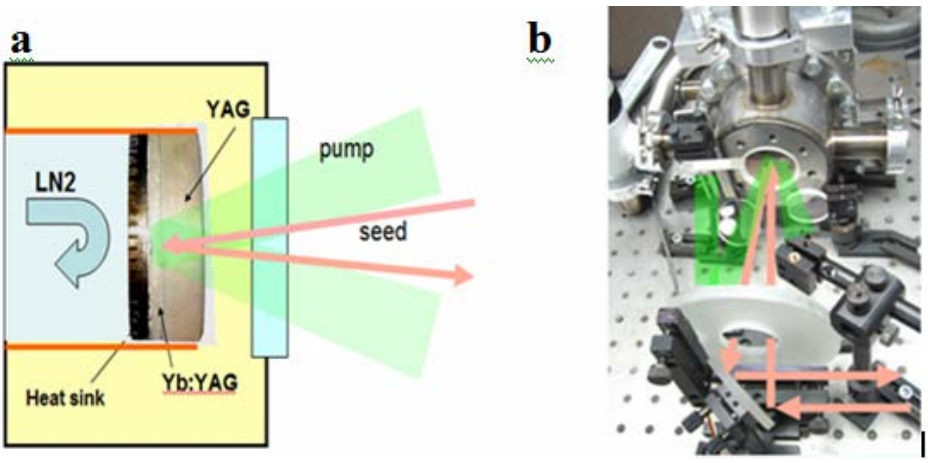

Fig. 1. Cooling scheme of Yb:YAG/YAG composite active element (a) and cryogenic disk laser head (b)

The current design of our laser system is described below. The seed laser system radiates a few mJ of output energy in 6 ns pulses at 1 kHz repetition rate. Next, the signal is amplified up to 30 mJ in the preamplifier based on the cryogenic disk laser head with 120 W pump power. Then, the signal is amplified in the main amplifier based on two cryogenic disk laser heads with composite active elements 20 mm in diameter. The total pump power ~ 2.4 kW for two laser heads is available in the main amplifier, and the pump beam diameter is 10 mm. Up to 0.14 J at 0.4 kHz is achieved currently at half of pump power used with a duty circle reduced by a factor of 2 (fig. 2a). The output pulse duration of 7 ns with spectrum width ~ 0.7 nm has been obtained. The main limitation on the output

energy is parasite lasing caused by strong ASE (fig. 2b). The plots for pump and luminescence intensities are shown in fig. 2b at different pump power in the cryogenic disk laser head used in the main amplifier. Strong saturation of luminescence is observed at pump power ~ 600 W (red curve in fig. 2b) and more, indicating parasite lasing in the sample. Composite active elements with undoped cup and cladding are under development now to suppress this effect. The output energy at CW pump mode is close to the output in the pulsed pump mode and 80 mJ is achieved at 1 kHz repetition rate of output pulses (fig. 2a).

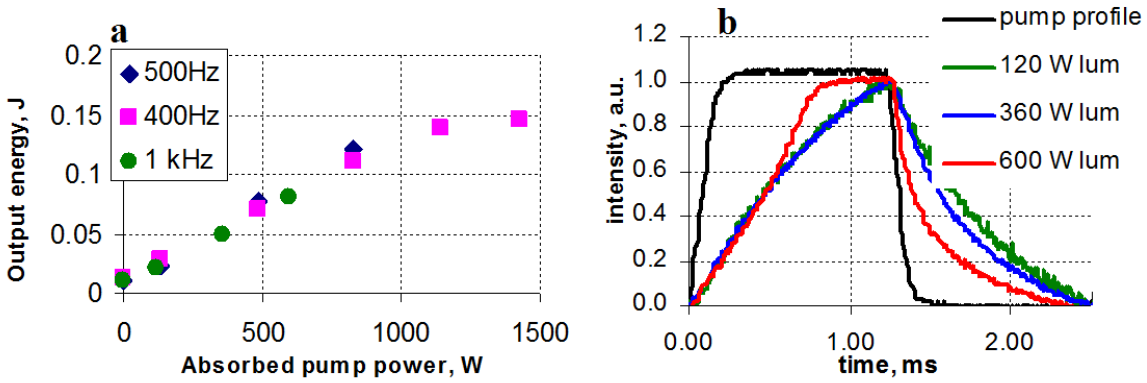

Fig. 2. The dependence of output energy on pump power at different repetition rates of output pulses (a) and temporal profiles of normalized pump and luminescence intensities (b)

A powerful picosecond laser for OPCPA applications will be developed based on the achieved results. A fiber femtosecond laser will be used as a seed source. One part of a seed signal will be used for further amplification in cryogenic disk amplifiers up to 1 Joule and the next amplification stage is under development now. The maximum pump power in the new cryogenic amplifier will exceed 3 kW with pump beam diameter ~ 20 mm. Another part of the femtosecond signal will be used for more careful adjusting of cryogenic disk laser output parameters from the point of view of OPCPA amplification.

References

1. J. Speiser, “Thin disk laser–Energy scaling”, *Laser Physics*, **19**(2), 274-280.
2. Y.H. Peng, Y.X. Lim*, J. Cheng, Y.B. Tan, E. Lau, and K.S. La, “Multi-kW High Brightness Yb:YAG Thin Disk Laser”, Proc. of SPIE, 2013, **8599**, 85991B.
3. M. Siebold, M. Loeser, U. Schramm, J. Koerner, M. Wolf, M. Hellwing, J. Hein, K. Ertel, “High-efficiency, room-temperature nanosecond Yb:YAG laser”, *Optics Express*, 2009, **17**(22), 19887.
4. E.A. Perevezentsev, I.B. Mukhin, I.I. Kuznetsov, O.V. Palashov, E.A. Khazanov, "Cryogenic disk Yb:YAG laser with 120-mJ energy at 500-Hz pulse repetition rate", *Quantum Electronics*, 2013, **43**(3), 207-210.
5. O.L. Vadimova, I.B. Mukhin, I.I. Kuznetsov, O.V. Palashov, E.A. Perevezentsev, E.A. Khazanov, "Calculation of the gain coefficient in cryogenically cooled Yb:YAG disks at high heat generation rates", *Quantum Electronics*, 2013, **43**(3), 201-206.
6. I.B. Mukhin, E.A. Perevezentsev, O.V. Palashov, “Fabrication of composite active elements by a new thermal diffusion bonding method”, *Optical Materials Express*, 2014, **4**(2), 266-271.

Invited

HIGH AVERAGE POWER LASER FROM YB:YAG THIN-DISK AMPLIFIERS AND ITS APPLICATIONS

Yo. Ochi, K. Nagashima, M. Maruyama, M. Tsubouchi, F. Yoshida, and **A. Sugiyama**

Japan Atomic Energy Agency, Kizugawa, Kyoto, Japan, ochi.yoshihiro@jaea.go.jp

Abstract. We developed a high average power picosecond laser based on the chirped pulse amplification technology using Yb:YAG thin-disk amplifiers. The Yb:YAG thin-disk regenerative amplifier at room temperature provided 10 mJ pulses at the repetition rate of 1 kHz. The spectrum after the regenerative amplifier has Gaussian shape with FWHM width of 1.2 nm. The pulses were recompressed to be 1.3 ps. By employing this picosecond pulse as a pump source, a THz pulse at the center frequency of 0.3 THz with micro joule class energy has been obtained by the optical rectification in Mg-$LiNbO_3$ crystal.

High average power picosecond laser system

The Yb:YAG is a very attractive medium for high average power picosecond lasers owing to its suitable emission bandwidth, long fluorescence life time (~ 1ms), small quantum defect, and good thermal properties. The thin-disk geometry is also preferable for high average power operation due to a good cooling efficiency provided by a high surface-to-volume ratio [1, 2]. In this study, we have developed a picosecond laser with 10 mJ energy and 1 kHz repetition (average power ~10 W) based on the chirped pulse amplification using a Yb:YAG thin-disk amplifier.

A schematic diagram of the laser system is shown in Fig. 1. The system consists of a master oscillator, a pulse stretcher, a fiber pre-amplifier, a regenerative amplifier, and a pulse compressor. The master oscillator is a mode-locked Ti:Sapphire laser operating at the central wavelength of 1030 nm with band width of 6 nm. The laser frequency is 80 MHz and the power is 200 mW. The pulse stretcher with a reflection grating gives a chirp of 400 ps/nm to each pulse. The throughput power from the pulse stretcher is 65 mW. The pulse energy is amplified up to 2 W in a laser diode pump Yb-doped fiber amplifier. Then 1 kHz pulses are picked up by an optical shutter consisting of Pockels cell and half wave plate picks. Then the pulses are injected into the regenerative amplifier. Here the input pulse energy is approximately 10 nJ. The amplification medium is 7 at.% doped Yb:YAG ceramic thin-disk with 0.2 mm thick and 10 mm diameter mounted on a water cooled copper heat sink. The thin-disk is wedged at an angle of 0.1 degree in order to prevent interference in the cavity due to unwanted reflections. The front side and the back side are anti-reflection (AR) and high-reflection (HR) coated, respectively, for both pump and laser wavelengths. The pump light is 940 nm laser extracted from the laser diode coupled with a fiber of 400 μm core diameter.

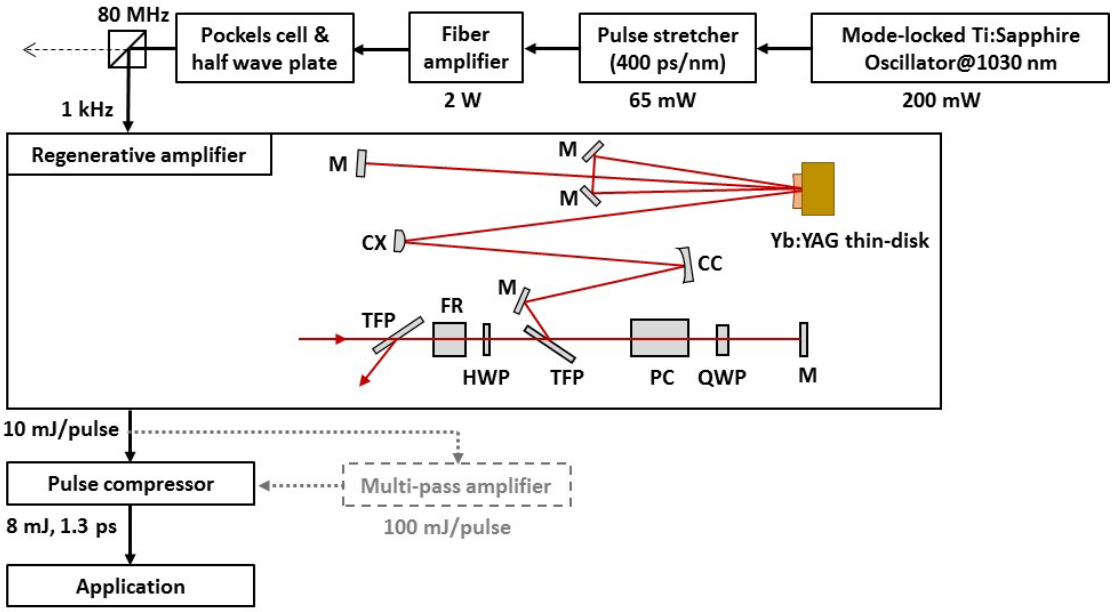

Fig. 1. Schematic diagram of the laser system. TFP: thin film polarizer, FR: Faraday rotator, HWP: half wave plate, QWP: quater wave plate, PC: Pockels cell, M: plane mirror, CC: concave mirror, CX: convex mirror

Pump light exciting the fiber is imaged on the thin-disk with a spot diameter of 2.5 mm and then folded 24 passes by a parabolic mirror and reflecting prisms. The cavity is configured so that the seed laser passes through the gain region 8 times (4 bounces) per a cavity round trip. The beam sizes on the thin-disk are designed to be 2.0 mm at the $1/e^2$ intensity. At a pump power of 100 W, the seed laser energy is reached to be 10 mJ by around 40 round trips. After the regenerative amplifier the spectral shape of the laser has a nearly Gaussian shape with the FWHM bandwidth of 1.2 nm. The laser pulse is recompressed to be 1.3 ps, which is almost Fourier transform limit duration, in the pulse compressor with a pair of gold coated gratings of 1740 grooves/mm. With the throughput efficiency of 0.8, 8 mJ, 1.3 ps, 1 kHz pulses are delivered from the system and are in operation now. In the near future, we will increase the pulse energy up to 100 mJ by adding a 1 kW pumped Yb:YAG thin-disk multi-pass amplifier after the regenerative amplifier.

THz generation

By employing the 1.3 ps pulse as a pump, we acieved the THz pulse generation by the optical rectification in a Mg doped stoichiometric $LiNbO_3$ crystal [3]. The THz waveform was measured by the electro-optical (EO) sampling method. In order to obtain the precise THz waveform, the EO probe pulse should be shorter than THz pulse duration and temporally synchronized with the pump. Therefore we made a 200 fs probe pulse from a 1.3 ps pump pulse as follows; firstly, the light leaking through the HR mirror was picked up. Then the light was injected into the optical fiber to broaden the spectral band by the self-phase modulation. The broadened pulse was recompressed by a transparent grating pair. The measured THz waveforms by 1.3 ps and 200 fs probe pulses are shown in Fig. 2 (a). The THz spectra derived from the Fourier transform of the temporal waveform shown in Fig. 2 (b), indicate that the center frequency is 0.3 THz. Currently a THz energy of 1.5 μJ was obtained with the pump energy of 3.6 mJ.

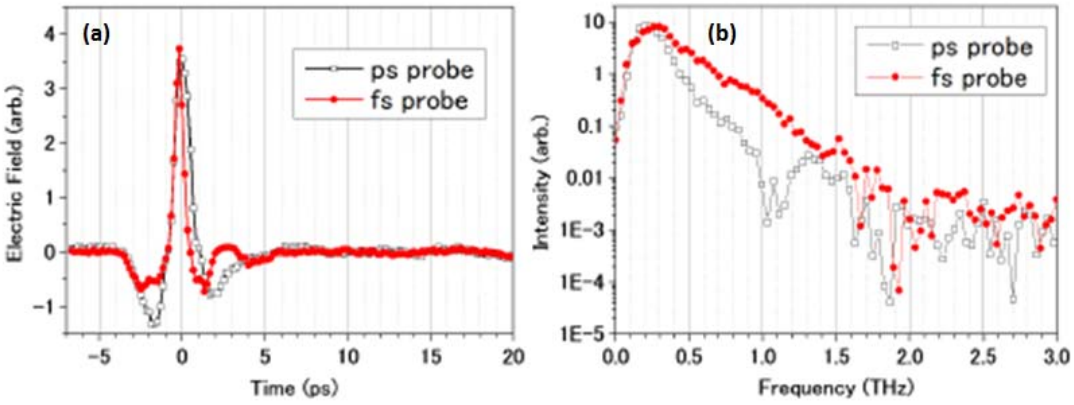

Fig. 2. Measured THz waveforms (a) and Fourier transformed spectra (b).
Open square and solid circle indicates data obtained by 1.3 ps and 200 fs probe pulses, respectively

Acknowledgements

This work was supported by the "*Consortium for Photon Science and Technology*" program promoted by MEXT, Japan.

References

1. C. Hönninger, I. Johannsen, M. Moser, G. Zhang, A. Giesen, and U. Keller, *Appl. Phys. B*, 1997, **65**, 423-426.
2. A. Killi, I. Zawischa, D. Sutter, J. Kleinbauer, S. Schad, J. Neuhaus, and C. Shmitz, *Proc. SPIE*, 2008, **6871,** 68710L.
3. J. Hebling, G. Almási, I.Z. Kozma, and J. Kuhl, *Opt. Express*, 2002, **10**, 1161-1166.

Invited

J-KAREN LASER UPGRADE AND PERSPECTIVES

A.S. Pirozhkov, H. Kiriyama, M. Mori, M. Nishiuchi, Y. Fukuda, H. Kotaki, K. Ogura, A. Sagisaka, H. Sakaki, Y. Hayashi, A. Kon, M. Kanasaki, T.Zh. Esirkepov, J.K. Koga, S.V. Bulanov, P.R. Bolton, T. Kawachi, M. Kando, and **K. Kondo**

Kansai Photon Science Institute, Japan Atomic Energy Agency, Kizugawa, Kyoto, Japan
pirozhkov.alexander@jaea.go.jp

Abstract. J-KAREN is a state-of-the-art high-power laser with hybrid OPCPA/Ti:Sapphire, double CPA architecture. Due to high temporal and spatial beam quality, the on-target intensity exceeds 10^{21} W/cm^2 with an f/2 focusing. The temporal contrast is high enough for shooting 1 μm foils without plasma mirrors. These allowed us to demonstrate proton acceleration up to energies exceeding 40 MeV and Al ion acceleration up to 320 MeV (12 MeV/nucleon). We present the current laser performance, recent experimental achievements, and the upgrade plan to achieve the on-target peak power of 1 PW and repetition rate of 0.1 Hz.

J-KAREN laser system

The J-KAREN laser [1] is a hybrid OPCPA/Ti:Sapphire laser employing double CPA architecture. It consists of a commercial CPA Ti:Sapphire laser system (Femtolasers, FemtoPower Compact Pro), stretcher, OPCPA preamplifier, three multi-pass amplifiers (pre-amplifier, power amplifier, and booster amplifier), and vacuum compressor. The laser features a number of innovations. In particular, the temporal contrast is enhanced with the double CPA scheme, AOPDF system, OPCPA preamplifier, two saturable absorbers, and ultrafast Pockels cell; the thermal lensing is removed by cryogenically cooling the power amplifier; the pumping beam profiles are improved with diffractive optics; the transverse lasing in large-aperture Ti:Sapphire crystal is controlled with an index-matching liquid; the long-term stability is ensured with several automatic beam alignment systems. The J-KAREN laser provides on-target peak power of up to 250 TW, high beam quality allowing focusing to ~2–3 μm spot and achieving intensity exceeding 10^{21} W/cm^2 using a f/2 off-axis parabola, and a possibility of daily operation during long experimental campaigns. All these made possible several discoveries and pioneering experiments, some of them are described below.

Proton and ion acceleration experiments

The temporal contrast of the laser pulses is high enough to employ ~1 μm thick foil targets without plasma mirrors. Thus, the pulse energy and beam focusability are preserved up to the target, and easily accessible target systems like tape driver can be used. Using only ~7 J pulse energy at the power of 200 TW and intensity exceeding 10^{21} W/cm^2, we demonstrated proton acceleration up to 40 MeV [2], which at that time significantly surpassed the previous long-standing record achieved with 10 J pulse energy (24 MeV) [3]. We also demonstrated Al ion acceleration up to 320 MeV (12 MeV/nucleon) [4].

High-order harmonics from relativistic electron spikes

We discovered a novel regime of high-order harmonic generation by multi-TW femtosecond lasers in gas jet targets [5]. In this regime, comb-like spectra with hundreds of even & odd harmonic orders reaching the 'water window' spectral range are generated by either linearly or circularly polarized pulses. The harmonics are generated by sharp, structurally stable, oscillating electron spikes at the joint of the wake wave and bow wave boundaries.

J-KAREN-P upgrade plan

These achievements allowed us to get funds for the major facility upgrade which is now underway. In particular, we will increase the repetition rate up to 0.1 Hz and on-target peak power up to 1 PW, Fig. 1 [6]. The beam diameter will be increased up to 25 cm, with the corresponding replacement of the pulse compressor, beamlines, and two experimental chambers. Major efforts will be devoted to the achievement of high wavefront quality, absence of angular chirp, good temporal compression, and ultrahigh contrast. We will also pay particular attention to the infrastructure required for efficient laser use in advanced experiments, including precision alignment techniques, auxiliary laser beams, monitors, etc. The upgraded laser, J-KAREN-P, will be first used for proton acceleration up to energies exceeding 100 MeV [7] and coherent keV x-ray generation.

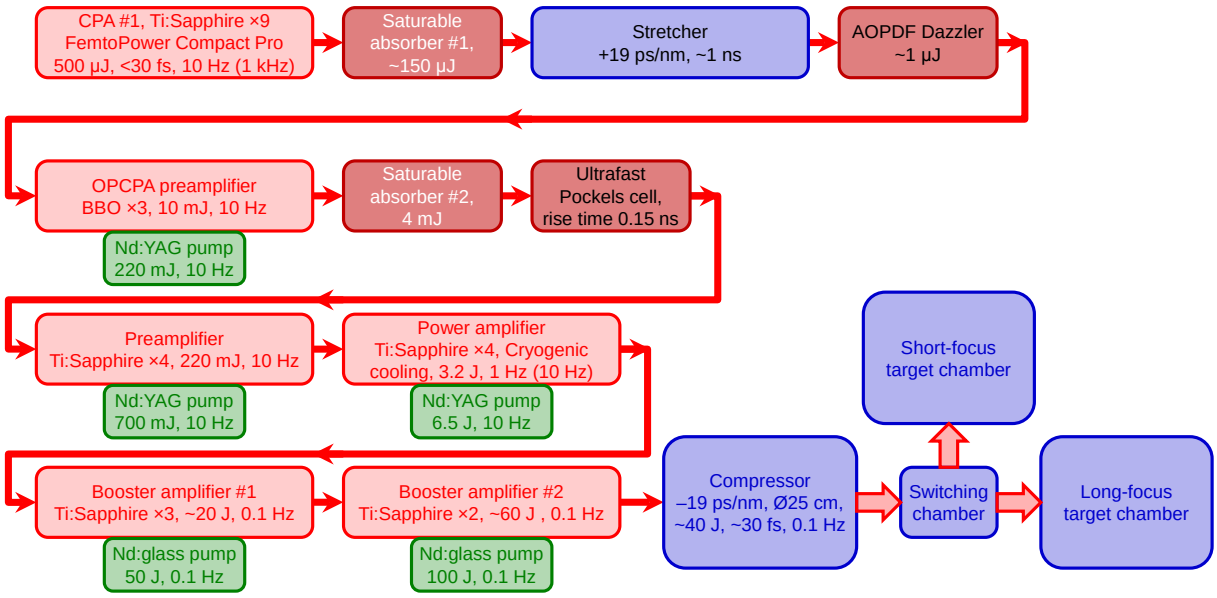

Fig. 1. Schematic of the J-KAREN-P laser system [6]

Acknowledgements

We are grateful to H. Okada, M. Tanoue, S. Kondo, S. Kanazawa, Y. Nakai, T. Shimomura, M. Okamoto, K. Torimoto, and T. Sato for the excellent technical support. We acknowledge financial support from the Ministry of Education, Culture, Sports, Science, and Technology of Japan (MEXT) (Supplemental Budget and Kakenhi 23740413, 25287103, 25390135, and 26707031).

References

1. H. Kiriyama et al., *Appl. Sciences*, 2013, **3**, 214-250.
2. K. Ogura et al., *Opt. Lett.*, 2012, **37**, 2868-2870.
3. A. J. Mackinnon et al., *Phys. Rev. Lett.*, 2002, **88**, 215006-4.
4. M. Nishiuchi et al., *Rev. Sci. Instr.* 2014, **85**, 02B904-3.
5. A.S. Pirozhkov et al., *Phys. Rev. Lett.*, 2012, **108**, 135004-5.
6. H. Kiriyama et al., (submitted) *IEEE J. Quantum Electron.*
7. T.Zh. Esirkepov et al., *Nucl. Instr. Methods Phys. Res. Sect. A*, 2014, **745**, 150-163.

Invited

HIGH ENERGY/INTENSITY LASERS FOR HED SCIENCE AT EUROPEAN XFEL

G. Priebe[1,2], M. Nakatsutsumi[1], I. Thorpe[1], B. Mueller[3], A. Pelka[1,4], K. Appel[1], Th. Tschentscher[1], and **Max Lederer[1]**

[1]European XFEL, Germany
[2]High Field Laser Consultants Ltd., UK
[3]Laboratoire pour l'Utilisation des Lasers Intenses, France
[4]Helmholtz-Zentrum Dresden-Rossendorf, Germany

Free-electron laser facilities provide new applications in the field of high-pressure research including planetary materials. The European X-ray Free Electron Laser (XFEL) in Hamburg will start user operation in 2017 and will provide photon energies of up to 25 keV. With a photon flux of about 10^{12} photons/pulse, with a pulse duration of 2–100 fs and a repetition rate of up to 4.5 MHz during 600 µs long bursts with a repetition rate of 10 Hz, rendering up to 27000 pulses per second, this facility will provide unique opportunities to study material under extreme conditions. The high-energy density science instrument (HED) is one of the six baseline instruments at the European XFEL. It enables the study of dense material at strong excitation and high pressures, studying structural and electronic properties of excited states with hard x-rays. Besides the use of the x-ray FEL beam as a possible pump and/or probe, it will be equipped with a high contrast PW-class ultra-high power, a temporal shaped ultra-high energy, KJ-class and amJ-class MHz repetition rate, matching the X-ray burst structure, laser facility. Probing of the laser-generated excited states will be performed with the x-ray free electron laser.

REGISTRATION OF SPATIO-TEMPORAL PROPERTIES OF ULTRASHORT LASER PULSES IN HIGH-POWER MULTICHANNEL FACILITIES

G.S. Rogozhnikov[1], V.V. Romanov[1], S.A. Bel'kov[1], M.Ya. Schelev[2], N.S. Vorobyev[2], and **P.B. Gornostaev[2]**

[1] FSUE "RFNC-VNIIEF", Sarov, Russia, g.s.rogozhnikov@mail.ru
[2] GPI RAS, Moscow, Russia

Abstract. In order to efficiently apply laser radiation of multichannel laser facilities in experiments concerning fast processes diagnostics in dense hot plasma, accurate information about spatio-temporal properties of laser pulses is required. One of the most promising solutions is using high-speed streak cameras. This paper deals with methods of laser beams alignment on the target, experimental results on measuring ultrashort laser pulses properties are discussed.

Introduction

For efficient application of high-energy radiation in experimental physics, including interaction of such radiation with matter, high-temperature plasma in the course of laser-fusion experiments, etc. it is important to know precise information on spatial-time behavior of picosecond laser pulses at each point along the whole optical path of this multichannel laser facility, as well as separation of single laser pulses from each other in space and time [1].

The Institute for Laser Physics Research at FSUE "RFNC-VNIIEF" runs several high-power multichannel laser facilities and single-channel short-pulse laser facilities such as TW-class 12ch. ISKRA-5 and 4ch. LUCH facilities, a TW-class 1ch.PICO and a PW-class 1ch. FEMTO facility [2–4]. They all may need a precise diagnostic system that will be capable not only to provide the spatial-temporal measurements with picosecond and ten-microns precision but which will be easily integrated into a digital computer system controlling the operation of the whole laser system.

One of the suitable solutions is to use ultrafast image-converter streak cameras providing accurate measurements of laser radiation within the spectral range from soft x-ray radiation (0.1 nm) up to near IR (1.6 μm) with sub picosecond time resolution and tens of microns (≥30 line pairs/mm) spatial resolution and capable of being integrated into any digital control system of a multichannel laser facility.

A PS-1/S1 picosecond streak camera designed by GPI RAS was tested for time –space resolved measurements of ultrashort laser pulses generated by the FEMTO petawatt laser facility.

Experiments

In order to see all laser pulses hitting the target in the alignment purposes the streak camera must watch the target from a rather long distance of half to several meters. So a wide-aperture telescopic system is needed to gather the light scattered by the target. To simplify the challenge, a single-channel FEMTO 100 fs-pulse facility was used in preliminary experiments with a beam divided into several spatially and time-shifted beams.

For this purpose a 15mm and a 1 mm thick plane -parallel glass (K-8 type) plates were installed on the input streak camera slit (at half of its length). Thus the calibrated time delay between two parts of the same beams was equal to 25ps and 1.66 ps, correspondingly. The PS1/S1 streak-camera recorded chronogram and its corresponding microdensitometry trace which were obtained during present experimental tests were perfectly resolved at streak speed of about 160fs/pixel.

Another set of the experimental tests was devoted to measure the PS-1/S1 streak camera ultimate time-response function. The best camera response function (FWHM) was equal to 1.1ps (6.99pixels). The autocorrelator trace reveals ~ 100fs pulse duration for this particular experiment.

Conclusion

Thus, on the basis of the experimental results obtained during the PS-1/S1 streak camera tests at FEMTO laser installation it is possible to make the following conclusions:

– PS-1/S1 streak camera is quite capable of measuring single laser pulses of approximately one picosecond duration, as well as a train of single laser pulses separated by not less than one picosecond from each other.

- PS-1/S1 streak camera may be also used for delay monitoring of single picosecond laser pulses irradiating a target to control spatial distribution of laser radiation incident on the target.
- Due to a large range of PS-1/S1 streak velocities, such a camera may be also used to record laser pulses of nano and sub-nano durations, which permits using this camera to control slow high-power channels of multi-channel laser installations.

References

1. G. Rogozhnikov, R. Kostyunin, N. Rukavishnikov, and I. Mishina, *Lasers Measur.*, 2012, 134-137.
2. V. Annenkov, V. Bezuglov, A. Bessarab et al., *Quantum Electron.*, 2006, **6**(36), 508.
3. S. Garanin, A. Zaretskii, R. Ilkaev et al., *Quantum Electron.*, 2005, **4**(35), 299.
4. S. Garanin,V. Romanov, I. Ryzhov et al., *Proc. 2nd All-Russian School on Las.Phys. and Tech.*, Sarov, 2008, 228-236.

PETAWATT LASER SYSTEM FOR HIGH-SPEED PROCESSES DIAGNOSTICS IN DENSE HOT PLASMA

V.V. Romanov, S.A. Belkov, and **S.G. Garanin**

RFNC–VNIIEF, Sarov, Russia

Abstract. The paper deals with the project concerning the development of a petawatt multi-channel laser system for high intensity physics processes research using laser plasma electromagnetic fluxes created by intensive ultra-short laser pulses with high temporal resolution.

Introduction

Construction of the megajoule laser facility was recently started in Russia [1]. This paper deals with the construction of a multi-channel petawatt laser system based on the 4-channel "Luch" facility [2] that will serve as a prototype of the diagnostic system for the future megajoule laser facility. The system is designed according to the CPA principle (Chirped Pulse Amplification) using a chirped pulse directly amplified by neodymium amplifiers, and will generate from one to four pulses with 1 kJ energy at 1054 nm wavelength. The goal of the project is to develop a diagnostic system that will be used to study fast-going processes related to the physics of high energy densities with high temporal resolution, with pulses of X-ray radiation of laser plasma generated by the intense ultra-short laser pulses. The key components of the system to be developed and practiced are: phase and amplitude control of the wideband laser pulse spectrum; amplification of the chirped pulse in parametric pre-amplifier and primary amplifier based on neodymium phosphate glass; remote data control and collection; mutual synchronization of several laser pulses; regulation of wave trains in the range from 10 to 100 ps; development and practicing of focusing methods, etc.

The principles underlying the design of a laser system

The design of a prospective petawatt laser system used to diagnose fast-going processes in hot dense plasma is stipulated by the need for spectral correction of wideband laser pulse, as well as by pre-amplification in the non-linear parametric light amplifier, direct amplification of the chirped pulse in neodymium phosphate glass and temporal pulse compression inside laser compressor, based on integral or composite diffraction gratings.

A multi-channel petawatt laser system works according to the following algorithm: generation of a short laser pulse ($\tau \sim 250$ fs); its stretching; amplification in pre-amplification cascades; division into the required number of beams from 1 to 4; amplification in laser channels of "Luch" facility and temporal compression in laser compressor up to $\tau \sim 1$ ps. The laser beam at each of the four channels outputs will have the aperture of 20×20 cm. Each of the beams will be passed through its own laser compressor. Each of the four compressors will generate one ultra-short pulse that will irradiate the auxiliary target located close to the object under study.

The basic parameters of the multi-channel petawatt laser system used to diagnose fast-going processes in hot dense plasma are central wavelength: 1054 nm; controllable pulse duration: 1–50 ps; number of laser beams: 1-4; radiation energy per each pulse: 1000 J; radiation divergence: 5×10^{-5} rad; focal length of off-axis mirror: 0.8 m; intensity of laser radiation at the supplementary target: $\geq10^{18}$ W/cm^2 per each beam at 1 ns laser pulse duration.

Super-powerful ultra-short laser pulse irradiates the supplementary target and generates a short ($\tau_{X\text{-}ray} < 10$ ps) pulse of hard X-ray radiation which penetrates through the object under study. Records of 2-D image of the object allow restoring density distribution inside the object. Time sweep of gas-dynamic flow in plasma of the object is made when the train of super-powerful ultra-short laser pulses is formed with the adjustable interval of pulses sequence (10–100 ps), which correspondingly irradiate the supplementary target. To diagnose fast-going processes in the object under study the authors propose to use linear X-ray radiation with $h\nu \sim 5$–40 keV energies (lines K_α, Sn, Dy) [3] or the continuous spectrum.

The method known as radiography (proton or X-ray ones, depending on which radiation is involved) is actively applied at the NIF facility as an individual sub-system named ARC (Advanced Radiography Capability) [4], at Z-accelerator (Sandia National Labs, USA) [3] and at LMJ facility under construction as a diagnostic sub-system named PETAL (Petawatt Aquitaine Laser) [5].

In order to obtain an ultra-short pulse at laser compressor output it is necessary to preserve its form and spectrum width, corresponding to duration of the pulse at the output of the system. A method of wideband acceleration fits well for this purpose, which is based on parametric light amplifiers and is successfully applied in RFNC-VNIIEF at super-powerful laser facility "Femto" [6]. However, these methods are still technologically too sophisticated and costly for the lasers with a large beam aperture. That is why in our system we will use the principle of parametric amplification of wideband chirped pulses only at pre-amplification stage (from several nano-joules to tens of milli-joules) [7].

We will use the neodymium glass amplifier of "Luch" facility as the main amplifier. Since the amplification band in neodymium phosphate glass is not wide enough to uniformly amplify the wideband pulse, the pulse spectrum at the output is narrowed and changed, which, in its turn, results in the distorted time form of the pulse after it has been compressed. Several methods to widen the effective amplification band of neodymium amplifiers are available [8, 9]. The promising method to save and broaden the pulse spectrum during amplification is to use the adaptive control of individual frequencies (spectral components) of the laser pulse, so it will be used in the laser system presented in this paper. A handy instrument for changing the spectrum of the chirped pulse being amplified is the acousto-optical light dispersive delay line (LDDL) [9]. This apparatus is developed jointly by ILFI RFNC-VNIIEF (Sarov), Acousto-Optical Research Center NUST MISIS (Moscow) and the Moscow Engineering Physics Institute (Moscow). Experimental research carried out with the help of LDDL on spectral correction of chirped laser pulses in an Nd-doped phosphate glass regenerative amplifier (RA) were characterized by high gain ((~ 4×107) [10].

The factors that limit the output power of the laser system are radiation resistance and the dimension of diffraction gratings of the laser compressor. The laser compressor optical scheme based on four parallel reflecting diffraction gratings will be implemented [6]. In our laser system multi-layered dielectric (MLD) gratings will be implemented having destruction threshold over 3.5 J/cm^2 [11].

Conclusions

A prototype of the unique super-powerful multi-channel laser system is under development in RFNC-VNIIEF based on the classical "Luch" facility, reaching petawatt power level to diagnose fast-going processes in hot dense plasma featuring temporal resolution (< 10 ps) that can't be attained by other methods.

The project implicates multiple studies to be performed and different sub-systems to be developed, such as those used for the combined amplification of wideband pulses in parametric and neodymium amplifiers; adaptive control of laser pulse spectrum; generation of the train of pulses with adjustable period (10–100 ps); synchronization between picosecond and nanosecond pulses. Methods for focusing and converging several pulses on the target will be developed along with the method of aligning diffraction gratings.

The laser system to be built in the framework of the project may find applications in the other fast developing scientific branches, such as communication, metrology, biophysics, medicine, chemistry etc.

References

1. S.A. Belkov, S.G. Garanin, Yu.V. Shagalkin, *ICONO/LAT* 2013, LFB2.
2. S.G. Garanin, R.I. Ilkaev, G.A. Kirillov, et al., *Quantum Electronics*, 2005, **35**(4), 299-301.
3. J. Schwarz, P. Rambo, M. Geissel, et al., *Proc. of SPIE*, 2011, **8080**, 80800E-1 - 80800E-14.
4. S. Glenn, P.M. Bell, L.R. Benedetti, et al., *Proc. of SPIE*, 2011, **8144**, 814409-1 - 814409-8.
5. D. Batani, *Int. Workshop, COST Meeting*, Bordeaux, March 2014.
6. A.A. Shaykin, G.I. Freidman, S.G. Garanin, et al., *Proc. CLEO/Europe-EQEC* 2009 (Munich, Germany: OSA, 2009, Paper CG_P2).
7. C. Dorrer, I.A. Begishev, A.V. Okishev, J.D. Zuegel., *Optics Letters*, August 1, 2007, **32**(15), 2143-2145.
8. N.V. Vysotina, N.N. Rosanov, and V.E. Yashin, *Opt. Spectrosc*., 2011, **110**, 1029.
9. P. Tournois, *Opt. Commun*. 140, 245 (1997).
10. S.I. Chizhikov, S.G. Garanin, L.V. Goryachev, V.Ya. Molchanov, V.V. Romanov, N.N. Rukavishnikov, S.V. Sokolovskii, I.N. Voronich and K.B. Yushkov., *Laser Phys. Lett*., 2013, **10**, 015301 – 015306.
11. H.P. Howard, A.F. Aiello, J.G. Dressler, et al., *Applied optics*, 2013, **52**(8), 1682-1692.

Invited

THE VISUALIZER OF 2 μm LASER RADIATION BASED ON CaF_2:Ho

P.A. Ryabochkina[1], A.A. Lyapin[1], E.A. Garibin[2], S.N. Ushakov[3], and **P.P. Fedorov[3]**

[1] Ogarev Mordovia State University, Russia
[2] INCROM Ltd., St. Petersburg, Russia
[3] A.M. Prokhorov General Physics Institute of the Russian Academy of Sciences, Moscow, Russia

Abstract. A method for visualization of IR radiation in the two-micron range using CaF_2:Ho crystals is proposed. The energy efficiency of conversion of two-micron laser radiation to radiation in the red spectral range 620–690 nm by a CaF_2:Ho crystal is estimated. A study of upconversion processes in CaF_2:Ho crystals is presented.

One of the significant problems of modern photonics is the search of materials for visualisation of IR laser radiation. From the available information, the currently used commercial visualizers can convert to the visible light only the IR radiation with wavelengths not exceeding 1.7μm. For example, the working spectral range of visualizers produced by Roithner Lasertechnik (Germany) is 0.7–1.7 μm [1]. At the same time, visualizers are required for converting the IR radiation in the spectral range above 1.7 μm. For example, they need to visualize two-micrometer laser radiation.

Anti-Stokes luminescence under excitation at the energy level $^4I_{13/2}$ of Er^{3+} ions in various compounds is the physical basis of most currently existing visualizers of IR radiation. At the same time, beginning from the 1960-s, the anti-Stokes luminescence of Ho^{3+}-doped fluorite-type crystals (MF_2:Ho, where M = Ca, Sr, Ba) in the visible and near-IR wavelength regions has been extensively studied. Currently, there is a large number of works devoted to the study of anti-Stokes luminescence in crystals CaF_2:Ho [2–9]. Results of these works show that CaF_2:Ho crystals can be used in infrared visualizers.

However, we have found no studies of anti-Stokes luminescence in CaF_2:Ho crystals excited by two-micron radiation to the $^5I_7$ level of Ho^{3+} ions. In the present work, we studied the anti-Stokes luminescence in CaF_2: Ho crystals under excitation of the $^5I_7$ level of Ho^{3+} ions and assessed the possibility of using this material as a visualizer of two-micron laser radiation.

A detailed study of upconversion processes in CaF_2:Ho crystals is presented. Near-infared to visible upconversion luminescence of Ho^{3+} ions at the transitions $^5G_4$, $^5G_4$, $^5G_5$, $^5F_3$, $^5S_2(^5F_4)$, $^5F_4$, $^5I_4{}^5I_8$, $^5I_5$, $^5I_6$, $^5I_7 \rightarrow {}^5I_8$, $^5I_5 \rightarrow {}^5I_7$, $^5F_5 \rightarrow {}^5I_7$, $^5F_5 \rightarrow {}^5I_6$, $^5S_2 \rightarrow {}^5I_7$, $^5F_3 \rightarrow {}^5I_6$ were observed in CaF_2:Ho crystals under laser excitation of 1912 nm. Results of the study of decay kinetics of luminescence of Ho^{3+} with levels of $^5F_3$, $^5S_2(^5F_4)$, $^5F_5$, $^5I_4$ and the dependence of luminescence intensity on excitation power density show that the excited-state absorption and energy transfer process are responsible for the presence of anti-Stokes luminescence in CaF_2:Ho crystals.

We estimated the energy efficiency of the conversion of two-micron laser radiation to radiation in the red spectral range 620–680 nm by the CaF_2:Ho crystals. The energy efficiency of the conversion of two-micron laser radiation to radiation in the red spectral range 620–680 nm by the CaF_2-1mol %HoF_3 crystal does not exceed 0.02 %.

We demonstrated the possibility of visualization using a display in the form of an aluminium substrate coated, with the help of a binder, by a powder milled from CaF_2:Ho crystals. When illuminating this visualizer by the radiation of a $LiYF_4$:Tm laser, we observed a bright red spot.

Acknowledgement

This work was supported by the State Order for Research of the Ministry of Education and Science of the Russian Federation (Project No. 384.2014/K).

References

1. www.roithner-laser.com
2. M.R. Brown, W.A. Shand, *Physics Letters*, 1964, **11**, 219-220.
3. C.M. Verber, D.R. Grieser, W.H. Jones, *J. Appl. Phys*., 1971, **42**, 2767-2769.
4. M.B. Seelbinder, J.C. Wright, *Phys. Rev. B*, 1979, **20**, 4308-4320.
5. P.A. Apanasevich, R.I. Gintoft, A.G. Makhanek, *J. Appl. Spectros*., 1972, **16**, 443-452.
6. S.H. Tang, H.Y. Zhang, M.H. Kuok, S.C. Kee, *Phys. Stat. Sol. (b)*, 1991, **16**, 8351-359.
7. X. Zhang, J.P. Jouart, M. Bouffard, G. Mary, *Phys. Stat. Sol. (b)*, 1994, **184**, 559-571.
8. S.R. Bullock, B.R. Reddy, P. Venkateswarlu, *J. Opt. Soc. Am. B*, 1997, **14**, 553-559.
9. M. Mujaji, J.D. Comins, *Phys. Stat. Sol. (c)*, 2004, **9**, 2372-2377.

Invited

AN OVERVIEW OF THE OPTICAL MATERIALS AND COMPONENTS FOR SG LASER FACILITIES

J. Shao[1], Y. Dai[2], and **Q. Xu[3]**

[1] Shanghai Institute of Optics and Fine Mechanics, Chinese Academy of Sciences, Shanghai, P. R. China, jdshao@mail.shcnc.ac.cn
[2] Laser Fusion Research Center, China Academy of Engineering Physics, Mianyang, P. R. China
[3] Chengdu Fine Optical Engineering Research Center, Chengdu, P. R. China

Abstract. Owing to the prospect to achieve human being's dream for clean, carbon-free energy, researchers around the world have made tremendous efforts toward achieving inertial confinement fusion (ICF) using laser [1–3]. Scientists in China have also been devoted to the development of laser driver for ICF since the late 1960s. During the past decades, numerous works have been dedicated to optimize the materials and fabrication process to enhance the performance of the optical components to meet the requirements of increasingly larger and more powerful laser systems. Significant progresses on the essential raw materials, such as hafnium and potassium dihydrogen phosphate, as well as the main optical materials, including the Nd-doped phosphate glass, KDP/DKDP crystal, K9 glass and fused silica, have been achieved. In general, a complete supporting system of optical materials and components has been developed in China to meet the demands of the SG laser facilities.

Raw materials

High-purity hafnium and potassium dihydrogen phosphate are essential raw materials. To achieve high purity hafnium, a production line and purification process have been established, with which the metal hafnium produced has met the requirements for preparing high power dielectric coatings. For high-purity potassium dihydrogen phosphate, the improvement in the purification process and environmental control enables a impurity metal ion content of less than 0.1 ppm, the anion content and the organic carbon content are lower than 1 ppm and 10 ppm, respectively. The overall purity is higher than 99.9%. The technological breakthroughs in these key raw materials provide a guarantee for preparing high-power laser coating and high-performance laser crystal, respectively.

Main optical materials

As the laser gain medium in the ICF laser drivers, Nd-doped phosphate glass is required to have the high net gain, high efficiency of energy storage and extraction, high resistance laser-induced damage resistance, and high optical homogeneity. The investigation of Nd-doped phosphate laser glass in China began in 1970's. Till now, series Nd-doped phosphate laser glasses (N21, N31, N41) with large size, high homogeneity and high gain coefficients have been developed and well used in the SG series facilities. In the past few years, one of the main progresses in producing the Nd-doped phosphate glass is the development of continuous melting process. With this process, laser glass slab with size of 460 × 850 × 40 mm have been fabricated. Compared with traditional pot melting process, the continuous melting process can obviously increase the performance and volume at lower cost.

K9 glass is used as the substrate of the mirror coating. The large size K9 glass with stress less than 5 nm/cm has been developed.

As the key material of focus lens, diffractive optics, and debris shield in the ICF laser drivers, the high quality fused silica glass with size larger than Φ500 mm and index homogeneity about $3\sim5 \times 10^{-6}$ has been achieved.

KDP and DKDP crystal are used as electro-optic switch and frequency converter, due to their specific physical properties, including the optical transparency in a wide region, high nonlinear conversion efficiency, reproducible growth to the required large size, and ease of fabrication. One of the recent progresses in crystal growth is the development of the new method to grow large KDP crystal, the so-called "point-seed" method. With the new method, the growth rate can be increased to 10 mm/day, whereas the growth rate using the traditional method is only around 1–2 mm/day. With the progress in the raw material and the growth method, high performance KDP crystal with size of 635 × 555 × 530 mm and DKDP crystal with size of 510 × 390 × 520 mm have been produced.

Optical components

To fulfill the requirements, including optical property, laser damage resistance and wavefront quality, of optical components used in SG laser facilities, tremendous works have been done to investigate the optical finishing and coating deposition technology.

Optical finishing process has been investigated and optimized against the features of Nd-doped phosphate glass, K9, fused quartz and crystal, respectively. The wavefront quality over different spatial frequency regions as well as the surface quality of the optics have been effectively controlled.

Coating production has been studied as systematic engineering, including the preparation, coating deposition and post treatment process. By investigation of the substrate cleaning, deposition parameter and post treatment technique, the laser damage resistance of the coating has been enhanced. In addition, research on the stress evolution and aging, as well as optimization of the deposition parameter enable the efficient stress control of the coatings.

The cladded N31 glass have been used in the SG laser facility, after being pumped by 2500 shots of high energy xenon lamp, no interface damage, no peeling and no spraying have been observed. Large size dielectric mirrors and polarizers with LIDT higher than 22 J/cm^2 (1064 nm, 3ns) and 10.5 J/cm^2 1064 nm, 3 ns) have been achieved, respectively. The Sol-gel AR coatings on fused silica with LIDT of 35 J/cm^2 (1064 nm, 3 ns) and 14 J/cm^2 (355 nm, 3 ns), as well as the Sol-gel AR coatings on crystal with LIDT of 15 J/cm^2 (1064 nm, 3 ns) and 10 J/cm^2 (355 nm, 3 ns) have been achieved. A pulse compressed grating with the size of 430 × 350 × 80 mm has been prepared and used in SG II-U-PW system (290 × 105 mm oval beam spot) to achieve 380 J/5 ps laser output, fortunately, no damage was observed on PCG.

Summary

With the demands of SG laser facilities, significant progress has been made in optical materials and optical components in China. Now, the key raw materials (metal hafnium and potassium dihydrogen phosphate) and optical materials (laser neodymium glass, K9 glass, fused quartz and crystal) can be domestically supplied. The development of finishing equipment, the advancement in the optical finishing process, as well as the optimization of coating production process, enable the rapid improvement of the various optical components. The larger size optical components, including the continuous melting neodymium glass, KDP and DKDP crystal, continuous phase plate (CPP), as well as mirror and polarizer have been achieved.

References

1. J.H. Campbell, et al., *SPIE 2004 Photonics West*, USA, 2004, 84-101.
2. C.J. Stolz, *Advances in Optical Thin Films III*, U.K., 2008, 700115.
3. J.J. De Yoreo, A.K. Burnham, and P.K. Whitman, *International Materials Reviews*, 2002, **47**(3), 113-152.

PULSE SPLITTING AS A WAY TO INCREASE EFFICIENCY, TO DECREASE SHAPE DISTORTION, AND TO PREVENT OPTICAL ELEMENTS BREAKDOWN IN HIGH ENERGY SOLID STATE LASERS

A. Shaykin

Institute of Applied Physics, Russian Academy of Science, Nizhny Novgorod, Russia
shaykin@appl.sci-nnov.ru

Abstract. A method for decreasing flattop pulse distortion in a high energy solid state laser in a high saturation regime is proposed. It's basic idea is pulse splitting and consistent amplification of all replicas in the same active elements. This method allows increasing the amplifiers efficiency and output energy. Another advantage of this method is prevention of optical elements breakdown is.

Introduction

The efforts to achieve high output intensity and/or high amplifier efficiency are accompanied by strong pulse shape distortions. This occurs because the pulse energy is comparable with the saturation energy of laser transition. Distortions of the shape are insignificant for bell-shaped, quasi-Gaussian pulses. Saturation results, primarily, in pulse displacement in time [1]. For pulses with a steep leading edge, shape distortions are very important. The pulse at the amplifier output resembles a triangle with a steep leading and a flat rear edge. The effective pulse duration decreases and probability of laser elements damage increases. We propose a method that would enable reducing distortions of the amplified pulses and achieving steplike pulses at the amplifier output.

Shape distortion parameter of a pulse with steep edges

Distortions in the shape of pulses with steep edges can be best assessed by parameter N defined as the ratio of the gain at the initial G_0 and final G_{end} moments of time.

By using the Frantz-Hodvik equation [2]

$$E_{out} = E_s \ln\left[\left(\exp\left(\frac{E_{in}}{E_s}\right)-1\right)G_0+1\right]$$

we can show that

$$N = \left(G_0\right)^{\eta} = \exp\left(\frac{E_{out}-E_{in}}{E_s}\right), \text{ where } \eta = \frac{E_{out}-E_{in}}{E_{sat}}.$$

If the amplifier comprises several (m) cascades, then the parameter $N_{total} = \prod_{j=1}^{m} N_j$.

For several (n) pulses propagating successively through the amplifier, we can analogously obtain the formula $N_{total} = \prod_{i=1}^{n} N_i$.

The concept of reducing shape distortions

For obtaining a steplike pulse at the amplifier output, the input pulse must have the ratio of the intensities at the rear and front edges equal to N_{total}. But for n pulses of the same total energy, the ratio of each i-th pulse is much less, and is equal to $\sqrt[n]{N_{total}}$ in the ideal case.

Hence, in the high saturation regime (when N_{total} is large) division even into two pulses greatly reduces distortions. It is rather easy to obtain two pulses by dividing them according to their polarizations. This will allow changing the ratio of their energies at the amplifier input. They may be either summed at the amplifier output in the polarizer or in the SHG of the second type, or may be used independently as different pump channels.

Results of calculations of distortions of two pulses v/s one pulse for the pump laser of the pearl facility

Consider as an illustration results of computation of distortions of the shape of the pulse with steep edges at amplification in a 7 cascade Nd:glass rod amplifier. Part of the Gaussian beam with a duration of 5 ns, with monotonic edges was taken as a model pulse.

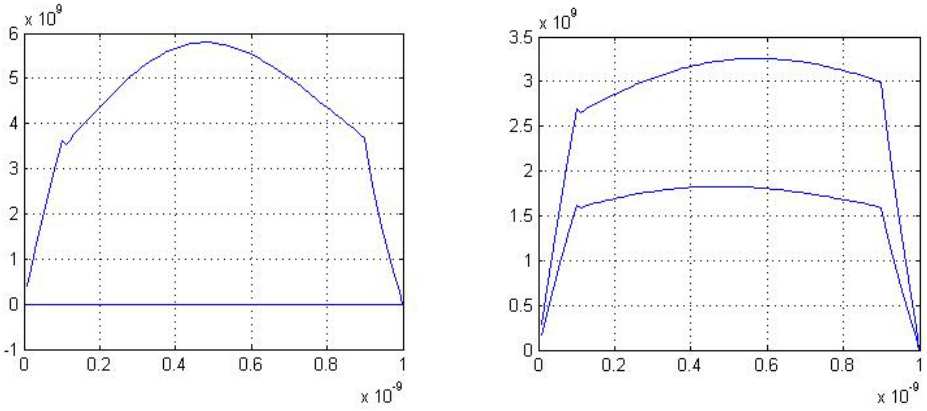

a **b**

Fig. 1. Output single pulse (a) and two pulses (b) with the same total energy

Clearly, for a single input pulse, the ratio *N* of the intensities at the front and rear edges is more than 30 times. In the case of two input pulse replicas, the ratio *N* of intensities does not exceed 6 times, and the output pulse shape is much closer to the rectangle (see Fig. 1).

References

1. M.A. Martyanov, G.A. Luchinin, A.K. Potyomkin, E.A. Khazanov, *Quantum Elektroniks*, 2008, **38**, 103.
2. L.M. Frantz, J.S. Nodvik, “Theory of pulse propagation in a laser amplifier”, *Journal of Applied Physics*, 1963, **34**, 2346.

Invited

ADVANCES IN TITANIUM SAPPHIRE MULTI-PETAWATT LASERS

C. Simon-Boisson, F. Lureau, G. Matras, S. Laux, O. Casagrande, C. Radier, O. Chalus, and **L. Boudjemaa**

Thales Optronique S.A., 2 avenue Gay-Lussac, 78995 Elancourt Cedex, France
Contact e-mail address: christophe.simonboisson@fr.thalesgroup.com

Abstract: We review the recent results achieved on Titanium Sapphire PetaWatt lasers. Key enabling technologies are presented. Perspectives towards higher peak power of 10 PW are discussed.

1. Introduction

Ultra high intensity laser pulses are required by researchers for a growing number of applications. The advent of Titanium Sapphire (TiSa) as a laser material has overcome many limitations existing with the traditional Neodymium doped glasses in terms of installation size, cost and repetition rate. The Chirped Pulse Amplification (CPA) concept [1] has made possible the amplification to very high energy levels, while keeping a very short pulse duration.

Thanks to these breakthroughs several research teams worldwide have built installations based on the TiSa technology, some of them delivering peak power above PetaWatt level up to 2 PW [2]. The first operation of the Petawatt laser system at a repetition rate of 1 Hz has been reported [3, 4] on BELLA at Lawrence Berkeley National Laboratory and more recently the first PetaWatt operation below 25 fs [5] has been demonstrated on the laser system built for the CETAL (Center of the Excellence for Advanced Laser Technology) project.

We report on the performance of these 2 systems, the key enabling technologies supporting high performance laser operation and the perspectives towards 10 PW operation.

2. Latest PetaWatt results

A 1 Hz PetaWatt laser system has been built, installed and commissioned at Lawrence Berkeley National Laboratory by Thales Optronique in September 2012 with the first PetaWatt laser shot at 1 Hz demonstrated in July 2012. This laser system is based on a double CPA configuration with a 2 crystals XPW filter [6] inserted between the 2 CPA in order to increase the temporal contrast by 4 orders of magnitude at least. The 2 final power amplifiers are pumped by high energy frequency-doubled Nd:YAG lasers working at 1 Hz. An output energy level before compression up to 70 J has been obtained. The initial PetaWatt laser shot at 1 Hz has been produced with an energy per pulse after compression of 42.4 J and a pulse duration of 40 fs. This laser system is now in full operation since the end of 2012 and routinely produces a laser beam to drive ongoing acceleration experiments.

Another PetaWatt laser system has been demonstrated and commissioned in November 2013 at INFLPR in Romania for the CETAL project. This laser system works at a repetition rate of 0.1 Hz as frequency-doubled Neodymium glass lasers are used to pump the final amplifier stage. A careful amplification design to minimise gain-narrowing effects as well as insertion in the early part of the second CPA of the AOPDF device to correct high orders of residual spectral phase have led to produce a beam with 52 nm spectral width (FWHM) resulting in a 23.7 fs (FWHM) compressed pulse duration at full laser power measured with a one-shot autocorrelator. Then the 26.5 J energy level reached after compression allowed to produce a 1.12 PW peak power.

3. Perspectives towards 10 PW laser systems

The scientific community of particle acceleration has several requirements to improve the performance of drive laser beams. One of them is to increase the peak power.

Thales Optronique is involved since July 2013 in the construction of 2 laser beamlines delivering 10 PetaWatt each at 1 shot per minute for the ELI-NP (Extreme Light Infrastructure – Nuclear Physics) located in Romania.

Design of the beamlines will be presented as well as the main technical challenges to reach the expected performance like a further reduction of pulse duration close to 20 fs through the insertion of new solutions like spectral filters [7] to compensate accurately gain-narrowing effects.

4. Conclusions & outlook

We have demonstrated the performance of 2 PetaWatt laser systems with emphasis on high repetition rate and short pulse duration. The Titanium Sapphire technology will be again used to build the next generation of higher peak power lasers, 10 PW class, therefore extending capabilities of lasers for particle acceleration physics.

5. References

1. D. Strickland and G. Mourou, “Compression of amplified chirped optical pulses”, *Optics Communications*, 1985, **56**(3), 219-221.
2. Yu. Chu & al., “High contrast 2.0 PetaWatt Ti:sapphire laser system”, *Optics Express*, 2013, **21**(24), 29231-29239.
3. S. Laux & al., “Suppression of parasitic lasing in high energy, high repetition rate Ti:sapphire laser amplifiers”, 2012, *Optics Letters*, **37**(11), 1913-1915.
4. F. Lureau & al., “High repetition rate PetaWatt Titanium Sapphire laser system for laser plasma acceleration”, *Ultrafast Optics*, 2013.
5. G. Matras & al., “First sub-25 fs PetaWatt laser system”, *Advanced Solid State Lasers* (ASSL) 2013, AF2A.3.
6. Jullien Fuchs & al., “Highly efficient nonlinear filter for femtosecond pulse contrast enhancement and pulse shortening,”, *Opt. Lett.*, 2008, **33**, 2353-2355.
7. F. Giambruno & al., “Design of a 10 PW (150 J/15 fs) peak power laser system with Ti:sapphire medium through spectral control”, *Applied Optics*, 2011, **50**(17), 2617-2621.

THERMALLY INDUCED DISTORTIONS OF RADIATION IN FARADAY ISOLATORS FOR MAGNETOOPTICAL ELEMENTS AND LASER BEAMS WITHOUT AXIAL SYMMETRY

A.V. Starobor and **O.V. Palashov**

Institute of applied physics RAS, Nizhny Novgorod, Russia, astarobor@mail.ru

Abstract. A model for numerical calculation of depolarization in complex configurations of a magnetooptical element (MOE) and a complex beam profile is created. The model is supported by experiments. It is shown that in the disk geometry of the MOE there is a strong dependence of thermally induced depolarization on beam diameter. It is demonstrated that the degree of isolation in a "multichannel" Faraday isolator (FI) may be increased by a factor of 6–8 as compared to the traditional FI.

The Faraday isolator is an important part of laser systems, but it is one of the optical devices that is most influenced by thermal self-action because of the relatively strong absorption (~10^{-3} cm^{-1}) in the magnetooptical elements (MOEs). The absorption-induced nonuniform cross-sectional temperature distribution leads to linear birefringence (photoelastic effect) and to distortions of the transmitted beam wavefront (thermal lensing). These factors limit maximum working laser power of the FI [1, 2].

With the development of high-power laser systems, there arise a need in a Faraday isolator with elements that have other than cylindrical symmetry. One of the important examples of such configurations are beams with a square /rectangular cross-sectional profile, which are often used in lasers with high average and high peak power to increase fill-factor of the active elements of amplifiers and generators. Also, these configurations are useful for creating FI for nonpolarized light where both beams of different polarization pass through a single magneto-element. This allows reducing dimensions of the device and thermally induced depolarization.

In such cases no analytical expressions for the depolarization can be obtained. So, a three-dimensional numerical model for thermal depolarization investigation has been developed.

It calculates temperature distribution and thermal stresses in the element with the finite element method. Based on this refractive index, changes related to the photoelastic effect and depolarization are calculated. Calculations can be performed on elements of any shape and any intensity distribution of the beam. Calculations are confirmed by test experiments.

The degree of depolarization γ is calculated by integrating the local depolarization profile taking into account the profile of radiation intensity in the beam cross section. Calculation of γ is carried out in 3 steps. The first step is calculation of the temperature distribution in the sample by solving the heat equation with a source proportional to the absorption coefficient and the spatial distribution of the laser intensity. The resulting temperature gradient is used as a source of thermal expansion for the elasticity equation. Further, from this equation strain tensor in three-dimensional space is calculated. Heat and elasticity equations are solved in 3D by the finite element method (using a combination of Comsol and Matlab software systems). Then, the impermeability tensor elements are calculated. They are associated with the strain tensor with the photoelastic tensor coefficients and rotation matrices for the Euler angles, which allows taking into account the orientation of the crystallographic axes of the element. Further phase shift integration is performed along the beam axis.

As a model experiment the dependence of the depolarization on the diameter of a Gaussian beam in a disk MOE (TGG, ø20 mm, L = 7 mm) was calculated and measured. It is shown that with increasing radius of the beam from 1.4 to 8 mm, the depolarization decreases by a factor of seven, which is in a good agreement with the theoretical curve (fig. 1a).

Also, as a model experiment the dependence of the depolarization on the shift of the beam relative to the crystal in a cylindrical MOE (TGG, ø10 mm, L = 20 mm) was calculated and measured (fig. 1b). The depolarization difference between the central and the shifted positions of the beam does not exceed 40%. All experiments show good agreement between the measurements and the calculations, so the model is quite accurate.

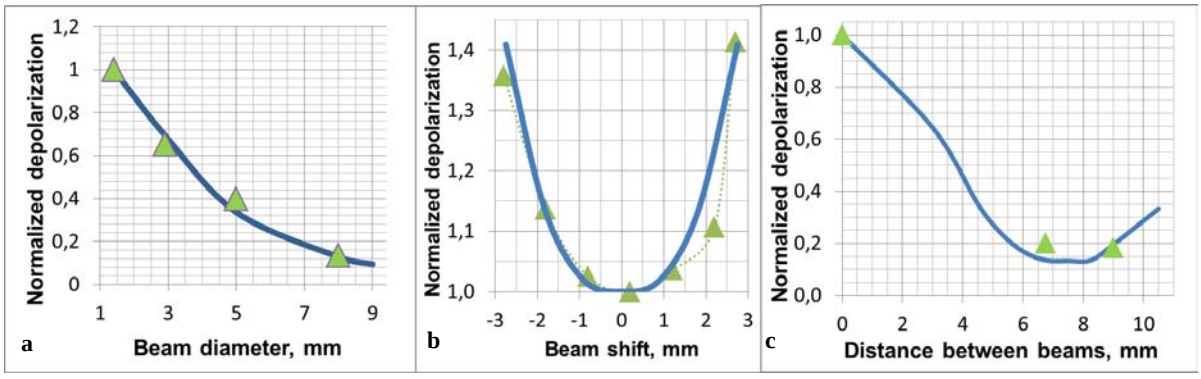

Fig. 1. The dependence of normalized thermal depolarization on a) beam diameter in disk MOE, b) beam shift in cylindrical MOE, c) distance between beams in slab MOE. The curves correspond to calculations, the triangles to experimental data

A Faraday isolator with slab geometry with two spatially separated beams was modeled (the MOE was made of magnetooptical glass, length 30 mm, 8×20 mm^2 in cross-section, beam diameter 6 mm at the level of $1/e^2$). In this situation, in the case of independent beams thermally induced depolarization can be reduced by a factor of 4, and calculations show that in the case of the optimal distance between the beams, depolarization can be further reduced by a factor of 1.5 in the cylindrical geometry of MOE and 2 times in the slab geometry of MOE (fig. 1c).

Conclusion

Thus, a model for numerical calculation of depolarization in complex configurations of a MOE and a complex beam profile has been created. The model has been confirmed by the experiments. It was shown that in the disk geometry of MOE there is a strong dependence of the thermally induced depolarization on the beam diameter. For the "multichannel" FI, a possible increase in the degree of isolation by a factor of 6-8 compared to the traditional FI was demonstrated.

Acknowledgements

This work was supported by the mega-grant of the Government of the Russian Federation No. 14.B25.31.0024 executed at the Institute of Applied Physics RAS.

References

1. A.N. Malshakov, G. Pasmanik, and A.K. Poteomkin, "Comparative characteristics of magneto-optical materials," *Appl. Opt.*, 1997, **36**, 6403-6410.
2. G. Mueller, R. S. Amin, D. Guagliardo, D. McFeron, R. Lundock, *et al.*, "Method for compensation of thermally induced modal distortions in the input optical components of gravitational wave interferometers," *Classical and Quantum Gravity*, 2002, **19**, 1793-1801.

PROBLEMS AND PERSPECTIVES OF CREATION OF HIGH INTENSITY FEMTOSECOND LASER SYSTEMS WITH COHERENT BEAM COMBINING

S.N. Bagayev, V.I. Trunov, E.V. Pestryakov, S.A. Frolov, V.E. Leshchenko, V.A. Vasiliev

Institute of Laser Physics SB RAS, Novosibirsk, Russia, trunov@laser.ncs.ru

Abstract. The basic design principles of high intensity laser systems based on coherent combining of radiation of multichannel laser complexes are considered. The influence of the instability of parameters of individual components of radiation on coherent combining efficiency is analyzed, and requirements to their values for realization of high efficiency coherent combining are determined. Experimental results showing the fundamental possibility of coherent combining of parametrically amplified femtosecond pulses with energy up to 100 mJ and 20 fs pulse duration are presented and analyzed. The peculiarities of the coherent summation of radiation in multichannel scheme are discussed.

Introduction

The major problem of the creation of ultra-high intensity laser systems is reaching technological limit of the linear single-channel approach to their construction. In this way, peak intensity claimed in single channel laser systems such as Apollo10P and Vulcan10P does not exceed 10^{23}–10^{24} W·cm^{-2} whereas projects based on a promising technique of coherent beam combining such as ELI and XCELS plan to achieve peak intensity higher than 10^{25} W·cm^{-2}. Coherent beam combining shows great promise owing to overcoming limitations on maximum available single-channel peak power restricted by maximum available aperture of amplifier and compressor. Thus coherent beam combining is the key technique for creation of ultra-high intensity femtosecond laser facilities. One of the main problems appearing with the necessity of coherent beam combining implementation is the high requirements on the identity of combined beams, especially in the phase domain [1]. These requirements are unlikely to be implemented using laser amplifiers due to the significant aberrations (mainly thermal aberrations) induced during amplification. This problem can be overcome using parametric amplifiers instead of laser ones owing to the practical absence of phase distortions caused by thermal effects with a proper choice of nonlinear optical crystals having small absorption for all interacting waves.

Coherent beam combining

Investigations performed at the Institute of Laser Physics of the Siberian Branch of the Russian Academy of Sciences (ILP SB RAS) concern the development of principles for generating extreme light fields and creating the multichannel femtosecond laser system of ultra-relativistic intensity based on the coherent combining of femtosecond pulses amplified by using the OPCPA method under picosecond pumping. At present dual-channel laser system based on broadband parametric amplification of chirped Ti:Sa laser pulses in BBO and LBO crystals is designed and created at ILP SB RAS. Each channel consists of three-stage parametric amplifiers with pump pulses of 532 nm wavelength and 90 ps pulse duration. Parametric amplification for its part requires precise synchronization of seed and pump pulses with sub pulse duration accuracy. We developed the optoelectronic system for locking both lasers to the same reference standard (optical clock) with the accuracy less than 200 fs. The amplified pulses are further compressed with grating compressor to duration of about 20 fs in each channel. For the first time the coherent combining of two pulse sequences with energy of ~150 mJ and 10 Hz repetition rate is experimentally realized [2]. The coherent combining efficiency of 95 % is reached with the use of original relative jitter two–loop stabilization setup with a slow loop based on amplified pulse error signal registration and a fast loop based on unamplified pulse error signal measurement, that allows to keep residual jitter as low as 40 as [3]. The spatial distribution of the radiation under coherent combining using sharp focusing (F/6.4 paraboloid) with the total peak intensity ~ $2\cdot10^{19}$ W·cm^{-2} is shown on Fig. 1. Analysis of experimental data shows that reduction of F/D parameter and compensation of aberrations should allow potentially reaching a level of intensity ~10^{20}–10^{21} W·cm^{-2} in created system.

An analysis of the dependence of the efficiency of coherent combining on the number of channels for different instabilities performed by us in [1] are shown the only meaningful dependence of the timing jitter on the number of combined beams. No other parameters have any significant dependence on the number of channels, so will not result in a sufficient efficiency reduction in a multichannel laser setup. Thus developed system of active stabilization of the relative jitter that demonstrated high

efficiently coherent combining of radiation for the two channels can be used in multichannel scheme (N channels) like shown in Fig. 2. In the presented scheme all N-1stabilization systems operate independently, which should lead to rapid achievement of stabilization mode in a multichannel scheme.

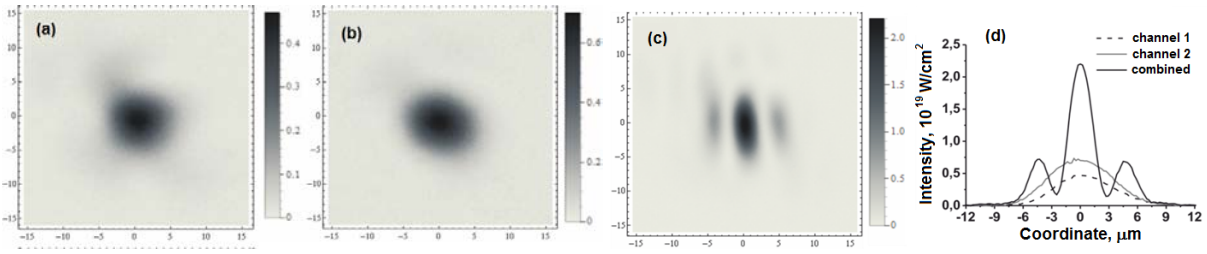

Fig. 1. Beam profiles in the focal plane for the first channel (*a*), the second channel (*b*), for a combined pulse (*c*) and horizontal data projection (*d*)

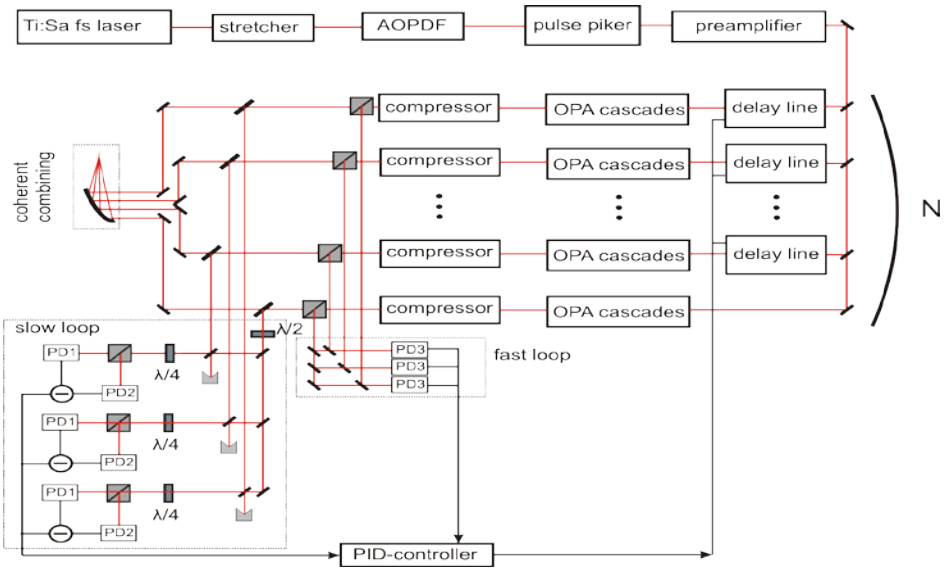

Fig. 2. Scheme of coherent multibeam coherent combining using two loops active systems of relative jitter stabilization

To create an ultra-high-intensity laser system, not only should the number of channels be increased but also the peak power and energy in each channel should be enhanced too. Energy scaling can be realized by increasing the LBO crystal size and the pump energy at the final amplification stage. The results of numerical simulations based on the extended model of parametric amplification assert that a 10 PW single channel level can be achieved using LBO crystals with a diameter of about 30 cm [1]. Some projects aimed at the creation of diode pumped laser with an energy of about 100 J operating at high repetition rate. The possible schemes of using such lasers for pumping of booster parametric amplifiers are discussed .Thus experimental results and the analysis presented in the paper provide a basis for the creation of a new generation of high-intensity laser sources based on coherent beam combining.

Acknowledgements

This work is supported in part by RAS Program “Extreme light fields”, registration number 01201266430 and Government program, registration number 01201374306.

References

1. S.N. Bagayev, V.I. Trunov, E.V. Pestryakov, *Laser Physics*, 2014, **24**, 074016.
2. V.E. Leshchenko, V.I.Trunov, S.A. Frolov, *Laser Physics Letters*, 2014, accepted.
3. S.N. Bagayev, V.E. Leshchenko, V.I. Trunov, *Optics Letters*, 2014, **39** (6), 1517-1520.

ADAPTIVE OPTICAL AND HOLOGRAPHIC CORRECTION IN LASER SYSTEMS: COMPARISON AND POSSIBLE COMBINING

V.Yu. Venediktov

St.-Petersburg State Electrotechnical University "LETI", St.-Petersburg, Russia, vlad.venediktov@mail.ru
St.-Petersburg State University, Faculty of Physics, St.-Petersburg, Russia

Abstract. The review paper considers “traditional” adaptive optics and dynamic holography as two competitive alternative tools for laser beam control and at the same time reveals some fields of technology, where these two techniques can be combined.

The traditional approach to adaptive optics (AO) is based on the idea of using the system comprised of some wavefront sensor (WS; most usually – Shack-Hartman sensor), computer, and actuator (the mirror with the controlled shape or liquid crystal spatial light modulator), correcting the wavefront. The computer analyses the data from WS and controls the actuator so as to eliminate the distortions imposed into the wavefront by laser medium, atmospheric turbulence etc. It is also well known (see, for instance, [1]) that a similar task can be also fulfilled by the use of dynamic holography. In this case the distortions are read out by the beam of coherent radiation and then the dynamic hologram of distortions is recorded in liquid crystal valve or some other device. This hologram is used as the corrector. The advantages of holographic approach are well known – the depth of distortions is not limited by the actuator stroke, the system is much simpler, it lacks computer and mechanical elements. Its disadvantages are also well known: the holographic systems are less flexible, they reveal strong chromatism (accurate correction is available in a much narrower spectral range than in the case of traditional AO; the latter, however, is not very important in the case of laser applications), and the present day technology of holographic record is not very suitable for the high power applications.

One has to note that historically these two approaches, which obviously fill into one and the same field of science and technology, were developed by different communities and were even described in different terms. In our review paper we try to unite these two halves of one common science, to describe them in standard terms, to determine parallelism and also to eliminate some popular misunderstandings.

For instance, traditionally the AO was treated as the numerical technique, while the holographic approach was treated as the analogous one. However, there exist some technologies which do not correspond to this dichotomy. For instance, one can record the zero diffraction order corrector in analogous scheme [2], and, at the same time, one can use computer-generated dynamic hologram as the AO actuator [3].

We also discuss some possible systems, comprising both AO and dynamic holography principles, first of all in WS design, like the so-called holographic WS [4], incoherent digital holography etc.

References

1. M.V. Vasil’ev, V.Yu. Venediktov, and A.A. Leshchev, *Quantum Electronics*, 2001, **31** (1), 1-15.
2. M.A. Vorontsov, M.E. Kirakosyan, and A.V. Larichev, *Quantum Electronics*, 1991, **21** (1), 105-108.
3. M.T. Gruneisen, J.R. Rotge, R.C. Dymale et al., *Opt. Eng.*, 2004, **43**(6), 1387-1393.
4. G. Andersen, P. Gelsinger-Austin, R. Gaddipati et al., *Opt Express*, 2014, **22**(8), 9432-41.
5. J. Hong, M.K. Kim, *J. Europ. Opt. Soc. Rap. Public*, 2013, 8, 13077 – 8.

THE INFLUENCE OF ELASTIC ANISOTROPY ON THERMALLY INDUCED BEAM DISTORTIONS IN CUBIC SINGLE CRYSTALS

A.G. Vyatkin and **E.A. Khazanov**

Institute of Applied Physics of the Russian Academy of Sciences, Nizhny Novgorod, Russia
vyatkin@appl.sci-nnov.ru

Abstract. Thermally induced distortions of laser beam polarization and phase on passing active elements made of single crystals with cubic symmetry were calculated for a particular temperature distribution taking into account anisotropy of the elastic properties of the materials. The isotropic expressions for the induced birefringence were extended for the case of a thin disk and modified for the long rod geometry. The depolarization degree and the focal length of the thermal lens were found.

Parasitic thermal effects are one of the major factors limiting the output power of solid-state lasers [1]. Absorption of pump radiation in active elements leads to nonuniform heating due to quantum defect. Then, thermal expansion of the medium results in elastic stresses. Finally, the photoelastic effect leads to a variation of the dielectric tensor. In a general case, the medium becomes biaxial, therefore the transmitting laser beam sustains distortions of both polarization and phase.

The piezooptic tensor that characterizes the photoelastic effect is a fourth rank material tensor [2]. In cubic crystals it depends on the crystallographic axes orientation [defined by the first two Euler angles (α, β)]. By now phase and polarization distortions in cubic media have been analyzed at arbitrary crystal orientation in the approximation of the isotropic elasticity problem [3–5]. However, the elastic compliance tensor **s** is a four rank tensor as well and thus varies with crystal orientation, too. This dependence is characterized by the elastic anisotropy ratio

$$\xi_s = s_{44} \big/ \left[2\left(s_{11} - s_{12}\right) \right], \tag{1}$$

where s_{ij} are the components of **s** in Nye's notation. For isotropic materials, e. g., glasses, $\xi_s = 1$. The elastic anisotropy is negligibly small in widely used garnets (YAG, TGG, GGG, YIG, etc.) and some other materials (e. g., BaF_2) since $\xi_s \approx 1$ within 10 %. It is however substantial for some other cubic crystals: CaF_2 ($\xi_s = 1.77$), SrF_2 ($\xi_s = 1.25$), KCl ($\xi_s = 2.69$), etc.

In the works concerning thermal depolarization in cubic crystals the photoelastic anisotropy parameter is used to describe the dependence of the induced birefringence on crystal orientation. This material property is introduced in the form of either stress-optic anisotropy ratio ξ_π or strain-optic anisotropy ratio ξ_p:

$$\xi_\pi = \pi_{44} \big/ \left[\pi_{11} - \tfrac{1}{2}\left(\pi_{12} + \pi_{21}\right) \right], \quad \xi_p = 2\,p_{44} \big/ \left[p_{11} - \tfrac{1}{2}\left(p_{12} + p_{21}\right) \right], \tag{2}$$

where π_{ij} and p_{ij} are the components of the piezooptic and the elastooptic tensors in Nye's notation, respectively. Since $\xi_\pi = \xi_p \xi_s$, these two formulas of the photoelastic anisotropy parameter are not equivalent for materials with anisotropic elastic properties. Therefore, it is not clear which value describes the effects proposed in these papers properly. We note that there is no such problem for the second parameter of photoelastic anisotropy ξ_d (which is nonzero for 23 and m3 crystals) since

$$\xi_d = \left(\pi_{12} - \pi_{21}\right) \big/ \left[\pi_{11} - \tfrac{1}{2}\left(\pi_{12} + \pi_{21}\right) \right] = \left(p_{12} - p_{21}\right) \big/ \left[p_{11} - \tfrac{1}{2}\left(p_{12} + p_{21}\right) \right]. \tag{3}$$

We have analyzed the influence of the elastic compliance tensor anisotropy on thermally induced beam distortions in cubic single crystals. Starting from the known thermoelasticity problem solution for a particular temperature distribution [6, 7], we obtained the phase incursion and depolarization degree in the approximations of the radially cooled long rod and thin disk at arbitrary crystal orientation. In the disk, if the stress-optic anisotropy ratio ξ_π is used as the parameter of photoelastic anisotropy, the expression for the photoelastic additive to the dielectric tensor copies the elastically isotropic one except for a minor refinement of the dimensionless power definition and for a new orientation dependent multiple F defined by s_{ij} (see the figure). Thus, in the case of small birefringence, the depolarization degree is multiplied by F^2. Moreover, the component of phase incursion that stands for the change of thickness of the active element becomes astigmatic due to non-axial-symmetric deformation. In a long rod, beam distortions caused by the photoelastic effect are described in a form that is substantially different from the isotropic one.

In addition, in cubic crystals of symmetry groups 23 and m3, the anisotropy of elastic properties leads to the fallacy of the known estimates for orientations with minimal depolarization. The shift of the optimal orientations is different for a long rod and a thin disk.

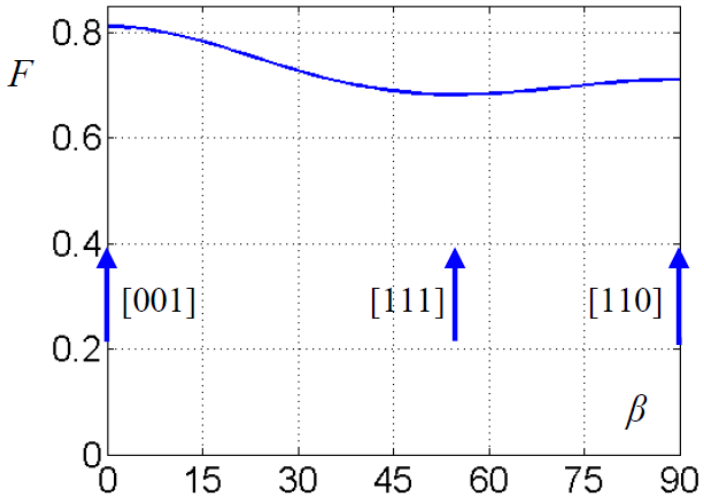

Factor F in CaF_2 as a function of the Euler angle β at $\alpha = \pi/4$ ([MMN] orientations).
The simplest orientations are shown by arrows

Acknowledgements

This work was supported by the mega-grant of the Government of the Russian Federation No. 14.B25.31.0024 executed at the Institute of Applied Physics RAS.

References

1. W. Koechner, *Solid-State Laser Engineering*, Springer-Verlag, Berlin, 1999.
2. J.F. Nye, *Physical Properties of Crystals*, Oxford University Press, 1964.
3. E. Khazanov, N. Andreev, O. Palashov, A. Poteomkin, A. Sergeev, O. Mehl, and D. Reitze, *Appl. Opt.* **41**, 483–492 (2002).
4. I.B. Mukhin, O.V. Palashov, E.A. Khazanov, and I.A. Ivanov, *JETP Lett.* **81**, 120–124 (2005).
5. A.G. Vyatkin and E.A. Khazanov, *JOSA B*. **28**, 805-811 (2011).
6. Ju.D. Golyaev, K.N. Evtyukhov, and L.N. Kaptsov, *Vestnik MGU* [Moscow State Uni. Bulletin]. **21**, 29–35 (1980).
7. V. Parfenov, V. Shashkin, and A. Stepanov, *Appl. Opt*. **32**, 5243–5255 (1993).

Invited

ROUTE AND RECENT PROGRESS ON HIGH CONTRAST ULTRAINTENSE FEMTOSECOND LASER

Zh. Wei

Beijing National Laboratory for Condensed Matter Physics, Institute of Physics,
Chinese Academy of Sciences, Beijing, 100190, China
Email: zywei@iphy.ac.cn

The progress of chirped-pulse amplification CPA technology provides great opportunities for studying laser-matter interactions with on-target intensity exceeding 10^{22}W/cm^2. To date, several laser systems with peak power up to PW have been realized with different schemes, and the effort to deliver 200 PW peak power with Ti: sapphire laser system has been pursued through the Extreme Light Infrastructure (ELI) project. For laser-matter interaction experiments at such intense level, the contrast is required as high as 10^{-10} to prevent pre-plasma dynamics. In order to suppress the noise, several pulse-cleaning techniques have been developed. For example, in 1998 Itatani et al. increased the ASE contrast by two orders from 10^{-5} to 10^{-7} with saturable absorbers. In particular, contrasts as high as 10^{-10} to 10^{-11} have been achieved by using the cross-polarized wave (XPW) generation, nonlinear polarization rotation (NPR), double-CPA and OPCPA. Although those techniques are improved continuously, up to now they are mainly achieved at a limited power level.

In this talk, I will present the recent progress of our XL-III laser facility with PW level peak power following the review on the high contrast techniques. By replacing the previous regenerative amplifier with a new CPA system and a non-collinear femtosecond optical-parametric amplifier, the pulse contrast ratio reached 10^{-10} on the tens picoseconds scale. In this scheme, a homemade broadband Ti:sapphire laser was used as the seeding source, the sub-10 fs output laser was divided into two beams with powers of 70 % and 30 % respectively. Then the higher power beam was used as the seed for the CPA I, following the stretcher and two stages multi-pass amplifiers, the laser was frequency doubled to 405 nm after the compressor as the pump for the NOPA. The other lower power beam was used as the signal for the NOPA. A Herriott-type telescope was used to delay the signal beam for experiencing the same optical length with the pump beam. Under the pump energy of 100 mJ at 532 nm from a commercial laser (Quantry PRO-170), we got 5 mJ laser at 50 fs pulse duration from the CPA I. After 2 stage NOPAs, the signal laser was boosted to 26 μJ. To pursue even higher power, we injected the high contrast laser into the CPA II as the seeding pulse. The CPA II consists of an Offner-triplet stretcher, three stage multi-pass Ti:sapphire amplifiers and a vacuum compressor. Before amplification, we first extended the signal laser to 600 ps, then amplified the chirped-laser to 20 mJ at 10 Hz repetition rate. Following that, we divided the laser repetition rate to 1 Hz to match the 3 J Nd:YAG laser (Beamtech Inc). With optimized amplification, laser energy up to 780 mJ was obtained. The final stage amplifier was dual pumped with a 120 J Nd:glass laser at 527 nm wavelength at single shot per 20 minutes (Beamtech Inc), two uniform plates were used to smooth the beam profile of pump lasers. Under full energy pump, the optimized average amplified energy was 46.8 J. The amplified pulses from the final stage amplifier were enlarged to the diameter of 150 mm and then recompressed by a grating based compressor installed in the vacuum chamber. To minimize the pulse duration, we used a commercial FROG to monitor the dispersion compensation and pulse duration. With the ray tracing simulation and optimized alignment, we measured the average pulse duration to be 27.9 fs. According to the 69 % measured transmission of the compressor, it implies a compressed energy of 32.3 J, corresponding to a peak power up to 1.16 PW. Our preliminary experiment with laser matter interaction has proved the brightness enhancement of Kα X ray compared to the conventional high power Ti:sapphire laser, the detailed result will be introduced in this talk.

MEASUREMENTS OF OPTICAL ANISOTROPY PARAMETERS OF BaF_2 AND SrF_2CRYSTALS

A.I. Yakovlev[1], I.L. Snetkov[2], and **O.V. Palashov[2]**

[1]Lobachevsky State University of Nizhny Novgorod,Nizhny Novgorod, Russia, yaknnalex@gmail.com
[2]Institute of Applied Physics of the Russian Academy of Sciences, Nizhny Novgorod, Russia

Abstract. The thermally induced depolarization caused by thermally induced birefringence can be characterized by the optical anisotropy parameter ξ. The optical anisotropy parameters ξ of BaF_2 and SrF_2 were measured for three probing wavelengths of 531 nm, 633 nm and 1076 nm. With the experimental accuracy these materials have the same value of optical anisotropy parameter ξ equal to –0.34±0.03 and didn't show a significant dependence on the used wavelength of the probing radiation.

Introduction

With the passage of laser radiation through and optical element there arise negative thermal effects associated with heating of the medium. One of these effects is thermally induced birefringence that arises in the optical elements due to the photoelastic effect caused by temperature gradients. It results in depolarization of transmitted radiation and therefore in additional losses of power. The thermally induced depolarization can be characterized by the optical anisotropy parameter ξ which depends on the material of the optical element. In single-crystal optical elements this parameter at fixed size and distribution of heat radiation completely determines optimal direction, in which depolarization takes the minimal value. In case of single-crystal materials with a negative value of optical anisotropy parameter ξ, there is the orientation of crystallographic axes in which the thermally induced depolarization vanishes [1, 2], and also such materials can be used in well-known schemes of compensation of thermally induced depolarization without using a reciprocal quartz rotator [3, 4].

Measuring the optical anisotropy parameters

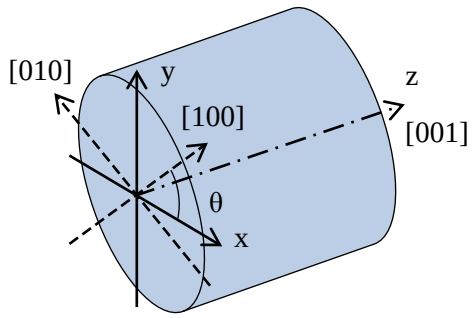

Fig. 1. Geometry of crystal. θ determines the angle of crystallographic axes & polarization of radiation, *(r, φ)* are polar coordinates

We can characterized laser radiation after the crystal by local depolarization

$$\Gamma(r,\phi)=\frac{\left|\overrightarrow{E_2}(r,\phi)\cdot\overrightarrow{y_0}\right|^2}{\left|E_0(r,\phi)\right|^2}$$

and integral depolarization

$$\gamma=\frac{\int_0^{2\pi}d\phi\int_0^{\infty}E\cdot\left|r_0(\ ,\phi)\right|^2dr}{\int_0^{2\pi}d\phi\int_0^{\infty}\left|E_0(r,\phi)\right|^2\cdot rdr}$$

When the crystal is rotated around the *z* axis, the integral depolarization takes on the minimum and maximum value. In [2, 5] it was shown that, if

$$|\xi|<1,\quad \gamma(\theta=\frac{\pi}{4})=\gamma_{\max},\quad \frac{\gamma_{\min}}{\gamma_{\max}}=\xi^2$$

$$|\xi|>1, \quad \gamma(\theta=0)=\gamma_{\max}, \quad \frac{\gamma_{\max}}{\gamma_{\min}}=\xi^2$$

Using the original method [2], we measured the optical anisotropy parameters ξ of cubic crystals of BaF_2 and SrF_2. A Yb-fiber 300 W laser at the wavelength 1076 nm with linear polarization and Gaussian profile was used as a source of heating radiation and two diode lasers with wavelengths of 531 nm, 633 nm were used as sources of probing radiation.

After passage of calcite wedge 1, probing radiation from the diode laser with linear polarization was propagated to the sample, where it was combined with heating radiation. Glan prism 2 cross-polarized with the calcite wedge was tuned up to minimum signal – depolarized component of the transmitted field. The intensity distribution was recorded by a CCD camera.

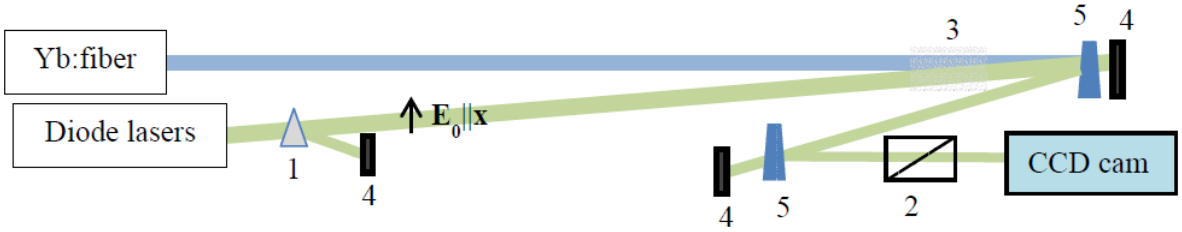

Fig. 2. Scheme of experiment. 1 – calcite wedge, 2 – Glan prism, 3 – crystal sample, 4 – absorbers, 5 – quartz wedges

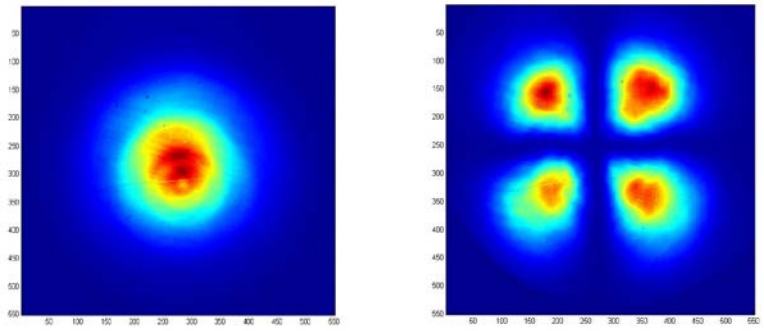

1 2

Fig. 3. Images from CCD camera. Polarized (1) and depolarized (2) field components

Conclusion

The optical anisotropy parameters ξ were determined from the measurements of the thermally induced depolarization depending on the power of heat radiation at different positions of the crystals. To the experimental accuracy, these materials have the same value of optical anisotropy parameter equal to –0.34 ± 0.03 and do not show significant dependence on the used wavelength of the probing radiation.

References

1. R.E. Joiner, J. Marburger, and W.H. Steier, *Appl. Phys. Lett.*, 1977, **30**(9), 485-486.
2. I.L. Snetkov, A.G. Vyatkin, O.V. Palashov, and E.A. Khazanov, *Opt. Express*, 2012, **20**(12), 13357-13367.
3. I.L. Snetkov and O.V. Palashov, *Appl. Phys. B*, 2012, **109**(2), 239-247.
4. A.G. Vyatkin, I.L. Snetkov, O.V. Palashov, and E.A. Khazanov, *Opt. Express*, 2013, **21**(19), 22338-22352.
5. A.V. Mezenov, L.N. Soms, and A.I. Stepanov, *Termooptika tverdotel'nykh lazerov* [*Thermooptics of solid-state lasers*], Mashinostroenie, Leningrad, 1986. (in Russian)

OFFNER TRIPLET TELESCOPE STRETCHER FOR PEARL SYSTEM

A.S. Zuev and **I.V. Yakovlev**

IAP RAS, Nizhny Novgorod, Russia, Alan.zuev@yandex.ru

Abstract. It is intended to upgrade the front-end of the PEARL laser system by replacing the femtosecond oscillator and stretcher. The OPCPA scheme with frequency conversion will be replaced by the classical OPCPA scheme. Reliability and stability of the laser system will be increased. Various perspective stretcher schemes are analysed in this presentation. Our choice has been substantiated, calculations have been performed and the scheme of the Offner triplet telescope stretcher has been optimized.

The PEtawatt pARametric Laser system (PEARL) based on the optical parametric chirped pulse amplification (OPCPA) scheme with frequency conversion [1] operates in IAP RAS (Nizhny Novgorod, Russia). The principal difference of this scheme from the traditional OPCPA is that the stretched radiation at 1250 nm from a femtosecond Cr:forsterite laser is injected into the first amplification cascade, and the radiation with another wavelength generated as a result of three-wave interaction in the first cascade is directed to the subsequent cascades and to the compressor.

For increasing the reliability and stability of the laser system PEARL, it is planned to upgrade the front-end part. The femtosecond Cr:forsterite oscillator with central wavelength of 1250 nm will be replaced by a Ti:sapphire laser with central wavelength of 910 nm, which generates 40 fs pulses with an energy of 5.5 nJ. The original stretcher with a pair of prisms between the diffractive gratings will be replaced by a traditional stretcher. Thus, the classical OPCPA scheme will be used instead of the OPCPA scheme with frequency conversion.

Various schemes of stretchers were examined and analyzed. The Martinez stretcher [2] and the Offner triplet telescope stretcher [3] with parabolic and spherical mirrors were studied in detail. The Offner triplet telescope stretcher with spherical mirrors has been chosen for PEARL, because the residual phase of the laser system connected with the fourth order dispersion is minimal.

The optimal focal length of the concave mirror and the impact parameter were selected to reduce the size of the optical elements of the stretcher and the value of the residual phase of the system. The value of the angular chirp (the frequency dependence of the direction of the output radiation) for different values of the impact parameter was analyzed, and it was shown that the value of the angular chirp is smaller than the diffraction divergence. For stretcher compactness, the focal length of 90 cm concave mirror and 3 cm impact parameter were chosen (Figure 1). The optimal sizes of the optical elements of the stretcher were calculated.

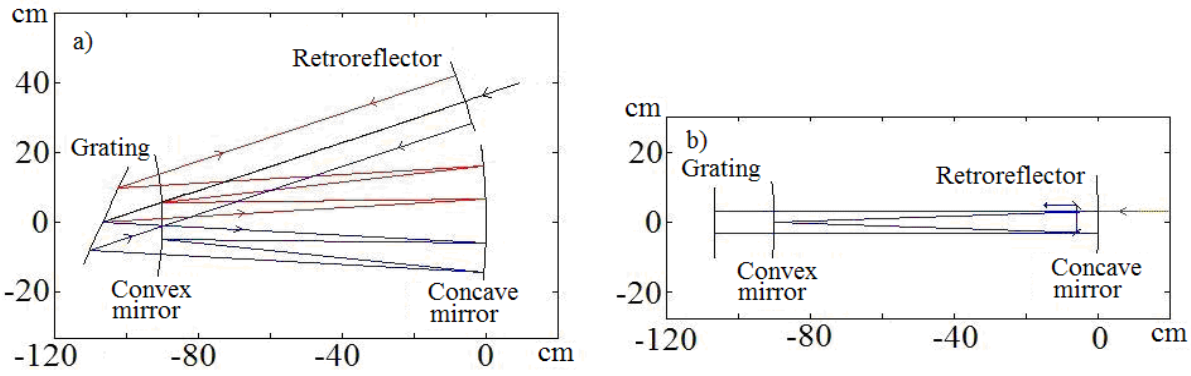

Fig. 1. Offner triplet telescope stretcher for PEARL laser system (top view (a) and side view (b))

The possibility of residual dispersion compensation due to translation and rotation grating of the stretcher was examined. It is shown that the residual dispersion of the fourth order distorts the temporal pulse profile only slightly. The residual phase of the system is calculated and it was shown that the value of the phase is less than the residual phase in the stretcher-compressor. So, the phase introduced by the amplifier can be neglected.

References

1. V.V. Lozhkarev, G.I. Freidman et al., *Laser Phys. Lett.*, 2007, **4**, 421.
2. O.E. Martinez, *IEEE Journal of Quantum Electronics*, 1987, **23**, 59.
3. Offner, *U.S. Patent 3,748,015*, 1973.

International Symposium

TOPICAL PROBLEMS OF NONLINEAR WAVE PHYSICS

NWP-3:

NONLINEAR PHENOMENA IN GEOPHYSICS

Invited

LIGHTNING LEADER EVOLUTION – OBSERVATIONS AND SIMULATIONS

M. Chen and **Ya-P. Du**

The Hong Kong Polytechnic University, HKSAR, China
mingli.chen@polyu.edu.hk

Abstract. This talk summarizes the authors' work on lightning leader formations in last decades. It includes two parts: (1) highly time-resolved observations of leader developments, and (2) simulations of leader evolutions. Part (1) includes: i) optical images of downward stepped leaders in natural lightning and bidirectional leaders in triggered lightning observed with ALPS, ii) spatial evolutions of leaders in triggered lightning observed with broadband VHF interferometer, and iii) charge evolutions of leaders based on simultaneous optical and electrical observations of leaders. Part (2) includes a 2D model for bi-directional leaders and a 3D self-organized model for downward stepped leaders.

Leader Observations

Downward Stepped Leader observed with ALPS: The first return stroke in cloud-to-ground lightning is always preceded by a stepped leader that travels downward. The stepped leader is generally thought to involve both a stepping and a more or less continuous charge transfer processes. With a high-speed digital 16 × 16 photodiode array photographic system (ALPS), the relative light intensities as a function of height and time for two negative downward stepped leaders (A and B) were recorded and investigated [1]. For the leader A, it was found that the light waveform for each segment of the leader channel started with a series of sharp light pulses followed by several slow-rising and longer-lasting light surges. Both the light pulses and surges appeared to superimpose on a continuous luminosity slope having a long rising front followed by an almost constant light level. Analysis showed that each light pulse involved a stepping process, which originated at the leader tip and propagated backward. The pulses suffered little degradation within the first tens to hundreds of meters from the leader tip backward (bright tip length), but with a severe attenuation behind the bright tip. The light surges behind the bright tip kept almost a constant in amplitude as it propagated upward at a speed of about 10^8 m/s. The leader had an overall downward speed of 4.5–11.2×l0^5 m/s, a step interval of 5–50 μs, and a step length of 7.9–19.8 m. Similar results were obtained for the leader B. Based on these results, it was inferred that the current of a stepped leader may consist of two parts: an impulsive current within the leader bright tip and a continuing current behind the tip. After propagating along the bright tip up, because of increasing impedance of the leader channel behind the tip, the impulsive current attenuates rapidly into part of a continuing current.

Bi-directional leader observed with ALPS: Based on highly time-resolved optical images observed with the ALPS and electric fields observed with slow and fast antenna at a close distance to the rocket launcher, 5 altitude-triggered lightning flashes were recorded and analyzed [2]. The data showed that all the 5 flashes had a similar chronological sequence of events, including a bi-directional leader system followed by a mini-return stroke and a bi-directional discharge process. It was found that the bi-directional leader system consisted of an upward positive leader initiated from the top of the floating wire and a downward negative stepped leader from the bottom of it, with the onset of the former prior to the latter by 3 to 8.3 ms. The downward leader appeared to pause and resume several times, while the upward leader extended forward continuously. With the downward leader close to ground, a mini-return stroke occurred between ground and the bottom of the wire. The mini-return stroke propagated upward with a speed of 1–2×10^8 m/s and emitted intense light similar to a normal return stroke. It became invisible after entering the wire and appeared again as a bright upward discharge from the top of the wire several microseconds later. This bright upward discharge ceased after propagating forward several hundreds of meters at a speed of 1.5–5.4×10^7 m/s. The cessation of this bright upward discharge was obviously associated with the disintegration of the floating wire at that moment. Right after the cessation of the upper bright discharge, a bi-directional discharge process started from the bottom of the wire with its positively charged part having an upward speed of 3–10×10^5 m/s and its negatively charged part a downward speed of 2–2.6×10^5 m/s. Reflection of current waves at the bottom of the wire due to the wire explosion at that moment may be a major reason for the occurrence of this lower bi-directional discharge.

Leaders observed with VHF interferometer: A leader process may be invisible to an optical instrument but may emit intense VHF impulses. Based on a combination of a camera and a broadband VHF interferometer, the 3D spatial evolutions of the initiation leader process and the two leader-return

stroke processes involved in a classically-triggered lightning flash were rebuilt and analyzed. It was found that the initiation leader might start in the cloud and firstly propagated downward from about 930 m to 300 m high in a vertical manner and then moved in zigzag manner towards the tip of the triggering wire. Such a downward initiation leader process is not common in triggered lightning in the literature. The speed of the initiation leader decreased from 3.7 to 0.3×10^6 m/s as it descended. The leader preceding the first return stroke (L1) included three stages: L1a, L1b and L1c. At stage L1a, the leader started inside the cloud and propagated downward, but with a different channel to that of the initiation leader. At stage L1b, as the leader descended to about 300 m high, it turned to propagate along the same zigzag portion of the initiation leader trace toward the tip of the triggering wire trace. At stage L1c, as the leader attached to the tip of the triggering wire trace, it turned to propagate upward along the same vertical portion of the initiation leader trace. The stage L1c might be a reflection of L1a at the tip of triggering wire trace due to different conductivities between the leader channel in air and the melt triggering wire trace. The speed for L1a showed a decrease from 2.32 to 0.32×10^6 m/s as it descended, while that for L1c showed an increase from 0.85 to 2.7×10^6 m/s as it ascended. The speed for L1b was in a range of $0.4\sim1.1\times10^6$ m/s. The leader preceding the second return stroke (L2) behaved similarly to that of L1 but with higher speeds.

Leader charge evolution: Besides the leader spatial evolution, knowing the evolution of the leader charge is also critical to understanding the mechanism of initiation and propagation of the leader. However, the leader charge along its channels has not been well-documented, mainly due to the lack of means to measure the charge density directly. In a recent study [3], we presented an approach for retrieving the temporal and spatial evolution of the charge density and the current of a steadily-developing upward leader based on ground observations of electrical fields and high speed camera images of two upward positive leaders initiated by a classically-triggered lightning technique. For the two leaders, both the leader speed and the charge density, hence the leader current, showed a trend of increase as the leader propagated upward. There was a good consistency in the variation trend between the calculated leader current and the leader channel brightness. The calculated leader current agreed well with the current measured at the channel base, indicating that our proposed method for retrieving the leader charge density is effective and reliable. More recently, similar works have been done for two downward negative leaders too.

Leader Simulations

To make more improvements to existing models, we presented recently two leader models: a 2D bidirectional leader model and a 3D self-organized model for downward negative stepped leader [4–5]. In this 3D model, the characteristic features of stepped leaders were generalized, so that parameters such as the charge density along the leader channel, leader corona sheath radius, leader step length, step time interval, and step advance speed were calculated. A stepwise growth of 3D leader channel was developed stochastically. Parameters predicted by the model were qualitatively compatible with observation results, while the engineering approximation of the model for convenient lightning protection analysis was derived thereafter. Moreover, the lightning striking distance to flat ground was also defined and calculated. It was found that the striking distance is well associated with the charge density (or electrical potential) of the leader tip near to ground rather than the total charge in the leader channel. Finally, based on appropriate physical understanding, the striking distance was linked to the return stroke peak current that follows the leader.

Acknowledgements

This work was supported by The Hong Kong Polytechnic University and Research Grant Council of Hong Kong Government (Grant no.: PolyU512511E).

References

1. M. Chen, N. Takagi, T. Watanabe, et al., *J. G. R.*, 1999, **104**(D22), 27573- 27584.
2. M. Chen, T. Watanabe, N. et al., *J. G. R.*, 2003, **108**(D8), doi: 10.1029/2002JD002676.
3. M. Chen, D. Zheng, Y. Du, Y. Zhang, *J. G. R.*, 2013, **118**, 4670-4678, doi:10.1002/jgrd.50446.
4. M. Chen, X. Gou, Y. Du, *Atmos. Res.*, 2013, **125**, 76-83, doi:10.1016/j.atmosres.2012.08.019.
5. Y. Xu, M. Chen, *IEEE Trans. (PWRD)*, 2013, **28**(4), 2342-2355, doi:10.1109/TPWRD.2013.2263846.

THE INFLUENCE OF AIR HUMIDITY ON AUTO-OSCILLATIONS ON GROUND SURFACE

V. Chernov

Institute of Applied Physics RAS
e-mail: vcher@appl.sci-nnov.ru

We report results of experimental study of the action of acoustic radiation on ground for a small loudspeaker height. Apart from the nonlinear effects observed in experiment [1], active impact of air humidity on the ground was revealed. Air humidity influences the amplitude and spectra of auto-oscillations in systems with positive feedback.

Auto-oscillations in air are known to be excited in the "microphone-amplifier-loudspeaker-air" system. These auto-oscillations are continuous. The air has no nonlinearity and dispersion in a wide range of pressures. We know that air humidity weakly influences sound velocity [2]. We know that ground is a porous medium with high nonlinearity. This property of ground was studied by a number of researchers [3, 4]. How does humidity of air influence auto-oscillations on ground surface? In particular, it would be very informative to investigate the phase relationship between a seismic signal in the ground and a source signal.

We study in experiment some features of the impact of air humidity on ground surface. The scheme of the experiment is shown in fig. 1. The signal from a generator is radiated by a vibrator which we mount on the ground surface (or a loudspeaker which is situated above ground surface). The seismic signals are received by accelerometers placed at different depths of the ground. The phase difference between the radiated and propagating signal is measured by a phase meter. Our observations show that the phase difference is not constant, it is changing in time [1].

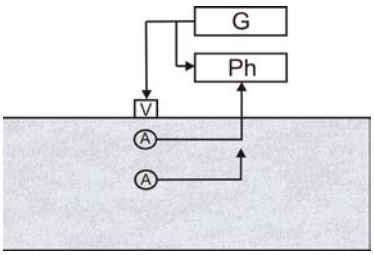

Fig. 1. The scheme of the experiment

Based on this phenomenon we could observe an interesting effect. Figure 2 shows a system with positive feedback.

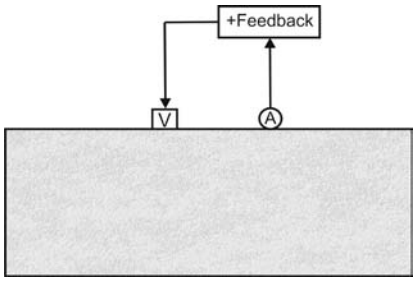

Fig. 2. The scheme of autooscillatory system: V – vibrator, A – accelerometer, + Feedback – amplifier

The ground area is included in this chain too. A vibrator or a loudspeaker may generate oscillations. The amplification coefficient in this system is about 60 dB. According to Nyquist criterion [5], this system is unstable, if the phase difference due to the chain is $\Delta\varphi = 2\pi n$, $n = 0, 1, \ldots$. The auto-oscillations generated in such a system are determined by the amplitude-frequency characteristic of the vibrator on the ground surface. This characteristic has resonance, and the oscillation frequency is defined by the following formula [6]:

$$\omega^2 = \frac{E\sqrt{S}}{kM},$$

where E is the modulus of elasticity defined by elastic properties of the ground; S is the area of contact of vibrator and ground; M is vibrator mass; κ is the coefficient of the base geometry. In the vicinity of resonance frequency, the phase characteristic has a jump by one pi. Thus, in the vicinity of resonance frequency, there exists a frequency which compensates the phase difference in other parts of the system.

The air humidity changes the elastic properties of the ground. However, this effect is not observed if the humidity is less than 30%. This phenomenon was verified by the following experiment. If we increase or decrease air humidity, we will observe resonance frequency changes (Figure 3). If the air humidity is less than 30%, we observe the influence of the temperature on the resonance frequency. Figure 4 illustrates the resonance frequency behavior with increasing or decreasing temperature.

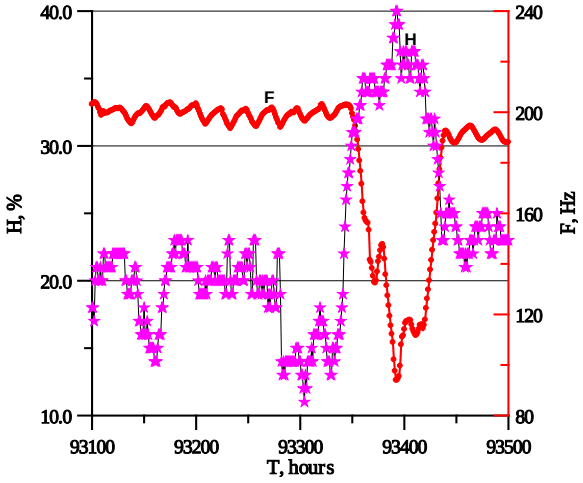

Fig. 3. The influence of humidity on autooscillation frequency

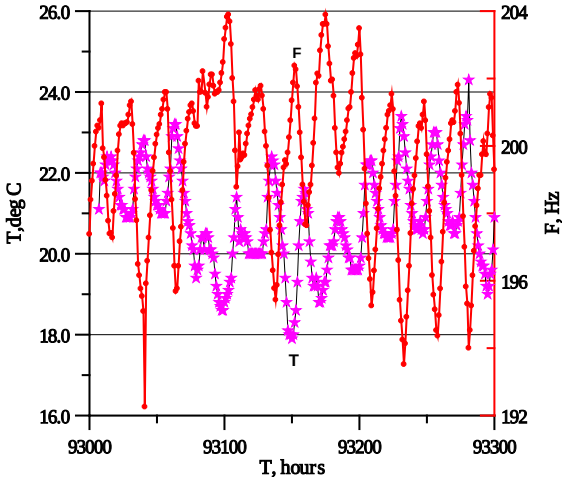

Fig. 4. The influence of temperature on autooscillation frequency for the humidity less than 30 %

Thus, air humidity and temperature influence elastic properties of the ground surface and resonance frequency of auto-oscillations in a system with positive feedback on the ground.

References

1. V. Chernov, "Some features of auto-oscillations on ground surface", *Proceedings of International Symposium "Topical Problems of Nonlinear Wave Physics* – 2008, Nonlinear dynamics of electronic systems (NDES'2008)", Nizhny Novgorod, 2008, p. 12-13.
2. V.A. Babincev, E.A. Vinogradov, and K.F. Shipilov, "The Influence of the humidity on the sound velocity in air", http://zhurnal.ape.relarn.ru/articles/2003/215.pdf.
3. A.S. Aleshin, V.V. Guschin, M.M. Krekov, A.V. Nikolaev, A.V. Sokolov, and G.M. Shalashov, "The experimental investigations of nonlinear interactions of surface seismic waves", *DAN USSR*, 1981, **260**(3), 574-575.
4. A.V. Nikolaev, "The problems of nonlinear seismology", 1987, M., Nauka.
5. H. Nyquist, *Bell System Techn. J.*, 1932, **11**, 126-147.
6. I.P. Pasechnik "The research of the resonant phenomena in the ground - seismograph system", *Izv. AN USSR, A series geophysical*, 1952, **5**.

ELECTROMAGNETIC RESPONSE OF THE INHOMOGENEOUS ANISOTROPIC ATMOSPHERE TO A SINGLE LIGHTNING DISCHARGE

S.S. Davydenko[1], **S.A. Savikhin**[2], **A.S. Sergeev**[1], and **S.A. Zolotov**[2]

[1] Institute of Applied Physics of the Russian Academy of Sciences, Nizhny Novgorod, Russia
[2] Special Computing Technologies LCC, Nizhny Novgorod, Russia

Abstract. 3D numerical model of the electromagnetic environment of an isolated lightning discharge in the plane atmosphere is developed. Spatiotemporal distribution of the discharge current depends on the flash type and generally consists of different components, such as the return stroke and continuous current. Disturbance of the electric conductivity inside the thundercloud and anisotropy of the upper atmosphere conductivity are taken into account. The model describes both the quasistatic electric field burst caused by the Maxwell's relaxation of the charge disturbance and electromagnetic pulse generated mainly by the return stroke. An application of the model to both direct and inverse problems of the atmospheric electrodynamics is discussed.

Introduction

The developed models of the electrical response of the atmosphere to the lightning discharge are based on the curl-free (quasi-static) approximation for the electric field or on the complete set of Maxwell equations. The quasistatic axially symmetric models, in particular, are used to simulate the dynamics of sprite halos and sprite streamers (see, for instance, [Qin et al., 2013]) and to estimate the lightning discharge contribution to the global circuit [Mareev et al., 2008]. The models based on the complete set of Maxwell's equations are able to describe also the lightning-induced electromagnetic pulse, so these are usually used for simulation of the upper atmosphere heating/ionization after the lightning discharge and optical emissions known as elves (see, for instance, [Marshall, 2012]). Being focused on the upper atmosphere response to the electromagnetic pulse, these models consider a short time interval after the discharge. However, it is important to consider the lightning-induced atmospheric electric field at larger times to estimate an influence of the upper atmosphere on the charge transfer and currents induced by the lightning discharge. Some evidences that this influence may be significant were presented by Ma et al. [1998]. Here, we consider a 3D model of the electric environment of an isolated lightning discharge based on a complete set of the Maxwell's equations. The model describes both the electromagnetic pulse generated mainly by the return stroke and slow transient electric field driven by the Maxwell relaxation of the lightning-produced disturbance of the charge density.

Model Basics and Sample Results

The electric (**E**) and magnetic (**H**) fields in the vicinity of the lightning discharge in the plain atmosphere are determined by the Maxwell's equations:

$$\nabla\times\mathbf{E}=-\mu_0\frac{\partial\mathbf{H}}{\partial t},\quad \nabla\times\mathbf{H}=\boldsymbol{\sigma}\mathbf{E}+\varepsilon_0\frac{\partial\mathbf{E}}{\partial t}+\mathbf{j}_{\text{ext}}(\mathbf{r},t),\quad \nabla\cdot\mathbf{E}=\rho/\varepsilon_0,\quad \nabla\cdot\mathbf{H}=0. \tag{1}$$

Here $\mathbf{j}_{\text{ext}}(\mathbf{r},t)$ is the discharge (source) current density, tensor $\boldsymbol{\sigma}(\mathbf{r})$ describes the conductivity of the medium, ρ is the charge density, ε_0 and μ_0 are the electric and magnetic constants, respectively. Generally, distributions of both the source current and conductivity are assumed to be arbitrary. Since the Cartesian coordinate system is adopted in the model, the computational domain has the shape of a parallelepiped with a height of (up to) 150 km and horizontal sizes of a few hundreds kilometers. The top and bottom plane boundaries of the domain are assumed to be perfect conductors. The equations (1) were solved numerically using the FDTD method.

The atmospheric conductivity is assumed to be isotropic up to the height of 70 km and anisotropic at higher altitudes. In the lower atmosphere away from the source region the conductivity grows exponentially with the height *z* according to the relation $\sigma_0\exp(z/H)$, where $\sigma_0=5\cdot10^{-14}$ S/m is the conductivity near the ground (at the height z = 0) and $H=6\cdot10^3$ m is the scale height of the conductivity profile. Near the source, inside the thundercloud of arbitrary shape, the conductivity is assumed to be disturbed: the ratio of the conductivities inside and outside the thundercloud at the same altitude is one of the parameters of the model. The source current is localized inside the thundercloud and may have an arbitrary direction and spatial distribution. Depending on the discharge type (intracloud or cloud-to-ground) the source current may include different constituents, such as the

return stroke, continuous current, and M-component, with the appropriate temporal profiles (see [Davydenko et al., 2011]).

To illustrate the capabilities of the model, the electric field of the symmetric source in anisotropic upper part of the atmosphere is presented (see Fig.1). Here, the source represents the vertical cloud-to-ground discharge with the height and radius of the arisen charged region of about 9.5 and 4 km, respectively, the total neutralized electric charge is equal to 1 C; the source current reaches the maximum within 40 μs, total duration of the discharge is equal to 1 ms. At the heights of more than 70 km the conductivity is anisotropic, so the parallel, Hall and Pedersen components of the conductivity tensor are taken into account; the geomagnetic field is inclined at 40° to the vertical axis.

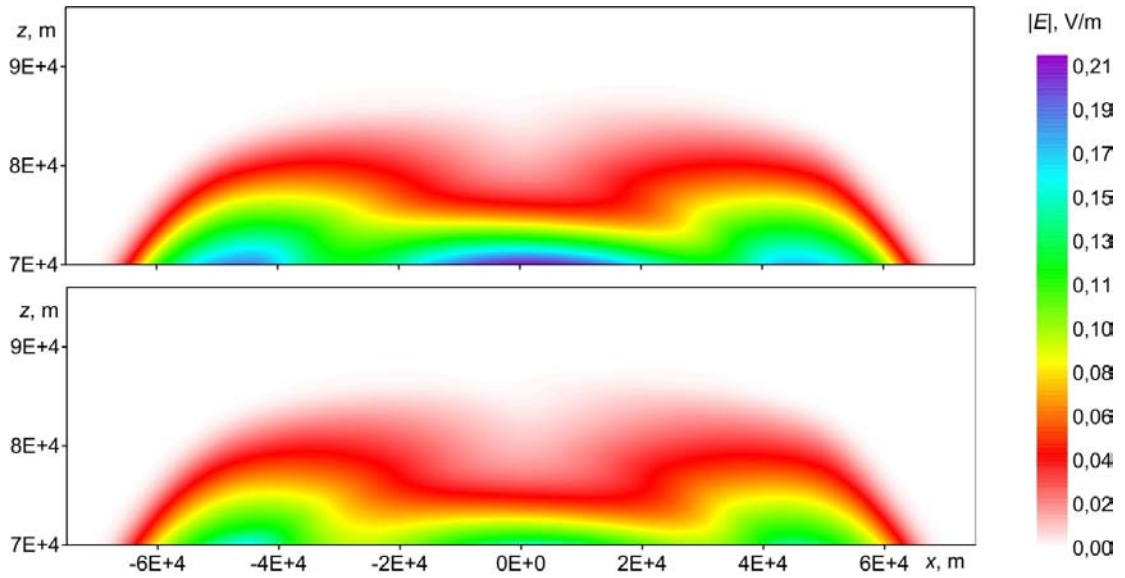

Fig. 1. The vertical cross-sections of the electric field distribution at the time moment 0.3 ms after the vertical cloud-to-ground discharge. The cross-section plane contains both the vertical axis and geomagnetic field vector. The top and bottom panels represent distributions of the absolute values of the electric field and its transversal (normal to the geomagnetic field) component, respectively. An asymmetry of the total electric field distribution and formation of the ELF pulse are well recognized

The presented model describes both the quasistatic electric field and the electromagnetic pulse of a single lightning discharge in the plain atmosphere taking into account disturbance of the electric conductivity inside the thundercloud and anisotropy of the upper atmosphere. The model can be applied to both direct and inverse problems of the atmospheric electrodynamics. These are tightly connected with the TLE modeling and retrieving information on the electric properties of the lightning discharge, in particular the temporal profile of the discharge current, location of the charged region(s) arisen due to the discharge, and disturbance of the electric conductivity inside the thundercloud.

Acknowledgements

The work is supported in part by the Russian Foundation for Basic Research (projects 13-05-01100 and 13-05-97063) and Government of the Russian Federation (contract 14.B25.31.0023).

References

1. S.S. Davydenko, E.A. Mareev, A.S. Sergeev, and Yu.V. Shlyugaev, "Modeling Atmospheric Electromagnetic Field Following a Lightning Discharge", *Proc. XIV Int. Conf. Atmospheric Electricity, 07-12 August, 2011, Rio de Janeiro, Brazil*, 2011, paper 229, 1-4.
2. Z. Ma, C.L. Croskey, and L.C. Hale, "The electrodynamic responses of the atmosphere and ionosphere to the lightning discharge", *J. Atmos. Solar-Terr. Phys.*, 1998, **60**(7-9), 845-861.
3. E.A. Mareev, S.A. Yashunun, S.S. Davydenko, T.C. Marshall, M. Stolzenburg, and C.R. Maggio, "On the role of transient currents in the global electric circuit", *Geophys. Res. Lett.*, 2008, **35**, L15810.
4. R.A. Marshall, "An improved model of the lightning electromagnetic field interaction with the D-region ionosphere", *J. Geophys. Res.*, 2012, **117**, A03316, doi:10.1029/2011JA017408.
5. J. Qin, S. Celestin, and V.P. Pasko, "Dependence of positive and negative sprite morphology on lightning characteristics and upper atmospheric ambient conditions", 2013, **118**, 2623-2638.

ON THE ELECTRICAL STRUCTURE OF THE ARTIFICIAL CHARGED AEROSOL CLOUD

S.S. Davydenko[1], **D.I. Iudin**[1,2], **V.Yu. Klimashov**[2], **A.Yu. Kostinskiy**[1,3], and **V.S. Syssoev**[1,4]

[1] Institute of Applied Physics of the Russian Academy of Sciences, Nizhny Novgorod, Russia
[2] Radiophysical Research Institute, Nizhny Novgorod, Russia
[3] Higher School of Economics, Moscow, Russia
[4] High Voltage Research Centre, All-Russia Institute of Electrical Engineering, Istra, Moscow region, Russia

Abstract. Based on the assumption that the charge density can be represented as a superposition of the regular and irregular parts, a model of the electrical structure of the artificial charged aerosol cloud is developed. The regular part of the charge density is calculated in the stationary current approximation taking into account the source current structure and disturbance of the electric conductivity in the vicinity of the cloud. The irregular part describes random spatiotemporal fluctuations of the charge density. It is shown that the charge density fluctuations can lead to a significant local enhancement of the electric field and serve as one of the important mechanism of the spark initiation.

Introduction

An original aeroelectrical facility based on the source of the aquated ions and high-voltage discharger was recently developed in High Voltage Research Centre of the All-Russian Institute of Electrical Engineering (Istra, Moscow region). The facility generates a unipolar charged aerosol cloud with a volume of about 30 cubic meters under atmospheric conditions. The artificial charged cloud can serve as a hand-operated source of spark discharges similar to the thunderstorm lightning discharges. The goal of this study is to consider an influence of the random inhomogeneity of the charge density inside the electrified cloud on the small-scale local enhancement of the electric field that could play a crucial role in the lightning initiation [Trakhtengerts et al., 2002; Iudin et al., 2003].

Model Basics and Main Results

It is assumed that the electric structure of the cloud consists of the steady-state and perturbed components. The steady-state component of the charge density is calculated in the framework of the stationary current approximation. Since the electrified cloud is generated by the given flow of the charged aerosols (see [Andreev et al., 2014]), the model assumes that the source current is started upward from a point at the ground level and has a cone shape. The value of the source current is equal to 90 μA. The electric conductivity in the vicinity of the cloud is assumed to be about 200 times more than the unperturbed conductivity of the atmosphere. As a result, the steady state distribution of the charge density and corresponding distribution of the electric field are obtained.

The perturbed component of the electric structure represents the random fluctuations of the charge density within the electrified cloud. It is assumed that the charge density is proportional to the aerosol volume density. For initial estimates, the spatial structure of the perturbations is represented as a set of the Gaussian disturbances with the spatial scales ranged from a few decimeters to several meters and standard deviations decreasing with the scale according to the power low. The magnitude of the perturbations is proportional to the value of the steady-state component of the charge density (see Fig. 1). The perturbed component of the electric field is calculated using the Coulomb low taking into account the perfectly conducting ground (since the decay time of the perturbed component is substantially less as compared to the Maxwell relaxation time in the vicinity of the cloud, such approach seems valid).

A sample structure of the total, both steady-state and perturbed, electric field for typical parameters of the charged aerosol cloud is presented in Fig. 2. For the selected parameters of the cloud, the maximal value of the steady-state electric field is less than 10 kV/cm, i.e. the field does not exceed the threshold of the negative streamer development. According to the model, taking into account the contribution of the perturbed component provides a significant local enhancement of the electric field. Namely, under considered parameters of the cloud the maximal value of the total field exceeds the threshold value more than 2.5 times. Based on the above results, one can conclude that the fluctuations of the electric charge density inside the artificial cloud could lead to the discharge development and serve as one of the important mechanisms of the spark initiation.

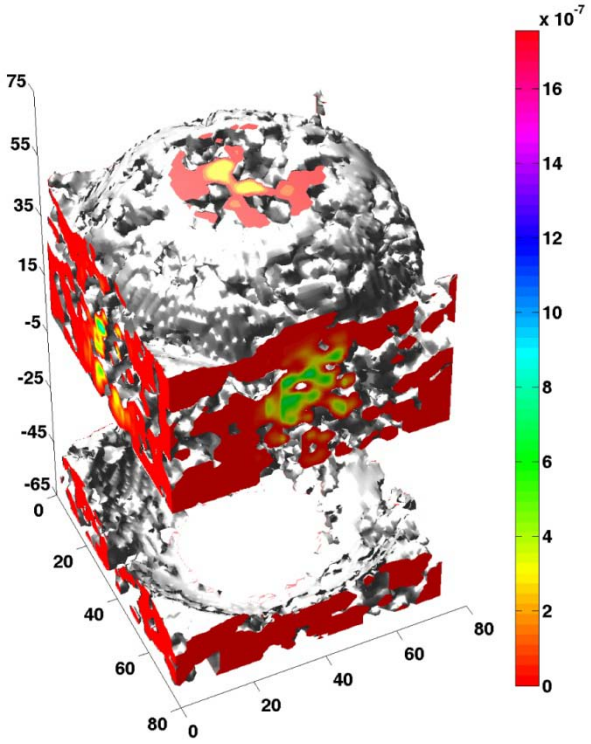

Fig. 1. Distribution of the perturbed component of the electric charge density. The plane $z = 0$ corresponds to the ground level

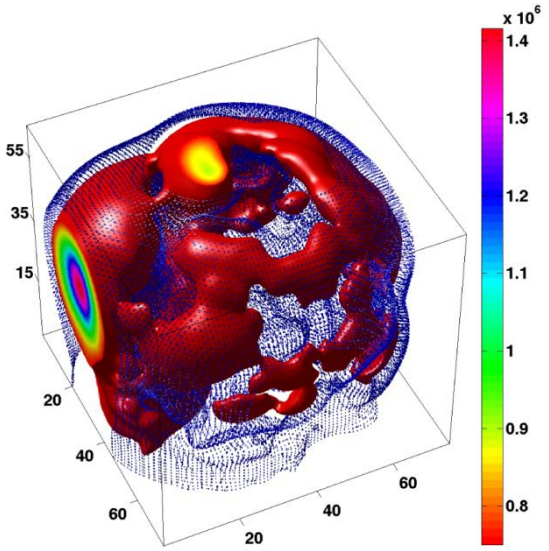

Fig. 2. Spatial structure of the total electric field. The red surface corresponds to the electric field magnitude of 7.5 kV/cm. The surface represented by the blue cones corresponds to the electric field magnitude 7 kV/cm. The plane $z = 0$ corresponds to the ground level, the colour scale is graduated in kilovolts per centimetre, the horizontal and vertical axes are graduated in decimetres

Acknowledgements

The work is supported in part by the Russian Foundation for Basic Research (projects 13-05-01100 and 13-01-97063) and Government of the Russian Federation (contract No.11.G34.31.0048.).

References

1. M.G. Andreev, N.A. Bogatov, A.Yu. Kostinskiy, L.M. Makal'sky, E.A. Mareev, D.I. Sukharevsky, V.S. Syssoev, "First detailed observations of discharges within the artificial charged aerosol cloud", 2014, *Proc. XV Int. Conf. Atmospheric Electricity, 15-20 June, 2014, Norman, Oklahoma, USA.*
2. D.I. Iudin, V.Y. Trakhtengertz, and M. Hayakawa, "Fractal dynamics of electric discharges in a thundercloud", *Phys. Rev. E*, 2003, **68**, 016601, doi:10.1103/PhysRevE.68.016601.
3. V.Y. Trakhtengerts, D.I. Iudin, A.V. Kulchitsky, and M. Hayakawa, "Kinetics of runaway electrons in a stochastic electric field", *Phys. Plasmas*, 2002, **9**(6).

THE AXIALLY-SYMMETRIC PLASMA-CHEMICAL MODEL OF HALO

A.A. Evtushenko and **F.A. Kuterin**

Institute of Applied Physics RAS, Nizhny Novgorod, Russia
a_evtushenko@inbox.ru

Abstract. We developed the plasma-chemical self-consistent model to describe the influence of halo on the chemical balance of the mesosphere and lower thermosphere as well as the optical emissions in different bands. An isolated cloud-to-ground discharge is considered as a source of the electromagnetic field at the heights of mesosphere.

We upgrade our 1D plasma-chemical model for high-altitude discharges [1] to the axially-symmetric one and apply it for halo modeling. To describe chemical composition of mesosphere we take into account 61 chemical constituents (neutrals, electrons, positive and negative ions) and use 267 chemical reactions. As a source of the electric field at the mesospheric heights we consider an isolated cloud-to-ground discharge [2]. Electric charge is accumulated on the disk with radius 10 km and 2D Gaussian distribution of electric charge density with a standard deviation of 2 km. A temporal profile of the discharge current consists of the return stroke and continuous current components. Taking into account high conductivity of the Earth's surface we use the dipole approach to calculate the electric field at the heights of the mesosphere.

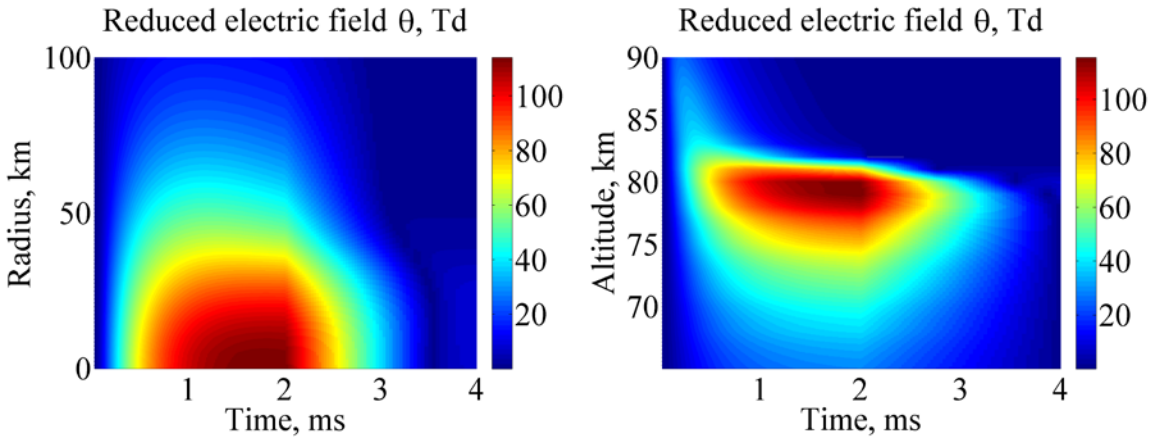

Fig. 1. Radial and altitudinal dependence of electric field

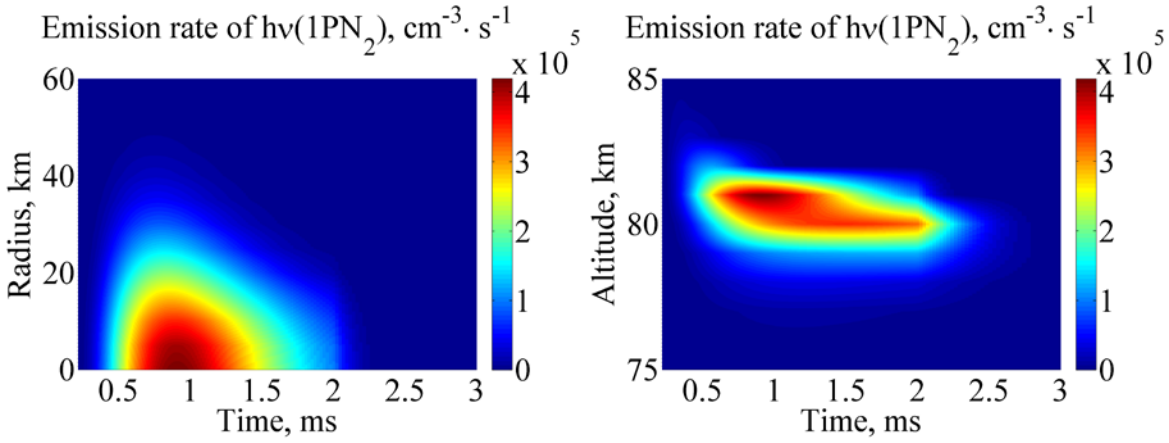

Fig. 2. Emission rate in the first positive band of nitrogen

The total electric charge on the disc is an integral of electric current in the lightning channel during discharge (2 ms) and after the end of current flow electric charge decreases exponentially during 2 ms. The halo discharge begins 0.5 ms after the beginning of lightning discharge at the height near 81 km. The maximum value of electric field in the mesosphere is around 110 Td at the height of 80 km, exceeds 100 Td at the heights between 77.5 and 80.5 km and when the radius is smaller than 20 km (Fig. 1). The characteristic relaxation time of the electric field is several hundreds of microseconds.

The duration of halo emission is about 2 ms at the bottom and 1 ms on the top of the discharge. The emission rate in the center of halo (radius doesn't exceed 10 km) is 2 times more intensive than for the radius of 20 km.

Conclusions

We developed a plasma-chemical self-consistent axially-symmetric model of the halo influence on the chemical balance of mesosphere as well as the optical emissions in different bands. It is shown that halo practically does not disturb chemical balance of the mesosphere. Most intensive optical emissions are in the first and the second positive bands of nitrogen. The halo radius is about 20 km and the vertical size is not more than 3 km.

Acknowledgments

This work was supported in part by the RFBR (project No.13-05-01139, 13-05-12103), and the Russian Government contract No 14.B25.31.0023.

References

1. A. Evtushenko, E. Mareev, *J. Radiophys. Quantum Electron.*, 2011, **54**(2), 123–140.
2. A. Evtushenko, F. Kuterin, E. Mareev, *J. Atmos. Sol. Terr. Phys.*, 2013, **102**, 298–310.

Invited

GLOBAL EMPIRICAL RECONSTRUCTION OF COMPLEX SYSTEMS: GENERAL APPROACH & APPLICATION TO CLIMATE MODELING

A.M. Feigin[1,2], **D.N. Mukhin**[1], **E.M. Loskutov**[1], and **A.S. Gavrilov**[1,2]

[1] Institute of Applied Physics of the Russian Academy of Sciences, Nizhny Novgorod, Russia,
[2] Nizhny Novgorod State University, Nizhny Novgorod, Russia
feigin@appl.sci-nnov.ru

Abstract. The report surveys the current state of the new empirical approach to reconstructing an unknown evolution operator of complex (high-dimensional, spatially distributed, with a broad spectrum of temporal scales) systems.

The main goal of the reconstruction is prognosis (as long as possible) of the system evolution, and natural (environment and life) systems are the main application objects of the approach. The goal necessitates correct (as far as possible) reconstruction of deterministic properties of the system. The target applications make it impossible to reconstruct correctly even such a crucial deterministic attribute as embedding dimension: observed time series of natural variables are nearly always too noisy and short.

To overcome this critical contradiction the proposed approach combines several ideas:

i. To decompose the underlying system into *weakly coupled space-time patterns* ("modes") that make the basic contribution to the observed time series.

ii. To construct a models of the separate modes in the form of a *low-dimensional random dynamical system*.

iii. To optimize the mode models based on the Bayesian (probabilistic) approach, aiming at finding *optimal models that have optimal complexity*.

iv. To use the optimal models of extracted modes as building blocks for construction of the simplest possible adequate model of the system as a whole.

The apparent merit of the proposed approach is its objectiveness, in the first place. The intrinsic feature of the constructed model is description of the properties of the system that determine its evolution registered in experiments. Second, complexity (i.e., dimension and number of structural parameters) of such models are optimal in terms of their adequacy to available data, in particular, adequacy to the volume of information contained in the data about the system.

The methods of realization of the first three ideas are described. The capabilities of these methods are illustrated by both really measured and generated numerically vector time series of climatic observables. Three related papers of the same authors are devoted to detailed discussions of the proposed methods.

DECOMPOSITION OF COMPLEX SYSTEMS: NONLINEAR MODE EXTRACTION

A.S. Gavrilov[1,2], **D.N. Mukhin**[1], **E.M. Loskutov**[1], and **A.M. Feigin**[1,2]

[1] Institute of Applied Physics of the Russian Academy of Sciences, Nizhny Novgorod, Russia
[2] Nizhny Novgorod State University, Nizhny Novgorod, Russia
gavrilov@appl.sci-nnov.ru

Abstract. The method for constructing nonlinear basic dynamic modes by multivariate time series is presented. We apply the Bayesian approach for finding both time series of latent modes and the parameters of nonlinear transformation from modes space to observation data space. The simplest evolution law for each mode is included as prior information about the decomposition. The Bayesian evidence criterion is proposed to optimize the transformation structure parameters characterizing the degree of the parameterization nonlinearity. The method is tested on an example of a strongly nonlinear two-dimensional model and is applied to spatially distributed sea surface temperature time series over the Globe. It is shown that nonlinearity improves the data variance capturing by the modes.

Introduction

The task of reducing phase space dimension is very important in empirical climate modeling. The principal component analysis (PCA) applied to the matrix of correlations of data with itself can help to complete the task when the spatio-temporal data is close to the sum of a few modes in the form of time-dependent principal components (PCs) multiplied by space-dependent empirical orthogonal functions (EOFs), i.e. the sum of linear functions of the time series. But usually the observed global climate data cannot be presented in this form due to nonlinearity of spatio-temporal connections.

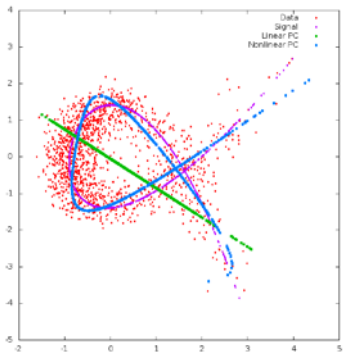

Fig. 1. Principal curves in the 2d data space (model example): noisy data (*red*), true signal (noiseless data) (*violet*), linear mode (*green*), nonlinear mode (*blue*)

The nonlinear principal component analysis assumes the modes to be inhomogeneous in space. The data is considered as a sum of nonlinear functions of PCs time series corresponding to nonlinear data projections. Evidently, such data representation is closer to the nature when the underlying system is a set of several weakly interacting nonlinear subsystems.

Optimal nonlinear dynamic modes: Bayesian approach

According to the nonlinear principal component analysis we search the nonlinear modes in the form of principal curves [1]. In this work a hierarchical algorithm for finding each curve is used. The first mode describes nonlinearly of the observed data; the second mode does the same with data residuals which are not described by the first component; and so on. The model generating the given data $\mathbf{X} = \{\mathbf{X}_1,\ldots,\mathbf{X}_N\}$ from the latent principal component time series $\mathbf{p} = \{p_1, \ldots, p_N\}$ on each step of the algorithm is written in the following form:

$$\mathbf{X}_i = \mathbf{F}(\boldsymbol{\mu}, p_i)+\sigma\cdot\xi_i, \qquad i = 1, \ldots, N. \tag{1}$$

Here $\mathbf{F}$ is nonlinear function of p parameterized by $\boldsymbol{\mu}$. It represents the nonlinear mode data set generated by the principal component. ξ_i is white Gaussian noise. Geometrically, equation (1) defines a set of points which are located in the σ-vicinity of the curve $\mathbf{F}$ in the data space.

The latent vector $\mathbf{p}$ as well as unknown parameters μ and σ are found from the Bayesian probabilistic approach. It leads to the following cost function which should be minimized over μ and $\mathbf{p}$ (σ can be excluded analytically):

$$L(\boldsymbol{\mu},\mathbf{p}) = \frac{N}{2}\ln\left(\frac{1}{N}\sum_{i=1}^{N}\left|\mathbf{X}_i - \mathbf{F}(\boldsymbol{\mu}, p_i)\right|^2\right) + \sum_{i=1}^{M}\left(\frac{\mu_i^2}{\sigma_{\mu_i}^2} + \ln\sigma_{\mu_i}^2\right) + \sum_{i=2}^{N}\left(\frac{(p_i - p_{i-1})^2}{\sigma_p^2} + \ln\sigma_p^2\right). \tag{2}$$

The first term of (2) corresponds to the likelihood of the model (1) for the observation data set. The second term describes the prior information about the form of the curve. It usually depends on the parametrization type and is needed to restrict curve properties such as smoothness or curvature. The third term is very important from the physical point of view, because it contains prior information about the PC dynamics. Mathematically, without this term we would have many equally probable parametrizations by parameter p for each curve, especially if the curve has self-intersections. Here we

suggest the simplest prior information restricting the time scale of the PC. We define nonlinear dynamic modes as the PCs restricted by prior information about their dynamics.

Another important question is: what is the maximal "degree of nonlinearity" which can be extracted from observed data without overfitting? The answer is given by the Bayesian evidence criterion (see, e.g. [2]). In the simple approximation it appears to be a well-known Schwartz criterion. We use a more general approximation leading to the cost function which should be maximized among parametrization types:

$$\Phi = L(\boldsymbol{\mu}^{\mathbf{m}}, \mathbf{p}^{m}) + \frac{1}{2}\ln|\mathbf{Q}| - \frac{M+N}{2}\ln 2\pi \,. \qquad (3)$$

Here **Q** is the matrix of the second derivatives of **F** with respect to **μ** and **p** at the point ($\boldsymbol{\mu}^{m}$, $\mathbf{p}^{m}$) corresponding to the minimum of (2).

Note that, if **F** is a linear function, then we have to choose PCs among linear directions in data space. In this case, prior information is not needed because the problem is well-posed, and as a result we get the standard PCA method with standard EOFs defining data components.

We tested the described approach by means of the model 2-dimensional dataset which was generated by strongly nonlinear mapping of the Lorentz system scalar variable corrupted by noise. The resulting linear and nonlinear modes in the 2d data space are shown in Fig. 1. The PCs time series are shown in Fig. 2. Evidently, nonlinear PC is much better in discovering latent signal properties.

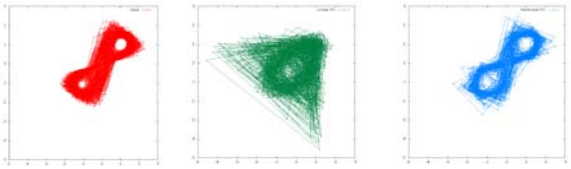

Fig. 2. 2D-delayed projection of latent signal (a), linear PC (b) and nonlinear PC (c)

Nonlinear dynamic modes of sea surface temperature anomalies

We applied the proposed approach to analysis of the sea surface temperature anomalies dataset lasting from 1981 to 2014. The data is taken from the satellite observations over the Globe [3] and has spatial resolution of 1×1 degree. The linear PC analysis gives about 100 EOFs which have a total variance of 88 %. We use the space of these EOFs as data space for nonlinear procedure, with PCs variances rescaled in the initial Earth surface space. The first two nonlinear PCs are shown in Fig. 3. They have the same time scale as the 1st linear PC.

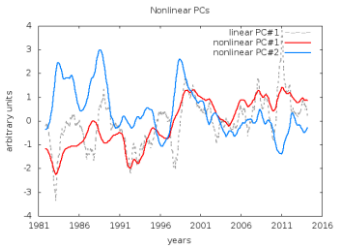

Fig. 3. 1st and 2nd nonlinear PCs compared to 1st linear PC

We also calculated the contributions of nonlinear modes to the data variance. It is known that linear PCA gives PCs variances spectrum with a heavy tail. The histograms of linear and nonlinear PCs variances are shown in Fig. 4. We can see that the nonlinear dynamic modes improve the variances separation in their spectrum: the 1st nonlinear mode appeared to capture significantly both the 1st and the 2nd linear modes. Let us note also that the ENSO phenomenon is mainly determined (90 %) by the 1st and 2nd linear modes, i. e. by the 1st nonlinear mode. In other words, it behaves like a “subsystem”, and it is in good correspondence with the previous investigations of ENSO.

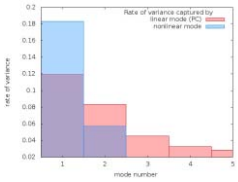

Fig. 4. Contributions of linear (red) and nonlinear (blue) modes to the data

Acknowledgements

The research is supported by the Ministry of Education of the Russian Federation (project No. 14.Z50.31.0033).

References

1. T. Hastie and W. Stuetzle, *Journal of the American Statistical Association*, 1989, **84**(406) (Jun.), 502-516.
2. H. Jeffreys, 1961, Theory of Probability, 3rd ed., Oxford University Press.
3. http://www.climatedatalibrary.cl/SOURCES/.NOAA/.NCEP/.EMC/.CMB/.GLOBAL/.Reyn_SmithOIv1/.monthly/.ssta/

PREDICTION OF LIGHTNING ACTIVITY BASED ON DIRECT ELECTRIC FIELD CALCULATIONS

S.O. Dementyeva[1,2], N.V. Ilin[1,2], and **E.A. Mareev[1,2]**

[1] Institute of Applied Physics RAS, Nizhny Novgorod, Russia, ilyin@appl.sci-nnov.ru
[2] N.I. Lobachevsky State University of Nizhny Novgorod, Nizhny Novgorod, Russia

Abstract. In this paper a new lightning prediction algorithm based on direct electric field calculations is presented. The model shows results that correlate with experimental data better than available indexes used for thunderstorms prediction.

Forecasting and nowcasting of lightning activity are fundamental problems and an extremely important goal for meteorological applications. Modern numerical weather prediction systems do not include any electricity effects such as electrification, Coulomb's forces etc. and therefore cannot explicitly predict lightning occurrence.

There are some attempts to predict lightning activity by indirect nonelectrical parameters [1–3]. Different indexes such as KI, CAPE, CPTP, and others are widespread in meteorology. Nowadays one of the most perspective indexes is Lightning Potential Index (LPI). The potential of modern numerical models and sufficient computation capacity allow applying direct algorithms of lightning forecasting based on electric field calculations. That is why an electric field and electric potential calculation algorithm innovative for forecasting systems was developed.

Forecasting of lightning activity in numerical weather prediction models

In this research we used the Weather Research and Forecasting (WRF) model [4]. WRF is a numerical system for weather prediction and simulation of the atmosphere, which can be used for scientific research, meteorological applications and education.

Nowadays Lightning Potential Index (LPI) [5, 6] is proposed as a new tool for predicting the lightning activity. It is intended for microphysical schemes including water vapor, cloud water, rain water, ice, snow and graupel as kinetic energy of the updraft in the developing thundercloud, scaled by the potential of charge separation. LPI has advantages over thermodynamical indexes, therefore, for natural data it significantly underestimates the size of the potential dangerous area.

Calculations of electric parameters

Because of inaccuracy of indexes as a lightning prediction tool, we worked out a new method of lightning flashes forecasting based on electric parameters calculations. We considered a noninductive mechanism of charge separation [7–9] with two types of particles which can transfer charge (graupel and ice in the WRF model). In the lower part of thundercloud (until temperature reaches the value of the reverse point –15 ºC at the height of 6 km [7]) ice particles transfer negative charge and graupel pellets transfer positive charge. In the upper part charge signs are reversed.

The WRF model predicts mixing ratios of hydrometeors:

$$q = m/m_{dry\ air}, \tag{1}$$

where q and m are mixing ratio and density (total mass in elementary air volume) of hydrometeors, $m_{dry\ air}$ – dry air density.

We suggest that charge densities of ice and graupel are proportional to its mass in elementary air volume. As the first normalization condition we chose electric neutrality in the vertical air column, which is in accordance with the suggestion of vertical charge separation due to collisions between falling graupel pellets and carried upward by updraft wind ice crystals. The second condition was maximum value of graupel charge $Q_g^{max} = 3 \cdot 10^{-12}$C, $n_g^{max} = 200$ m^{-3} [10]. Charge densities of graupel and ice are determined by the following equations:

$$\rho_g = (q_g/q_g^{max})\cdot Q_g^{max}\cdot n_g^{max}, \qquad \rho_i = (q_i/q_i^{max})\cdot\alpha, \tag{2}$$

where q are mixing ratios of hydrometeors, q^{max} are their maximum values, Q_g^{max} is maximum charge, collected on the graupel particle, n_g^{max} is maximum graupel concentration, α is the coefficient calculated from the neutrality condition.

For determining the electric field we solved the 3D Poisson's equation:

$$\Delta\varphi(x,y,z,t) = -\rho_\Sigma(x,y,z,t)/\varepsilon_0, \tag{3}$$

where φ is electric potential, ρ is charge density. The boundary conditions were periodical for x and y coordinates, zero-condition at lower boundary $\varphi(z = 0) = 0$ and typical value of the potential at upper boundary $\varphi(z = 20$ km$) = 250$ kV.

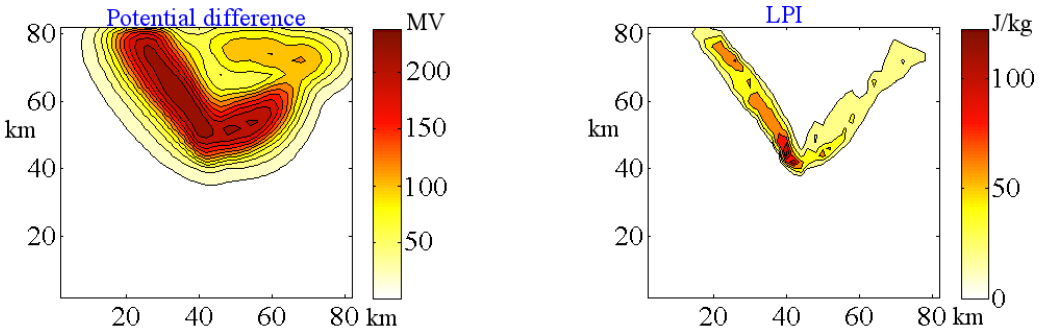

Fig. 1. Comparison of average potential difference and average LPI

Figure 1 shows the potential difference (between ground and cloud layer at the height of 7 km) and LPI averaged through the calculation time for the supercell test case of the WRF model. As we can see from figure 1, LPI indicates lightning activity over small concentrated areas, while at the same time the potential difference shows that the probability of dangerous thunderstorm occurrence is high over larger areas. Comparing figure 1 and results from [5, 6], we can make a conclusion that prediction of lightning activity based on the proposed electric field calculation method can be more reliable than the majority of current indirect prediction tools. Despite the rough assumption that charge densities are proportional to hydrometeors densities, based on it, the electric field calculation model shows results which correlate with natural data [11, 12] such as values of charge densities up to 2 nC/m^3, electric field up to 35 kV/m and potential difference up to 250 MV.

Conclusions

Comparison between experimental data and topographical maps of LPI (and other indexes) shows that LPI significantly underestimates the size of the area of potential lightning flashes occurrence. New algorithm of lightning prediction based on calculations of electric potential and electric field in thunderclouds is proposed. This method allowed comparing electric parameters, which are results of numerical simulations, with natural data. Results of electric field calculations correlate well with experimental data. The model shows that potential difference (between 0 and 7 km) reaches sufficient for discharge value on the area, which is wider than it is predicted by the lightning potential index.

Acknowledgements

This work was supported by the Russian Government (contract No. 14.B25.31.0023).

References

1. W.A. Petersen and S.A. Rutledge, *J. Geophys. Res.: Atmos.*, 1998, **103**(D12), 14025-14040.
2. D.J. Cecil, S.J. Goodman, D.J. Boccippio, E.J. Zipser, and S.W. Nesbitt, *Mon. Weather Rev.*, 2005, **133**(3), 543-566.
3. W.A. Petersen, H.J. Christian, and S.A. Rutledge, *Geophys. Res. Lett.*, 2005, **32**(14), L14819.
4. *www.wrf-model.org*.
5. Y. Yair, B. Lynn, C. Price, V. Kotroni, K. Lagouvardos, E. Morin, A. Mugnai, and M. del C. Llasat, *J. Geophys. Res.*, 2010, **115**(D4), D04205.
6. B. Lynn and Y. Yair, *Adv. Geosci.*, 2010, 23, 11-16.
7. C. Saunders, *Planetary Atmospheric Electricity*, Springer, 2008, 335-353.
8. A.A. Evtushenko and E.A. Mareev, *Atm. Res.*, 2009, **91**(2), 272-280.
9. A.A. Evtushenko and E.A. Mareev, *Izv. Atm. Ocean Phys.*, 2009, **45**(2), 242-252.
10. H. Volland, *Atmospheric Electrodynamics*, Springer-Verlag, Berlin, 1985, p. 201.
11. M.G. Bateman, T.C. Marshall, M. Stolzenburg, and W.D. Rust, *J. Geophys. Res.*, 1999, **104**(D8), 9643-9653.
12. M. Stolzenburg and T.C. Marshall, *J. Geophys. Res.*, 1998, **103**(D16), 19777-19790.

CELLULAR AUTOMATON MODELLING OF INTRACLOUD LIGHTNING

D.I. Iudin

Institute of Applied Physics of the Russian Academy of Sciences, Nizhny Novgorod, Russian Federation
iudin_di@nirfi.sci-nnov.ru

Abstract. There is a controversy in the lightning community regarding the origin and the role of the lower positive charge region in the cloud. Whatever the source of the lower positive charge, it is generally thought that it serves to enhance the electric field at the bottom of the main negative charge region and thereby facilitate the launching of a negatively-charged leader toward ground. On the other hand, the presence of an excessive lower positive charge region may prevent the occurrence of negative cloud-to-ground discharges by "blocking" the progression of the descending negative leader from reaching ground. Based on the graph theory and percolation theory, we develop a fractal simulation code to take into account the detailed space and temporal dynamics of the cloud discharge, and the fine structure of the electric field and charge in a cloud. The results will be compared with observations to address some problems of lightning initiation physics. We quantitatively and qualitatively examine the dependence of lightning type statistics on the magnitude and lateral structure of the lower positive charge region.

Introduction

Processes in a TC are very diverse and complicated. A classical cloud to ground (CG) lightning discharge includes three stages: Preliminary breakdown, leader formation and return stroke [7]. The existing theoretical models of lightning discharges are based on its similarity with a laboratory long spark. It actually relates to the leader formation and return stroke. But there is a very important difference, which concerns a preliminary stage of the discharge. In the case of a laboratory spark electrical charge is accumulated on a conducting wall(s) of a discharge space and flows down easily into the spark channel. It is not clear what mechanism could provide the electric charge gathering over all cloud volume (or over its considerable part) to the leader channel. Apparently a certain important process which ensures this gathering takes place during the preliminary breakdown stage. In its most developed phase, the preliminary breakdown stage lasts approximately one tenth of a second, and consists of numerous (up to 10.000) relatively weak discharges [6]. The experimental investigations have demonstrated several peculiarities at the preliminary stage, proving it to be a very complex and puzzling phenomenon.

Assuming that the preliminary breakdown pulse train is a manifestation of the interaction of a downward-extending negative leader channel with the lower positive charge region, Nag and Rakov recently qualitatively examined the inferred dependence of lightning type on the magnitude of this charge region [3]. We skip here the discussion of different hypotheses regarding the origin of the lower positive charge region (LPCR) that were particularly reviewed by Rakov and Uman [7].

Model

The lightning modeling tradition approach [4] is based on the well-known consideration [5, 10] where the self-similar structure of the discharge pattern is caused by features of an algorithm of Laplace fractal growth. The pattern grows stepwise. At each modeling time step only one bond is added to the pattern, linking a point of the pattern with a new point. We consider an electrical breakdown model which is principally different from the model outlined above [1, 2, 8, 9]. We are going to bring the idea that we can expect more adequate pictures on the development of discharge pattern if we change the above model at two points. The first suggestion is that streamers could develop simultaneously at different pattern peripheral points. Secondly, we suggest that the probability of streamer development has an essential anisotropy caused by the presence of a large-scale thunderstorm electricfield. Both changes are closely connected to each other. The point is that independent growth of various points of the pattern periphery pulls our problem together with the percolation one [1, 2].

Result and conclusion

The model discussed allows us to reproduce the lightning discharge patterns that may arise depending on the magnitude of the LPCR. If the magnitude of the lower positive charge relative to the main negative charge is smaller than a quarter, the descending negative leader will traverse the positive charge region and continue to propagate in a predominantly vertical direction to ground.

When the magnitude of LPCR is comparable in magnitude to that of the main negative charge, a descending negative part of discharge tree is likely to change its direction of propagation to predominantly horizontal (see Fig. 1).

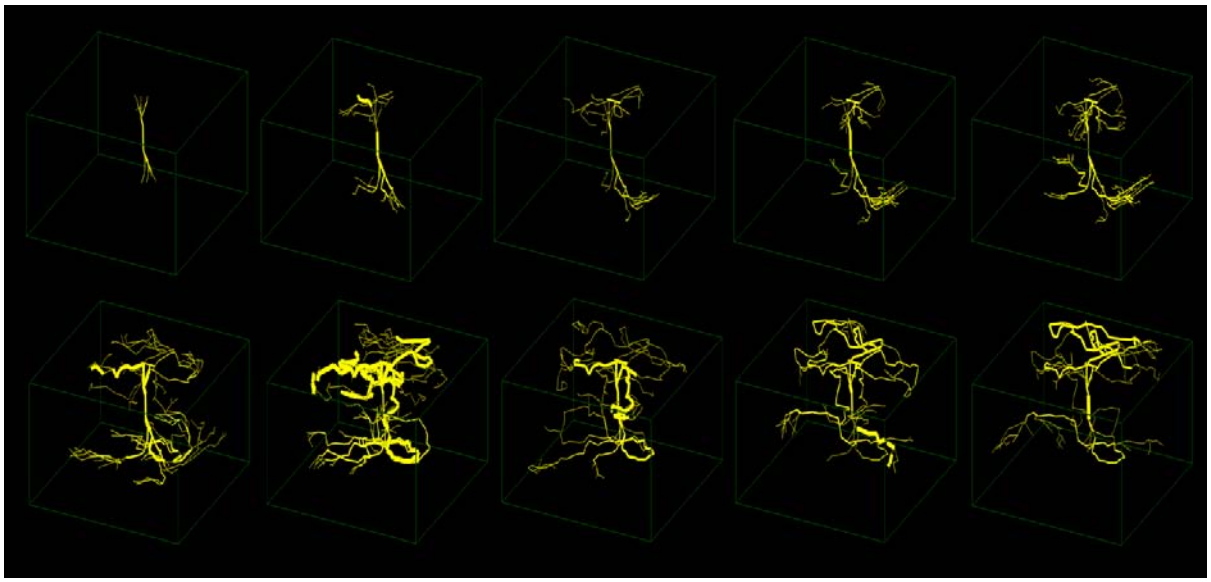

Fig. 1. The model 3D lightning discharge pattern for the case when the magnitude of LPCR is comparable in magnitude to that of the main negative charge

Our model reproduces four conceptual lightning scenarios that may arise depending on the magnitude of the LPCR. These scenarios were recently suggested and qualitatively discussed in [3].

Acknowledgements

This work was supported in part by the grants from the Government of the Russian Federation (contracts No. 14.B25.31.0023; No. 11.G34.31.0048) and by the Russian Foundation for Basic Research (project No. 13-01-97063).

References

1. D.I. Iudin, V.Y. Trakhtengertz, and M. Hayakawa, “Fractal dynamics of electric discharges in a thundercloud”, *Phys. Rev. E*, 2003, **68**, 016601, doi:10.1103/PhysRevE.68.016601.
2. M. Hayakawa, D.I. Iudin, and V.Y. Trakhtengerts, “Modeling of thundercloud VHF/UHF radiation on the lightning preliminary breakdown stage”, *J. Atmos. Solar-terr. Phys.*, 2008, **70**, 1660-1668, doi:10.1016/j. jastp.2008.06.011.
3. A. Nag and V.A. Rakov, “Some inferences on the role of lower positive charge region in facilitating different types of lightning”, *Geophysical Research Letters*, 2009, **36**, L05815, doi:10.1029/2008GL036783.
4. E.R. Mansell, D.R. MacGorman, C.L. Ziegler, J.M. Straka, “Simulated three-dimensional branched lightning in a numerical thunderstorm model”, *Journal of Geophysical Research*, 2002, **107**(D9), 4075, 10.1029/2000JD000244.
5. L. Niemeyer, L. Pietronero, and H.J. Wiesmann, “Fractal dimension of dielectric breakdown”, *Phys. Rev. Lett*., 1984, **52**(12), 1033-1036.
6. D.E. Proctor, R. Uytenbogaargt, and B.M. Meredith, “VHF radio pictures of lightning flashes to ground”, *Journal of Geophysical Research*, 1988, **93**(D 10), 12683-12727.
7. V.A. Rakov, and M.A. Uman, “Lightning: Physics and Effects”, 2003, Cambridge Univ. Press.
8. V.Y. Trakhtengerts, D.I. Iudin, A.V. Kulchitsky, and M. Hayakawa, “Kinetics of runaway electrons in a stochastic electric field”, *Phys. Plasmas*, 2002, **9**(6), June.
9. V.Y. Trakhtengerts, D.I. Iudin, A.V. Kulchitsky, and M. Hayakawa, “Electron acceleration by a stochastic electric field in the atmospheric layer”, Phys. Plasmas, 2003,**10**, 3290; doi: 10.1063/1.1584679.
10. H.J. Wiesmann, and H.R. Zeller, “A fractal model of dielectric breakdown and prebreakdown in solid dielectrics”, *J. Appl. Phys*., 1986, **60**, 1770-1773.

NUMERICAL ANALYSIS AND ANALYTICAL RELATIONS FOR STATIONARY AND NON-STATIONARY MODELS OF THE GLOBAL ELECTRIC CURCUIT

A.V. Kalinin[1,2], **E.A. Mareev**[1,2], **N.N. Slyunyaev**[1,2], and **A.A. Zhidkov**[2]

[1] Institute of Applied Physics, Russian Academy of Sciences, Nizhny Novgorod, Russia
[2] University of Nizhny Novgorod, Nizhny Novgorod, Russia, avk@mail.ru

Much attention has been given recently to the study of the global atmospheric electric circuit and, in particular, to its modeling [1–5].

We discuss and analyze different problem formulations concerning modeling the global atmospheric electric circuit within steady-state and non-stationary approaches. We study the question of whether the problem is well-posed for several possible approaches to establishing the boundary conditions which are natural from the physical perspective. In particular, we discuss problem formulations in which the ionospheric potential – that is, the potential difference between the Earth's surface and the upper boundary of the atmosphere – is not explicitly specified but is uniquely determined from the solution. We also find well-posed problem formulations for the electric potential in the case where the conductivity is anisotropic due to the substantial influence of the magnetic field at altitudes exceeding 70 km. In particular, we analyze the problem formulation in which the boundary condition at the outer boundary requires that the values of the potential at magnetically conjugate points be equal [6, 7].

For all the discussed problems we find equivalent formulations in the form of integral identities, which serve as the foundation for the development of projection numerical algorithms (employing, e.g., the Ritz method or the Galerkin method). We obtain and justify discrete relationships within the framework of the finite-element approach.

We also discuss a number of analytical relationships which make it possible to determine the ionospheric potential from the given spatial distributions of the conductivity and the external current density, the latter describing generators of the global electric circuit.

Acknowledgements

This work was supported by the grant from the Government of the Russian Federation (contract no. 11.G34.31.0048).

References

1. M.J. Rycroft and R.G. Harrison, "Electromagnetic atmosphere-plasma coupling: The global atmospheric electric circuit", *Space Sci. Rev*., 2012, **168**, 363–384, doi:10.1007/s11214-011-9830-8.
2. M.J. Rycroft and R.G. Harrison, "Electromagnetic atmosphere-plasma coupling: The global atmospheric electric circuit", Space Sci. Rev., 2012, **168**, 363–384, doi:10.1007/s11214-011-9830-8.
3. B.A. Tinsley and L. Zhou, "Initial results of a global circuit model with variable stratospheric and tropospheric aerosols", *J. Geophys. Res*., 2006, **111**, D16 205, doi: 10.1029/2005JD006988.
4. E.R. Wiliams, "The global electrical circuit: A re-view", *Atmos. Res*., 2009, **91**, 140–152, doi:10.1016/j.atmosres. 2008.05.018.
5. E.R. Williams and E.A. Mareev, "Recent progress on the global electrical circuit", *Atmos. Res*., 2014, **135–136**, 208–227, doi:10.1016/j.atmosres.2013.05.015.
6. P.B. Hays and R.G. Roble, "A quasi-static model of global atmospheric electricity, 1. The lower atmosphere", *J. Geophys. Res*., 1979, **84**, 3291–3305, doi:10.1029/ JA084iA07p03291.
7. T. Ogawa, "Fair-weather electricity", *J. Geophys. Res*., 1985, **90**, 5951–5960, doi:10.1029/JD090iD04p05951.

DATA-DRIVEN CLIMATE MODELING AND PREDICTION

D. Kondrashov[1], M.D. Chekroun[1], and M. Ghil[1,2]

[1]University of California, Los Angeles, USA
dkondras@atmos.ucla.edu
[2] Geosciences Department & Laboratoire de Météorologie Dynamique (CNRS and IPSL),
Ecole Normale Supérieure, Paris, France

Abstract. Comprehensive dynamical climate models aim to simulate past, present and future climate; more recently, they also attempt to predict climate on longer and longer time scales. These models, commonly known as general circulation models or global climate models (GCMs), represent a broad range of time and space scales and use a state vector that has many millions of degrees of freedom. Considerable work, both theoretical and data-based, has shown that much of the observed climate variability can be represented with a substantially smaller number of degrees of freedom. While detailed weather prediction out to a few days requires high numerical resolution, it is fairly clear that a major fraction of climate variance can be predicted in a much lower-dimensional phase space. Low-dimensional models (LDMs) can simulate and predict this fraction of variability, provided they are able to account for (i) linear and nonlinear interactions between the resolved high-variance climate components; and (ii) the interactions between the small number resolved components and the daunting number of unresolved ones. LDMs hold great promise to provide predictive understanding of natural hazards from the consequences of global warming and climate change.

Multilayered Stochastic Modeling (MSM) [Kondrashov et al., 2014] is a data-driven LDM approach that aims to obtain a low-order nonlinear system of prognostic equations driven by stochastic forcing, and estimates both the dynamical operator and the properties of the driving noise directly from observations or from a high-order model's simulation. MSM is a system of stochastic differential equations (SDEs) involving hidden (auxiliary) variables ranked by layers, which interact with the macroscopic (observed) variables to model the dynamics of the latter. MSMs represents a natural continuous-time counterpart of Empirical Model Reduction (EMR) models advocated by Kravtsov et al. [2005], Kondrashov et al. [2005], Kravtsov et al. [2009]. To represent correctly cross-interactions of the large and slow scales of motion with the much large number of unobserved modes that represent the small and fast scales, EMR requires the inclusion of memory effects via auxiliary variables of additional model levels.

MSM dynamics of the observed variables can be naturally decomposed into three types of interactions: (a) nonlinear deterministic Markovian part; (b) non-Markovian part conveying memory effects of interactions with hidden variables; and (c) noise term to account for the random fluctuations that are not modeled by the terms in (a) and (b). When the underlying partially observed dynamical system possesses a physical invariant measure, an MSM is shown to be consistent with the Mori-Zwanzig (MZ) formalism, and a practical test is identified to assess its degree of consistency with the generalized Langevin equation predicted within the MZ framework.

Typically, data-reduction methods such as in Artificial Neural Networks (ANN) [Mukhin et al. 2014a, b] and MSM [Kondrashov et al. 2014] are applied to a subset of leading components of Empirical Orthogonal Functions (EOFs) from classical Principal Component Analysis (PCA) of the spatio-temporal (ST) field(s) of interest. However, data projection onto the leading EOFs has an important drawback: resulting principal components (PCs) describe only the instantaneous correlations between points of the spatial grid, and it does not take into account time-lagged relationships. The latter, however, are important to the effects of delayed feedbacks and external forcing in global climate phenomena of coupled atmosphere-ocean system. An illustrative example is delayed oscillator mechanism of El-Nino Southern Oscillation (ENSO). In that context, Mukhin et al. (2014b) have proposed to use leading ST-PCs from Multichannel Singular-Spectrum Analysis (MSSA) [Ghil et al. 2002] as dynamical variables for ANNs model construction. The effectiveness of this approach was illustrated by predicting the behavior of the intermediate complexity coupled ocean-atmosphere model of ENSO [Mukhin et al. 2014b].

Here we further investigate such MSSA application by obtaining MSM for the Lorenz 96 model (L96) [Lorenz 1996], commonly accepted to be a 'toy model' of the atmosphere. Figure 1 demonstrates successful MSM-MSSA results for L96. In particular, statistical features of MSSA-filtered dataset (panel (c)) are successfully reproduced in stochastic integration of resulting MSM model (panel (d)). Memory effects conveyed by MSM layers are crucially important for reproducing L96 dynamics.

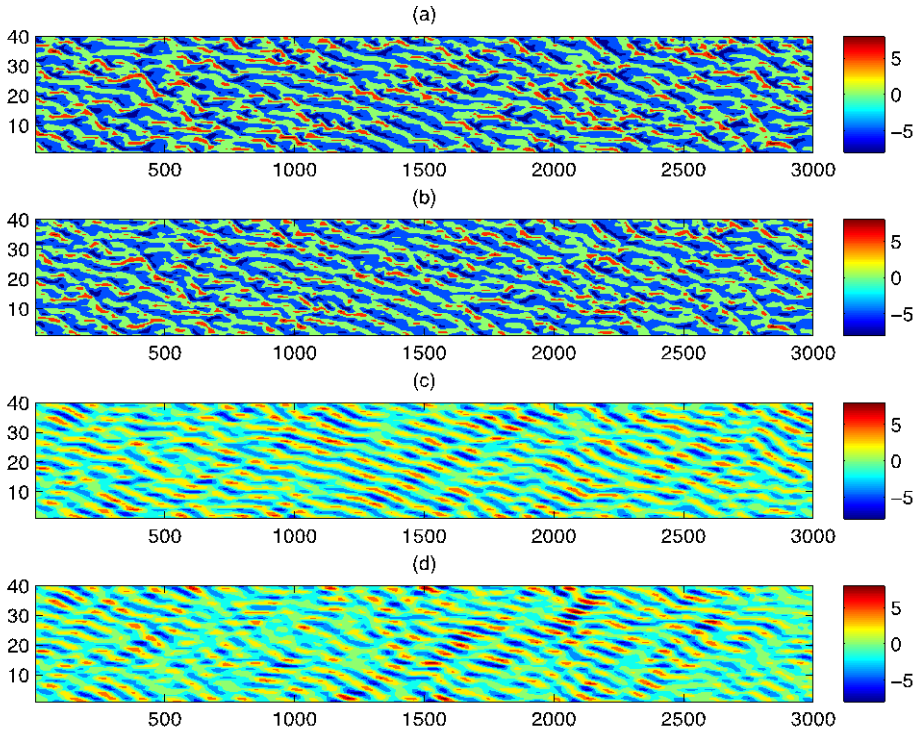

Fig. 1. Top to bottom: (a) original spatio-temporal dataset for L96 model, x-axis is time, y-axis are L96 variables, (b) PCA-prefiltered L96 dataset, (c) Reconstruction of (b) by using subset of leading ST-PCs of MSSA, and (d) stochastic integration of MSM model derived from subset of leading ST-PCs of MSSA

Acknowledgements

This research was supported by the grant ONR-MURI N00014-12-1-0911 from the Multi-University Research Initiative of the Office of Naval Research, by the National Science Foundation grants DMS-0934426 and OCE-1243175, and by the Government of the Russian Federation (Agreement No. 14.Z50.31.0033).

References

1. M. Ghil, et al., "Advanced spectral methods for climatic time series", *Rev. Geophys.*, 2002, **40**, 3.1-3.41.
2. E. Lorenz, "Predictability – A problem partly solved", 1996, Pp. 1-18 in Proceedings of seminar on predictability: Volume 1. ECMWF, Reading, UK.
3. D. Kondrashov, S. Kravtsov, A.W. Robertson, and M. Ghil, *J. Climate*, 2005, **18**, 4425-4444.
4. S. Kravtsov, D. Kondrashov, and M. Ghil, *J. Climate*, 2005, **18**, 4404-4424.
5. S. Kravtsov, D. Kondrashov, and M. Ghil, *Empirical Model Reduction and the Modeling Hierarchy in Climate Dynamics*, invited chapter in Stochastic Physics and Climate Modeling (T. Palmer and P. Williams, Eds), Cambridge University Press, 2009, p. 35-72.
6. D. Mukhin, E. Loskutov, A. Mukhina, A. Feigin, I. Zaliapin and M. Ghil, *J. Climate*, 2014a, sub judice.
7. D. Mukhin, D. Kondrashov, E. Loskutov, A. Gavrilov, A. Feigin, and M. Ghil, *J. Climate*, 2014b, sub judice.
8. D. Kondrashov, M. Chekroun, and M. Ghil, *Physica D*, 2014, sub judice.

Invited

RECONSTRUCTING SPATIOTEMPORAL CHARACTERISTICS OF SEA-LEVEL PRESSURE VARIABILITY USING A FEATURE TRACKING APPROACH

S.V. Kravtsov[1,2], **I. Rudeva**[3,2], and **S.K. Gulev**[2,4]

[1] University of Wisconsin-Milwaukee, Milwaukee, USA, kravtsov@uwm.edu
[2] P. P. Shirshov Institute of Oceanology, RAS, Moscow, Russia
[3] University of Melbourne, Melbourne, Australia
[4] Moscow State University, Moscow, Russia

Abstract. This paper is aimed at quantifying the contribution of synoptic transients to the full spectrum of space–time variability of sea-level pressure (SLP) in middle latitudes. In the authors' previous work it was shown that tracking cyclones and anticyclones in an idealized atmospheric model allow reconstructing a surprisingly large fraction of the model's variability, including not only synoptic, but also its large-scale low-frequency component. Motivated by this result, the authors performed tracking of cyclones and anticyclones and estimated cyclone/anticyclone size and geometry characteristics in the observed SLP field using 1948–2008 NCEP/NCAR reanalysis data set. The reconstructed synoptic field was then produced via superimposing radially symmetrized eddies moving along their actual observed trajectories. It was found that, similarly to earlier results for an idealized model, the synoptic reconstruction so obtained accounts for a major fraction of the full observed SLP variability across a wide range of time scales, from synoptic to those associated with the low-frequency variability (LFV). The synoptic reconstruction technique developed in this study helped elucidate connections between the synoptic eddies and LFV defined via more traditional spatiotemporal filtering. In particular, we found that the zonal-index (ZI) variability is synonymous to random ultra-low-frequency redistributions of cyclone/anticyclone trajectories and, hence, is inseparable of that in the storm-track statistics.

Motivation and methodology

Snapshots of sea-level pressure are dominated in mid-latitude regions by synoptic-scale features known as cyclones (SLP minima) and anticyclones (SLP maxima); see Fig. 1. These features have lifetimes on the order of a few days, propagate and bring about what we all know as ever-changing weather. They may also be important in forcing and modifying low-frequency climate variability (LFV), with time scales longer than a week and spatial scales from regional to global. A traditional way of singling out this synoptic field is via high-pass time filtering. However, it turns out that the spectrum of atmospheric variability is continuous and monotonic, so there is no clear time scale separation between synoptic field and LFV.

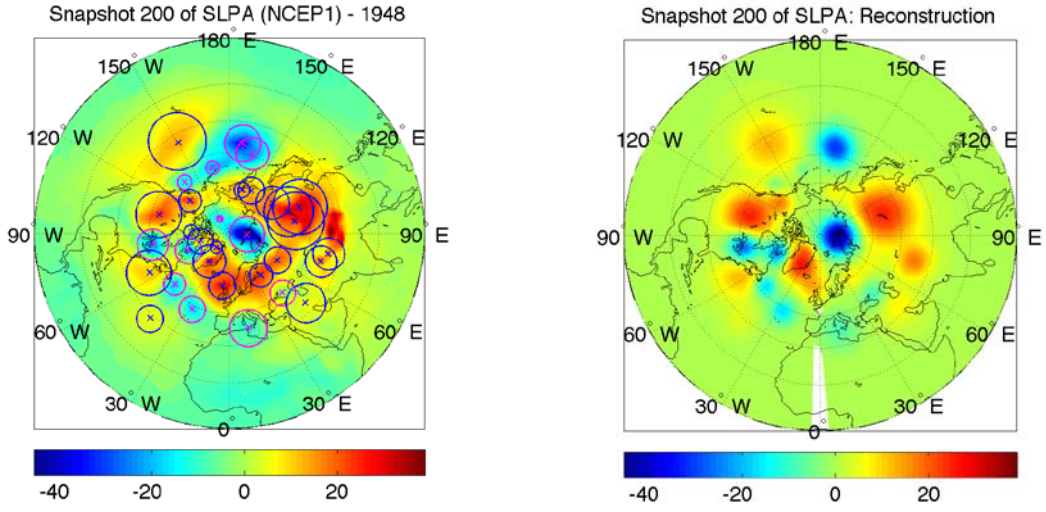

Fig. 1. Example of tracking-based reconstruction of sea-level pressure anomalies (hereafter SLPA) with respect to the instantaneous NH-mean SLP. Left: Observed SLPA (mb), with cyclones and anticyclones shown. Right: Reconstructed SLPA (see text)

What we propose here is an alternative strategy of isolating the synoptic field based on identifying and tracking the evolution of individual cyclones and anticyclones [1, 2]. In particular, we identify locations of all cyclones and anticyclones present in a given SLP snapshot, and approximate the actual SLP maxima and minima by positive and negative axially symmetric anomalies of Gaussian shape,

with size and depth derived from the observed field (see Fig. 1, *left panel*). We then sum up all these anomalies to create a reconstructed synoptic field for each SLP snapshot (Fig. 1, *right panel*); this field essentially has the large-scale background removed. The main question we attempt to address is how well the synoptic field so reconstructed describes the total variability present in the raw SLP field. What we will find is that this synoptic field describes a perhaps surprisingly large fraction of the total SLP variability, including most of its LFV!

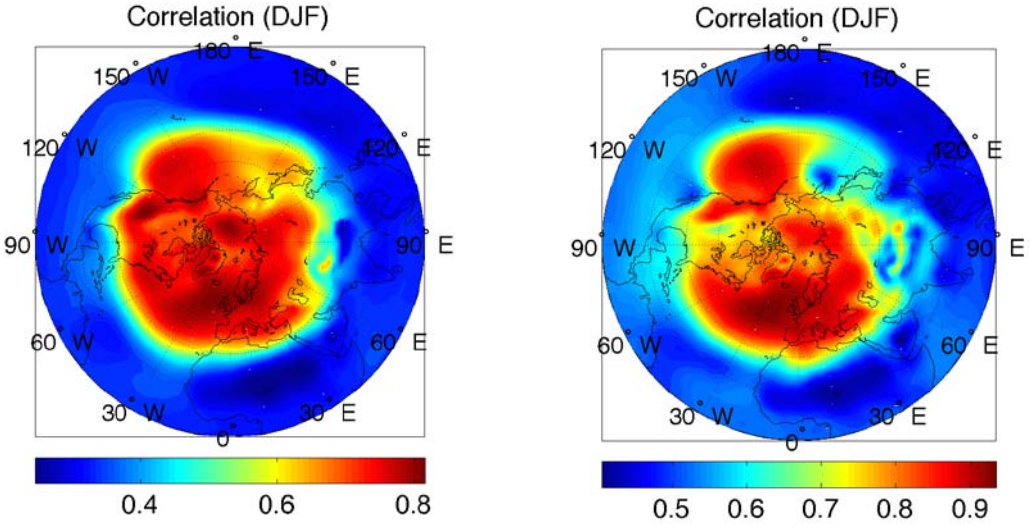

Fig. 2. Correlation between the observed and reconstructed SLPA time series, for the DJF season. The results for other seasons (not shown) are very similar. *Left panel*: correlations for raw data; *right panel*: correlations for the 20-day boxcar running mean filtered data

Skill of synoptic reconstruction

We used the correlation between the actual and reconstructed SLPA time series as a measure of the reconstruction skill (Fig. 2). The mean correlation averaged over the region north of 30º N exceeds 0.7 (0.8 for the low-pass filtered data). Note that the cyclone/anticyclone tracking was confined to the region north of 20ºN, so we don't expect a substantial reconstruction skill in the tropical regions. Further anatomy of the reconstruction skill in the work [3] reveals that: (i) the synoptic reconstruction is most skillful in reproducing large-scale teleconnection patterns and breaks down on local scales and short time scales due to the round-eddy approximation; (ii) the LFV of teleconnection patterns is synonymous to the variations of the synoptic-eddy pathways; and (iii) the low-frequency redistribution of cyclones and anticyclones precedes changes in the large-scale flow patterns.

Discussion

The methodology presented in this work provides a striking evidence for inseparability of synoptic variability from larger-scale climate signals, and suggests novel means for the identification and prediction of climate change. These results are thus of utmost theoretical and practical importance.

Acknowledgements

This work was funded by the NSF grant #1243158 (SK) and the contract with the Russian Ministry of Education and Science 14.B25.31.0026 (SKG and IR).

References

1. I. Rudeva, and S. Gulev, "Climatology of cyclone size characteristics and their changes during the cyclone life cycle", *Mon. Wea. Rev.*, 2007, **135**, 2568–2587.
2. S. Kravtsov, and S. Gulev, "Kinematics of eddy–mean flow interaction in an idealized atmospheric model", *J. Atmos. Sci.*, 2013, **70**, 2574–2595.
3. S. Kravtsov, I. Rudeva and S. Gulev, "Reconstructing sea-level pressure variability by using a feature-tracking approach", *J. Atmos. Sci.*, 2014, submitted.

SIMULATION OF WIND WAVES ON GORKY RESERVOIR IN THE FRAMEWORK OF WAVEWATCH III MODEL

A.M. Kuznetsova[1], D.A. Zenkovich[1], V.V. Papko[1], A.A. Kandaurov[1,2], G.A. Baidakov[1,2], M.I. Vdovin[2], D.A. Sergeev[1,2], and **Yu.I. Troitskaya[1,2]**

[1] Institute of Applied Physics, Nonlinear Oscillations and Waves, Nizhny Novgorod, Russian Federation, yuliya@hydro.appl.sci-nnov.ru

[2] Nizhny Novgorod State University, Nizhny Novgorod, Russian Federation

Abstract. Simulation of ocean and sea waves is a generally adopted technique of operational meteorology, but wave modeling is less developed for moderate and small inland water reservoirs and lakes, though being of considerable interest for inland navigation. In this paper test numerical experiments on simulating waves on the surface of the lake-like basin of the Gorky Reservoir using WAVEWATCH III is reported. In the series of calculations moderate winds of different directions blowing steadily all over the surface of the reservoir were compared with the data collected by the field observations and measurements. Finally we discuss the problem of the discrepancy of the experimental data and the data of the numerical experiment.

Nowadays operational meteorology widely uses simulation of ocean and sea waves like an instrument for the improvement of the weather forecasts. Third-generation wave models such as WAM, SWAN and WAVEWATCH III are mainly focused on the description of the ocean and sea waves including coastal zones. Meanwhile, wave modeling is less developed for moderate and small inland water reservoirs and lakes, though being of considerable interest for inland navigation.

In this paper, test numerical experiments on simulating waves on the surface of the lake-like basin of the Gorky Reservoir using WAVEWATCH III are reported. The results of the wave simulation are compared with the experimental data collected by the field in-situ observations and measurements in the Gorky Reservoir [1]. Gorky Reservoir is an artificial lake in the central part of the Volga River formed by a hydroelectric dam of Gorky Hydroelectric Station between the towns of Gorodets and Zavolzhye. It extends for 427 km from the dam of Rybinsk to the dam of Gorodets through several regions of Central Russia. Whilst it is quite narrow and follows the natural riverbed of Volga in the upper part, it becomes up to 15 km wide downstream the town of Yuryevets. Its maximum depth is 22 m, the surface area is 1590 km^2, the accumulated water volume amounts to 8.71 km^3. The field experiments were carried out in the south part of the Gorky reservoir from the boat. In the course of the experiment we simultaneously measured profiles of wind speed and surface wave spectra using instruments placed on the Froude buoy, which measures the following parameters: i) the module and the direction of the wind speed using ultrasonic wind sensor WindSonic Gill instruments, located on the 4 levels from 0.1 to 5 m long; ii) profile of the surface waves with 3-channel string wave-gauge with the base of 5 cm, iii) the temperature of the water and air with a resistive sensor. 3D spectra of surface waves were retrieved by Fourier dimensional method developed in [2]. Wind velocity parameters (wind friction velocity and roughness height) were retrieved from wind velocity profiles averaged over 10 minutes.

In the series of calculations we considered moderate winds (u_{10} is up to 9 m/s) of different directions blowing steadily all over the surface of the reservoir and the waves developing from some initial seeding spectral distribution (Gaussian in frequency and space, cosine in direction). The range of the observed significant wave height was from less than 1 cm up to 40 cm. We considered deep water case with real bathymetry of the reservoir. The effects connected with the changing the depth and shallow water (refraction, bottom friction, depth-induced breaking, bottom scattering, triad interactions) were ignored.

1-D spectra of the field experiment were compared with those obtained in numerical experiments with different parameterizations of wind input provided in WAVEWATCH III (Tolman & Chalikov input & dissipation, WAM 3 input & dissipation, WAM 4 input & dissipation). The fetch depended on the wind direction because of the geometry of the Gorky Reservoir, and for the cases with long fetch (e.g., fig.1 a – South wind, fetch ≈ 6 km) the result of numerical simulation were in agreement with the 1-D spectra of the field measurements. For the case with short fetch (e.g., fig.1 b – East-North-East wind, fetch < 1 km) the discrepancy of the experimental data and the data of the numerical experiment was very big.

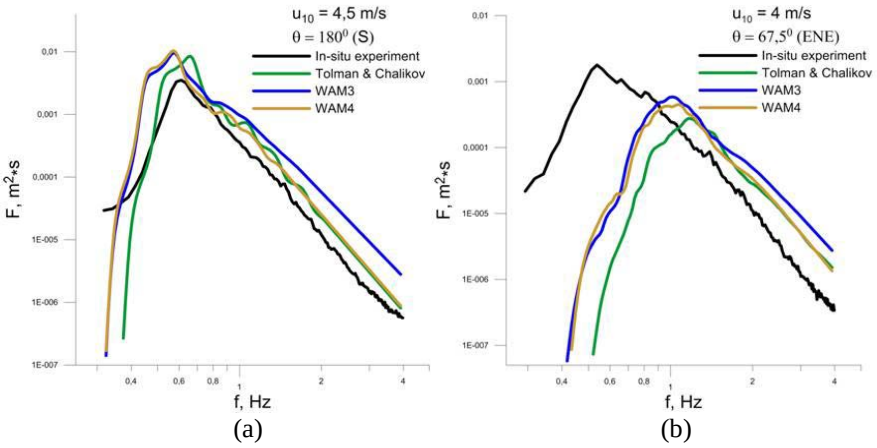

Fig. 1. Frequency spectra for a) long fetch (South wind, u10 = 4,5 m/s); b) short fetch (East-North-East wind, u10 = 4 m/s). Black line is for field experiment, green, blue and golden lines are for numerical experiment (Tolman & Chalikov, WAM 3, WAM 4 input & dissipation term package accordingly)

For long fetches (fig. 1 a) spectral maxima calculated by WAVEWATCH III shows the downshifting compared with the measured data. For all cases, wave amplitude characteristics were overestimated. This discrepancy is connected with the parameterization of the wind input, because built-in parameterizations were made for the ocean and sea conditions, and it is not correct for the conditions of the inland reservoirs or lakes. Thus, extra tuning of the model is required. The dependence of the friction velocity u_* on the 10 m wind speed u_{10} is presented in fig.2 a. It is seen that curves for the experiment and parameterizations are different. When the wind velocities u_{10} corresponding to the experimental u_* were taken, the coincidence of the spectra became better (fig. 2 b).

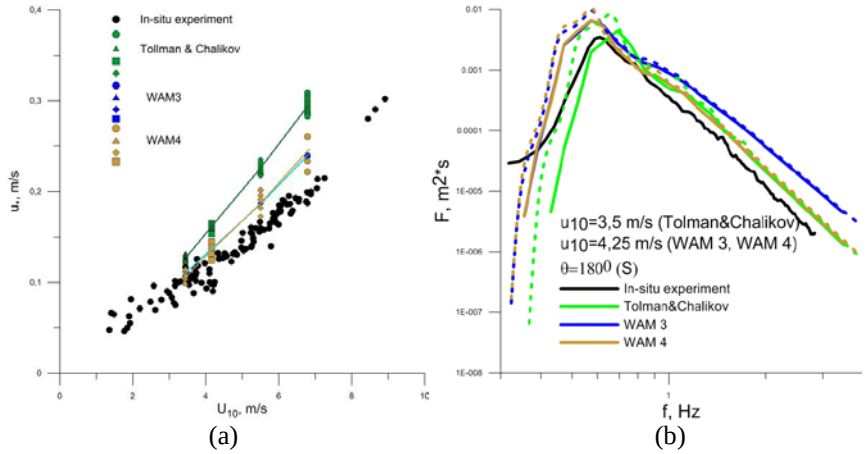

Fig. 2. a) Friction velocity u_* *versus* 10 m wind speed u_{10} for the field experiment (black dots); b) Frequency spectra for South wind, solid line is for the u_{10} setting without parameterization details, dash line is for the improved u_{10} setting. Green, blue and golden lines are for Tolman & Chalikov, WAM 3, WAM 4 input & dissipation term package accordingly

To conclude, we have discussed the applicability of several parameterizations for the wave action source terms available in WAVEWATCH III. New parameterization of wind input for wind wave modeling in inland reservoirs and lakes is needed.

Acknowledgements

The work was supported by the Russian Foundation for Basic Research under Grant No. 13-05-97068.

References

1. Yu. Troitskaya, V. Papko, G. Baidakov, M. Vdovin, A. Kandaurov, and D. Sergeev, *Geophysical Research Abstract*, 2013, **15**, EGU2013-2576.
2. Y.I. Troitskaya, D.A. Sergeev, A.A. Kandaurov, G.A. Baidakov, M.A. Vdovin, and V.I. Kazakov, *J. Geophys. Res*., 2012, **117**, C00J21.

Invited

NEW RESULTS OF TALL-OBJECT LIGHTNING OBSERVATION IN GUANGZHOU

Weit Lu[1,2,3], Luwen Chen[4], Ying Ma[1,2], Yang Zhang[1,2], and **Yijun Zhang[1,2]**

[1] State Key Laboratory of Severe Weather, Chinese Academy of Meteorological Sciences, Beijing, China
wtlu@cams.cma.gov.cn
[2] Laboratory of Lightning Physics and Protection Engineering,
Chinese Academy of Meteorological Sciences Beijing, China
[3] Collaborative Innovation Center on Forecast and Evaluation of Meteorological Disasters,
Nanjing University of Information Science & Technology, Nanjing, Jiangsu, China
[4] Lightning Protection Center of Guangdong Province, Guangzhou, Guangdong, China

Abstract. Some new results of analysis of tall-object lightning flashes obtained at the Tall-Object Lightning Observatory in Guangzhou during 2009–2012 are summarized. The three-dimensional and two-dimensional propagation characteristics of the downward leader, the upward connecting leader, and the unconnected upward leader are given. The non-"Tip-to-Tip" connection phenomenon in the attachment process is presented and the diversity of the connecting behavior of the downward and upward leaders during the attachment process is discussed.

Experiment

A field lightning experiment, mainly focusing on the observation of lightning flashes terminating on tall structures has been conducted since 2009 in Guangzhou, Guangdong, China (Lu et al., 2010, 2012, 2013). The Tall-Object Lightning Observatory in Guangzhou (TOLOG) was established. Two observation stations are involved in our experiment for the three-dimensional (3-D) optical observation of the lightning channel. The main observation station is located on a ~100 m building and the sub-station on a ~70 m building. At the main station, several types of instruments are installed to simultaneously measure the acoustic, optical (high-speed and ordinary-speed), electric field, and magnetic field signals produced by lightning discharges, while at the sub-station, only two ordinary-speed video cameras are installed to capture images continuously.

During 2009–2012, more than 100 flashes were captured at the TOLOG. Some cases are selected to analyze the characteristics of the downward leader (DL), the upward connecting leader (UCL), and the unconnected upward leader (UUL). Some new results are presented in this summary. All of the flashes given in the following are downward negative flashes, so the polarity of the DL is negative and that of the upward leader is positive.

Results

To reconstruct the 3-D lightning channel from dual-station optical observation, we developed a reconstruction method, in which the minimum elevation angle difference based on the azimuths intersection is used to match the direction angles (Gao et al., 2014).

Six downward negative flashes captured in 2012 are analyzed in 3-D. The 3-D length values of the six positive UCLs range from 180 to 818 m. There are 38 3-D speed values which are calculated combining the 3-D UCL channel and the high-speed images obtained at the main station for the six UCLs. The 3-D speed values range from 0.8 to 14.3×10^5 $m\cdot s^{-1}$ and four of them (11 %, 4/38) are on the order of 10^6 $m\cdot s^{-1}$. The two-dimensional (2-D) parameters are calculated using the single-station high-speed images. The values of the 2-D length and speed range from 147 to 610 m and 0.3 to 10.6×10^5 $m\cdot s^{-1}$, respectively. The average value of the 3-D speed is 1.3 times the 2-D value. The speed of the UCL increases with time. When the UCL's 3-D length is shorter than 300 m, 77 % (20/26) of the UCL's 3-D speed values are smaller than 5×10^5 $m\cdot s^{-1}$. When the UCL extends longer than 300 m or its tip is higher than 650 m, its 3-D speed is faster than 5×10^5 $m\cdot s^{-1}$.

The 3-D propagation speeds of the primary branch of the downward leader (PBDL) that facilitates connection to a 440 m high building and the UCL in F1215 versus time are shown in Fig. 1. It can be seen that both the PBDL and the UCL in F1215 have 3-D propagation speeds mainly on the order of 10^5 $m\cdot s^{-1}$. The speed of the PBDL shows no clear changing trend, except for the final 200 μs prior to the beginning of the return stroke, while that of the UCL tends to generally increase, especially during the last 1 ms. The 3-D speed of the UCL in F1215 reaches a value on the order of 10^6 $m\cdot s^{-1}$ finally when the distance between the PBDL and the UCL is less than 200 m.

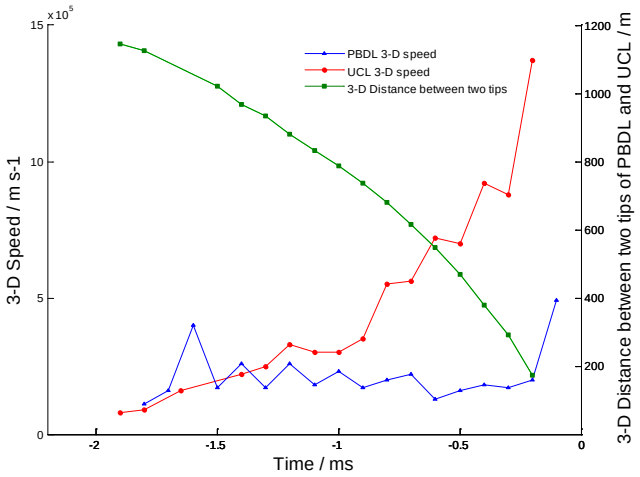

Fig. 1. The 3-D propagation characteristics of downward and upward leaders in F1215 versus time

The high-speed images, with a temporal resolution of 20 μs, of a flash that terminated on a 440 m high building exhibited an unexpected behavior in that the DL's tip connected to the lateral surface of the ~400 m UCL below its tip (Fig. 2). The high-speed images of 18 flashes show that the leaders' connecting behavior can be grouped in four types: Type I, "Tip-to-Tip", i.e., the DL's tip to the UCL's tip, accounts for 33 % (6/18); Type II, the DL's tip to the lateral surface of UCL, accounts for 50 % (9/18); Type III, the UCL's tip to the lateral surface of DL, accounts for 6 % (1/18); and Type IV, the combination of at least two of the aforementioned three types, accounts for 11 % (2/18).

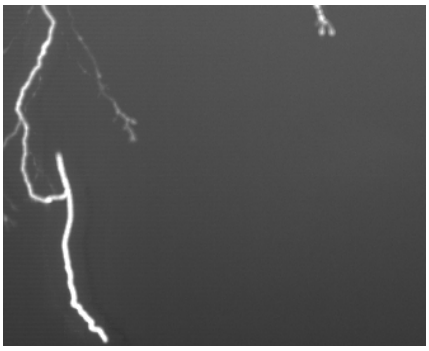

Fig. 2. The optical evidence of the phenomenon that the downward leader tip connects to the lateral surface of the UCL (Lu et al., 2013)

Forty-five UULs that have occurred in 19 flashes are analyzed (Lu et al., 2012). The results show that: no UUL with an inception time prior to return stroke greater than 0.5 ms is initiated from a structure lower than 300 m; the UULs with inception heights lower than 300 m seldom exhibit lengths longer than 50 m and only can be initiated by flashes within approximately 600 m, while those higher than 400 m can even reach several hundred meters and be initiated by flashes over 1 km away; the maximum distances for the downward leaders to attract the UULs with inception heights from 100 to 200 m, 200 to 300 m, and over 400 m are approximately 350 m, 450 m, and 600 m, respectively.

Acknowledgements

This work was supported in part by the National Natural Science Foundation of China (grants 41075003 and 41175003) and the Basic Research Fund of Chinese Academy of Meteorological Sciences (Grant 2013Z006).

References

1. W. Lu, Y. Zhang, L. Chen, et al., *Proc. 30th International Conference on Lightning Protection*, Cagliari, Italy, 2010, 1060-1-5.
2. W. Lu, L. Chen, Y. Zhang, et al., *JGR*, 2012, **117**, D19211, doi:10.1029/2012JD018035.
3. W. Lu, L. Chen, Y. Ma, et al., *Geophys. Res. Lett.*, 2013, **40**, doi:10.1002/2013GL058060.
4. Y. Gao, W. Lu, Y. Ma, et al., *Atmospheric Research*, 2014, doi: 10.1016/j.atmosres.2014.06.008.

Invited

CLIMATE RESPONSE AND CLIMATE PREDICTION

V. Lucarini[1,2]

[1] Institute of Meteorology, CEN, University of Hamburg, Germany, valerio.lucarini@uni-hamburg.de
[2] Department of Mathematics and Statistics, University of Reading, UK

Abstract. The sensitivity of the climate system to increasing CO_2 concentration and the response at decadal time scales are still major factors of uncertainty for the assessment of the long and short term effects of anthropogenic climate change. Here we demonstrate that it is possible to use Ruelle's response theory to predict the impact of an arbitrary CO_2 forcing scenario on the global surface temperature of a general circulation model. Response theory puts the concept of climate sensitivity on firm theoretical grounds, and addresses rigorously the problem of predictability at different time scales. Conceptually, our results show that climate change assessment is a well-defined problem from a physical and mathematical point of view. Practically, our results show that considering one single CO_2 forcing scenario is enough to construct operators able to predict the response of climatic observables to any other CO_2 forcing scenario, without the need to perform additional numerical simulations, thus paving the way for redesigning climate change experiments from a radically new perspective.

Introduction

One of the main goals of climate science is to predict the impact on the statistical properties of the system of modulations on different time scales of internal or external parameters such as the greenhouse gases (GHG) concentration or the solar constant. The assessment of the future impacts of climate change under a variety of CO_2 forcing scenarios and the evaluation of the climate sensitivity to the increase of CO_2 concentration ($[CO_2]$) mostly rely on the use of general circulation models (GCM) of the climate system. Despite the intense efforts put by the scientific community having led to impressive improvements in the GCMs complexity and computational performances, after several decades large uncertainties are still present even in the evaluation of the Equilibrium Climate Sensitivity, in the predictive skills of the models on decadal time scales and the role of feedbacks in determining the response of the system. The need of substantial advances in the scientific ideas on the basis of climate modelling strategies is more and more clear in the climate community.

Response Theory

The response theory is a classical instrument of equilibrium statistical mechanics. The cornerstone of the theory is the fluctuation-dissipation theorem (Kubo 1966), which relates forced and free fluctuations. For forced-dissipative systems far from equilibrium, of which the climate system is an example, the fluctuation-dissipation theorem in general does not hold. However, it has been shown relatively recently how in many cases of physical interest deviations from a nonequilibrium steady state (NESS) under the application of a weak forcing can be computed by linear response formulas formally very similar to the equilibrium case (Ruelle 2009). The response theory can be framed as follows. We apply a weak forcing so that the evolution equation can be written as $\dot{x} = F(x) + X(x)f(t)$, where $F(x)$ represents the unperturbed dynamics, $X(x)$ defines the pattern of the forcing, and $f(t)$ is its time modulation. The expectation value of an observable Φ in the forced system can be computed as a perturbative expansion $\langle \Phi \rangle_f(t) = \langle \Phi \rangle_0 + \sum_{n=1}^{+\infty} \langle \Phi \rangle^{(n)}(t)$, where $\langle \Phi \rangle_0$ is the unperturbed value. In particular, the first term in the series gives the linear response:

$$\langle \Phi \rangle_f^{(1)}(t) = \int_{-\infty}^{+\infty} d\sigma_1 G_\Phi^{(1)}(\sigma_1) f(t-\sigma_1), \quad (1)$$

where $G_\Phi^{(1)}(t)$ is the first order Green function given by the expectation value of a (complicated) observable defined on the unperturbed flow. We use this framework to study climate change and climate response. The numerical model used in this study is PLASIM (Fraedrich et al. 2005), a simplified GCM developed at the University of Hamburg. We consider as our observable the globally averaged surface temperature T_s and as forcing the convergence of radiative fluxes due to the increase in the logarithm of $[CO_2]$ (the radiative forcing scales approximately logarithmically with $[CO_2]$ (IPCC2013). Therefore $\langle \Phi \rangle_f^{(1)} = \langle T_s \rangle_f^{(1)}$ is the expectation value of the increase in T_s in the linear regime and $f(t)$ represents the temporal evolution of the radiative forcing due to a chosen CO_2 forcing scenario.

Main Results

In the control run, [CO_2] is set to 360 ppm, representative of the present-day value. We then perform two sets of forcing experiments (each populated by 200 ensemble members), prototypical of the IPCC scenarios, for estimating the climate sensitivity and the impact of CO_2 forcings on the climate system. In the first set of experiments we double instantaneously the CO_2 concentration and we keep it fixed at 720 ppm afterwards. This corresponds to a radiative forcing represented by a Heaviside function times a constant. From these experiments we can derive the Green function as follows:

$$G^{(1)}_{T_S}(t) = \left. d\left[\langle T_s\rangle^{(1)}_f(t)\right] \right/ dt \tag{2}$$

In the second set of experiments [CO_2] is increased by 1% per year until reaching 720 ppm (after about 70 years), and it is kept fixed afterwards. The corresponding radiative forcing is a ramp function $g_\tau(t) = \frac{f^{2x}_{CO_2} t}{\tau}$ for $0 \le t \le \tau$ and $g_\tau(t) = f^{2x}_{CO_2}$ for $t > \tau$ with $\tau \approx 70\ years$. We use the Green function given in Eq. (2) derived from the first set of experiments to predict the T_s response to the second set of experiments using Eq. (1). In Figure 2 we compare the ensemble average of the simulations and the prediction for $\langle T_s\rangle^{(1)}_{g_\tau}$ obtained using the estimate of the Green function shown in Figure 1. The agreement is excellent both on the short and long term. Discrepancies of less that 10 % are present during the transient in the window between 25 and 100 years, because of the ice-albedo feedback. The degree of precision of the prediction obtained with the linear response theory is remarkable, considering the complexity of the underlying dynamics.

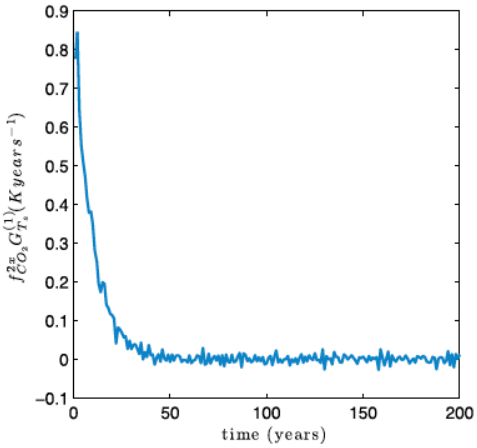

Fig. 1. Green Function for T_S; CO_2 forcing

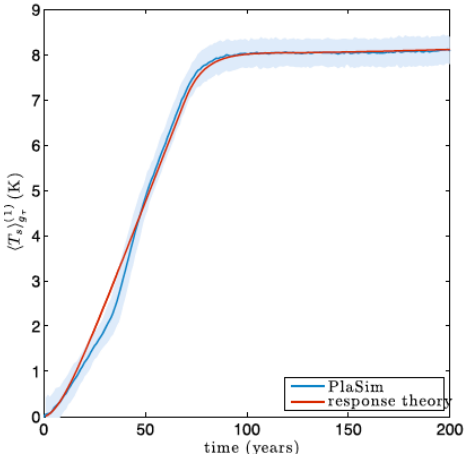

Fig. 2. T_S change predicted by Response Theory (red) vs model simulations (blue)

Conclusions

These results (Ragone et al. 2014) suggest that the response theory may provide extremely powerful tools for addressing the problem of climate change and climate response (Lucarini and Sarno 2011). This approach comes in synergy with recent results on the pullback attractor (Chekroun et al. 2011).

Acknowledgements

The author acknowledges the support by FP7-ERC through the Starting Investigator Grant NAMASTE and by the DFG Cluster of Excellence CLISAP.

References

1. M. Chekroun, E. Simonnet, & M. Ghil, *A Physica D: Nonlinear Phenomena*, 2011, **240**, 1685-1701.
2. K. Fraedrich, H. Jansen, U. Luksch, & F. Lunkeit, *MeteorologischeZeitschrift*, 2005, **14,** 299-304.
3. R. Kubo, *Reports on Progress in Physics*, 1966, **29**, 255-284.
4. IPCC, Climate Change 2013: The Physical Science Basis, CUP, Cambridge, 2013.
5. V. Lucarini and S. Sarno, *Nonlinea. Processes Geophysics*, 2011, **18**, 7-28.
6. F. Ragone, V. Lucarini, & F. Lunkeit, arXiv:1403.4908v1 [physics.ao-ph].
7. D. Ruelle, *Nonlinearity*, 2009, **22**, 855-870.

Invited

VARIETY OF ELECTRICAL DISCHARGES IN ELECTRIFIED CLOUDS

E.A. Mareev[1], A.Yu. Kostinskiy[1,2], V.S. Syssoev[1,3], N.A. Bogatov[1], and **V.A. Rakov[1,4]**

[1] Institute of Applied Physics, Russian Academy of Science, Nizhny Novgorod, RF
[2] National Research University Higher School of Economics, Moscow, RF
[3] High-Voltage Research Center of the All-Russia Institute of Electrical Engineering, Istra, Moscow region, RF
[4] Department of Electrical and Computer Engineering, University of Florida, USA

Physical processes leading to lightning initiation, including formation and propagation for a leader discharge, remain poorly understood in spite ofa long history of their studies [1, 2]. Recent experiments, using modern observation means such as high-speed video cameras, triggering lightning, Lightning-Mapping-Array technique, provided new information on the variety of cloud discharge forms and their dynamics under different physical and meteorological conditions (i.e., [3–5]). There is evident progress in the study of laboratory lightning analogues - long spark and artificial cloud discharges.

In this paper, we review recent experimental results and theoretical concepts concerning different forms of electrical discharges in clouds. We review and discuss particularly the streamer-to-leader transition process, the mechanisms governing individual step formation for negative leaders, a possible role of space stems or space leaders, the nature of recoil leaders, thermal-ionization instability as a possible common mechanism of the plasma channel formation in the cloud and cloud-to-ground discharges.

A particular attention is paid to the novel experiments devoted to the study of discharges within the artificial charged water cloud with specially chosen parameters [6]. We have observed the intracloud discharge with plasma parameters close to the parameters recorded in the long spark discharges. In particular, new plasma structures (which we termed *stalkers*) were detected in the cloud of negatively and positively charged droplets. These plasma structures were recorded with the use of a high-speed IR camera (at the wavelength of 3.8–4.9 μm) simultaneously with the visible radiation recorded by high-speed visible cameras and photomultiplier tubes with interference filters. The wavelength range of the IR camera gave us a unique opportunity for diagnostics of the structures within the cloud formed by drops with a typical radius of 0.5 μm. Elongated discharge channels are often organized into different clusters of complicated structure. We hypothesize that *stalkers* are separate plasma objects with their own physical mechanism of formation.

Acknowledgements

The authors are grateful to the Ministry of Education and Science of the Russian Federation for the financial support (project No. 14.B25.31.0023).

References

1. E.M. Bazelyan, Yu. P. Raizer, *Spark Discharge*. CRC Press, 1997.
2. V. Rakov and M. Uman, *Lightning: Physics and Effects*. Cambridge Univ. Press, 2003.
3. V. Mazur, L.H. Ruhnke, T.A. Warner, and R.E. Orville, "Recoil Leaders Formation and Development", *J. Electrostatics*, 2013, **71**, 763-768.
4. D. Petersen, and W.H. Beasley, "High-speed video observations of a natural negative steppA brief review of the problem of lightning initiation and a hypothesis of initial lightning leader formation", *J. Geophys. Res.*, 2013, **118**(12), 110-12, 119.
5. C.J. Biagi, M.A. Uman, J.D. Hill, D.M. Jordan, V.A. Rakov, and J. Dwyer, "Observations of stepping mechanisms in a rocket-and-wire triggered lightning flash", J. Geophys. Res., 2010, **115**, D23215.
6. M.G. Andreev, N.A. Bogatov, A.Yu. Kostinskiy, L.M. Makal'sky, E.A. Mareev, D.I. Sukharevsky, and V.S. Syssoev, "First Detailed Observations of Discharges within the Artificial Charged Aerosol Cloud", *XV ICAE*, June 16–20, 2014, Norman, Oklahoma, USA.

FIELD MEASUREMENTS OF WIND-WAVE INTERACTION IN THE ATMOSPHERIC BOUNDARY LAYER OVER A RESERVOIR

N. Marinina, Yu. Troitskaya, D. Sergeev, V. Papko, G. Baidakov, M. Vdovin, A. Kandaurov, D. Zenkovich, and **A. Kuznetsova**

Institute of Applied Physics, Nizhny Novgorod, Russian Federation

Information about wave roughness for inland and coastal zone is important from a practical point of view (in terms of safety of navigation, especially on the riverside, as well as the problem of erosion of shores). Also, the waves significantly affect the parameters of wind and transfer processes in the atmospheric boundary layer, and hence the evaporation and temperature regime that are the main factors in the water balance of internal reservoirs, lakes and rivers. At the present the majority of the models for wind wave evolution describe ocean and sea conditions. At the same time, the wave roughness in small reservoirs has its own features (very steep, the influence of the banks and shallows, small fetches, etc.) that must be taken into account when developing models. For this, it is necessary to obtain experimental data on the wind-wave regime of the reservoir. We report results of field experiments on wind-wave coupling carried out at the Gorky Reservoir.

The measuring equipment was installed on Froude buoy including the following instruments: 1) four 2-component ultrasonic wind velocity sensors WindSonic Gill instruments located at four different levels (from 0.1m up to 5m height from the water); 2) a 3-channel string wave-gauge with a triangular configuration with a base of 5 cm for measuring surface elevation; 3) a resistive sensor for measuring the temperature of the water and air. Such arrangement of the gauges allowed simultaneous measurements of wind flow profiles and surface wave spectra.

Using approximations of the obtained wind profiles, we calculated the basic parameters of the turbulent boundary layer: friction velocity, wind speed at the standard height of 10 m U_{10} and drag coefficient C_D. The dependence $C_D(U_{10})$ obtained for the Gorky Reservoir was compared with similar data of the Australian Shallow Water Experiment carried out on the Lake George [2]. A good agreement between the results of the experiments carried out in two inland waters (deep Gorky reservoir and shallow Lake George) with different parameters was shown. To understand the cause for such similar behavior of the drag coefficients under strongly different conditions we analyzed surface roughness parameters. Measurements have shown that for both cases the surface wave spectra have almost the same asymptotics (spatial spectrum – k^{-3}, frequency spectrum ω^{-5}) corresponding to the Phillips saturation spectrum. These spectra are typical for the steep surface waves, for which the basic dissipation mechanism is wave breaking. The similarity of the short-wave parts of the spectra may be regarded to be a probable cause of coincidence of the dependence of drag coefficient of the water surface on wind speed.

References

1. Y.I. Troitskaya, D.A. Sergeev, A.A. Kandaurov, G.A. Baidakov, MA. Vdovin, and V.I. Kazakov, “Laboratory and theoretical modeling of air-sea momentum transfer under severe wind conditions”, *J. Geophys. Res*., **117**, C00J21, doi:10.1029/2011JC007778.
2. M.A. Donelan, A.V. Babanin, I.R. Young, M.L. Banner, C. McCormick, “Wave follower field measurements of the wind input spectral function”, Part I: Measurements and calibrations, *J. Atmos. Oceanic Technol*., 2005, **22**, 799-813.

Invited

OFFSHORE OBSERVATION OF EARTHQUAKES AND RELATED TSUNAMIS

H. Matsumoto[1], **Y. Kaneda**[2], **M.A. Nosov**[3], and **S.V. Kolesov**[3]

[1] JAMSTEC, Yokosuka, Japan, hmatsumoto@jamstec.go.jp
[2] Nagoya University, Nagoya, Japan
[3] M.V. Lomonosov Moscow State University, Moscow, Russia

Abstract. Offshore observations make it possible to detect tsunamis in advance prior to their arrivals at the shoreline. For this purpose, ocean bottom pressure gauges are traditionally used. However, in near- and intermediate fields, ocean bottom pressure records usually exhibit a complicated interference of signals related not only to gravitational, but also to hydroacoustic and seismic waves. Network of offshore observatories recently developed and deployed in Japan provide high sampling records of ocean bottom pressure and seismic (acceleration and velocity) signals. In the present study, by taking advantage of simultaneous measurements of pressure and seismic signals that were recorded during some recent tsunamigenic earthquakes, we reveal particular features of these signals and develop a practical method for selecting a tsunami signal from ocean bottom pressure records.

Introduction

Offshore observatories have been deployed since 1970s in Japan, which consist of ocean-bottom seismometers (OBSs) and bottom pressure gauges (PGs) connecting with land stations by submarine cables. Such kind of observatory allowed us to examine the mechanism of tsunami generation directly in the tsunami source by making use of near-field observations (e.g., Nosov and Kolesov, 2007). In the traditional observatory, however, OBS and PG are located a few kilometers away, and moreover there are some uncertainties with orientation of seismic sensors. These difficulties complicate quantitative comparative analysis of PG and OBS records. The present study aims at evaluating the bottom pressure records during the tsunamigenic earthquake. The target earthquake here is selected to be a moderate-to-large earthquake that occurred off Japan (M7.1), which was a normal fault typed outer-rise earthquake (Fig. 1). The tsunami warning was issued after the earthquake, and maximum 30 cm tsunamis were observed along the NE Japan coast.

In-situ data of PGs

The superior advantages of the recently developed dense ocean-floor network for earthquakes and tsunamis, namely DONET, are that pressure and seismic sensors are deployed at the same location. Vertical component of seismic sensor is controlled by gimbals just after the deployment. This is why we can evaluate the bottom pressure records by making use of bottom vibration. We review the pressure records during the earthquake obtained approximately 700 km away from the observatory.

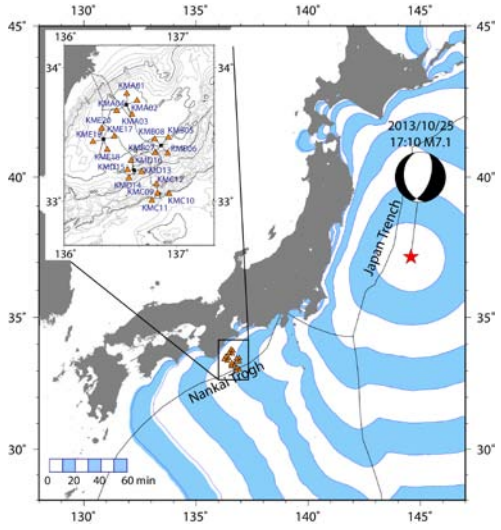

Fig. 1. A map of the outer-rise earthquake with the tsunami travel time and DONET observatories' location

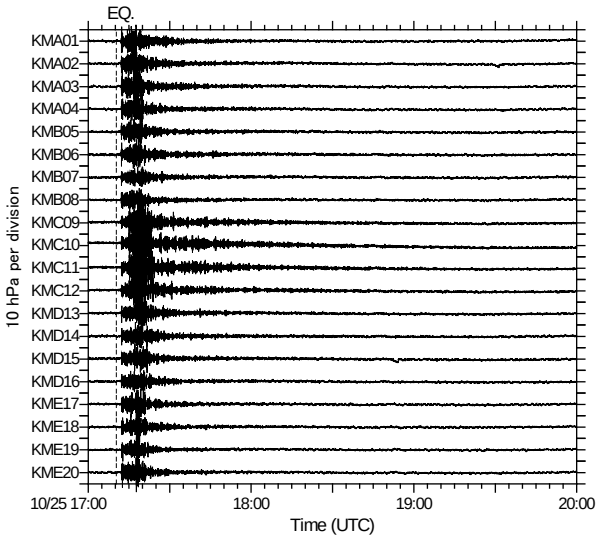

Fig. 2. Pressure records obtained by DONET observatories

DONET has 20 observatories now, in which accelerometer, broadband seismometer (velocity meter), pressure gauges etc. are contained. All datasets have been obtained during the earthquake, in which pressure records are shown in Fig. 2. Pressure fluctuations were observed during the earthquake. KMC09 to KMC12 are relatively deep observatories, and records observed by those observatories tend to amplify the pressure fluctuations.

Comparison with OBSs

It is well known that bottom pressure during the earthquakes depends on the bottom deformation. However, there hasn't been any opportunity to compare the bottom pressure and bottom deformation directly before (Matsumoto and Kaneda, 2013). DONET seismometers are deployed at the same location to the pressure gauge at each observatory as mentioned above, hence we can compare the measurements obtained by them during the earthquake without corrections. Here is an example of the deep observatory at KMC12 in Fig. 3. Three waveforms seem to be independent at a glance.

We compare three waveforms in the frequency domain in Fig. 4 in which acceleration and velocity are converted to their equivalent pressure unit by considering water depth. Indicators *f*g1 and *f*ac1 represent characteristic frequencies which correspond to lower and upper limit frequencies of forced oscillation band, respectively. Gravitational waves are produced by bottom deformation in lower frequency than *f*g1, whereas hydroacoustic waves are produced in a higher frequency band than *f*ac1.

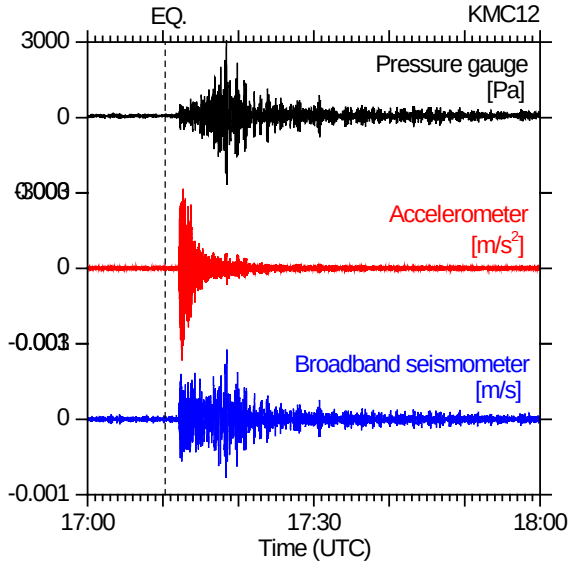

Fig. 3. Bottom pressure, acceleration, and velocity waveforms at KMC12

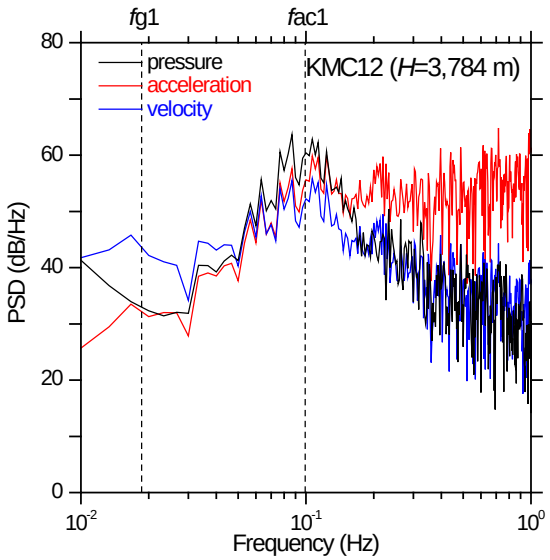

Fig. 4. Comparison of spectrum waveforms of bottom pressure, acceleration, and velocity at KMC12

Discussion and conclusions

According to Fig. 4, the peak frequency of bottom pressure record exhibits near *f*ac1. The characteristic frequency *f*ac1 is fundamental acoustic resonance of water layer. Therefore, acoustic resonance was to be possibly observed. The bottom pressure records obviously follow the bottom acceleration and the velocity in the intermediate and high frequency bands, respectively. The boundary appears at the frequency *f*ac1.

We evaluate the bottom pressure together with the bottom acceleration and velocity. These unique datasets reveal the bottom phenomena such as bottom pressure enhancement by bottom deformation, i.e., bottom velocity and bottom acceleration, depending on the frequency band.

Acknowledgements

This study was supported by the Japan Society for the Promotion of Science (JSPS) and the Russian Foundation for Basic Research (RFBR project 13-05-92100) under the Japan-Russia Research Cooperative Program.

References

1. M.A. Nosov and S.V. Kolesov, *Nat. Hazards Earth Syst. Sci.*, 2007, **7**, 243-249.
2. H. Matsumoto and Y. Kaneda, *Proc. 11th SEGJ Int'l. Symp., Yokohama, Japan*, 2013, 493-496.

Invited

SEMIDIURNAL INTERNAL WAVE GLOBAL FIELD

E.G. Morozov

Shirshov Institute of Oceanology, Moscow, Russia
egmorozov@mail.ru

Abstract. Estimates were made for semidiurnal internal wave generation over submarine ridges based on the models of wave generation. The fluxes of internal wave energy from submarine ridges greatly exceed the fluxes from the continental slopes because the dominating part of the tidal flow is directed parallel to the coastline. They account for about one-fourth of the total energy loss from the barotropic tides. Submarine ridges if normal to the tidal flow form an obstacle that can cause generation of large internal waves. Energy fluxes from most submarine ridges were estimated. The decay of internal tide during propagation was estimated from the measurements on buoys in the ocean and from numerical models. Combined calculations and measurements result in a map of the global internal wave amplitude distribution. Extreme amplitudes were found near the Mascarene Ridge in the Indian Ocean, Mid-Atlantic Ridge in the Southern Atlantic, Great Meteor Bank, and Strait of Gibraltar.

We analyze observations of internal tides in the World Ocean on the basis of long-term moored measurements and numerical modeling. Internal waves of semidiurnal frequency are recorded almost everywhere in the ocean. Their amplitudes are generally much greater than the background level characterized by the Garrett-Munk model [2]. Intense field measurements, theoretical study, and numerical modeling brought us to the level of such understanding of the process that it is possible to study the mechanisms governing semidiurnal internal wave energy distribution in the ocean. The generation of internal tides occurs mainly due to the interaction of the barotropic tide currents with the bottom topography. The currents flowing over the bottom features acquire vertical components, thus leading to periodical vertical displacements of the isopycnals and generating progressive tidal internal wavers.

We use the model developed by P. Baines [1] to estimate the energy of internal tides generated over submarine ridges. Originally the model was developed for the continental slopes but we extended it to submarine ridges and calculated energy fluxes from the main submarine ridges in the Atlantic, Pacific, and Indian oceans. A total of 50 ridges were analyzed. The total energy flux of internal tides from all ridges was calculated. It appeared approximately equal to one fourth of the barotropic tide dissipation. We compared these results with the measurements on 1000 moorings in the ocean and plotted a chart of the amplitudes of internal tides in meters. The greatest amplitudes were found near submarine ridges. Combined calculations and measurements result in a map of the global internal wave amplitude distribution. Extreme amplitudes were found near the Mascarene Ridge in the Indian Ocean, Mid-Atlantic Ridge in the Southern Atlantic, Great Meteor Bank, and the Strait of Gibraltar.

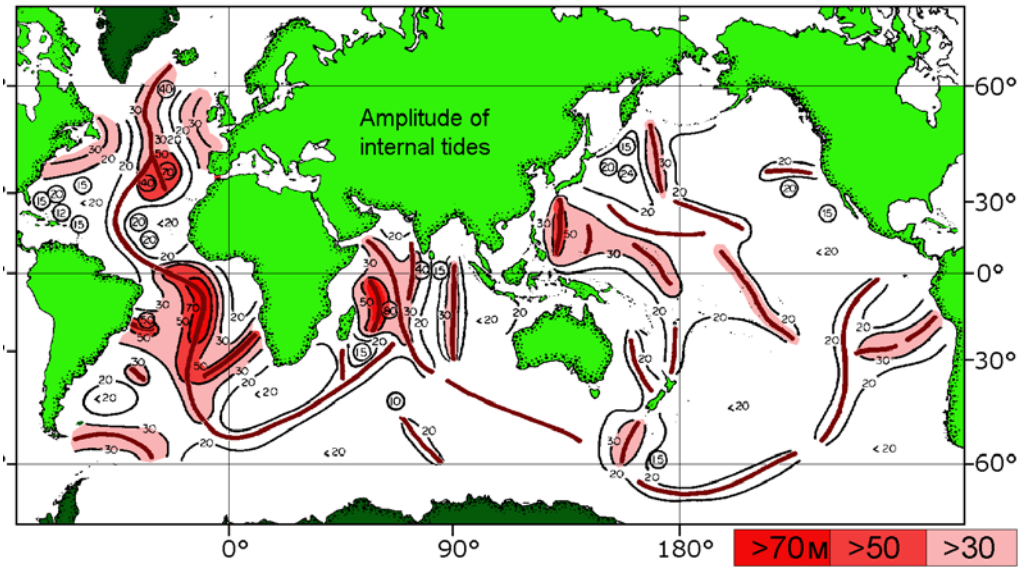

Chart of internal tide amplitudes in the ocean (meters).
Numerals in circles indicate measurements on moorings

The energy fluxes of internal waves generated over submarine ridges exceed several times those of internal waves generated over continental slopes. The currents of the barotropic tidal wave in most parts of the ocean are parallel to the shores, and only a small part of the mass flux crosses the slope line. Many of submarine ridges are perpendicular to the tidal currents and form an obstacle that provides an intense internal wave generation.

Nevertheless there is evidence of large internal waves amplitudes generated over continental slopes and over the ridges connecting arcs of islands. High amplitudes of internal tide were recorded in the Bay of Biscay and in the Strait of Gibraltar. These intense tidal internal waves are generated, when a great part of the tidal flow crosses the continental slope.

The amplitudes of internal tides are high if:

(1) The barotropic tide is strong

(2) Tidal currents are normal to the ridge

(3) The ridge crests are high and surrounding waters are deep

(4) The slopes coincide with the characteristic lines of equations for internal tides

(5) Stratification is strong

References

1. P.G. Baines, *Deep-Sea Research*, 1982, **29**, 307-338.
2. C. Garrett and W. Munk, *Geophysical Fluid Dyn*., 1972, **3**, 225-264.

Invited

LIGHTNING LOCATING SYSTEMS: OVERVIEW OF CHARACTERISTICS AND VALIDATION TECHNIQUES

A. Nag[1], M.J. Murphy[1], W. Schulz[2], and **K. L. Cummins[3]**

[1]Vaisala Inc., Louisville, Colorado, USA, amitabh.nag@vaisala.com
[2]OVE-ALDIS, Vienna, Austria
[3]Department of Atmospheric Sciences, University of Arizona, Tucson, Arizona, USA

Abstract. Lightning locating systems, often referred to as lightning detection networks, are the most common way to geolocate lightning. Such systems also report a variety of characteristics associated with lightning events (cloud-to-ground return strokes, M-components, ICC pulses, and cloud lightning pulses). We summarize the various methods to geolocate lightning, both ground-based and satellite-based, and discuss the characteristics of lightning data available from various sources. The performance characteristics of lightning locating systems are determined by their ability to accurately geolocate lightning events and report various features such as lightning type and intensity. Methods used to validate the performance characteristics of lightning locating systems are discussed.

Introduction

The most common way to geolocate lightning is by using a lightning locating system (LLS), often referred to as a lightning detection network. An LLS is typically a network of a minimum of 4 to 5 sensors and a central processor. Each sensor measures the electromagnetic signal produced by a lightning discharge and sends back information about the associated waveform characteristics to the central processor. Once the same lightning event is measured by multiple sensors in a network and reported to the central processor, one or more techniques can be used at the central processor to geolocate the lightning event. The two most common techniques used for lightning geolocation are time-of-arrival (TOA) and magnetic direction finding (MDF) (e.g., Cummins et al., 1998 [1], Cummins and Murphy 2009 [2]). Modern LLSs are able to determine the location, intensity, and type of lightning and the movement of thunderstorms in real time. This information can be used for various purposes including lightning warning, nowcasting, forecasting, and safety applications, locating lightning-caused damage to resources and infrastructure, risk assessment, geophysical research, insurance, and a variety of other real time and forensic applications.

In the presentation, we will summarize various methods of lightning geolocation in ground-based networks. We will review satellite-based lightning geolocation and characteristics of lightning data from various sources. Additionally, we will discuss methods to validate the performance characteristics of lightning locating systems.

Validation of Lightning Locating System Performance Characteristics

The performance characteristics of an LLS determine the quality of the lightning data available. These performance characteristics include (1) detection efficiency for cloud (IC) and cloud-to-ground (CG) flashes and CG strokes, (2) location accuracy, (3) peak current estimation accuracy, and (4) lightning classification accuracy. These performance characteristics can be evaluated using a variety of techniques which are summarized below.

Network self-reference

In this technique, statistical analysis of parameters (e.g., Schulz, 1997 [3]) such as standard deviation of sensor timing error, semi-major axis length of the 50 % confidence ellipse, and the number of reporting sensors, is used to infer the LA and DE of an LLS. This method requires data collected by the network after it has been properly calibrated. It can provide a good estimate of the network's performance in a cost-effective, practical manner.

Rocket-triggered lightning and tall object studies

These methods use data from rocket-triggered lightning experiments or lightning strikes to tall objects (e.g., instrumented towers) as ground-truth to evaluate the performance characteristics of an LLS within whose coverage area the triggered lightning facility or the tall object is located. The LA, DE, peak current estimation accuracy, and lightning classification accuracy of an LLS can be measured using these methods (e.g., Nag et al., 2011 [4], Diendorfer et al. 2000 [5]). While these methods provide the best ground-truth data for performance characteristics validation for CG lightning

(and are the only ways to directly validate peak current estimation accuracy of an LLS), they may be very expensive, may not be practical for all regions (as there are only a few triggered lightning facilities and instrumented towers across the world), and are a valid indicator of LLS performance only for the region where the rocket-triggered lightning facility or tall object is located (especially in cases where the performance of the LLS is expected to vary significantly from region-to-region). Additionally, rocket-triggered lightning provides data for return strokes similar to only subsequent strokes in natural lightning. No data for first strokes in natural lightning can be obtained using this technique.

Video camera studies

Lightning data obtained using video cameras can be used as ground-truth to evaluate the performance characteristics of an LLS within whose coverage area the lightning discharges occurred. The LA, DE, and lightning classification accuracy of an LLS can generally be estimated using this method. Camera studies examining the detection efficiency and location accuracy of the U.S. National Lightning Detection Network were performed, for example, by Idone et al. (1998a, b) [6, 7]. In this method, data collection can be time consuming and challenging because the exact locations of lightning discharges to be captured on video cannot be predicted. Additional instrumentation such as antennas measuring electric field from lightning discharges is often required for this technique.

Inter-comparison among networks

The performance of one LLS that is being tested can be compared to another LLS that may be used as reference, as long as the reference LLS is well calibrated and its performance has been characterized independently. This method allows inferences to be made about the detection efficiency and location accuracy of the test LLS relative to the reference LLS. If the reference network provides VHF lightning mapping, inference about the test network's IC detection efficiency, and even IC location accuracy, can be made. An example of recent studies include Poelman et al. (2013 [8]). Indeed, given that IC flashes are mostly or entirely obscured from view, high-resolution VHF lightning mapping information is the only means of doing detailed validation of the IC lightning performance of another LLS.

While one or a combination of the above techniques can be used to evaluate the performance characteristics of an LLS, it is important to understand the strengths and weaknesses of the methods used, in order to obtain reliable estimates of LLS performance characteristics.

References

1. K.L. Cummins, M.J. Murphy, E.A. Bardo, W.L. Hiscox, R.B. Pyle, and A.E. Pifer, "A combined TOA/MDF technology upgrade of the U.S. National Lightning Detection Network," *Journal of Geophysical Research*, 1998, **103**(D8), 9035-9044.
2. K.L. Cummins and M.J. Murphy, "An overview of lightning locating systems: History, techniques, and data uses, with an in-depth look at the U.S. NLDN," *IEEE Trans. Electromagn. Compat*., 2009, **51**(3), 499–518, doi:10.1109/TEMC.2009.2023450.
3. W. Schulz, "Performance Evaluation of Lightning Location Systems," Ph.D. Thesis, Technical University of Vienna, 1997.
4. A. Nag, S. Mallick, V.A. Rakov, J.S. Howard, C.J. Biagi, J.D. Hill, M.A. Uman, D.M. Jordan, K.J. Rambo, J.E. Jerauld, B.A. DeCarlo, K.L. Cummins, and J.A. Cramer, "Evaluation of U.S. National Lightning Detection Network performance characteristics using Rocket-triggered lightning data acquired in 2004-2009," *J. Geophys. Res*., 2011, **116**, D02123, doi:10.1029/2010JD014929.
5. G. Diendorfer, M. Mair, W. Schulz, and W. Hadrian, "Lightning current measurements in Austria – Experimental setup and first results," In Proc. 25th Int. Conf. on Lightning Protection, Rhodes, Greece, 2000a, 44-47.
6. V.P. Idone, D.A. Davis, P.K. Moore, Y. Wang, R.W. Henderson, M. Ries, P.F. Jamason, "Performance evaluation of the U.S. National Lightning Detection Network in eastern New York, 1. Detection efficency," *J. Geophys. Res*., 1998a, **103**, D8, 9045-9055.
7. V.P. Idone, D.A. Davis, P.K. Moore, Y. Wang, R.W. Henderson, M. Ries, P.F. Jamason, "Performance evaluation of the U.S. National Lightning Detection Network in eastern New York, 2. Location accuracy," *J. Geophys. Res*., 1998b, **103**, D8, 9057-9069.
8. D.R. Poelman, W. Schulz, and C. Vergeiner, Performance Characteristics of Distinct Lightning Detection Networks covering Belgium, *J. Atmos. Ocean. Tech*., 2013, **30**, 942-951, 2013.

Invited

TWO LIGHTNING PROCESSES PRODUCING RELATIVELY SHORT DURATION BIPOLAR ELECTROMAGNETIC RADIATION SIGNATURES

A. Nag[1] and **V.A. Rakov**[2]

[1]Vaisala Inc., Louisville, Colorado, USA, amitabh.nag@vaisala.com
[2] University of Florida, Gainesville, Florida, USA

Abstract. The preliminary breakdown and the compact intracloud discharge are lightning processes that produce characteristic microsecond-scale bipolar radiation field signatures. Such characteristic electromagnetic signatures in conjunction with engineering-type models allow us to study these processes and make inferences about various parameters of these lightning discharges.

Introduction

Lightning processes produce electromagnetic field changes often with characteristic signatures that allow them to be identified and examined. Such characteristic electromagnetic signatures in conjunction with engineering-type models (e.g., Rakov and Uman, 2003, Chapter 12) [1] allow us to make inferences about various parameters of lightning discharges. In this presentation we discuss two lightning processes, the preliminary breakdown (PB) and the compact intracloud discharge (CID), that produce microsecond-scale bipolar radiation field signatures and review engineering models for these processes.

Preliminary Breakdown Pulse trains

The first stroke leader in a cloud-to-ground lightning discharge is thought to be preceded by the initial or preliminary breakdown. The preliminary breakdown can be defined as an in-cloud process that involves the formation of one or more channels in the cloud with the channels extending in seemingly random directions from the cloud charge source, with one of them evolving into the stepped leader that bridges the cloud charge source and the ground. The preliminary breakdown process in ground flashes is often viewed as a leader-like process bridging the main negative and lower positive charge centers. The preliminary breakdown often produces a train of pronounced microsecond-scale electric field pulses. The characteristics of these pulses have been examined in various studies over the years (see Rakov and Uman, 2003 [1], Chapters 4 and 9 for a review). The pulses are typically bipolar and in CG flashes, the polarity of the initial half-cycle is the same as that of the following return-stroke pulse.

Nag and Rakov (2009) [2] interpreted the preliminary breakdown pulse train in negative cloud-to-ground discharges as being generated when a negatively-charged channel extends downward from the main negative charge region and interacts with the lower positive charge region. This interpretation is generally supported by the high-speed video observations of Campos and Saba (2013) [3]. Nag and Rakov (2014) [4] used a modified transmission line model to reproduce the characteristic bipolar electric field pulse train associated with preliminary breakdown. In doing so, they assumed that the preliminary breakdown pulse train in negative cloud-to-ground discharge is generated when a negatively-charged channel extends downward from the main negative charge region and interacts with the lower positive charge region. It is assumed that during preliminary breakdown the negatively-charged channel extends downward in a stepped fashion through the relatively-high-field region between the main negative and lower positive charge centers and then through the relatively-low-field region below the lower positive charge center. At each step, an equivalent current source is activated ahead of the channel tip, resulting in a step current wave that propagates upward and facilitates downward extension of the channel. Each step produces a bipolar electric radiation field signature with successive steps producing a characteristic preliminary breakdown pulse train.

Compact Intracloud Discharges

Cloud lightning discharges that produce both (1) single, usually solitary bipolar electric field pulses having typical full widths of 10–30 μs and (2) intense HF-VHF radiation bursts (much more intense than those from any other cloud-to-ground or "normal" cloud discharge process) are referred to as compact intracloud discharges (CIDs). These discharges were first reported by Le Vine (1980) [5] and later characterized by Willett et al. (1989) [6] and Smith et al. (1999) [7], among others.

On the basis of experimental evidence of multiple reflections and modeling, *Nag and Rakov* (2010a) [8] inferred that, from the electromagnetic point of view, the CID is essentially a bouncing

wave phenomenon. The process can be viewed as a long wave repeatedly folding on itself, so that the electromagnetic field signature (narrow bipolar pulse) duration is not necessarily a measure of radiator length. Reflections at channel extremities may result in corona-like electrical breakdown there, because a reduction of current is accompanied by an increase of line charge density and associated voltage. This breakdown at channel ends is likely to produce intense bursts of HF-VHF radiation which are a characteristic feature of CIDs. *Nag and Rakov* (2010a) [10] showed via modeling that reflections were responsible for fine structure of wideband electric field and d*E*/d*t* waveforms. From modeling the CID as a wave traveling on an elevated vertical transmission line and comparing model-predicted electric fields with measurements, they estimated that the effective current reflection coefficients at channel ends (additionally accounting for current attenuation along the channel) should be in the range of 0 to –0.5, that the wave propagation speed ranges from 0.3 to $3 \cdot 10^8$ m/s, and the channel length is less than 1000 m. Further, *Nag and Rakov* (2010a) [8] showed that the current distribution along the CID channel is often not much different from uniform, as expected for a Hertzian (electrically short) dipole, because of relatively short channel length, relatively long current waveform, and relatively high propagation speed. Both the bouncing wave model and the Hertzian dipole approximation were shown to be capable of reproducing two-station CID electric field measurements. *Nag and Rakov* (2010b) [9] estimated electrical parameters of 48 located CIDs using their measured electric fields and vertical Hertzian dipole approximation. For all 48 events, geometric mean values of peak current, zero-topeak current risetime, and charge transfer for the first 5 μs were inferred to be 74 kA, 5 μs, and 164 mC, respectively. The geometric mean peak radiated power, and energy radiated for the first 5 μs were 29 GW and 31 kJ, respectively. For nine events, they were able to estimate CID channel length from channel traversal times measured in d*E*/d*t* waveforms and assumed propagation speeds of $2 \cdot 10^8$ m/s to $3 \cdot 10^8$ m/s, which limit the range of allowed speed values. For $v = 2.5 \cdot 10^8$ m/s (average value), the channel lengths for these nine events ranged from 108 to 142 m. The corresponding geometric mean values of peak current, zero-to-peak current risetime, and charge transfer for the first 5 μs are 143 kA, 5.4 μs, and 303 mC, respectively. The uncertainty in either current or charge transfer calculated for the nine events was estimated to be $\leq$ 25 %. The geometric mean peak radiated power and energy radiated for the first 5 μs (both wideband) were calculated to be 29 GW and 24 kJ, respectively. Overall, the estimated CID current waveform parameters were found to be comparable to their counterparts for first strokes in cloud-to-ground lightning, while their peak radiated electromagnetic power was considerably higher.

References

1. V.A. Rakov, and M.A. Uman, Lightning: Physics and Effects, Cambridge Univ. Press, New York, 2003.
2. A. Nag and V.A. Rakov, "Some inferences on the role of lower positive charge region in facilitating different types of lightning," *Geophys. Res. Lett*., 2009, **36**, L05815, doi:10.1029/2008GL036783.
3. L.Z.S. Campos and M.M.F. Saba, "Visible channel development during the initial breakdown of a natural negative cloud-to-ground flash," *Geophys. Res. Lett*., 2013, **40**, 4756–4761, doi:10.1002/grl.50904.
4. A. Nag and V.A. Rakov, "An engineering model for preliminary breakdown in cloud-to-ground lightning discharges," *International Conference on Grounding and Earthing, 6th International Conference on Lightning Physics and Effects*, Manaus, Brazil, May, 2014.
5. D.M. Le Vine, "Sources of the strongest RF radiation from lightning," *J. Geophys. Res*., 1980, **85**, 4091–4095.
6. J.C. Willett, J.C. Bailey, and E.P. Krider, "A class of unusual lightning electric field waveforms with very strong high-frequency radiation," *J. Geophys. Res*., 1989, **94**, 16,255–16,267.
7. D.A. Smith, X.M. Shao, D.N. Holden, C.T. Rhodes, M. Brook, P.R. Krehbiel, M. Stanley, W. Rison, and R.J. Thomas, "A distinct class of isolated intracloud discharges and their associated radio emissions," *J. Geophys. Res*., 1999, **104**, 4189–4212.
8. A. Nag and V.A. Rakov, "Compact intracloud discharges: 1. Mechanism of electromagnetic radiation and modeling," *Journal of Geophysical Research*, 2010a, **115**, D20102, doi:10.1029/2010JD014235.
9. A. Nag and V.A. Rakov, "Compact intracloud discharges: 2. Estimation of electrical parameters," *Journal of Geophysical Research*, 2010b, **115**, D20103, doi:10.1029/2010JD014237.

RETRIEVAL OF IMPORTANT GAS CONCENTRATIONS FROM TIME SERIES OF OZONE MEASUREMENTS AT ALTITUDES OF 50 km TO 75 km

M.Yu. Kulikov and **A.A. Nechaev**

Institute of Applied Physics RAS, Nizhny Novgorod, Russia

One of the main directions in the Earth's atmosphere physics is the study of spatial distribution and dynamics of minor gas constituents. One of the problems arising in this connection is how to obtain information about the parameters of a certain atmospheric system, which are difficult to measure directly. The aim of this work is to retrieve the value of the control parameter of mesospheric photochemical system (MPCS), the water vapor concentration, from time series of ozone concentration measurements at altitudes of 50–75 km.

To solve the formulated inverse problem, the statistical Bayesian approach is applied [1]. The zero-dimensional differential system of MPCS modeling twenty photochemical reactions between the constituents of the families of odd hydrogen HO_x (H, OH, HO_2) and oxygen O_x (O, $O(^1D)$, O_3) is solved. Real height dependences of air temperature, air concentration, and photodissociation coefficients are used. As a result, a vertical profile of H_2O concentration is restored by three noisy measurements of ozone concentration. Accuracy of the retrieval is estimated depending on the length of the time series and the dispersion of the measurement noise. It is demonstrated that the solution to the given problem allows determining the spatio-temporal evolution of concentrations of all other constituents of the families of odd hydrogen and oxygen.

References

1. M.Yu. Kulikov, D.N. Mukhin, A.M. Feigin, Bayesian strategy of accuracy estimation for characteristics retrieved from experimental data using base dynamic models of atmospheric photochemical systems, *Radiophysics and Quantum Electronics*, 2009, **52**(9), 690-699.

Invited

PRIMARY AND SECONDARY EFFECTS THAT LEAD TO TSUNAMI GENERATION DURING AN EARTHQUAKE

M.A. Nosov

Faculty of Physics of M.V.Lomonosov Moscow State University, Moscow, Russia
nosov@phys.msu.ru

Abstract. Strong ocean-bottom earthquakes are the most widespread cause of devastating tsunami waves. In this talk, we shall first discuss the main, and nowadays widely accepted, mechanism of tsunami generation that is associated with the instant displacement of water by co-seismic (residual) ocean-bottom deformation. Second, on the base of offshore registration of earthquakes and related tsunamis by ocean bottom stations (JAMSTEC) both in the tsunami source and at intermediate source distance (400–800 km), the role of water compressibility and non-linearity will be examined.

Numerical simulation of tsunami is normally based on the shallow water theory, which deals with the equations of hydrodynamics averaged over the vertical coordinate [1]. As for the description of tsunami generation, an earthquake is considered to instantly cause residual deformations of the ocean bottom. Then, the assumption is made that the displacement of the bottom is simultaneously accompanied by formation at the surface of the ocean of a perturbation (initial elevation), the shape of which is fully similar to the vertical residual deformations of the bottom.

The traditional approach described above is not accurate for at least the following two reasons. First, the horizontal deformation components, which can also contribute to ousting the water in the case of a sloping bottom, are neglected. Second, the dynamics of rupture formation and the relevant time-dependent process of bottom deformations remain beyond consideration. In this talk, we shall present some of our recent findings that improve the state of the art understanding of tsunami formation by ocean bottom earthquake.

Instant ocean bottom deformation: the role of vertical and horizontal components

In recent years there appeared methods that permit determining detailed co-seismic bottom deformation in a tsunami source from finite fault models (FFMs). According to the FFM, the fault plane for an earthquake is divided into a number of rectangular subfaults. The bottom deformation caused by each of these subfaults is calculated analytically by using the Okada formulae [2]. Then, the contributions of all the elements are summed up. As a result we determine the vector field of the co-seismic bottom deformation. From the vector field and ocean bottom topography we calculated residual displacement of ocean bottom surface caused by an earthquake. The residual displacement allows us to determine volumes displaced by vertical and horizontal components of the bottom deformation.

In calculations of the vector field of co-seismic bottom deformation of tsunami sources, we rely on FFM data available at the sites of the California Institute of Technology, UC Santa Barbara, and US geological survey. Necessary bathymetric data were extracted from the 1-min digital atlas General Bathymetric Chart of the Oceans (GEBCO).

We examine 44 ocean-bottom earthquakes that occurred during the period of 1994–2012. For many seismic events several solutions have been provided. Thus, we deal with a total of 70 earthquake source models [3]. It was shown that the absolute value of the relative contribution of the horizontal components of bottom deformation to the displaced volume varies from 0.07 to 55 %, on the average amounting to 14 %. In the majority of cases, the horizontal components provide an additional contribution to tsunami and virtually never diminish the contribution of the vertical component. So, it is important to take into account the horizontal components of bottom deformation in tsunami simulation.

Time-dependent ocean bottom deformation: the role of water compressibility and non-linearity

In the second part of this talk, we shall first describe the character of linear response of water column to seismic motions of the ocean bottom as a function of motion frequency. For this purpose a set of characteristic frequencies and related frequency bands will be introduced [1, 4]. Then, we shall present data-sets recorded by the Japan Agency for Marine-Earth Science and Technology (JAMSTEC) ocean bottom pressure gauges (PG) and seismometers (OBS) during the 2003 Tokachi-

oki and the 2011 Tohoku earthquakes. The data processing results will be examined in terms of manifestations of hydroacoustic and non-linear effects [4, 5].

The possibility for separation of the tsunami problem into independent “compressible” and “incompressible” parts will be discussed making use of the Euler equations and characteristics of bottom pressure variations recorded during the 2003 Tokachi-Oki and the 2011 Tohoku earthquakes.

Acknowledgements

This work was supported by the Russian Foundation for Basic Research, projects 13-05-92100, 13-05-00337. We are grateful to USGS, Caltech, and UCSB for slip distribution data. Special thanks go to JAMSTEC for PG and OBS data.

References

1. B.W. Levin and M.A. Nosov, *Physics of Tsunamis*, Springer, Dordrecht, 2009, p. 327.
2. Y. Okada, *Bulletin of the Seismological Society of America*., 1985, **75**(4), 1135-1154.
3. M.A. Nosov, A.V. Bolshakova, and S.V. Kolesov, *Pure Appl. Geophys.*, 2013, DOI: 10.1007/s00024-013-0730-6.
4. A. Bolshakova, S. Inoue, S. Kolesov, H. Matsumoto, M. Nosov, and T Ohmachi., *Russ. J. Earth. Sci.*, 2011, **12**, ES2005, doi:10.2205/2011ES000509.
5. M.A. Nosov, S.V. Kolesov, and A.V. Denisova, *Advances in Geosciences*, 2008, **14**, 141-146.

OPTIMIZATION TECHNIQUE FOR RETRIEVING VERTICAL DISTRIBUTIONS OF ATMOSPHERIC OZONE FROM RADIOMETRY DATA

V.V. Perekatova[1,3] and **D.N. Mukhin**[1,2]

[1] Institute of Applied Physics of the Russian Academy of Sciences, Nizhny Novgorod, Russia
[2] N.I. Lobachevsky State University of Nizhny Novgorod, Nizhny Novgorod, Russia
[3] e-mail: ValeriyaPerekatova@gmail.com

Abstract. An optimization technique for retrieving vertical distributions (profiles) of atmospheric ozone from radiometry data is proposed. The technique is based on the statistical (Bayesian) approach to solution of inverse problems. It is assumed that initial data contains measurement noise, and *a priori* information about properties of the profile is used. It is proposed to approximate the sought profile by a linear combination of empirical orthogonal functions (EOF) calculated from statistics of the previous measurements. This approximation allows optimal inclusion of *a priori* information into retrieval procedure. Efficiency of the proposed technique is demonstrated on the modeled data.

Retrieval of ozone profiles from passive remote sensing of the atmosphere is considered to be an incorrect inverse problem that requires solution of a nonlinear integral equation [1-2]. The connection between the radiometry data and the sought profile is defined by an integral equation because emission from the whole range of sounded heights contributes to the received signal:

$$T_i(f_i) = \int_0^\infty T(z)N(z)K(f_i,z)exp\left(-\int_0^z N(z)K(f_i,z)dz\right)dz + \sigma_i\xi_i, \quad (1)$$

where $T_i(f_i)$ is the spectrum of the atmosphere self-radiation, $N(z)$ is the vertical distribution of ozone concentration, $K(f_i,z)$ is the effective cross-section of ozone molecule absorption, ξ_i is the measurement error.

Success of retrieval depends on the following factors. First, it is a correct strategy of seeking solutions. Second, it is a correct allowance for *a priori* information about the properties of the sought profile. Discreteness of the data and presence of noise give an infinite set of possible solutions, so it is necessary to formulate the problem statistically. In this case, the Bayesian approach is used for construction of probability posterior distribution of the sought profile.

Extensive statistics allows using it as a source of *a priori* information. Rodgers [3] proposed the method of statistical regularization which uses the covariance matrix derived from previous measurements. In this work modification of that statistical regularization method is proposed. The method includes approximation of the sought profile by a linear combination of the empirical orthogonal functions (EOF) calculated according to statistics of the previous measurements:

$$\boldsymbol{N} = \bar{\boldsymbol{N}} + \sum_i \alpha_i \boldsymbol{V}^i \quad (2)$$

Here $\bar{\boldsymbol{N}}$ is the average profile over *a priori* ensemble and $\boldsymbol{V}^i$ is the i[th] EOF. Actually, instead of using ozone concentration on each layer as parameters of the sought profile, it is suggested to use linear combinations of deviations from average ozone concentration at different layers. Practically, eigenvectors $\boldsymbol{V}^i$ of covariance matrix are derived, wherein covariance matrix can be represented in diagonal form. Therefore, the Bayesian-based cost function of the modified method is:

$$\chi^2 = \sum_i \frac{(T_i - \mathfrak{I}(\alpha, f_i))^2}{2\sigma_i^2} + \sum_k \frac{\alpha_k^2}{2\lambda_k}, \quad (3)$$

where $\mathfrak{I}$ is the integral entering into (1), which depends on ozone profile represented via parameter vector $\boldsymbol{\alpha}$, and the second term came from Rodger's *a priori* probability density written in terms of new variables $\boldsymbol{\alpha}$.

In this way, solution of the formulated problem reduces to finding α_k coefficients which minimize the cost function (3). The efficiency of the proposed technique is demonstrated on modeled data. The ensemble of ozone profiles measured near Nizhny Novgorod is used as *a priori* statistics. The modeled data simulating the spectrum of the atmosphere self-radiation is used for retrieving ozone profiles [4]. The results of reconstruction are presented in Fig. 1. It is worth noting that the reconstructed profile is obtained after a full set of α_k coefficients has been received.

Small-scale empirical orthogonal functions are smoothed by integral equation (1) and hence cannot be resolved from data. Consequently there arise a question of optimal number of components used in the retrieval algorithm. Reducing the number of components allows decreasing computational time and arising stability of numerical algorithms. In this work the optimality for finding appropriate number of EOFs is suggested. After averaging the difference between real and reconstructed profiles (as long as d principal components are considered) over an ensemble of profiles we can obtain a criterion of optimal number of components:

$$l(d) = \frac{1}{K}\sum_{k=1}^{K} L^k = \left\langle \frac{1}{M}\sum_{i=1}^{d}\left(\alpha_{ik}^t - \alpha_{ik}^r\right)^2 \right\rangle + \frac{1}{M}\sum_{i=d+1}^{M}\lambda_i . \quad (4)$$

The optimality condition (4) depending on the number of components taken into account is shown in Fig. 2. Intervals of estimation errors based on assumption of chi-square distribution of l value are also shown. There is an optimal value d_{opt}=10 for which additional small-scale components do not increase retrieval accuracy. It happens because these components tend to be scattered near zero, since the role of *a priori* term in (3) becomes dominant for them. Comparison of retrieval results with the full EOF basis (corresponding to the maximum value d =33) and the optimal number of components (which is d_{opt}=10) are shown in Fig. 1. It can be seen that the profile retrieved using an optimal number of components differs less from the initial profile than the profile using the full basis.

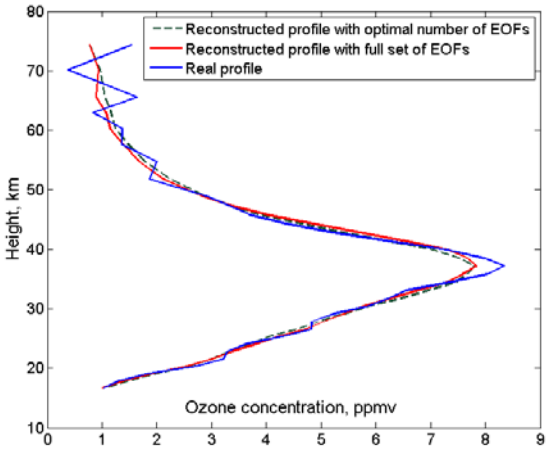

Fig. 1. Comparison between real and reconstructed profiles

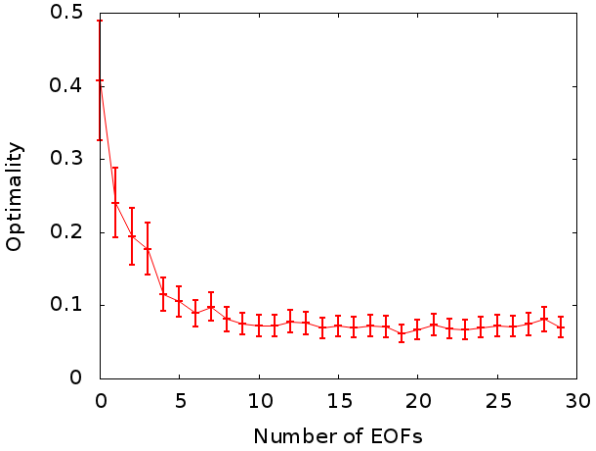

Fig. 2. Optimality value versus number of EOFs

Acknowledgements

This work was supported by the Russian Foundation for Basic Research (Grant No. 12-05-00999).

References

1. D.N. Mukhin, A.M. Feigin, Ya.I. Molkov and E.V. Suvorov, *Adv. Space Res.* 2006, **37**(12), 2292-2298.
2. Ya.I. Molkov, D.N. Mukhin, E.V. Suvorov, and A.M. Feigin, *Radiophysics and Quantum Electronics*, 2003, **46**, 8-9.
3. C.D. Rodgers, *Reviews of Geophysics and Space Physics*, 1976, **14**(4), 609.
4. E.P. Kropotkina, Yu.Yu. Kulikov, V.G. Ryskin, S.V. Solomonov, *Radiophysics and Quantum Electronics*, 2005, **48**, 10-11.

Invited

RECENT RESEARCH AT THE LIGHTNING OBSERVATORY IN GAINESVILLE, FLORIDA: A REVIEW AND UPDATE

V.A. Rakov, M.D. Tran, S. Mallick, and **V.B. Somu**

Department of Electrical and Computer Engineering, University of Florida, USA

In this paper, we will review some topics recently studied at theLightning Observatory in Gainesville (LOG), Florida. The LOG is part of the International Center for Lightning Research and Testing (ICLRT), which also includes the Camp Blanding (CB) lightning-triggering facility. The LOG was established on the University of Florida campus in 2004 primarily for measuring electromagnetic fields produced by lightning. Over the years the experimental setup has undergone upgrades, modifications, expansions, and relocation. It is currently located on the roof of the five-story New Engineering Building. The LOG includes a glass cupola providing over a 180° unobstructed view of the horizon. The cupola houses digitizing oscilloscopes, computers, and high-speed video cameras, with the various sensors and associated electronics being located nearby on the roof. The sensors currently include electric field antennas, electric field derivative (dE/dt) antennas, magnetic field derivative (dB/dt) antennas, and an X-ray detector. Signals from all the sensors are relayed by fiber-optic links to the glass cupola, where they are recorded. All records are GPS time stamped.

The Lightning Observatory in Gainesville (LOG), Florida, has been continuously operated since 2004. The results of observations at LOG have provided considerable insight into lightning properties and mechanisms. Among important findings are (a) evaluation of various equations for estimation of lightning peak currents from measured electric or magnetic fields, (b) inferences on the role of lower positive charge region in the cloud in facilitating different types of lightning, (c) characterization of positive lightning flashes in Florida, (d) discovery of the mechanism of electromagnetic radiation of compact intracloud discharges and estimation of their electrical parameters, (e) new inferences on the interaction of lightning electromagnetic pulse with the ionosphere, and (f) first observations of higher X-ray production by subsequent-stroke leaders compared to the first-stroke leader in the same flash. Selected new results will be presented in this paper, including updates on (1) X-rays produced by first and subsequent strokes in natural lightning, (2) lightning interaction with the ionosphere, and (3) lightning properties inferred from high-speed video camera observations.

EVOLUTION OF THE CONVECTIVE STRUCTURES IN A WATER LAYER WITH AN INTERNAL DRIFT FLOW AND INSOLUBLE SURFACTANT ON THE FREE SURFACE

V.P. Reutov and **G.V. Rybushkina**

Institute of Applied Physics RAS, Nizhny Novgorod, Russia
reutov@appl.sci-nnov.ru

Abstract. The convective structures arising in a thin horizontal water layer cooled from above are studied numerically. The layer contains a shear flow produced by tangential stresses on the top and an insoluble absorption-type surfactant film on the free surface. Evolution of patterns of the surface temperature is studied with increasing film elasticity, Reynolds number, and layer depth. The consideration is aimed at modeling the small-scale subsurface convective structures arising in open water basins in the presence of wind.

Investigation of the convective structures in open water basins is an important topic in the nonlinear geophysics. In this work we are concerned with modeling the small-scale subsurface convective structures arising in the presence of the tangential wind stresses and absorption-type surfactant. To this end, the evolution of the structures in a finite-depth water layer cooled from above is studied. The attention is focused on the role of the surfactant in the convective processes, which is insufficiently studied now.

The analysis is based on numerical solution of standard three-dimensional equations for the Boussinesq gravity-capillary convection supplemented with the equation governing the surfactant concentration [1]. The approximation of a nondeformable free surface, the linear dependence of surface tension on temperature and surfactant concentration, and the condition of thermal insulation at the bottom are adopted. A numerical procedure based on the pseudospectral method together with appropriate reformulation of the basic equations was employed [2]. We used the discrete Fourier transform including 128×128 harmonics along the horizontal directions x, y and discretization with 80 points in the vertical direction z. The parameters of the water layer were specified in accord with a minimal scale of subsurface convection in the seas for the reference temperature of 20 °C, namely: the length scale h = 1 cm, the velocity scale was ν/h (ν is the kinematic viscosity of water), and the temperature scale was qh/κ (q is the heat flux from the water surface, κ is the thermal conductivity of water). The dimensionless parameters of the flow are the Grashof (Gr), Prandtl (Pr), Marangoni (Ma), Reynolds (Re), and Biot (Bi) numbers as well as normalized elasticity (E') and diffusivity (D') of the surfactant film.

At first, the influence of the surfactant on patterns evolution with the growth of the Reynolds number was studied for a thin layer with normalized thickness $H=1$. The computations showed that, in the case of pure water ($\mathrm{E}'=0$), there appeared small-scale thermocapillary patterns on the background of large cells having the sizes of the order of the layer depth. Such different-scale patterns were earlier observed in the ethyl alcohol and water layers (see refs. [4] and [2]). With increasing Reynolds number, the large cells were elongated in the flow direction like in ethyl alcohol. When the film elasticity E' became large enough, the small patterns were suppressed totally and the large patterns demonstrated the cell-to-roll transition like at the purely bouncy-driven convection. It was found that the values of averaged (over all dimensions) kinetic energy of the velocity pulsations obtained can be attained in purely buoyancy-driven convection without surfactant at an essential (two-fold) effective decrease of Gr. Thus, the influence of the surfactant does not reduce merely to elimination of the thermocapillarity effects.

In the case of a thin layer ($H=1$) and large enough E', quasiregular well-recognized polygonal cells and rolls were obtained in the presence of a flow similarly to [5, 6]. For thick enough layers ($H\geq2$), cold water columns moving downwards (the so-called plumes) were revealed. The appearance of plumes was accompanied by swirl-like liquid rotations on the water surface. At small Re, the ordered cellular patterns were destructed by the swirls, and, at large enough Re, the longitudinal rolls could be distinguished (Figs. 1, 2). When the swirls appeared, the averaged kinetic energy increased by 6–7 times compared to the case of the thin layer ($H=1$). It was found that the plumes became unsteady and decayed in their lower part (Fig. 2). Under the action of the shear flow, the rotation regions were elongated in the flow direction as well.

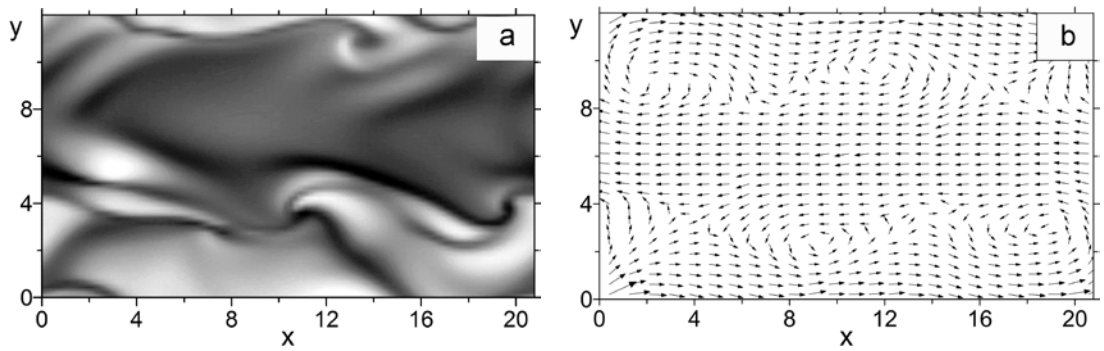

Fig. 1. Image of the surface temperature (a) and the corresponding vector lines of the surface velocity perturbations (b) illustrating the liquid swirl-like rotations. The black and white colors correspond to the minimal and maximal temperature, respectively; x-axis is oriented in the mean flow direction ($H = 3$, $\mathrm{Pr} = 7$, $\mathrm{Gr} = 4000$, $\mathrm{Ma} = 20000$, $\mathrm{E}'=7000$, $\mathrm{D}'=0.001$, $\mathrm{Bi} = 0.5$, $\mathrm{Re} = 20$, pictures at the time moment $t = 7.5$)

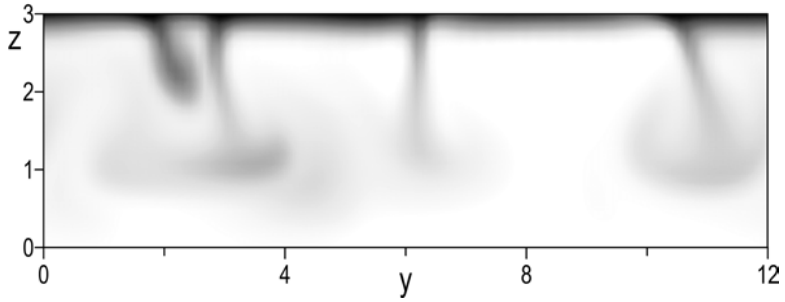

Fig. 2. The plumes in the vertical cross section orthogonal to the flow direction x at the same parameters as in Fig.1 ($z = 0$ and $z = 3$ correspond to the layer bottom and top, respectively; $t = 3.2$)

A mechanism of the swirls formation can be determined from the computations. As follows from Fig. 1, the liquid flows along the black lines on the surface, which are the lines of liquid sinking. Evidently, the velocity vector lines converge to the point of fastest sinking where the plume is formed beneath the surface.

Acknowledgements

The work was carried out with financial support from the Russian Foundation for Basic Research (project No. 13-05-97056-r_povolzhye_a).

References

1. A. Nepomnyashchy, I. Simanovskii, and J. Legros, *Interfacial Convection in Multilayer Systems*, Springer US (Appl. Math. Sci., vol. 179), 2012, p. 498.
2. V. Reutov and G. Rybushkina, *Phys. Fluids*, 2013, **25** (074101).
3. S. Bower and J. Saylor, *Int. J. Heat and Mass Transfer*, 2011, **54**(25-26), 5348–5358.
4. V. Reutov, V. Chernov, A. Ezersky, and P. Gromov, *Izvestiya, Atmos. Ocean. Phys.*, 2012, **48**(2), 185–192.
5. V. Reutov, A. Ezersky, G. Rybushkina, and V. Chernov, *J. Appl. Mech. Tech. Phys*, 2007, **48**(4), 469-478.
6. V. Reutov and G. Rybyshkina, *Fluid Dyn.*, 2008, **43**(1)**,** 49-58.

A NETWORK OF NETWORKS APPROACH TO INVESTIGATE THE INFLUENCE OF SEA SURFACE TEMPERATURE VARIABILITY ON MONSOON SYSTEMS

A. Rheinwalt[1,2], B. Goswami[1,3], N. Boers[1,2], J. Heitzig[1], N. Marwan1, R. Krishnan[4], and **J. Kurths[1,2]**

[1] Potsdam Institute for Climate Impact Research, Potsdam, Germany, aljoscha@pik-potsdam.de
[2] Name Humboldt-Universitat zu Berlin, Berlin, Germany
[3] University of Potsdam, Potsdam, Germany
[4] Indian Institute of Tropical Meteorology, Pune, India

Abstract. In this study we analyze large-scale inter-dependences between Sea Surface Temperature (SST) and rainfall variability using climate networks. On account of this analysis, we coarse-grain gridded SST and rainfall datasets by merging grid points that are dynamically similar to each other. We consider the SST and rainfall systems as two distinct climate networks and use established cross-network measures to understand their interrelations. As a first step, the spatial distributions of these cross-network measures illustrate regions which are of particular importance in the interaction between SST and rainfall. Secondly, we go into further detail by investigating the cross-network topology explicitly for these regions. Here, strong influences from regions in the SST system in relation to other regions in the rainfall system are detected. These influences structured in a spatially embedded directed network describe important mechanisms behind monsoon systems. For example, behind the Indian Summer Monsoon, which is known to be controlled by SST variability over the adjacent Indian Ocean.

Summary

The influence of global sea surface temperature (SST) variability on precipitation over Asia is studied on monthly scales by use of monthly time series for the years 1982 to 2008. SST data is obtained from the NOAA Optimum Interpolation SST V2 by NCEP on a one by one degree grid. Precipitation data over land is taken from the APHRODITE daily precipitation data product on a 0.5 by 0.5 degree grid. Monthly mean values were calculated from daily values in a pre-processing step. Here, anomalies are studied in contrast to the monthly mean values where the seasonal cycle would dominate correlation coefficients. Anomalies are calculated by subtracting from each value the long-term mean for that month and dividing by the corresponding long-term standard deviation.

Both data sets are then coarse-grained by clustering in correlation space. For each pair of time series of the same observable a distance is defined by the arc-cosine of the Spearman rank correlation coefficient. In this metric space a hierarchical clustering is performed so that all time series in a given cluster are positively correlated to each other with a Spearman's Rho of at least 0.5. The most central time series in a cluster, i.e., the time series with the highest mean correlation to all other time series in that cluster, is picked as a representative time series (RTS) for that cluster. Such clustering groups time series by similarity reduces the dimension of the problem and ensures a certain uniqueness of the time series. The clustering for both data sets is seen in Figs. 1 and 2 with black dots marking the location of RTS.

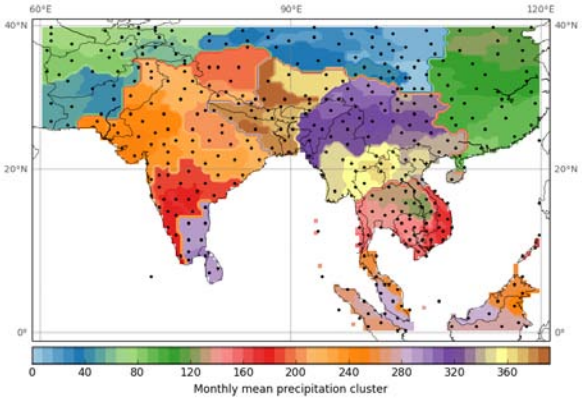

Fig. 1. Hierarchical clustering of monthly mean precipitation by Spearman correlation

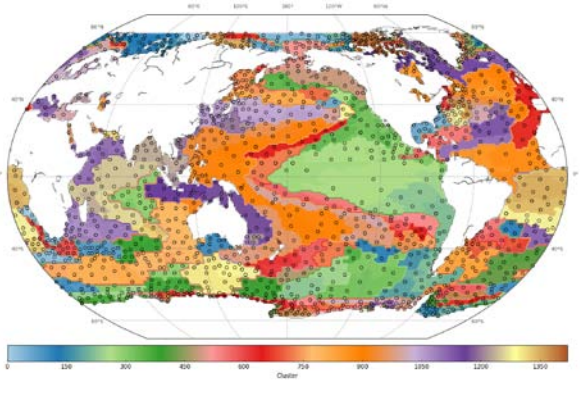

Fig. 2. Hierarchical clustering of monthly mean SST by Spearman correlation

In this analysis using Climate Networks, RTS from the SST as well as from the precipitation field are represented by network nodes. Nodes are connected by a link if the corresponding RTS are significantly correlated. The correlation is measured by a cross-correlation analysis using Spearman's Rho correlation coefficients. Links are considered to be directed depending on the time lag and weighted by the corresponding Spearman's Rho. This procedure results in one Climate Network for the SST field and one for the precipitation field. These two Climate Networks are connected by cross-links which represent the influence of SST on precipitation in our analysis. For reasons of simplicity we thereby neglect feedback and focus on links pointing from SST nodes to precipitation nodes only.In other words, on precipitation variability following SST variability.

The influence of a given SST RTS over the ocean on precipitation variability in Asia is visualized by the spatial pattern that results from a color-coded plot of all Spearman's Rho coefficients between that single ocean RTS and all different precipitation RTS over land. We observe that these patterns are often quite similar for different ocean nodes. Hence, we separate ocean nodes by their induced patterns over land into four different groups – so called influence modes. This grouping of ocean nodes with respect to the spatial correlation patterns they produce results in the red, purple, yellow and turqoise ocean regions shown in Fig. 3. The spatial correlation patterns induced by these four influence modes are shown in Fig. 4. Resulting correlation patterns are the land-node-wise average per standard deviation Spearman's Rho coefficients over all ocean nodes defining a given influence mode. The average per standard deviation pattern is more pronounced than the average only, leading to the conclusion that high correlation coefficients vary less within a given influence mode.

These induced patterns over land are related to ocean regions indicated by the color of the ocean in the corresponding map. For instance, the pattern over Asia seen in the small map with the red ocean is induced by the red ocean region seen in the global map (ENSO).

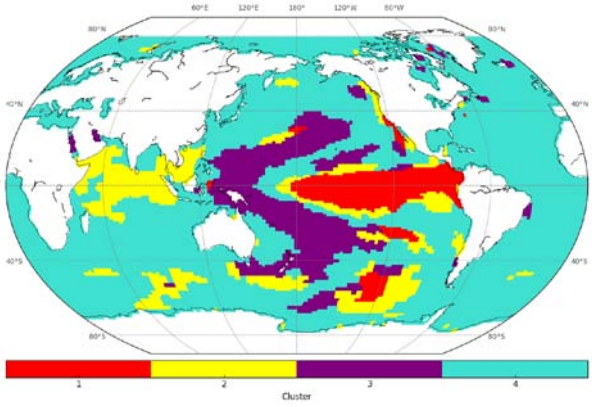

Fig. 3. Ocean regions of the four distinct influence modes

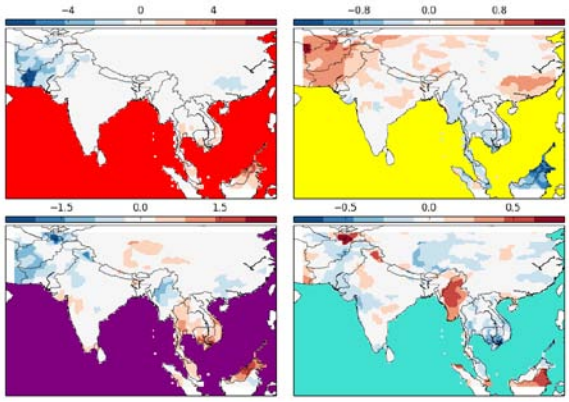

Fig. 4. Induced patterns over land of the four distinct influence modes

Acknowledgements

Funded by DFG, project Investigation of past and present climate dynamics and its stability by means of a spatio-temporal analysis of climate data using complex networks (MA 4759/4-1).

LABORATORY MODELING OF THE WIND-WAVE INTERACTION BY MODIFIED PIV TECHNIQUE

A. Kandaurov[1,2], Yu. Troitskaya[1,2], G. Caulliez[3], D. Sergeev[1,2], and **M. Vdovin[1,2]**

[1] Institute of Applied Physics of the RAS, Department of geophysical research, Nizhny Novgorod, Russian Federation
[2] Radiophysical department of the University of Nizhniy Novgorod, Russian Federation
[3] Mediterranean Institute of Oceanography, Marseille, France

Wind-wave interaction processes (momentum, heat and moisture transfer) under severe conditions in the air-sea boundary layers are of special interest first of all in the case of studying the hurricane dynamics. Parameterization of these processes used in forecasts models are based on the experimental data, but at present there is not enough information (experimental data) about them. The problems of carrying out measurements in the real ocean could be eliminated to some extent in laboratory conditions. Recently non-contact methods of the airflow above surface waves based on modern visualisation, particularly PIV methods were developed. Some measurements of the wind velocity field above surface waves were carried out in [1, 2]. However, in those works only low wind speed conditions were investigated and the standard PIV method gives velocity fields with the time period that is insufficient to characterize a turbulent air flow.

In the present work parameters of the air flow above a rough water surface for a wide range of wind speeds were measured using a modified Particle Image Velocimetry (PIV) technique. The experiments were carried out at the wind-wave stratified flume of IAP RAS (length 10 m, cross section of air channel 0.4×0.4 m, wind velocity up to 24 m/s) and at the Large Air-Sea Interaction Facility (LASIF) – MIO/Luminy (length 40 m, cross section of air channel 3.2×1.6 m, wind velocity up to 10 m/s).

A combination of PIV measurements, optical measurements of water surface form and wave gages were used for detailed investigation of the characteristics of the wind flow over the water surface. The modified PIV-method is based on the use of continuous-wave (CW) laser illumination of the air flow seeded by particles and high-speed video.

During the experiments on the wind-wave stratified flume of IAP RAS, a CW laser with 1.5 W output power was used as a source for light sheet. A high-speed digital camera VideoSprint (VS-Fast) was used for taking visualized air flow images with the frame rate of 2000 Hz. In the experiments on the LASIF, a more powerful Argon laser (4 W, CW) was used as well as a high-speed camera with higher sensitivity and resolution: Optronics Camrecord CR3000x2, frame rate 3571 Hz, frame size 259×1696 px. In both series of experiments spherical 0.02 mm polyamide particles with inertial time 7 ms were used for seeding the airflow. Using in LASIF new seeding system provided high particle density in PIV-images. In combination with high-resolution camera it allowed us to obtain momentum fluxes directly from measured air velocity fluctuations.

Velocity air flow field was retrieved by PIV images processing with adaptive cross-correlation method on the curvilinear grid following surface wave profile. The mean wind velocity profiles were retrieved using conditional in phase averaging like in [1]. This data was then compared to values retrieved from wind speed profiles [2].

Acknowledgements

This work was supported by RFBR grants (project code 13-05-00865, 13-05-12093, 12-05-01064, 14-08-31740, 14-05-31415), the President Grant for young scientists MK-3550.2014.5 and the grant of the Government of the Russia Federation designed to support scientific research project implemented under the supervision of leading scientists at Russian institutions of higher learning (project code 11.G34.31.0048).

References

1. N. Reul, H. Branger, J.-P. Giovanangeli, "Air flow separation over unsteady breaking waves", *Phys. Fluids*, 1999, **11**, 1959-1961.
2. F. Veron, G. Saxena, and S.K. Misra, "Measurements of the viscous tangential stress in the airflow above wind waves", *Geophys. Res. Lett.*, 2007, **34**, L19603, doi: 10.1029/2007GL031242.
3. Yu. Troitskaya, D. Sergeev, O. Ermakova, and G. Balandina, "Statistical Parameters of the Air Turbulent Boundary Layer over Steep Water Waves Measured by the PIV Technique", *J. Phys. Oceanogr*., 2011, **41**, 1421-1454.
4. Y.I. Troitskaya, D.A. Sergeev, A.A. Kandaurov, G.A. Baidakov, M.A. Vdovin, and V.I. Kazakov, “Laboratory and theoretical modeling of air-sea momentum transfer under severe wind conditions”, *J. Geophys. Res.*, 2012, **117**, C00J21.

NONLINEAR DYNAMICS OF BAROTROPICALLY UNSTABLE ROSSBY WAVE PACKETS AND FORMATION OF ZONALLY MODULATED VORTEX STREETS IN WEAKLY SUPERCRITICAL ZONAL FLOWS

S.V. Shagalov and **G.V. Rybushkina**

Institute of Applied Physics, Nizhny Novgorod, Russia, shagalov@appl.sci-nnov.ru

Abstract. This study explores the supercritical dynamics of Rossby wave packets comprised of weakly unstable barotropic and baroclinic normal modes feeding on the common critical layer (CL) of a horizontally sheared barotropically unstable zonal flow in the presence of vertical stratification. Self-consistent equations governing the evolution of the wave packets envelopes and CL vorticity distribution are derived with the aid of an asymptotic procedure. Nonlinear generation mechanisms of slowly modulated wave-trains and CL potential vorticity patterns are examined for the regimes of weakly nonlinear and strongly nonlinear dissipative CL.

A problem of fundamental interest in geophysical fluid dynamics is the development of the barotropic instability in a rotating fluid [1] which is directly relevant to the formation of large-scale vortical structures [2] and transition to turbulence [3] in horizontally sheared atmospheric and oceanic zonal flows. The physical mechanism feeding the instability near its onset in a weakly dissipative zonal flow is restricted to resonant extracting the kinetic energy from the flow by weakly unstable normal modes in the relatively thin critical layer (CL) surrounding a level where the wave speed of a marginal mode matches the mean flow. The study [3] seems to be the first to perform an asymptotic analysis of the transition to turbulence and chaotic advection in parallel shear flows on the basis of the nonlinear CL concept.

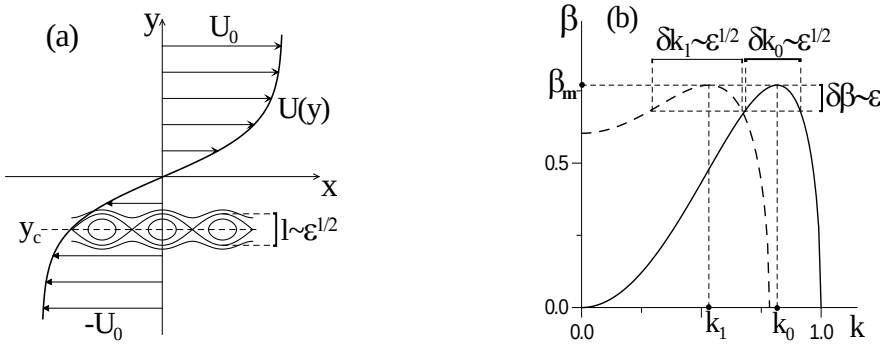

Fig. 1. (a) Schematic illustration of cat's eye streamline pattern in the nonlinear CL of a zonal mixing layer. (b) Stability boundaries of the barotropic mode (a solid line) and the main baroclinic mode (a dashed line) for the zonal flow $U = \tanh y$

This study employs the approach developed in [3] to continue an exploration of the effects arising from the stable density stratification in a weakly dissipative barotropically unstable zonal flow on a β-plane undertaken in [4]. Being specified by the mixing layer velocity profile $U(y)$, the background flow is assumed to be directed along the zonal x-axis and varies in the meridional y-direction (Fig. 1(a)). A simple model of stable density stratification in the vertical z-direction with constant buoyancy frequency is adopted. According to the linear inviscid theory the basic barotropic flow is capable of supporting barotropic and baroclinic unstable normal modes whenever the gradient of the Coriolis parameter β is less than a critical value $\beta_m = (U'')_{\max}$ [1]. Supercriticality of an inviscid flow defined as $\delta\beta = \beta_m - \beta$ is expressed through the small amplitude parameter ε: $\delta\beta = \varepsilon\beta_1$ (Fig. 1(b)). A notable feature of the problem is that the marginal modes corresponding to $\beta = \beta_m$ have the same phase speed c. As a consequence, the unstable waves limited to the narrow bands $\delta k_{0,1} = O(\varepsilon^{1/2})$ around the critical wavenumbers $k_{0,1}$ can be interpreted as wave packets, with central wavenumbers $k_{0,1}$, sharing common CL in the vicinity of a latitude $y = y_c$ where $U(y) = c$ (Fig. 1(a)). To capture the effects arising from small dissipation, the dimensionless viscosity parameter ν is also scaled in terms of ε: $\nu = \varepsilon^{3/2}\nu_*$. An analysis of the asymptotic expansions in ε outside and inside the CL employing the perturbation method of multiple scales and the matched asymptotics formalism is performed to derive a closed system of equations governing the evolution of the complex amplitude functions $a_j = a_j(\xi, t)$ ($j = 0,1$) of slowly modulated wave-trains and CL vorticity distribution $\Omega = \Omega(\xi, \eta, z, t)$

$$\frac{\partial a_0}{\partial t}+(c_{0g}-c)\frac{\partial a_0}{\partial \xi}+i\alpha_0\frac{\partial^2 a_0}{\partial \xi^2}=i\sigma_0 a_1^2+i\varphi_c^2\frac{k_0}{J}\int_0^1 dz\int_{-\infty}^{\infty}\left\langle \Omega e^{-ik_0\xi}\right\rangle d\eta, \quad (1)$$

$$\frac{\partial a_1}{\partial t}+(c_{1g}-c)\frac{\partial a_1}{\partial \xi}+i\alpha_1\frac{\partial^2 a_1}{\partial \xi^2}=i\sigma_1 a_0 a_1^*+i\varphi_c^2\frac{2k_1}{J}\int_0^1 \cos(\pi z)dz\int_{-\infty}^{\infty}\left\langle \Omega e^{-ik_1\xi}\right\rangle d\eta, \quad (2)$$

$$\frac{\partial \Omega}{\partial t}+U_c'\eta\frac{\partial \Omega}{\partial \xi}-2\,\mathrm{Re}\left\{\sum_{n=0,1} ik_n a_n\cos(\pi n z)e^{ik_n\xi}\right\}\frac{\partial \Omega}{\partial \eta}=F(\xi,z,t)+\nu\frac{\partial^2\Omega}{\partial \eta^2}, \quad (3)$$

where F contains terms describing supercriticality and nonlinearity, $\langle ...\rangle$ denotes local averaging over streamwise coordinate $\xi = x-ct$, $\eta = y-y_c$. Nonlinear resonant terms included in (1)-(2) account for resonant interaction between modes outside the CL which occurs when they satisfy $k_0 = 2k_1$. Under sufficiently small supercriticality with $\delta\beta \ll \nu^{2/3}$ and at $\sigma_{0,1}=0$ the CL-flow is shown to evolve in a quasi-steady weakly nonlinear regime. In this case equations (1)–(3) can be reduced to a set of two coupled quintic-cubic Ginzburg-Landau envelope equations describing simultaneous evolution of weakly unstable Rossby wave packets feeding on the common CL. The primary effect of nonlinear interaction within the CL turns out to be the suppression of the baroclinic modes. The finite amplitude barotropic state is shown to become unstable to sideband instability which leads to formation of stationary envelope modulations having the form of spatially extended or localized regular patterns.

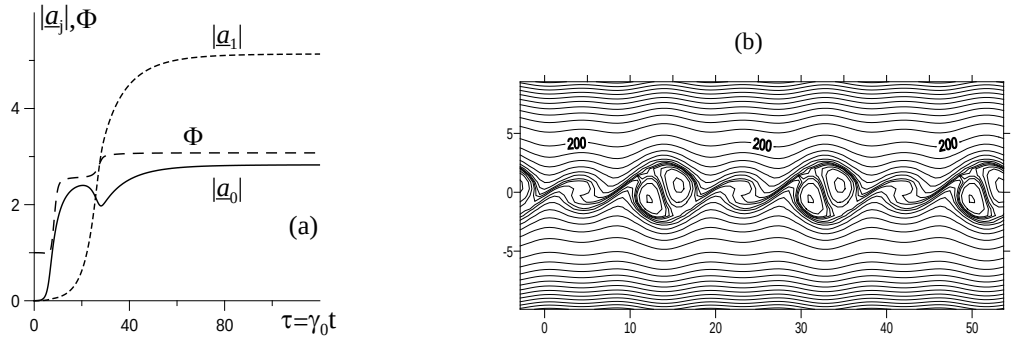

Fig. 2. (a) Time evolution of normalized mode amplitudes $\underline{a}_j = a_j / U_c' l_v^2$ and phase locking of resonantly coupled modes in the regime of strongly nonlinear CL. (b) Potential-vorticity pattern formed in the CL from the explosive growth of resonantly coupled modes

In the presence of nonlinear resonant coupling of the modes through the condition $k_0 = 2k_1$ a nonlinear mechanism of the explosive instability arising from nonlinear resonant interaction inside and outside the CL comes into play and instability saturates in the regime of strongly nonlinear CL even if $\delta\beta \ll \nu^{2/3}$. Weakly nonlinear Ginzburg-Landau equations, therefore, are no longer applicable and numerical analysis of equations (1)–(3) should be employed. Figure 2(a) (where only the most unstable modes are taken into account) shows simultaneous growth and saturation of the unstable modes started at $\delta\beta = O(\nu^{2/3})$. The amplitudes and the phase variable $\Phi = 2\varphi_1 - \varphi_0$ (where $\varphi_j = \arg a_j$) tend asymptotically to a state independent of the initial conditions for the amplitudes and phases. As a consequence, the flow evolves toward a coherent steady state consisting of phase-locked modes equilibrated in the regime of strongly nonlinear CL. This instability scenario is accompanied by the development of periodic coherent structures in the potential-vorticity distribution inside the common CL taking the form of a zonally modulated barotropic-baroclinic vortex chain (Fig. 2(b)).

Acknowledgements. The work was supported by a grant from the Russian Foundation for Basic Research (No. 12-05-01115-a).

References

1. J. Pedlosky, *Geophysical Fluid Dynamics*, Springer-Verlag, Berlin, 1982, p. 624.
2. F.J. Poulin, G.R. Flierl, *J. Phys. Oceanogr.*, 2003, **33**(10), 2173-2192.
3. S.V. Shagalov, V.P. Reutov, and G.V. Rybushkina, *Izv.,Atmos. and Oceanic Physics*, 2010, **46**(1), 95-108.
4. S.V. Shagalov, G.V. Rybushkina, *Progress in Turbulence V, Springer Proceedings in Physics*, 2014, **149**, 189-194.

Invited

INFERRING DIRECTIONAL COUPLINGS FROM TIME SERIES: AVOIDING SPURIOUS DETECTION, ESTIMATION OF LONG-TERM EFFECTS, AND APPLICATION TO CLIMATIC DATA

D.A. Smirnov[1] and **I.I. Mokhov**[2]

[1] V.A. Kotel'nikov Institute of RadioEngineering and Electronics of the Russian Academy of Sciences (Saratov Branch), Saratov, Russia, e-mail: smirnovda@yandex.ru

[2] A.M. Obukhov Institute of Atmospheric Physics of the Russian Academy of Sciences, Moscow, Russia

Abstract. Detection and characterization of directional couplings between complex systems from time series are considered. Several factors leading to spurious detections are highlighted, including low temporal resolution and unobserved state variables. It prompts special tests for coupling bidirectionality based on empirical modelling. In addition to short-term Granger causality characteristics, it is suggested to assess long-term effects of couplings based on fitting an empirical model and considering its behavior under special parameter variations. With all those approaches, time-varying mutual effects of Atlantic Multidecadal Oscillation and El-Nino/Southern Oscillation over the last 150 years are revealed.

In studies of ensembles of systems with nontrivial temporal evolution, it is fruitful to characterize their interactions which often determine basic features of the collective behavior. For a deeper understanding, it is particularly important to reveal "directional couplings", i.e. to answer the question "who drives whom". For example, one often looks for couplings between large-scale modes of climate variability (e.g. [1, 2]) or global climate processes (e.g. [3, 4]). One often must reveal couplings from passive observations of the systems behavior, e.g. from a time series of certain observed variables. Sometimes, solving such a problem appears feasible based on the celebrated concept of the Granger causality [5]. Its generalized version from information theory is called "transfer entropy" (TE) [6].

In case of two systems, one says that a system X "Granger causes" a system Y if knowledge of the past of X improves predictions of Y as compared to self-predictions. Prediction improvement (PI) is usually defined as a decrease in the one-step-ahead mean-squared prediction error. TE characterizes an "uncertainty reduction" in terms of Shannon entropies of the conditional probability distributions of the future Y. Similarly to PI, a statistically significant nonzero value of TE in the direction from X to Y is usually interpreted as a result of the influence "X to Y", and nonzero TEs in both directions as a result of bidirectional coupling. TE is invariant to any invertible change of variables. Many works concentrate mainly on its accurate estimation and imply that getting spurious causalities with TE is hardly possible as opposed to the mean-squared PI which is not invariant under changes of variables. However, it is discussed below that both approaches may lead to spurious coupling detection.

Furthermore, to characterize coupling strengths quantitatively and to trace their variations over time, one often uses just relative values of PI or TE. Yet, PIs and TEs may be rather small both for really unimportant couplings and for the cases where an observed dynamical regime would appear completely different if couplings were zeroed [3]. To improve coupling characterization, we extend the idea of long-term causality [3] here via long-term effects of special parameter variations.

Avoiding spurious couplings

Using benchmark models in the form of linear autoregressive processes and Markov chains [7] either with uni- or bidirectional couplings, we calculate PI and TE under realistic conditions of significant observational noise, hidden state variables, and low temporal resolution. The results are that both PIs and TEs may well be nonzero in both directions even in case of a unidirectional coupling, so that "spurious couplings" are rather possible to be inferred. Moreover, it appears possible for a "spurious" TE to be much greater than a "correct" TE.

Based on those results, special tests for coupling bidirectionality are developed. For that, we fit a model with unidirectional coupling (involving one of the above factors) to data. In particular, to test for possible low temporal resolution effect, we fit autoregressive models with a time step smaller than a time series sampling interval. If such a model reproduces all relevant properties of the data, e.g. covariance functions, then bidirectional coupling cannot be inferred from positive PIs or TEs and, thereby, spurious detections can often be avoided. This test is illustrated for exemplary mathematical systems and applied to climatic data. In particular, it has confirmed previously detected [8] bidirectional coupling between El-Nino/Southern Oscillation (ENSO) and Indian Monsoon.

Estimation of long-term effects

Characterization of diverse effects of directional coupling may not be achieved with PI or TE [3], but we propose to accomplish it via an empirical model as well. For that, we vary certain parameters and trace resulting changes in relevant statistics. Namely, one usually has an empirical model

$$\begin{aligned} x(t) &= a_{x,0} + \sum_{i=1}^{d_X} a_{x,i}\, x(t-i) + \sum_{i=1}^{d_{Y\to X}} b_{x,i}\, y(t-i) + \xi_x(t), \\ y(t) &= a_{y,0} + \sum_{i=1}^{d_Y} a_{y,i}\, y(t-i) + \sum_{i=1}^{d_{X\to Y}} b_{y,i}\, x(t-i) + \xi_y(t), \end{aligned} \tag{1}$$

where $x(t)$ and $y(t)$ are observed processes, a and b are model parameters, d's specify model orders, ξ's are Gaussian white noises. To characterize influence of the system X on the dynamics of the system Y, one can trace e.g. how the variance of y changes if one zeroes all the coefficients $b_{y,i}$. Relative change of the variance $C_{X\to Y} = (\sigma_y^2 - \sigma_y^2[b_{y,i}=0])\big/\sigma_y^2[b_{y,i}=0]$ (square brackets denote a condition) reflects relative importance of the coupling $X \to Y$ for the existence of that statistical property of Y. This quantity may well be negative. Alternatively, one may zero the variance of ξ_x, so that $N_{X\to Y} = (\sigma_y^2 - \sigma_y^2[\sigma_{\xi,x}^2=0])\big/\sigma_y^2[\sigma_{\xi,x}^2=0]$ shows to what extent an observed variance of Y decreases if the noise (i.e. "energy") source in X is switched off. This quantity is always positive for mutually uncorrelated ξ_x and ξ_y in (1). With mathematical examples we show that relative PIs may well be rather small (less than 0.01) while the suggested long-term effects may take large values, e.g. dozens per cent.

As an example of application of the suggested techniques to instrumental observation data from large-scale climatic processes, we analyzed Atlantic Multidecadal Oscillation (AMO) and ENSO (Nino3,4) monthly indices for the period 1870–2013. The analysis of the entire period reveals bidirectional coupling with highly significant relative PI in the direction from ENSO to AMO and 10 times weaker one in the opposite direction. Thus, the overall coupling seems bidirectional, with predominant effects from ENSO to AMO. The analysis in moving windows of various lengths (from 10 to 60 years) reveals significant couplings from AMO to ENSO for some time intervals, and sometimes even stronger influence in that direction, even though most of the time the influence "ENSO to AMO" dominates. Namely, $C_{ENSO\to AMO}$ and $N_{ENSO\to AMO}$ are highest over the intervals 1870–1900, 1920–1930, and 1960–1980, while the opposite characteristics are large over the intervals 1910–1920, 1930–1940, and 1990–2000. The last 20 years correspond to highly significant influence of AMO on ENSO and much weaker (and decreasing) one in the opposite direction. Thus, the moving window estimation of long-term effects reveals a change in the coupling character between ENSO and AMO during the last years.

Acknowledgements

The work was supported by the Government of the RF (Agreement 14.Z50.31.0033 dated by 24.03.2014), the President of RF (grants NSh 1726.2014.2, NSh 3894.2014.5), the RAS programs, and the Russian Foundation for Basic Research.

References

1. I.I. Mokhov and D.A. Smirnov, *Geophys. Res. Lett.*, 2006, **33**, L03708.
2. J. Runge, J. Heitzig, V. Petoukhov, and J. Kurths, *Phys. Rev. Lett.*, 2012, **108**, 258701.
3. D.A. Smirnov and I.I. Mokhov, *Phys. Rev. E*, 2009, **80**, 016208.
4. J. Lean et al. *Solar Physics*, 2005, **230**, 27-53.
5. C.W.J. Granger, *J. Econ. Dynam. Control.*, 1980, **2**, 329-352.
6. T. Schreiber, *Phys. Rev. Lett.*, 2000, **85**, 461-464.
7. D. Smirnov, *Phys. Rev. E*, 2013, **87**, 042917.
8. I.I. Mokhov, D.A. Smirnov, P.I. Nakonechny, S.S. Kozlenko, E.P. Seleznev, and J. Kurths, *Geophys. Res. Lett.*, 2011, **38**, L00F04.

INVESTIGATION OF THE COMPOUND SOLITON OF GARDNER'S EQUATION IN THE OCEANIC SHELF

I. Soustova[1,2], K. Gorshkov[1], and **A. Ermoshkin[1]**

[1]Institute of Applied Physics of the Russian Academy of Sciences, Nizhny Novgorod, Russia
[2]University of Nizhny Novgorod, Nizhny Novgorod, Russia
soustova@hydro.appl.sci-nnov.ru

Abstract. It is known that in the coastal zone the evolution of internal waves is well described by the Gardner equation with variable parameters. The dynamics of intense IW in the shelf zone will be calculated using a modified approximate approach developed by the authors' research team. Comparison of results of numerical simulation of Gardner equation with results of calculation by the compound solitons method shows a good agreement up to the moments of time when the scales of the change of parameters of the medium are comparable with the characteristic dimensions of the soliton.

In this work we propose an approximate description of non-quasistationary evolution of solitons of intense internal waves in the oceanic shelf zone with variable parameters. These solitons may be treated as compound structures formed by more "elementary" steady-state waves – kinks (field jumps). The presence of strongly differing scales of such solitons (relatively narrow fronts $\lambda_к$ and tails and extended, almost flat crests) allows considering the situations when the quasistationarity conditions are not fulfilled for the solitary wave as a whole, but are valid for the kinks. Investigation of the process of non-quasistationary soliton evolution is carried out within the framework of Gardner's equation with variable coefficients that describes, in particular, the evolution of large-amplitude internal waves:

$$\Phi_t + \Phi\left(\alpha(x,t) - \mu(x,t)\Phi\right)\Phi_x + \beta(x,t)\Phi_{xxx} = 0\,. \tag{1}$$

The sought solution is found by the method of matched asymptotic expansions and the small parameter ε is equal by the order of magnitude to the ratio $\lambda_k / \Lambda << 1$. The solutions obtained in neighboring regions are matched in each approximation. The main terms of expansion in internal regions are kink solutions whose parameters are defined by steady-state relationship with α, μ, β, and ϕ slowly varying in time and/or along the coordinate. The main terms of expansion in external regions have no fixed structure. However, as the magnitudes of the field in these regions vary slowly and smoothly compared to field variations in the regions of the kinks, their evolution is described by the initial Gardner's equation for a simple wave. The procedure of matching the main terms of the expansion of solutions from the internal and external regions gives the relationship for slowly varying fields $\phi_{\pm}(x,t)$ from the regions adjoining the kink of interest with center coordinate $x_k(t)$ for $x > x_k$ and, correspondingly, for $x < x_k$:

$$\phi_+\left(x_k,t\right) = \frac{\alpha\left(x_k,t\right)}{\mu\left(x_k,t\right)} - \phi_-\left(x_k,t\right). \tag{2}$$

By adding to this relation the dependence of kink velocity on parameters μ, $\alpha, \phi(x_k,t)$ we obtain

$$\frac{dx_k}{dt} = \frac{\alpha^2\left(x_k,t\right)}{6\mu\left(x_k,t\right)} + \frac{\phi\left(x_k,t\right)}{3}\left(\alpha\left(x_k,t\right) - \mu\left(x_k,t\right)\phi\left(x_k,t\right)\right). \tag{3}$$

As a result, the algorithm of constructing the general solution is successive finding of the fields $\phi(x,t)$ and kink trajectories $x_k(t)$, starting with the region before the first kink following the above sequence.The method of compound solitons is illustrated based on the evolution of the soliton of Gardner's equation, close to the maximum, in the case of a linear coefficient $\mu(t) = \mu_0(1+\varepsilon t), \mu_0 = const$. There is special interest in the case of variable coefficient $\alpha(\tau)$ with the quadratic nonlinearity. The results of experimental observation of intense internal waves on the shelf of the Kamchatka peninsula are presented in the works [Serebryany et al., 2008]. Data on soliton transformation, thermocline recession into an elevation wave are available. The leading front of the soliton is extended and the rare edge becomes steeper. As the preliminary result, we examined the case when the parameters of cubic nonlinearity and dispersion are constant, and the parameter of quadratic nonlinearity α changes linearly in the course of time: $\alpha = 1 + \varepsilon t$. The comparison of distributions

fields obtained within the framework of the approximate approach and numerical calculation of Gardner's equation is given in fig. 1. It is possible to establish not only the qualitative, but also quantitative correspondence between them. It is important that the approximate approach gives adequate description of the field distribution. Also, at the moment when $\alpha = 0$, the traditional quasi-stationary description is not applicable: the soliton characteristic size and field magnitude were found not to differ strongly from the limiting values. Comparison with the results of known real data and numerical computations demonstrate the efficiency and adequacy of the modified approach. On the basis of the method proposed it is possible to obtain field distribution at arbitrary moment of time.

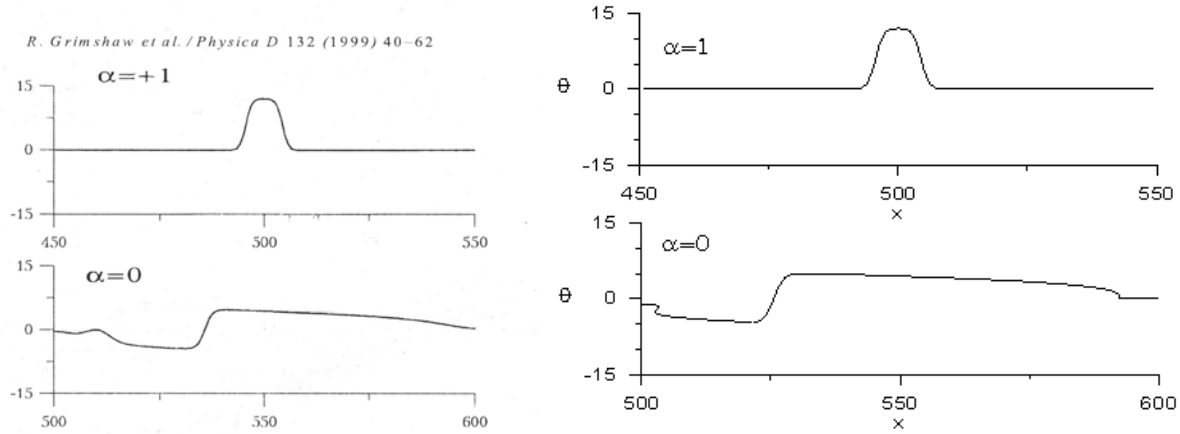

Fig. 1. Forms of quasisoliton at a critical point. The result of approximate theory (on the left) and numerical computation of Gardner equation (*on the right*)

Acknowledgements

The research was done under partial support from the Government of the Russian Federation (agreement No.11G34.31.0048), and RFBR grant No.12-05-00822a.

RISK AND PREDICTABILITY OF EURASIAN CLIMATE ANOMALIES ASSOCIATED WITH CLIMATIC QUASI-CYCLES LIKE ENSO

I.I. Mokhov and **A.V. Timazhev**

A.M. Obukhov Institute of Atmospheric Physics RAS, Moscow, Russia, mokhov@ifaran.ru

Abstract. Probability of climate anomalies (including anomalies of surface air temperature, precipitation and drought conditions) in Eurasian regions are analyzed with an assessment of El Niño/La Niña effects.

Significant contribution to the global climate anomalies is associated with the El Niño –Southern Oscillation. Probabilities of climate anomalies in the Eurasian regions by observations from the end of the 19th century to the beginning of the 21st century with an assessment of El Niño/La Niña effects are analyzed [1–3]. In particular, anomalies of surface air temperature, precipitation and drought index during spring-summer months in mid-latitudes for the European (ER) and Asian (AR) parts of Russia from observations since 1891 [4] are analyzed.

For estimation of the El Niño/La Niña effects, we used their indices characterized by the sea surface temperature (SST) in the Niño3 region (150°–90°W, 4°N–4°S) which is located in the equatorial latitudes of the Pacific Ocean. The El Niño (E) and La Niña (L) phases were distinguished using 5-months moving averaging of the SST anomaly in the Niño3 region (JMA index). El Niño (warm) and La Niña (cold) phases were defined by the index values of at least 0.5 °C and at most –0.5 °C, respectively, over six consecutive months (including October–December). All the other cases were believed to be neutral phases (N).

Positive temperature anomalies and large positive anomalies in spring-summer months are more frequent for ER for years starting with El Niño (E) events and the most frequent for transition to the La Niña (L) events (E→L). The E→L transition is characterized also by the lowest probability of negative temperature anomalies. The biggest probability of large negative temperature anomalies was obtained for the L→E transition and also for the N→E transition.

The most significant positive difference between probabilities for positive and negative precipitation anomalies in the ER are for years starting with El-Niño, in particular for E→L and E→E transitions and also for L→N transition. These transitions are characterized by the most frequent positive precipitation anomalies and by the lowest probabilities for negative precipitation anomalies. The biggest probabilities of negative precipitation anomalies were obtained for the L→E and N→N transitions.

The largest probability of drought conditions for ER was obtained for the E→L transition. The largest frequency of conditions with hot temperature (and drought) during spring-summer months in ER is characteristic for the E→L transition. Such conditions were realized for ER in summer 2010.

Similar estimates were obtained for AR.

Positive temperature anomalies and large positive anomalies in spring-summer months are more frequent for AR for years starting with La Niña (L) events and the most frequent for L→E transition. The L→E transition is characterized also by the lowest probability of negative temperature anomalies. The biggest probability of large negative temperature anomalies was obtained for the transition and also for the N→L transition.

The highest probability of negative precipitation anomalies is found for the L→L and E→E transitions, while the highest probability of the positive ones is revealed for the N→L and E→N transitions.

In the AR the probability of extremely dry conditions is maximal for the L→L and L→E transitions. The probability of moderately dry conditions is estimated to be maximal for the L→L and E→E transitions.

Acknowledgements.

The work was supported by the RF Government (Agreement 14.Z50.31.0033 dated 24.03.2014), the RF President (grant NSh 3894.2014.5), the RAS programs and the Russian Foundation for Basic Research.

References

1. I.I. Mokhov, *Res. Activ. Atmos. Oceanic Model*., 2005, WMO TD-No.1276, S.2, 7-8.
2. I.I. Mokhov, *Izestiya,, Atmos. Oceanic Phys.*, 2011, **47**(6), 653-660.
3. I.I. Mokhov and A.V. Timazhev, *Doklady Earth Sci.*, 2013, **453**(2), 211-214.
4. A.V. Meshcherskaya, V.M. Mirvis, and M.P. Golod, *Tr. GGO*, 2011, **563**, 94-121 (in Russian).

International Symposium

TOPICAL PROBLEMS OF NONLINEAR WAVE PHYSICS

WORKSHOP

"ULTRA-HIGH FIELDS IN PLASMAS: NEW MODELS, HIGH PERFORMANCE SIMULATIONS AND EXPERIMENTS"

METHOD FOR THE PHASE CORRECTION OF INTENSE ULTRASHORT LASER PULSES AT RAMAN BACKSCATTERING IN A PLASMA

A.A. Balakin and **G.M. Fraiman**

Institute of Applied Physics RAS, Nizhny Novgorod, Russia, balakin@appl.sci-nnov.ru

One of the most promising methods for obtaining ultraintense ultrashort laser pulses is currently based on the use of Raman backscattering in a plasma. It can provide an output power higher by a factor of 10^4–10^5 than that with the usual technique for amplifying frequency modulated pulses in the plasma [1]. The compression regime based on Raman backscattering in the plasma was experimentally implemented [2, 3]. In particular, the implementation of a nonlinear regime with depletion of the pump pulse was demonstrated. However, the nonlinear regime achieved in experiments was not transferred to the stage of a significant amplification of an output pulse. The reason was various parasitic effects responsible either for the enhancement of noise (thermal fluctuations of the plasma and the prepulse of the amplified pulse) or for the violation of the conditions of three- wave matching for Raman backscattering because of the inhomogeneity of the plasma density. Here, another method of the use of Raman backscattering in the plasma is proposed to obtain intense ultrashort laser pulses with a given phase front. In this case, requirements to the parameters of the plasma and to the duration of its existence in this regime are softer than those in the usual scheme of Raman compression. The method is based on the fact that phase perturbations of the pump pulse that are smooth in the longitudinal direction are concentrated in the weakest wave (plasma wave). As a result, the amplified pulse will have a weakly perturbed initial phase front and, correspondingly, good focusability.

References

1. V.M. Malkin, G. Shvets, and N.J. Fisch, *Phys. Plasmas*, 2000, **7**, 2232.
2. A.A. Balakin, D.V. Kartashov, A.M. Kiselev, S.A. Skobelev, A.N. Stepanov, and G.M. Fraiman, *JETP Lett.*, 2004, **80**, 12.
3. A.A. Balakin, G.M. Fraiman, N.J. Fisch, and S. Suckewer, *Phys. Rev. E*, 2005, **72**, 036401.

NEAR-THRESHOLD QED CASCADE IN THE STRONG LASER FIELD

V.B. Bashmakov[1], E.G. Gelfer[2], E.N. Nerush[1], I.Yu. Kostyukov[1], A.M. Fedotov[2], and **N.B. Narozhny[2]**

[1] Lobachevsky State University of Nizhny Novgorod, Nizhny Novgorod, Russia, v.bashmackov@gmail.com
[2] Moscow Engineering Physics Institute, Moscow, Russia

Abstract. We investigated the cascade development in laser field near its threshold for different field configurations. It was demonstrated that the threshold with respect to the total pulse power may be reduced using multiple pulse configurations. It was shown by numerical simulation that for eight pulses with a specific combination of polarizations the total power may be reduced to 8.9 PW, which is available with the modern technologies.

Multiple electron-positron pair production in a strong laser field due to development of the quantum electrodynamical (QED) cascade [1] is one of the most important predictions of the perturbative QED in external field. QED cascade is the consequence of processes such as photon emission by electrons or positrons and pair creation by photons. This phenomenon is actively investigated theoretically, but there is no experimental data since it's supposed that the field intensity and hence the power must be very high. The aim of our research was to determine how high it actually must be and how it is possible to reduce the power by a certain choice of field configuration.

Since the dynamics of the cascade is rather complicated even in the linear regime (when plasma effects are negligible), the main tool to investigate it is a numerical simulation. The most popular schemes are the particle-in-cells (PIC) method for particle-field interaction simulation and the Monte-Carlo method for quantum processes simulation [2].

Although we have mentioned the threshold for cascade development, strictly speaking a cascade does not have it, and we have defined it in an artificial way. We demand that, on the average, a new electron-positron pair must be born from every seed electron (which were initially at rest) during the time of interaction. A general idea is that the cascade effectively develops in a standing wave rather than in a plane traveling wave [1]. So, we considered the configurations constructed from pairs of pulses forming standing waves. Every laser pulse was modeled by the exact solution of Maxwell equations,having the form of a focused beam: [3]

$$\vec{A} = -\frac{1}{(2\pi)^2} e^{-\omega(it+b/c)} (\hat{z}\times\nabla_\perp)(\vec{C}\cdot\nabla_\perp)\frac{\sin(\omega\Re/c)}{\Re}.$$

Here b is a focusing parameter, $\vec{C}$ determines the polarization and $\Re = \sqrt{r_\perp^2 + (z-ib)^2}$ .The wavelength was equal to $1\mu m$ and the interaction time was equal to five laser periods (approximate duration of the modern high-power pulses). We used fifty electrons at rest as seed particles.

Num. of pulses	2	4	8 (c.p.)	8 (e.p.)
Num. of created positrons	**N < 1**	**N = 3**	**N = 11**	**N = 50**

Table 1. The number of the positrons created from fifty electrons for different field configurations. The total power for all cases is 8.9 PW. Data for eight pulses presented for different polarizations – one with all pulses circularly polarized (c.p.) and one with the most effective polarization described in the text (e. p.)

The most effective polarization was determined according to the supposition that the faster the parameter χ grows, the better the cascade develops. The other observation is that it's possible to reduce the required total power by dividing it between more pulses. According to this, we suggest a configuration with eight pulses, or four standing waves, focused at the same point and with the axis lying in the same plane. Two of the standing waves have circular polarization, one is linearly polarized and one is ellipticaly polarized with the coefficient of ellipticity $\sqrt{2}$. The determined total threshold power for such a configuration is P = 8.9 PW. Such power is available at the modern laser facilities, so the experimental investigation of QED cascades may start in the near future. The comparison with other configurations is presented in the Table 1.

Acknowledgements

This work was partially supported by the Government of the Russian Federation (Project No. 14.B25.31.0008) and by the Russian Foundation for Basic Research (Grant No. 14-02-31496).

References

1. A.R. Bell and J.G. Kirk, *Phys. Rev. Lett.*, 2008, **101**, 200403.
2. E.N. Nerush et al., *Phys. Rev. Lett.*, 2011, **106**, 035001.
3. A.M. Fedotov, *Laser Phys.*, 2008, 214-221.

GENERATION OF GEV PHOTONS IN ART REGIME IN THE ULTRA-INTENSE E-DIPOLE LASER FIELDS

E. Efimenko[1,2*], A. Bashinov[1,2], A. Gonoskov[1,2,3], I. Gonoskov[4], A. Ilderton[3], A. Kim[1,2], M. Marklund[3,4], A. Muraviev[1,2], and **A. Sergeev[1,2]**

[1]Institute of Applied Physics, Russian Academy of Sciences, Nizhny Novgorod, Russia
[2]University of Nizhny Novgorod, Nizhny Novgorod, Russia
[3]Department of Applied Physics, Chalmers University of Technology, Gothenburg, Sweden
[4]Department of Physics, Umea University, SE-90187 Umea, Sweden
*Author e-mail address: evgeny.efimenko@gmail.com

Abstract. In the present paper the results of theoretical investigation of the ART phenomenon in the presence of the electron-positron pair production process is discussed. Based on the PIC code simulations performed for the parameters of the upcoming large-scale facilities we propose a concept of an ultra-bright, well-collimated source of photons with energies up to several GeV.

Today's high-intensity laser systems can cause ultrarelativistic motion of electrons, providing various opportunities for conversion of optical energy into other forms, such as streams of charged particles and photons with high energy. Laser systems of the next generation will enable another fundamental mechanism of nonlinearity – an electron's significant recoil due to emission of photons, the so-called radiation reaction.

Until recently it was commonly assumed that radiation reaction can only lead to effective energy dissipation in the system of laser-plasma interaction, without causing significant changes in the dynamics of the system. However, recent theoretical studies have shown that a strong influence of radiation reaction can lead to profound counterintuitive changes even in the dynamics of a single electron. A strong enough effect of radiation reaction on an electron moving in the field of a plane standing electromagnetic wave leads to complex highly nonlinear dynamics, which cause a rapid "pulling" of the particle to the electric field spatial maximum, where the electron experiences the greatest possible influence of the field. This behavior contradicts the intuitive expectation that a system usually tries to minimize the impact on itself, and dissipation can only support this tendency. That is why the effect was called *anomalous radiative trapping* (ART) [1], as opposed to *normal radiative trapping* (NRT) which corresponds to electron localization in the vicinity of the electric field spatial minimum when radiation reaction contributes weakly in the case of lower wave amplitudes.

The electrons trapped by the ART effect are driven by the oscillating electric field of maximaum possible amplitude, which causes the particles' synchronous oscillation and emission along the electric field vector. This unique energy coupling between the electromagnetic field and the particles' kinetics, accompanied by the presence of a preferential direction of emission, provides an unprecedented opportunity for creation of an ultra-bright collimated source of photons with energies extending to the GeV level.

It is important that the mechanism of the ART phenomenon is very robust. This allows achieving entrapment of particles in the symmetric geometry of the so-called e-dipole wave (inverse emission of a dipole antenna). This kind of field structure is very interesting from the practical point of view. By virtue of the optimal energy focusing, it makes possible to reach the required level of intensity using several laser pulses focused from different directions, assuming parameters of laser systems now in development. However, for intensities triggering the ART regime, the process of particles capturing and trapping is accompanied by a growing avalanche of electron-positron pair production. Generation of a large enough number of particles can lead to the essential depletion/scattering of laser radiation forming the e-dipole wave that can eventually break the ART regime.

This paper presents the results of theoretical investigation of the ART phenomenon in the presence of the electron-positron pair production process and their mutual influence in the geometry of the e-dipole wave with varying intensity and duration. On the basis of the results we formulate general conclusions about the possibility of triggering and maintaining the regime of ART at the multichannel laser facilities of next generation. In particular, our calculations indicate that the produced electrons and positrons are immediately trapped by the ART mechanism, which happens until the number of particles in the central trapping state reaches 10^9. Further growth of the number of particles causes reduction of the field strength at the central point and a decrease of the particles and the emitted photon energy. This means that by choosing the appropriate initial density and laser pulse duration one

can reach the instant of the peak field strength, maintaining the ART regime for a large number of particles, and produce a well-collimated beam of photons with the highest possible energy for the setup of this kind. Based on the simulations performed for the parameters of the upcoming large-scale facilities, it is demonstrated that maximum photon energy is scaled proportionally to field amplitude and for 100 PW laser system can be as high as 3.8 GeV.

References

1. A. Gonoskov et al. “Anomalous radiative trapping in laser fields of extreme intensity”, arXiv:1306.5734 [physics.plasm-ph] (2013).

ANALYTICAL MODEL FOR ELECTRON SIDE INJECTION INTO LINEAR PLASMA WAVES

A.A. Golovanov[1,2,3] and **I.Yu. Kostyukov**[1,2]

[1] Institute of Applied Physics of the Russian Academy of Sciences, Nizhny Novgorod, Russia
[2] Lobachevsky State University of Nizhny Novgorod, Nizhny Novgorod, Russia
[3] e-mail: agolovanov256@gmail.com

Abstract. An analytical piecewise homogeneous model for electron side injection into linear plasma waves is developed. Betatron oscillation dynamics is studied. Longitudinal motion and electron trapping region are described. The results of the analytical model are verified by numerical calculations. The results predicted by piecewise homogeneous model are also compared to the results calculated using a more realistic inhomogeneous model.

Much attention has recently been given to plasma based acceleration methods. These methods can provide acceleration rate several orders of magnitude more than traditional methods. Experiments show a possibility of electron acceleration to several GeV energy over the length of several centimeters. These methods are based on the fact that a wakefield excited by a high intensity laser pulse or a particle beam propagating through plasma has a very high acceleration gradient.

Plasma itself can be used as a source of accelerated electrons for highly nonlinear plasma waves. However, high energy spread of accelerated particles and low reproducibility of the resulting beam properties limit the usage of the self-injection method. One possible solution is to use external electron beams, e.g. the ones generated by a compact photo-injector. There are different ways of electron beam injection into a plasma wave. One of them is the side injection of a beam at an angle into a laser wakefield to which our analysis is dedicated.

Piecewise homogeneous model

It is known that for a linear laser wakefield electron motion can be described by the following potential:

$$\Phi = \Phi_0 \cos(k_p \xi)\, g(r/R), \qquad (1)$$

where r is the radial coordinate, $\xi = x - v_g t$ is the longitudinal coordinate relative to the laser pulse and k_p is the plasma wavenumber. The motion system generated by this potential is nonlinear and is hard to analyze without usage of numerical methods. Therefore, we have decided to consider a model where transversal and longitudinal forces spatial distribution is piecewise homogeneous (Fig. 1). In this model only the sign of the forces is the same as in the inhomogeneous model determined by the potential (1).

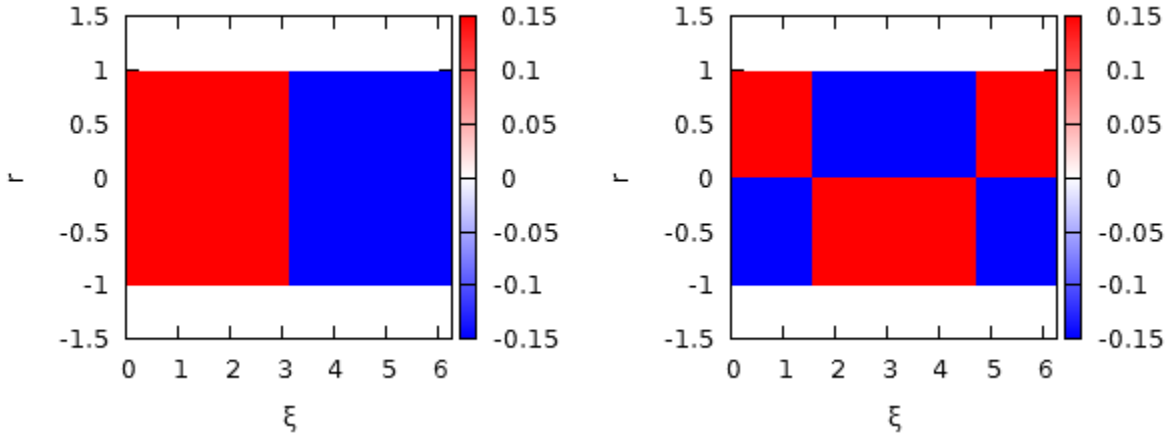

(a) Longitudinal force spatial distribution (b) Transversal force spatial distribution

Fig. 1. Spatial distribution of the plasma wave forces in the piecewise homogeneous model

It was shown that in the wave phase where the transversal force is focusing and the longitudinal force is accelerating, electrons can be trapped and can start oscillating near the plasma wave axis. The dynamics of these oscillations which are called betatron was studied and we analytically calculated envelopes for transverse momentum and transverse coordinate oscillations (Fig. 2). The longitudinal

motion of the electrons was also described. It was shown that betatron oscillations play an important role in acceleration because they lower the electron longitudinal velocity and therefore the electron can stay in the accelerating phase for a longer period of time. We also calculated the region of parameters p_0 (initial electron momentum) and ψ (electron injection angle) for which electrons can be trapped in the wave (Fig. 3).

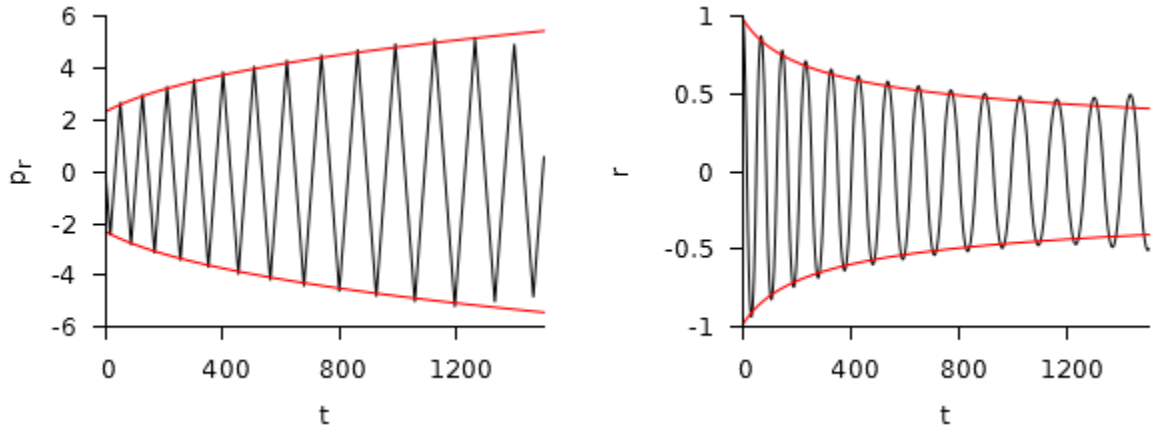

(a) (b)

Fig. 2. Numerical solution for the time dependence of (a) transversal momentum and (b) transversal coordinate. Analytically calculated envelopes are shown by red curves

We performed numerical calculations of the piecewise homogeneous system in order to verify the results predicted analytically and proved that these results are correct.

We also compared the piecewise homogeneous model to the more realistic inhomogeneous model. Numerical calculations for the inhomogeneous case showed that the piecewise homogenous model correctly predicts the nature of betatron oscillations. For both models the transversal momentum oscillations amplitude increases and the transversal coordinate oscillations amplitude decreases in the accelerating phase. In the decelerating phase the behavior is opposite. However, the trapping region formed for the inhomogeneous model is essentially different from the form predicted by the piecewise homogeneous model. This result suggests than heterogeneity of the focusing force can't be neglected when we describe trapping conditions.

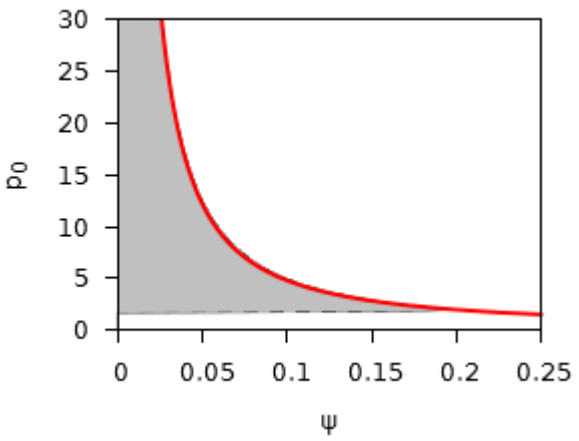

Fig. 3. Numerical solution for electron trapping region. Analytically calculated region border is shown by the red curve

Acknowledgements

This work was supported in part by the Government of the Russian Federation (Project No. 14.B25.31.0008), by the Russian Foundation for Basic Research (Grants Nos. 14-02-31496, 13-02-00886 and 13-02-00372).

References

1. E. Esarey, C.B. Schroeder, and W.P. Leemans, *Rev. Mod. Phys.*, 2009, **81**, 1229–1285.
2. X. Wang, R. Zgadzaj, N. Fazel, Z. Li, S.A. Yi, Xi Zhang, W. Henderson, Y.-Y. Chang, R. Korzekwa, H.-E. Tsai et al., *Nature communications*, 2013, **4**.
3. N.E. Andreev, L.M. Gorbunov, V.I. Kirsanov, K. Nakajima, and A. Ogata, *Phys. Plasmas*, 1997, **4**(4), 1145–1153.

ANOMALOUS RADIATIVE TRAPPING IN LASER FIELDS OF EXTREME INTENSITY

A. Gonoskov[1,2], **A. Bashinov**[2], **I. Gonoskov**[3], **E. Efimenko**[2], **C. Harvey**[4], **A. Ilderton**[1], **A. Kim**[2], **M. Marklund**[1], **A. Muraviev**[2], and **A. Sergeev**[2]

[1] Chalmers University of Technology, SE-41296 Gothenburg, Sweden
[2] Institute of Applied Physics, Russian Academy of Sciences, Nizhny Novgorod 603950, Russia
[3] Department of Physics, Umea University, SE-90187 Umea, Sweden
[4] Centre for Plasma Physics, Queen's University Belfast, BT7 1NN, UK

Abstract. We report the existence of a new regime of particle dynamics in ultra-intense light. We demonstrate that radiation losses of electrons moving in a strong enough electromagnetic standing wave, surprisingly, cause their localization in the vicinity of the electric field spatial maximum. This unusual behaviour, which we call "anomalous radiative trapping" (ART), can be achieved at the upcoming laser facilities via the many-sided focusing that reproduces reversed emission of a dipole antenna (*e*-dipole pulse). For this geometry, we demonstrate that ART can be used for particle control for studying fundamental physics, and for the generation of multi-GeV, directed, gamma rays and collimated, energetic particle beams.

Progress in laser technology has opened up possibilities for creating ultra-intense light sources [1, 2, 3] with the aim of studying phenomena at the interface of high-field and high-energy physics. Among these, radiation dominated particle dynamics and quantum electrodynamics effects are of current topical interest and are guiding the direction of upcoming laser programs.

For intensities below 10^{23} W/cm^2 the collective relativistic dynamics of electrons is predominantly determined by their coherent emission, which can be described in a self-consistent way via the macroscopic currents entering the Maxwell's equations. However, for higher intensities the high-frequency individual incoherent emission of electrons may affect their dynamics, which one can associate with recoils due to the emission of photons. This effect of radiation reaction can be treated either in continuous form as the so-called radiation friction or in quantized from depending on the parameters of interaction. Weak influence of radiation reaction may effectively lead to arising of a channel for energy dissipation from a system that includes the particles' kinetic energy, the energy of their coherent emission and the energy of the external radiation. This dissipation commonly does not cause a quick qualitative change of particles' dynamics and can only affect slow process, for example, suppress various instabilities in plasmas. However, our recent study [4] indicates that in ultra-intense laser fields strong enough effect of radiation reaction can cause quick cardinal changes in particle's dynamics in a rather unexpected way, providing anomalously intense and stable coupling between particles' kinetic energy and electromagnetic field energy.

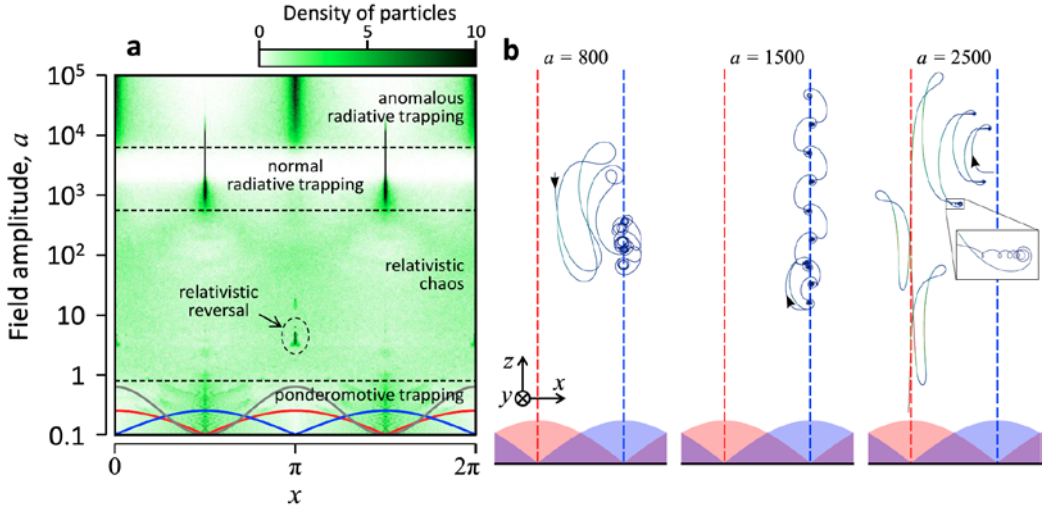

Fig. 1. (a) The long-term density distribution of electrons in a standing wave as a function of wave amplitude a given in relativistic units. The spatial distribution of the electric and magnetic fields, and the ponderomotive potential, are sketched with red, blue and grey lines, respectively. E (B) is orientated along z-axis (y-axis). (b) Typical particle trajectories in the x-z plane. The first and third are in the NRT and ART regimes respectively, while the second shows the transition between them. Dotted red (blue) lines show the locations of antinodes (nodes)

We studied regimes of a particle dynamics in the fields of an electromagnetic standing wave with various amplitudes. We simulated motion of initially uniformly distributed electrons with the radiation reaction taken into account in the quantized form. In fig. 1 (a) we plot a stabilized distribution of the particles density as a function of the wave amplitude. One can see various trapping phenomena. At low intensities, the trapping occurs in the minima of the ponderomotive potential, coinciding with the positions of the electric field spatial nodes. Due to relativistic effects, electrons are released from the ponderomotive trapping and move chaotically (except in relativistic reversal) for higher amplitudes. For intensities ($10^{24} – 10^{26}$ W/cm^2), as the role of radiation losses increases the particles subsequently become trapped once more in the same positions. We call this effect *normal radiative trapping* (NRT). However, at even higher intensities ($> 10^{26}$ W/cm^2), the electrons become attracted towards and are trapped around the positions of the antinodes, i.e. at the maxima of the ponderomotive potential. We call this counter-intuitive behaviour *anomalous radiative trapping* (ART). In fig. 1 (b) we show trajectories of electrons. The detailed analysis indicates the following mechanisms of the trapping phenomena (see [4] for details). NRT is originated from the higher average rate of the radiation losses in the vicinity of the magnetic field spatial maximum, which causes predominant migration towards this region for the electrons looping in a non-regular way. Whereas ART appears as a net migration of particles, when a regular motion is caused by the radiation reaction dominancy. This migration is originated from an asymmetry of temporal evolution of electron's gamma factor caused by intense radiation losses at specific parts of the trajectory.

Both mechanisms of trapping are very robust and are sensitive neither to the specific initial conditions nor to the shape of the field structure. Comprehensive numerical simulations show that the ART can be achieved in the field configuration of the so-called *e*-dipole pulse [5], which implies formation of reversed emission of a dipole antenna based on radiation focusing from different directions. The required level of intensity can be reached via many-sided focusing of several laser pulses at the proposed international facilities [1, 2, 3], assuming that the total peak power exceeds 50 PW.

The particles being trapped by ART mechanism oscillate synchronously in the spatial maximum of the electric field, providing the most optimal conditions for energy transformation. This opens up new opportunities for creation of ultra-bright sources of GeV photons and energetic particles.

References

1. ELI: www.extreme-light-infrastructure.eu.
2. XCELS: www.xcels.iapras.ru.
3. Gekko-EXA: www.ile.osaka-u.ac.jp/Gekko-EXA/.
4. A.A. Gonoskov et al. // E-print: arXiv:1306.5734 [physics.plasm-ph] (2013).
5. I. Gonoskov, A. Aiello, S. Heugel, G. Leuchs, *Phys. Rev. A*, 2012, **86**, 053836.

Invited

HIGH-VELOCITY MAGNETIZED PLASMA COLLISIONLESS INTERACTIONS USING HIGH-INTENSITY LASERS

D.P. Higginson[1], J. Béard[2], S.N. Chen[1], E. d'Humières[3], H. Pépin[4], Ph. Korneev[3], S. Pikuz[5], B. Pollock[6], R. Riquier[1], and **J. Fuchs[1]**

[1]LULI, École Polytechnique, CNRS, CEA, UPMC, Palaiseau, France, drew.higginson@polytechnique.edu
[2] LNCMI, UPR 3228, CNRS-UFJ-UPS-INSA Toulouse, France
[3]Université de Bordeaux, CNRS, CEA, CELIA, Talence, France
[4]INRS-EMT, Varennes, Québec, Canada
[5]Joint Institute for High Temperatures of the Russian Academy of Sciences, Moscow, Russia
[6]Lawrence Livermore National Laboratory, Livermore, CA USA

Abstract. The interaction of magnetized (20 T), counter-streaming high-velocity (~0.1 c) hydrogen plasmas accelerated using high-intensity ($8 \cdot 10^{19}$ W/cm^2) lasers is shown experimentally to create a strong increase in density at the interaction point. This feature is thought to be due to the pile-up of magnetic field leading to magnetic fields up to (500 T), causing the subsequent reflection of electron at the interaction region.

A major question in astrophysical plasmas collisions (e.g. supernovae remnants, Gamma-ray bursts) concerns the formation of collision-less shocks and the subsequent generation of high-energy particles, which are perhaps the source of the most energetic cosmic rays. Of particular interest is how such processes are encouraged and modified by ambient magnetic fields. To elucidate these phenomena, we have used the Titan laser facility in double-beam configuration (70 J/beam, τ = 650 fs) to accelerate high-velocity (v = 0.01–0.2 c) counter-streaming hydrogen plasmas (~10^{18} n/cm^3) via the target normal sheath acceleration (TNSA) mechanism. A pulsed Helmholtz coil driven [1] by a high-energy capacitor bank (10 kV/10 kA) is used to impose a constant 20 T (0.2 MG) external magnetic field during the plasma interaction. Interferometer measurements of the magnetized case observe a bump at the collision point that is a 3x increase in density compared to the un-magnetized case. This bump region is characterized as a large-scale (~100 μm) and long-lived (~100 ps) jump in electron density. Particle-in-cell (PIC) simulations [2] suggest that this phenomenon may be due to piling up of the magnetic field leading to increased field strength of up to 500 T (5 MG). Such a strong field causes the electrons to become reflected leading to the observed increase in density. The density variations present in the electrons may potentially be strong enough to seed other instabilities leading to the formation of a shock. The simulations are thus used to develop an in-depth understanding of the underlying physics and the consequences for astrophysical scenarios.

References

1. J. Béard, J. Billette, P. Frings, M. Suleiman, and F. Lecouturier, *J Low Temp Phys*, 2013, **170**, 442–44.
2. Ph. Korneev, E. d'Humières and V. Tikhonchuk, *Phys. Plasmas*, 2014, **21**, 022117.

SIMULATION OF LASER ION ACCELERATION IN TARGETS WITH SUB-WAVELENGTH SURFACE GRATING

A.V. Korzhimanov[1,2] and **M. Marklund**[2,3]

[1] Institute of Applied Physics of the Russian Academy of Sciences, Nizhny Novgorod, Russia,
kav@ufp.appl.sci-nnov.ru
[2] Umeå University, Umeå, Sweden
[3] Chalmers University of Technology, Göteborg, Sweden

Abstract. A method to enhance the efficiency of rare side ion acceleration by laser heated electrons is investigated numerically. The method is based on the idea to improve laser-target coupling by placing sub-wavelength grating on the irradiated surface. The optimal parameters of the grating is found and theoretically justified. It is shown that the optimal parameters for maximal total energy deposited to ions differs from those for maximal energy of the most energetic ion and both are far from the optimum of the laser energy absorption.

The recent dramatic progress in developing of high-peak-power laser systems opened up new possibilities for a wide range of important applications one of which is the laser-driven acceleration of ion bunches. The laser plasma sources of protons with energies up to tens of MeV have been already experimentally shown as well as the possibility to reach GeV level has been pointed out theoretically.

For intensities as high as 10^{18} – 10^{20} W/cm^2 the most efficient scheme for high energy ion production is so called Target Normal Sheath Acceleration (TNSA) which is also the most studied laser ion acceleration scheme. In this scheme the ions are accelerated at the rear side of a thin target in a quasielectrostatic sheath field created by fast electrons produced by the laser at the target front side.

Typical TNSA conversion efficiency (ratio between the laser energy and the total ion beam energy) is about a few percent. Much effort has been put forward recently in order to increase this efficiency by using specially designed targets. One of the possible approaches is to use surface grating at the irradiated side of the target in order to increase the amount of energy absorbed by electrons from the laser.

This approach has been verified both numerically and experimentally however there is still no systematic studies of how the efficiency depends on different parameters of the grating.

Here we report on an extensive study of this dependence in a wide range of grating parameters. We investigated gratings in the form of periodically placed rectangular ledges. Such a grating can be defined by three parameters: period of structure, width of a ledge and height of the ledge.

The study is based on numerical calculations made by means of fully relativistic electrodynamic Particle-In-Cell code PICADOR in two and three dimensions. The laser parameters for all simulations were fixed and correspond to a typical Ti:Sapphire 10TW system. The quasimonoenergetic spectra of accelerated ions has been achieved by using composite target made of gold ions and thin proton layer deposited on the rear side. We paid particular attention to the maximal energy of generated protons and the total amount of energy deposited to accelerated proton bunch.

The main result of the work is that the optimal parameters for maximal and total proton energies are not the same although are close to each other. And both of them are far from the optimum of the laser energy absorption. Indeed, the higher the ledges of grating the more energy can be absorbed by electrons for large enough grating period however this energy is converted to the energy of gold ions forming the grating rather than to the proton energy. So there is some optimal height for which the protons gain the maximal energy.

The optimal width of the ledges was found to be comparable to a skin-depth and thus depends on the plasma density. The optimal period was found to be about half-wavelength and slightly differs for maximal and total energies of protons.

Acknowledgements

The simulations were performed on resources provided by the Swedish National Infrastructure for Computing (SNIC) at High Performance Computing Center North (HPC2N).

GAMMA-RAY EMISSION EFFECT ON LASER-SOLID INTERACTION IN ULTRAHIGH INTENSITY REGIME

E.N. Nerush[1,2] and **I.Yu. Kostyukov**[1,2]

[1] Institute of Applied Physics RAS, 603950 Nizhny Novgorod, Russia
[2] University of Nizhny Novgorod, 603950 Nizhny Novgorod, Russia

Abstract. The ion acceleration in laser-produced overdense plasmas is a key topic of many recent investigations thanks to its potential applications. Besides, at forthcoming laser intensities ($I > 10^{23}$ W·cm^{-2}) the interaction of laser pulses with plasmas can be accompanied by copious gamma-ray emission. Here we demonstrate the mutual influence of gamma-ray emission and ion acceleration during relativistic holeboring in overdense plasmas with ultraintense laser pulses. If gamma-rays emission is abundant, the hole-boring velocity is lower, the whereas gamma-ray radiation pattern is narrower than in the case of low emission. Conservation of energy and momentum allows one to elucidate the effects of gamma-ray emission.

To investigate the influence of gamma-ray generation on hole-boring we consider an interaction geometry where a laser pulse is incident on a plasma slab producing reflected light, ion flow and high-energy photons (Fig. 1).

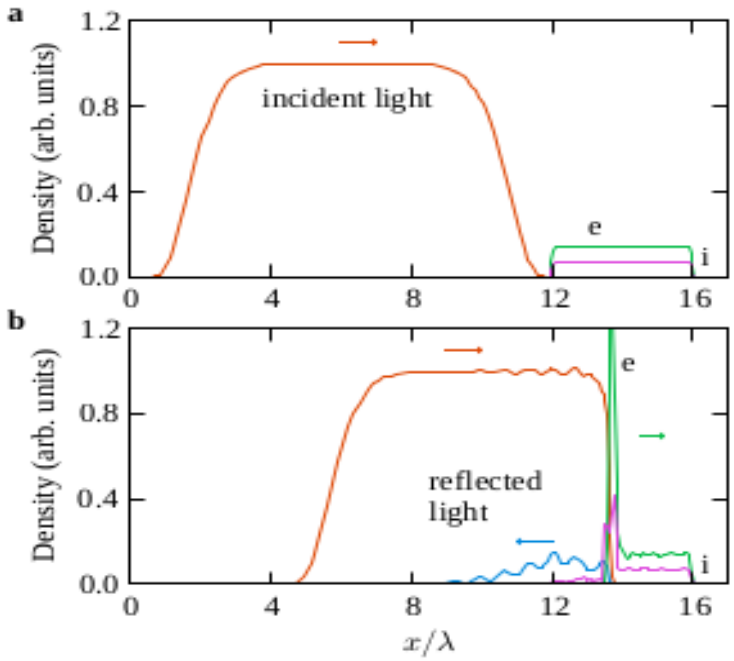

Fig. 1. On-axis shape of the incident (orange) and reflected (blue) laser pulses, electron density (green) and ion density (magenta) in a particle-in-cell simulation at time instances $t = 0$ (a) and $t = 4\lambda/c$ (b)

According to Ref. [1, 2], the ratio of the electron energy to the overall energy decreases as the intensity increases, and for $I > 10^{23}$ W·cm^{-2} electron energy can become negligible in the energy balance. Therefore, conservation of energy and momentum is given as:

$$(1-R)S_l = S_i + S_\gamma, \tag{1}$$

$$(1+R)S_l = \Pi_i + S_\gamma \cos\varphi, \tag{2}$$

where S_l, S_i and S_γ are the laser pulse energy, overall ion energy and overall energy of gamma-rays, respectively, Π_i is the overall ion momentum, $\cos\varphi$ determines the ratio of longitudinal momentum of gamma-rays to their energy (i.e., φ is the half-angle of the gamma-ray divergence), R is the reflection coefficient and c is the speed of light.

Conservation laws Eqs. (1), (2) can be written not only for the overall energy and momentum, but also for the energy flux and the momentum flux densities. It is convenient to use the hole-boring frame moving with velocity v_{hb}.

$$\left(1-R'\right)\frac{|\mathbf{E}'\times\mathbf{B}'|}{4\pi}=S'_{\gamma}, \tag{3}$$

$$\left(1+R'\right)\frac{|\mathbf{E}'\times\mathbf{B}'|}{4\pi}=2n'_{i}Mv_{hb}^{2}\gamma_{hb}, \tag{4}$$

where $\mathbf{E}'$ and $\mathbf{B}'$ are the electric and magnetic fields of the laser pulse in the hole-boring frame, n'_{i} is the unperturbed ion density in the hole-boring frame, M is the ion mass and γ_{hb} is the Lorentz factor associated with hole-boring velocity. Here it is assumed that the gamma quanta are emitted transversally, so they do not contribute to the momentum flux balance described by Eq. (4). It follows from Eq. (3) that the ions do not contribute to the energy flux balance because they are elastically reflected from the potential barrier at the hole-boring interface. If the gamma-ray emission is neglected ($S'_{\gamma}=0$), then by solving the system of equations (3) and (4) we get a well-known expression for hole-boring velocity:

$$v_{hb}=\mu^{-1},\quad \mu=\frac{1}{a_0}\sqrt{\frac{Mn_i}{mn_{cr}}}. \tag{5}$$

If we assume that electrons emit in the radiation dominated regime so $S'_{\gamma}=eE'c$. By solving the system of equations (3) and (4) R' and v_{hb} can be calculated. In the limit $\mu<<1$ we reproduce Eq. (5). In the reverse limit we have

$$v_{hb}=2^{-1/2}\mu^{-1}. \tag{6}$$

Therefore gamma-ray emission can lead to decreasing of the hole-boring velocity.

Acknowledgements

This work was partially supported by the Government of the Russian Federation (Project No. 14.B25.31.0008), and by the Russian Foundation for Basic Research (Grants No 13-02-00886, 13-02-00372).

References

1. E.N. Nerush, I.Yu. Kostyukov, L. Ji and A. Pukhov, *Phys. Plasmas*, 2014, **21**, 013109.
2. L.L. Ji, A. Pukhov, E.N. Nerush, I.Yu. Kostyukov, B.F. Shen, and K.U. Akli, *Phys. Plasmas*, 2014, **21**, 023109.

NUMERICAL SIMULATION OF ELECTRONS ACCELERATION IN LONG-SCALE-LENGTH UNDERDENSE PLASMA

P.A. Ksenofontov[1], A.V. Brantov[1], V.Yu. Bychenkov[1], A.B. Savel'ev[2], I.N. Tsymbalov[2], and **A. Drobinin[2]**

[1] P.N. Lebedev Physical Institute of the Russian Academy of Science, Moscow, Russia
[2] Lomonosov Moscow State University, Moscow, Russia

Abstract. In this work we report results of numerical simulations of relativistic laser interaction with long undercritical preplasma layer and discuss a complex mechanism of electron acceleration. Recently abnormally high energy electron bunches were observed when an additional controlled nanosecond prepulse created long preplasma from a solid target. Classical mechanisms such as ponderomotive acceleration, laser wake field acceleration (LWFA) and so on do not explain such results.

Simulation

For numerical simulation the full-relativistic 3D3V PIC-code "Mandor" was used. A target was chosen similar to the real target but with already formed undercritical preplasma layer with a linear density gradient. Simulations were performed with supercomputer "Lomonosov" at the Lomonosov Moscow State University. The simulations were performed in 3D and 2D regimes with different length of the preplasma layer (90, 25, 10 and 5 μm), different FWHM (50 fs and 300 fs) and different polarization. The time step was chosen to be 0.003 fs to meet the Courant condition, the cell size was the same in all directions in 2D regime – 0.01λ, similarly to the minimum Debye length, and particles per cell were chosen sufficient for correct simulations.

Results

It was found that complex interplay between different phenomena provides for the high energy electrons with a certain choice of preplasma parameters. In such conditions high energy electrons start acceleration from the area corresponding to relativistically shifted 0.2–0.3 N_{cr}, where self-focusing of the beam results in huge intensity increasing. Electrons from this area efficiently gain energy from laser field. Many processes such as Raman forward- and backscattering, two plasmon decay (TPD) play a significant role in electron acceleration.

Electric fields effect analysis demonstrates that the contribution to electron acceleration of the longitudinal component of electric field is more than from the transverse one. 3D and 2D regimes have been compared and significant differences have been found. For example, there are differences in the spectra of these regimes. It is important that 3D-results are more reliable but need much more computational resources.

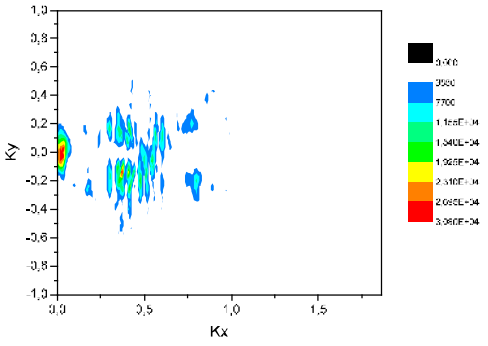

Fig. 1. Spectrum of longitudinal component of electric field for 50 fs laser pulse in plasma after self-focusing in 2D regime

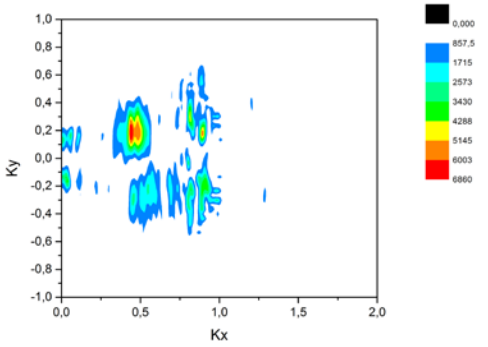

Fig. 2. Spectrum of longitudinal component of electric field for 50 fs laser pulse in plasma after self-focusing in 3D regime

Relativistic self-focusing in 300 fs laser pulse proceeds in an absolutely different way. It's obvious that a filament or a channel is formed which later splits into two, thus affecting electron acceleration. So, electrons apparently suffer two-phased acceleration or some kind of stochastic acceleration.

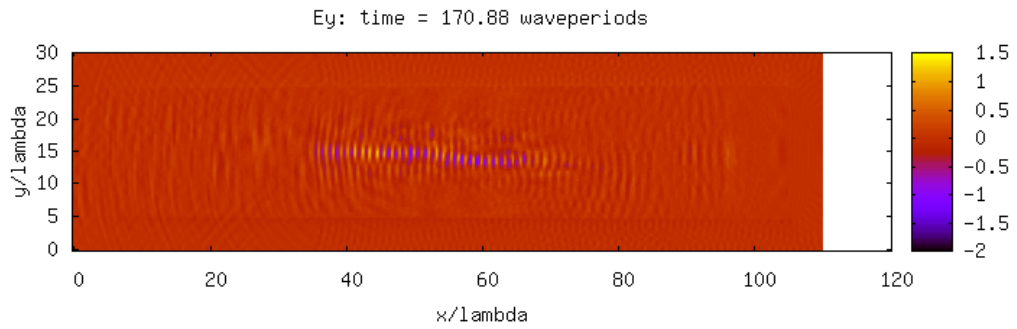

Fig. 3. The image of filament with split channels of 300 fs laser pulse in electron plasma

References

3. K. Ivanov, S. Shulyapov, A. Turinge et al., "X-ray diagnostics of ultrashort laser-driven plasma: Experiment and simulations", *Contributions to Plasma Physics*., 2013, **53**(2) 116–121.
4. O. Klimo, J. Psikal, V.T. Tikhonchuk, and S. Weber, "Two-dimensional simulations of laser–plasma interaction and hot electron generation in the context of shock-ignition research", *Plasma Phys. Control. Fusion*, 2014, **56**, 055010.

Invited

EFFECT OF THE RADIATION REACTION FORCE ON THE ELECTRONIC PARAMETRIC INSTABILITIES OF A STRONG LASER PULSE IN A PLASMA

N. Kumar[1], **K.Z. Hatsagortsyan**[1], and **C.H. Keitel**[1]

[1] Max-Planck Institute for Nuclear Physics, Heidelberg, Germany,
Email: kumar@mpi-hd.mpg.de

Abstract. Influence of the radiation reaction force on the electronic parametric instabilities, in particular, stimulated Raman scattering of an ultra-intense laser pulse in plasmas is studied. Inclusion of the Landau-Lifshitz radiation reaction force in the plasma electron dynamics enhances the growth of the forward Raman scattering by causing a phase shift in nonlinear current densities that drive the two Raman sidebands (anti-Stokes and Stokes waves) and manifesting itself into the nonlinear mixing of two sidebands.

Growth rate of the forward Raman scattering with the radiation reaction force

At ultra-high intensities $I_l > 10^{22}$ W/cm^2, the role of the radiation reaction force on plasma electron dynamics becomes important [1]. Thus, plasma scattering of the laser pulse, categorized as the parametric instabilities, must take into account the effect of radiation reaction force. Due to the radiation reaction force, the laser pulse suffers damping while propagating in a plasma. This damping provides an alternative source of free energy for the plasma perturbations to grow. These plasma perturbations are the seeds for the various parametric instabilities in the plasma. One of the well known parametric instabilities is the forward Raman scattering (FRS) in a plasma [2–3]. In this process, a pump laser decays into two forward moving daughter electromagnetic waves and a plasma wave. The excitation of plasma wave causes the frequencies of the daughter electromagnetic wave to go either up (anti-Stokes wave) or down (Stokes wave). We derive a general dispersion relation for the electronic parametric instabilities by including the leading order term of the Landau-Lifshitz force [4] in the equation of motion for plasma electrons. Afterwards, we solve it to derive the growth rate of the FRS. The growth rate of the FRS reads as (see Ref. [5] for details)

$$\Gamma_{frs} = \frac{-\omega_p^2 \epsilon a_0^2}{2\omega_{0r}} \pm \frac{1}{\sqrt{8}} \frac{\omega_p^2 a_0}{\gamma_0^2 \omega_{0r}} \cos\left(\theta/2\right) \sqrt{\left(1 + 2a_0^2\epsilon^2\gamma_0^4\right)^2 + \epsilon^2 a_0^4 \gamma_0^2 \left(\frac{\omega_{0r}}{\omega_p'}\right)^2},$$

$$\theta = arctan\left(\frac{-\epsilon a_0^2 \gamma_0}{\left(1 + 2a_0^2\epsilon^2\gamma_0^4\right)}\right), \tag{1}$$

where $\omega_p' = \omega_p/\gamma_0$, $\omega_p = \sqrt{4\pi n_0 e^2/m_e}$, n_0 is the electron plasma density, e and m_e are the electron charge and mass respectively, $\gamma_0 = \sqrt{1 + a_0^2/2}$, $a_0 = eA_0/m_e c^2$, A_0 and ω_{0r} are the vector amplitude and frequency of the pump laser pulse respectively, c is the velocity of the light in vacuum, and $\epsilon = e^2\omega_{0r}/3 m_e c^3$ denotes the radiation reaction force. From here the enhancement in the growth rate of the FRS is apparent. This enhancement is even stronger at lower plasma density ratios $\omega_p'/\omega_{0r} \ll 1$ and higher laser amplitude $a_0 \gg 1$. This enhancement occurs due to the radiation reaction force induced phase shift which leads to the mixing of the Stokes and the anti-Stokes waves. Intuitively, it can be understood as follows: since the radiation reaction force causes damping of the pump laser pulse, it essentially provides an additional source of free energy for the perturbations (scattering) to grow in the plasma. Figure 1 shows the growth rate ratio with $\left(\Gamma_{frs} - \delta\omega_{0r}\right)$ and without (Γ_0) the radiation reaction force and one can immediately notice that the radiation reaction force leads to enhancement in the growth of the FRS. The enhanced FRS of the laser pulse is important for the ultra-intense laser-plasma interaction as it can lead to significant change in the frequency spectra and shapes of extremely intense short laser pulses. Moreover, the enhanced FRS of the laser pulse provides an alternative way to detect the radiation reaction effects on the spectra of low-energy optical photons. This is in contrast to the scheme of the nonlinear Compton scattering of a counter-propagating relativistic electron in a strong laser field, which aims at discerning the signatures of the radiation reaction force on the spectra of high-energy gamma-ray photons [1].

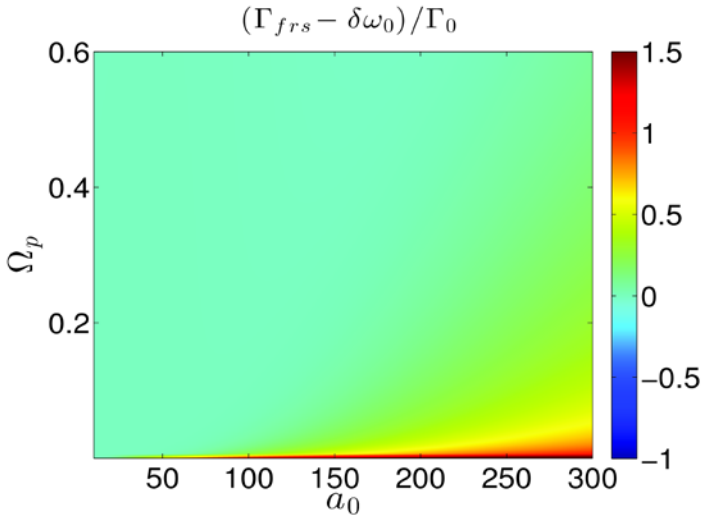

Fig. 1. Growth rate ratio of the FRS with $(\Gamma_{frs} - \delta\omega_{0r})$ and without (Γ_0) the radiation reaction force as a function of the normalized plasma density $\Omega_p = {}^{\omega_p}/_{\omega_{0r}}$ and normalized pump laser amplitude $a_0 = {}^{eA_0}/_{m_e c^2}$. The normalized growth rate is plotted on $\log_{10}$ scale

References

1. A. Di Piazza, C. Mueller, K.Z. Hatsagortsyan, and C.H. Keitel, *Rev. Mod. Phys.*, 2012, **84**, 1177-1228.
2. J.F. Drake, P.K. Kaw, Y.C. Lee, G. Schmid, C.S. Liu, and M.N. Rosenbluth, *Physics of Fluids*, 1974, **17**, 778-785.
3. W. Kruer, *The Physics of Laser Plasma Interactions (Frontier in Physics)*, Westview Press, Boulder CO, 2003, p. 73.
4. L.D. Landau and E.M. Lifshitz, *The Classical Theory of Fields*, vol. 2 of *Course of Theoretical Physics*, Fourth (Ed.), Butterworth-Heinemann, Oxford, 2005, p. 226.
5. N. Kumar, K.Z. Hatsagortsyan, and C.H. Keitel, *Phys. Rev. Lett.*, 2013, **111**, 105001-105005.

Invited

INTERACTION OF THE RELATIVISTIC LASER PULSE WITH THE MELTED GALLIUM SURFACE

A.S. Lar'kin[1], K.A. Ivanov[1], D.S. Uryupina[1], A.B. Savel'ev[1], C. Fourment[2], P.-M. Leguay[2], B. Chimier[2], V.T. Tikhonchuk[2], A.V. Brantov[3], and **V.Yu. Bychenkov[3]**

[1] International Laser Center & Faculty of Physics, Lomonosov Moscow State University, Moscow, Russia
[2] Name Centre Lasers Intenses et Applications, University Bordeaux - CNRS - CEA, Talence 33405, France
[3] P. N. Lebedev Physical Institute, Russian Academy of Sciences, 119991 Moscow, Russia
E-mail: alexeylarkin@yandex.ru

Abstract. The impact of laser pulse with a short weak prepulse which is ahead of the main pulse for a few nanoseconds on the melted gallium surface could significantly increase the hard x-rays yield from laser plasma. This effect is associated with formation of dense microjets above the target surface after the action of the prepulse. The microjet formation is explained based on the results given by both optical diagnostics and hydrodynamic modeling by a collision of shocks originated from two distinct zones of laser energy deposition. Also, results of the experiments on hard x-rays generation from the microjets are reported.

Introduction

Femtosecond laser plasma is a well-known effective source of high-energy particles and ultrashort hard x-ray radiation in the wide energy range. Such x-ray and gamma sources can have a large number of applications, for example in x-ray spectroscopy with high temporal resolution or some medical and biological research.

To increase the yield of x-ray radiation and maximal energy of gamma photons we can increase the intensity of the laser pulse. On the other hand, we can use special targets, for example, the microstructured ones. Using a melted metal target is promising due to the dynamical microstructuring of the liquid target surface as a formation of dense plasma microjets above the surface after the action of the laser prepulse. The interaction of the main pulse with these microjets leads to a significant increase of the hot electron temperature and hard x-rays yield [2].

Thus, our task was to clarify the mechanism of microjets formation and also to conduct the experiments on the interaction of the relativistic laser pulse with these microjets.

Investigation of the microjets formation

The microjets formation was observed with the optical shadowgraphy of the plasma plume formed by the prepulse. The plasma was created by a laser pulse delivered by the Ti:Sa laser system of ILC MSU with the pulse duration of 50±5 fs, the energy up to 20 mJ at 10 Hz repetition rate [1]. Laser radiation was split into two parts. The weaker one (referred to as a heating pulse) was used to produce plasma. The main part of laser radiation was delayed by 3–17 ns and used for visualization of the plasma plume. Simultaneously we measured the energy distribution within the focal area of the laser beam.

Figure 1 shows images of the plume obtained at time delays varying from 6 to 13 ns. The images were obtained at two different positions of the parabolic mirror with respect to the gallium surface – exact focus at the surface (Fig. 1a) and 40 μm below (Fig. 1b). In the first case, microjets were formed at the edges of the plume, while in the second case the strong jet was formed on the left side of the plume close to its center. The jet diameter was close to the optical resolution limit of 4 μm, while the velocity of the microjet propagation was about 4 km/s in the both cases.

These findings can be explained by the shape of the energy distribution in the focal area. The energy distribution in the case of the exact focus consists of the central core (Fig. 2a) with an almost gaussian profile surrounded by complicated inhomogeneous wings (see Fig. 2b). Several hot spots may be distinguished within these wings. In the case of the defocusing of the mirror the energy distribution reveals an inhomogeneous structure with four hot spots (Fig. 2c). The mean energy fluence in the hot spots is about 100 J/cm^2. We assume that these hot spots lead to the microjet formation. It occurs due to collisions of divergent shocks originated from different hot spots. For example, in the case of 40 μm defocusing two bottom hot spots with the highest energy fluence (see Fig. 2c) may generate a strong jet on the left side of the plasma plume close to its center as in Fig. 1b. Two other lower energy hot spots may generate a weaker jet on the right side of the plasma plume.

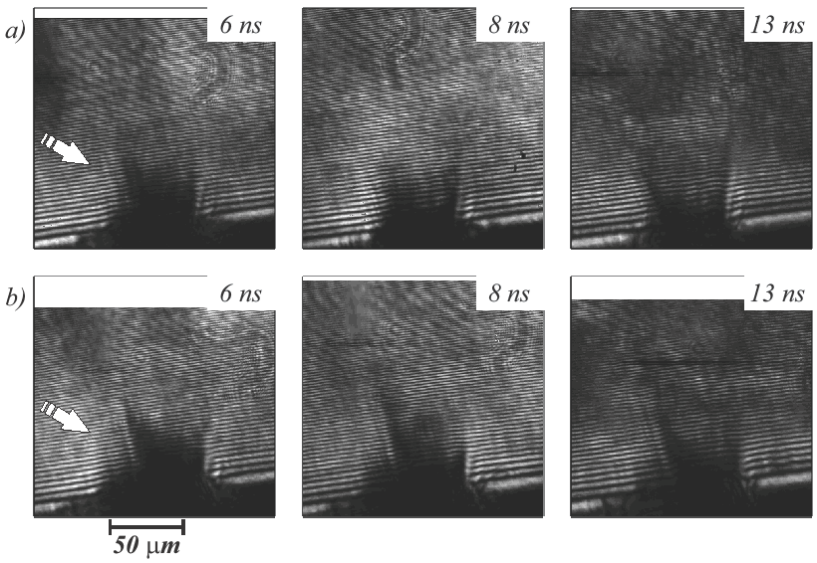

Fig. 1. Optical pump-probe shadow images of a plasma plume a) in the case of the exact focusing of the parabolic mirror and b) in the case of displacement of the target surface from the parabolic mirror focus by 40 μm towards the mirror obtained at different time delays after the action of the heating pulse. The energy of the heating pulse was about 180 μJ. The white arrow in the first image indicates the laser propagation direction

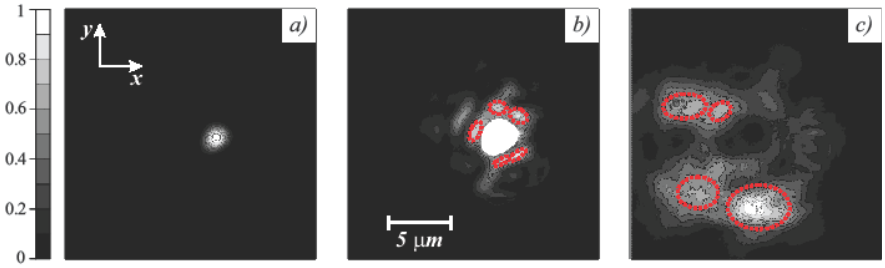

Fig. 2. Energy distributions in the exact focus (a), in the exact focus with the same scale as in the panel c (b), and with a 40 μm defocusing of the parabolic mirror (c). Panels a and c are normalized to their respective maxima

Hard x-rays generation from dense microjets

In the experiments on the x-rays generation, microjets were formed by the manually created prepulse. Thus, we were able to vary the energy of the prepulse and the delay of the main pulse. For this purpose laser radiation was split into two parts: the weaker one was used as a prepulse, and the main pulse was delayed by several nanoseconds with respect to the prepulse. For the registration of the x-ray spectra in a single photon regime we used the photomultiplier tube with NaI(Tl) scintillator.

When the energy of the prepulse was about 200 μJ, the intensity of the main pulse was about $3 \cdot 10^{18}$ W/cm^2 and its delay was 11 ns, gamma photons with energies up to 5 MeV were detected. The estimated hot electron temperature was 1125±25 keV in this case. This effect is related to the interaction of the main pulse with dense plasma microjets which were observed in the shadow images. When the delay of the main pulse was 7 ns and 15 ns there was no large increase of the hot electron temperature as in the previous case. It can be explained by the fact that, when the delay time was 7 ns, the main pulse interacted with still growing microjets, while at 15 ns the microjets had already dissipated.

Acknowledgements

This work was partially supported by the Russian Foundation for Basic Research under the grants 10-02-91060-NCNI-a, 12-02-33045, 13-02-00337, 13-02-00619.

References

1. K.A. Ivanov et al., *Plasma Physics Reports*, 2010, **36**, 99.
2. D.S. Uryupina et al., *Phys. Plasmas*, 2012, **19**, 013104.

THEORY AND SIMULATIONS OF LASER-PLASMA GENERATION OF FREQUENCY-TUNABLE MID-INFRARED PULSES

I.D. Laryushin[1], **N.V. Vvedenskii**[1,2], **V.A. Kostin**[1,2], and **A.A. Silaev**[1,2]

[1] University of Nizhny Novgorod, Nizhny Novgorod, Russia, e-mail: ilaryushin@mail.ru
[2] Institute of Applied Physics, Russian Academy of Sciences, Nizhny Novgorod, Russia

We examine a new method for generation of coherent few-cycle mid-infrared pulses. The method utilizes gas ionization by ultrashort incommensurate two-color laser pulses. These incommensurate two-color pulses contain the fields at two different frequencies. One of the frequencies is detuned from the doubled value of the other one. Such incommensurate pulses can be obtained with the use of the nonlinear crystal (for example, BBO or KDP) or with the use of the optical parametric amplifier. In the latter case, the main (in the respect of intensity) field component has greater central frequency than the weaker field; and the frequency of the weaker field can be reasonably easily tuned around the halved value of central frequency of the main field which stays fixed [1].

We calculate the electron current which is excited by such a two-color pulse in a gas during ionization through the use of the semiclassical approach both analytically and numerically and find out that the low-frequency component of that current can have central frequency in the mid-infrared range, which can be controlled by tuning the frequency of the weaker optical field. The full-dimensional simulations based on the quantum-mechanical approach (the solution of the 3D time-dependent Schrödinger equation) support the results obtained from the semiclassical approach. We estimate energy radiated by that current and discuss the possibilities of employing the phenomenon for creating the tunable source of coherent few-cycle mid-infrared pulses.

Acknowledgements

This work was supported by the Government of the Russian Federation (Agreement No. 14.B25.31.0008) and the Russian Foundation for Basic Research (Grants No. 14-02-00847, No. 13-02-00964, and No. 14-02-31722).

References

1. N.V. Vvedenskii, A.I. Korytin, V.A. Kostin, A.A. Murzanev, A.A. Silaev, and A.N. Stepanov, "Two-color laser-plasma generation of terahertz radiation using a frequency-tunable half harmonic of a femtosecond pulse", *Physical Review Letters*, 2014, **112,** 055004-1-5.

Invited

NON-FILAMENTED ULTRA-INTENSE AND ULTRA-SHORT PULSES IN RAMAN SEED AMPLIFICATION

G. Lehmann[1] and **K.H. Spatschek**[1]

Institute for Theoretical Physics I, 40225 Düsseldorf, Germany, goetz@tp1.uni-duesseldorf.de

Abstract. Ultra-intense and ultra-short laser pulses may be generated up to the exawatt-zetawatt regime due to parametric processes in plasmas. The minimization of unwanted plasma processes leads to operational limits. We discuss these limits with respect to filamentation. It is shown that the limit for transverse filamentation, which originally was derived for plane waves, is actually less stringent for seed pulse propagation. Because of fast motion the leading pulse front can stay filamentation-free, whereas the rear parts show transverse modulations. Results from three-dimensional (3D) three-wave-interaction models are compared with one-dimensional PIC and Vlasov simulations. Although wave-breaking occurs, the kinetic simulations show that the leading pumped pulse develops a form similar to that obtained from the three-wave-interaction model.

The tremendous increase in achievable maximum laser intensity over the past 30 years was triggered by the invention of chirped pulse amplification (CPA). Today intensities of up to 10^{22} W/cm^2 and above can be realized in table top setups and allow to study a great number of relativistic effects occurring in the interaction of intense radiation and matter. Typically the radiation interacts with a large ensemble of particles in the form of plasma. Nonlinear plasma effects can then be utilized to accelerate particles (electrons, protons) or for the generation of secondary radiation.

Current top-class laser systems can achieve powers of the order of 10 PW and reach intensities of up to 10^{24} W/cm^2, values at which even proton motion will become relativistic. Still, the electric field strength of about 10^{15} V/m will fall short of the Sauter field $E_s = m^2c^3/eh \approx 10^{18}$ V/m, at which direct access to the nonlinear QED regime will be possible, by three orders of magnitude. Reaching these intensities using CPA technology seems very complicated at least. Amplifier crystals and compressor gratings would need to be scaled up by magnitudes in order to keep the energy fluence below damage threshold level.

To overcome damage issues of solid-state technology the use of plasma-based laser pulse amplification and compression schemes was proposed [1]. In these schemes the energy of a long pump pulse is scattered into a short seed pulse by a plasma oscillation. The plasma oscillations can be either an electron (stimulated Raman scattering, SRS) or an ion (stimulated Brillouin scattering, SBS) mode. To achieve a resonant interaction between the three waves (pump, seed and plasma) the matching conditions $\omega_{pump}=\omega_{plasma}+\omega_{seed}$ and $\boldsymbol{k}_{pump}=\boldsymbol{k}_{plasma}+\boldsymbol{k}_{seed}$ have to be fulfilled. The amplification mechanism can in this case be approximately described by a three-wave coupling model, see e.g. [2] for SRS and [3, 4] for SBS. The three-wave models lack kinetic effects like Landau-Damping or wave-breaking, but still give an insight into the dominant dynamics in a broad parameter regime. The majority of literature on plasma-based laser pulse amplification treats one-dimensional models. We extended the "standard" three-wave model for Raman amplification to multi-dimensional geometry and implemented two- and three-dimensional numerical simulations of this system of equations [5]. This allows us to study the influence of transversal pump-intensity variations and the influence of transverse perturbations during amplification.

Transverse filamentation might impose limitations on the maximum amplification length and the amplifier diameter, respectively. The first large-scale PIC simulations demonstrated that amplification is possible, even for beam diameters of several μm [6]. Our multi-dimensional three-wave model allows studying filamentation, self-focusing and cross-beam interaction in more detail and with a dramatically reduced computational effort.

Filamentation of laser beams in nonlinear media is a well-known effect and has been treated extensively in the literature, however mostly in the plane wave approximation. From plane wave calculations one can easily find the growth rate $\gamma = 10^{-5}\,\omega_0\,n_e/n_c\,I_{14}\,\lambda_0^2$ and the wavelength of the most unstable transverse perturbation [5]. Due to its larger intensity we consider only filamentation of the seed pulse. For an intensity of 10^{16} W/cm^2 and typical plasma parameters the time-scale for filamentation is on the order of 10 ps.

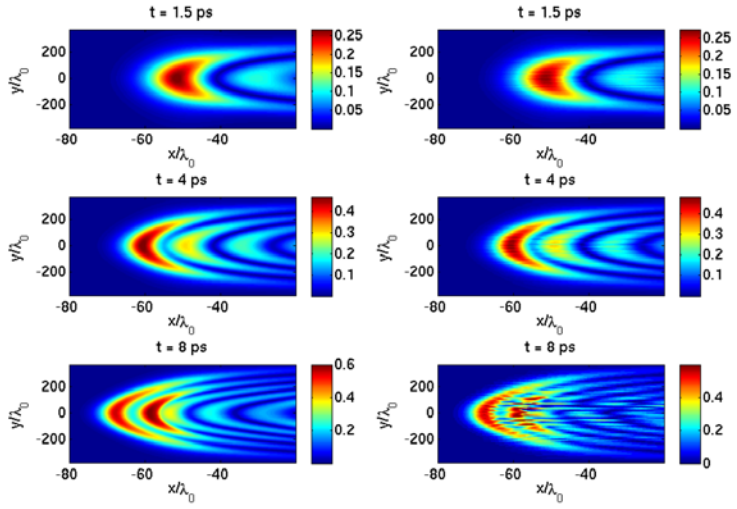

Fig. 1. Amplitude $|E_{seed}|$ of seed pulse envelope during amplification process in dimensionless units. *Left column*: Amplification without initial transverse perturbation of seed. *Right column*: Amplification of seed with initial transverse perturbation

Figure 1 shows results obtained from two simulations for the amplification of a seed pulse of initial intensity 10^{15} W/cm^2. The pump intensity is 10^{15} W/cm^2, corresponding to 0.03 in dimensionless units used in the figure. The plots show the magnitude of the seed envelope in the co-moving frame which moves at the group velocity of the seed. For the simulation in the left column the initial seed profile was Gaussian with 50 fs FWHM duration. No transverse perturbation was present at $t = 0$. After 8ps we obtain a clean seed pulse which shows π-pulse like oscillations of the envelope along the propagation direction x, as expected for the pump-depletion regime [2]. Additionally we observe a curvature of the seed envelope, which is due to the transverse intensity profile of the pump beam. For the simulation shown in the right column of Fig. 1 all parameters are the same, but now the initial seed pulse envelope at t=0 contains a spectrum of transverse perturbations. In the course of the amplification we observe that filamentation sets in, but leaves the first oscillation of the seed pulse almost completely unharmed. The second oscillation of the seed envelope is filamented and shows a characteristic perturbation wavelength. The filamentation wavelength is in good agreement with predictions from plane wave theory. That the first envelope oscillation is left unharmed seems a surprising result at first. However, it can be understood as a result of the nonlinear evolution of the Raman amplified seed. In the nonlinear phase the maximum of the seed travels at superluminal speed, since the front interacts with an untouched part of the pump and is amplified the most. The back however interacts only with an already depleted seed [7, 8], which results overall in an apparently superluminal behavior. This effect is clearly visible in Fig. 1, the seed seems to move forward in the co-moving frame. By this mechanism the seed front is able to escape the initial transverse perturbation and eventually shed away all potentially spoiling modes. The second envelope oscillation however can not outrun the perturbation and becomes filamented.

Since the three-wave interaction model does not contain kinetic effects, we compared the three-wave results to Particle-in-Cell and full Vlasov simulations in one-dimensional geometry. We find that the results agree well for the first envelope oscillation, but in the kinetic description we observe wave-breaking, which strongly suppresses growth of following seed envelope oscillations.

Acknowledgements

The work was carried out under the auspices of SFB TR18 of Deutsche Forschungsgemeinschaft. Computer resources provided on JUROPA by the NIC of FZ Jülich are gratefully acknowledged.

References

1. G.A. Mourou, N.J. Fisch, V.M. Malkin, Z. Toroker, E.A. Khazanov, A.M. Sergeev, T. Tajima, and B. Le Garrec, *Opt. Communications*, 2012, **285**, 720.
2. V. Malkin, G. Shvets, and N.J. Fisch, *Phys. Rev. Lett.*, 1999, **82**, 4448.
3. A.A. Andreev, C. Riconda, V.T. Tikhonchuk, and S. Weber, *Phys. Plasmas*, 2006, **13**, 053110.
4. G. Lehmann and K.H. Spatschek, *Phys. Plasmas*, 2013, **20**, 073112.
5. G. Lehmann and K.H. Spatschek, *Phys. Plasmas*, 2014, **21**, 053101.
6. R.M.G.M. Trines, F. Fiuza, R. Bingham, R.A. Fonseca, L.O. Silva, R.A. Cairns, and P.A. Norreys, *Nat. Phys.*, 2011, **7**, 87.
7. N.A. Yampolsky, V.M. Malkin, and N.J. Fisch, *Phys. Rev. E*, 2004, **69**, 036401.
8. G. Lehmann, G. Sewell, and K.H. Spatschek, *Phys. Rev. E*, 2013, **87**, 063107.

Invited

NONLINEAR QED-EFFECTS IN STRONG LASER FIELDS

S. Meuren, F. Mackenroth, N. Neitz, C. H. Keitel, and A. Di Piazza

Max Planck Institute for Nuclear Physics, Heidelberg, Germany

Abstract. We have investigated various quantum electrodynamical (QED) processes inside strong laser fields. Among them are nonlinear (double) Compton scattering, (quantum) radiation reaction, the influence of radiative corrections (Lamb shift analog for free electrons) and vacuum polarization effects (photon propagation inside a strong plane-wave background field). The talk will give an overview about the resent results of our group.

Quantum electrodynamics (QED) is well understood in the perturbative regime called vacuum QED, where the field strengths of the electric and magnetic fields are much smaller than the critical field $E_{cr} = m^2c^3/(\hbar|e|) = 1.3\times10^{16}$ *V/cm* (*m* and *e* denote the electron's mass and charge, respectively). The critical field corresponds to a laser intensity of 4.6×10^{29} W/cm^2. In vacuum QED the strength of the interaction is characterized by the (effective) fine-structure constant α, which is a small parameter for feasible particle energies. Accordingly, the *S*-matrix can be calculated perturbatively, allowing for the most precise predictions nowadays available (e.g. the electron *g*-factor). This situation changes if strong external fields are present. The strength of a laser field can be characterized by the gauge and Lorentz invariant parameter $\xi = |e|E/(mc\omega)$, where E and ω are the peak electric field strength and central angular frequency, respectively. For $\xi \geq 1$ the laser field must be taken into account exactly in the calculations (available petawatt laser systems already reach $\xi \geq 100$). On the other hand, nonlinear quantum effects become important if the electric field of the laser reaches the critical field, which is experimentally feasible in the rest frame of ultra-relativistic particles [1].

We have recently investigated several interesting non-linear QED effects, which could, in principle, be tested experimentally with existing or upcoming laser facilities. In [2] double photon emission by electrons in the full nonlinear quantum regime was investigated. The photon spectra show interesting features that can be attributed to nonlinear effects in the laser field amplitude, the photon recoil and the short laser pulse duration. The recoil experienced by the electron due to the emission of several photons is closely related to radiation reaction. By using a kinetic approach, it was shown in [3] that the energy distribution of an electron beam spreads out when quantum effects become important. This is in contrast to the result obtained from classical electrodynamics, where radiation reaction tends to narrow the distribution. The interaction with a laser pulse can also change the properties of an electron beam without the emission of photons [4]. Due to quantum fluctuations different spin states are no more degenerated in energy (analogously to the Lamb shift in atoms) and a finite spin-flip probability is obtained. Vacuum polarization effects are also experienced by photons. Due to the creation of virtual electron-positron pairs the photon obtains a mass and has a nontrivial dispersion relation within a strong laser field [5].

Acknowledgements

SM is grateful to the Studienstiftung des deutschen Volkes for financial support.

References

1. Di Piazza et al., *Rev. Mod. Phys.*, 2012, **84**, 1177.
2. F. Mackenroth and A. Di Piazza, *Phys. Rev. Lett.*, 2013, **110**, 070402.
3. N. Neitz and A. Di Piazza, *Phys. Rev. Lett.*, 2013, **111**, 054802.
4. S. Meuren and A. Di Piazza, *Phys. Rev. Lett.*, 2011, **107**, 260401.
5. S. Meuren, C.H. Keitel, and A. Di Piazza, *Phys. Rev. D*, 2013, **88**, 013007.

Invited

HIGH-ORDER HARMONICS FROM SINGULARITIES OF RELATIVISTIC PLASMA

A.S. Pirozhkov[1], M. Kando[1], T.Zh. Esirkepov[1], T.A. Pikuz[1,2], A.Ya. Faenov[1,2,3], K. Ogura[1], Y. Hayashi[1], H. Kotaki[1], E.N. Ragozin[4], D. Neely[5], H. Kiriyama[1], J.K. Koga[1], Y. Fukuda[1], M. Nishikino[1], T. Imazono[1], N. Hasegawa[1], T. Kawachi[1], H. Daido[6], Y. Kato[7], P.R. Bolton[1], S.V. Bulanov[1], and **K. Kondo[1]**

[1] Kansai Photon Science Institute, Japan Atomic Energy Agency, Kizugawa, Kyoto, Japan
pirozhkov.alexander@jaea.go.jp
[2] Joint Institute of High Temperatures of the Russian Academy of Sciences, Moscow, Russia
[3] Institute for Academic Initiatives, Osaka University, Suita, Osaka, Japan
[4] P. N. Lebedev Physical Institute of the Russian Academy of Sciences, Moscow, Russia
[5] Central Laser Facility, Rutherford Appleton Laboratory, STFC, Chilton, Didcot, UK
[6] Applied Laser Technology Institute, Tsuruga Head Office, Japan Atomic Energy Agency, Kizaki, Tsuruga, Fukui, Japan
[7] The Graduate School for the Creation of New Photonics Industries, Nishiku, Hamamatsu, Shizuoka, Japan

Abstract. We have discovered a new regime of high-order harmonic generation in gas jet targets driven by multi-TW femtosecond lasers [A.S. Pirozhkov et al., *Phys. Rev. Lett.*, 2012, **108**, 135004-5]. In this presentation, we discuss the results of recent experiments demonstrating bright off-axis (~13°) XUV harmonic emission. High-resolution harmonic source imaging reveals that the radiation is emitted by tiny sub-μm sources, in accordance with the model prediction.

Introduction

Relativistic laser plasma emits extreme ultraviolet (XUV) and x-ray radiation generated via various mechanisms. Many important applications require temporally and spatially coherent radiation, which can be compressed to ultrashort pulses and focused to the tiniest possible spots or used to produce fine interference and diffraction patterns. We have discovered [1] a new regime of high-order harmonic generation in gas jet targets driven by multi-TW femtosecond lasers. Using PIC simulations with the REMP code [2] and catastrophe theory [3, 4], we have developed a harmonics generation model, which explains the experimental findings. According to the model, the harmonics are emitted by relativistic electron spikes [1], which are the density singularities resulting from catastrophes of a multi-stream relativistic plasma flow [5].

Experimental results

Apart from the explanation of the previously available experimental data, the model predicts interesting properties of the harmonics emission. First, the harmonics are emitted not from the whole focal spot volume, but from tiny sources – the electron spikes. Second, in addition to the previously observed on-axis harmonics, there should be off-axis emission. Here we present results of new experiments performed with the J-KAREN laser [6], demonstrating bright off-axis harmonics, with the XUV pulse energy within the 60 to 100 eV photon energy range and 13±5° off-axis observation angle exceeding 50 nJ. We have performed imaging of the XUV emission source in the same photon energy range onto a high-spatial-resolution LiF crystal detector [7]. Our measurements show that the radiation is indeed emitted by tiny sub-μm sources, in accordance with the model prediction.

Acknowledgements

We are grateful to H. Okada, M. Tanoue, S. Kondo, S. Kanazawa, Y. Nakai, T. Shimomura, M. Okamoto, K. Torimoto, and T. Sato for the excellent technical support. We acknowledge financial support from the Ministry of Education, Culture, Sports, Science, and Technology of Japan (MEXT) (Kakenhi 23740413 and 26707031).

References

1. A.S. Pirozhkov et al., *Phys. Rev. Lett.*, 2012, **108**, 135004-5.
2. T.Zh. Esirkepov, *Comput. Phys. Comm.*, 2001, **135**, 144-153.
3. T. Poston and I. Stewart, *Catastrophe theory and its applications*, Dover Pubns, Mineola, 1996.
4. V.I. Arnold, *Catastrophe theory*, Springer-Verlag, Berlin Heidelberg New York, 1992.
5. T.Zh. Esirkepov, Y. Kato, and S.V. Bulanov, *Phys. Rev. Lett.*, 2008, **101**, 265001-4.
6. H. Kiriyama et al., *Appl. Sciences*, 2013, **3**, 214-250.
7. T. Pikuz et al., *Optics Express*, 2012, **20**, 3424-3433.

QUANTUM-MECHANICAL DESCRIPTION OF GAS IONIZATION AND RESIDUAL-CURRENT EXCITATION BY TWO-COLOR LASER PULSES

A.A. Romanov[1], **A.A. Silaev**[1, 2], and **N.V. Vvedenskii**[1, 2]

[1] University of Nizhny Novgorod, Nizhny Novgorod, Russia
[2] Institute of Applied Physics, Russian Academy of Sciences, Nizhny Novgorod, Russia

Abstract. On the basis of analytical solution of the time-dependent Schrödinger equation the phenomenon of excitation of residual current density in plasma produced by the laser pulse is studied. It is assumed that the laser pulse contains along with a strong field at the fundamental frequency an additional field at the doubled frequency. We find analytical dependences of the residual current density on the laser pulse parameters in the ranges of parameters corresponding to the tunneling and multiphoton regimes of ionization.

This work is focused on analytical investigation of the phenomenon of excitation of low-frequency residual currents due to gas ionization by two-color laser pulses, which contain a strong field at the fundamental frequency and a low-intensity field at the doubled frequency. At present, this phenomenon is of great interest due to the possibility of using it to convert efficiently laser pulses into low-frequency radiation, in particular, into the radiation of the terahertz frequency band [1–6].

Previous analytical studies of this phenomenon were based on the so-called semiclassical approach which includes the hydrodynamic equation for the plasma current density and the adopted model expression for the tunneling ionization probability per unit time [4–6]. However, the range of applicability of the semiclassical approach is limited by the parameters of laser pulses corresponding to the tunneling regime of ionization, when the Keldysh parameter γ [7] (defined by the ratio of atomic ionization potential and the averaged kinetic energy of an electron in a laser field) is much less than unity [8]. Thus, recent studies [9–11] have attempted to find the low-frequency photocurrent using analytical solutions of the time-dependent Schrödinger equation in the multiphoton regime of ionization ($\gamma >> 1$), when the semiclassical approach is beyond its applicability. In these studies, in fact, the authors used the assumption that photocurrent is determined by the product of the average ionization probability per unit time and the most probable velocity of the electron (corresponding to the maximum of the velocity distribution function) [10].

In this work we find the analytical solution of the time-dependent Schrödinger equation using the approach developed in [7]. We obtain closed-form expressions for the residual current density in the ranges of laser pulse parameters corresponding to the tunneling and multiphoton regimes of ionization. We show that the above mentioned decomposition of low-frequency current density into the product of averaged ionization probability and the most probable velocity takes place only for the laser pulse parameters corresponding to the tunneling regime of ionization. When γ is greater than unity the dependence of residual current density on the laser pulse parameters may differ significantly from the predictions of [9–11], as well as from the results obtained by semiclassical approach [4–6]. We show the agreement of the obtained formulas with the results of numerical solution of three-dimensional time-dependent Schrödinger equation in the wide range of laser pulse parameters.

This work was supported by the Government of the Russian Federation (Agreement No. 14.B25.31.0008) and the Russian Foundation for Basic Research (Grants No. 14-02-00847, No. 13-02-00964, and No. 14-02-31044).

References

1. B. Clough, J. Dai, and X.-C. Zhang, *Mater. Today*, 2012, **15**, 50.
2. K.Y. Kim, A.J. Taylor, J.H. Glownia, and G. Rodriguez, *Nat. Photonics*, 2008, **2**, 605.
3. M.D. Thomson, V. Blank, and H.G. Roskos, *Opt. Express*, 2010, **18**, 23173.
4. I. Babushkin et. al., *New J. Phys.*, 2011, **13**, 123029.
5. K.Y. Kim, *Phys. Plasmas*, 2009, **16**, 056706.
6. N.V. Vvedenskii et al., *Phys. Rev. Lett.*, 2014, **112**, 055004.
7. L.V. Keldysh, *Sov. Phys. JETP.*, 1965, **20**, 1307.
8. A.A. Silaev and N.V. Vvedenskii, *Phys. Rev. Lett.*, 2009, **102**, 115005.
9. I.A. Kotelnikov, A.V. Borodin, and A.P. Shkurinov, *JETP*, 2011, **112**, 946.
10. A.V. Borodin et al., *J. Opt. Soc. Am. B*, 2012, **29**, 1911.
11. D.S. Bagulov and I.A. Kotelnikov, *JETP*, 2013, **116**, 20.

Invited

PRE-PULSE CONTROL OF FAST ELECTRONS PRODUCTION FROM SOLIDS AT RELATIVISTIC INTENSITIES

A. Savel'ev[1], K. Ivanov[1], S. Shulyapov[1], A. Lar'kin[1], I. Tsymbalov[1], D. Uruypina[1], R. Volkov[1], A. Brantov[2], P. Ksenofontov[2], V. Bychenkov[2], J. Breil[3], B. Chimier[3], and **V.T. Tikhonchuk[3]**

[1]Faculty of Physics and International Laser Center of Lomonosov Moscow State University, Moscow, Russia, e-mail: abst@physics.msu.ru

[2]P.N. Lebedev Physical Institute of Russian Academy of Sciences, Moscow, Russia

[3] Centre Lasers Intenses et Applications, University of Bordeaux - CNRS - CEA, Talence 33405, France

Abstract. We present experimental and theoretical data on the interaction of relativistic femtosecond pulses with pre-pulse created dense plasma. We show that the energy of fast electrons as well as conversion to gamma rays can be controlled efficiently by the proper choice of pre-pulse parameters. Experiments were made using the ILC MSU TW laser (45 fs, 10 Hz, up to 10^{19} W/cm^2). The 3D PIC code Mandor and the hydrodynamic code CHIC were used for numerical simulations. The interaction with a melted gallium target is considered in the second part of the paper. Here we also achieved huge increase in the gamma yield and electron energy but applying short a very intense femtosecond pre-pulse (advancing the main pulse by ~10 ns and having intensity of ~10^{16} W/cm^2).

We studied acceleration of hot electrons with three different and typical temporal contrasts: (i) strong, above the ablation threshold, nanosecond ASE accompanied by a few strong femtosecond pulses ahead of the main pulse; (ii) plasma creating femtosecond pre-pulse positioned 12 ps ahead of the main pulse with the ASE below the ablation threshold; and (iii) the same as previous with additional strong femtosecond pre-pulse 12 ns ahead of the main pulse. This enabled us to create pre-plasma with different spatial extent and density. We also present data obtained with two laser pulse durations (45 and 350 fs). In our study, we used radiation at a central wavelength of 805 nm from the 10 Hz Ti:Sapphire laser system at ILC MSU with the pulse duration τ_L = 45±5 fs and energy after compression up to 50 mJ per pulse. The *p*-polarized radiation was focused by the off-axis parabola (*F/D*=5) onto the surface of a flat solid plate made of stainless steel or lead at the incidence angle of 45 degrees.

The anomalously high energy gamma emission is observed if the scale length of pre-plasma, formed by the ASE on metal targets, is long enough (of the order of 100 μm). High energy electron component did not appear if the ASE was suppressed below the breakdown threshold. Moreover, this high energy component was not observed if a pre-plasma was created by the short femtosecond pulse with advance time of 12 ns. Hence, extended undercritical pre-plasma is needed for the appearance of high energy electrons (and gammas). Gamma quanta with energies up to 1.5 MeV were detected at the intensity of ~$7\cdot10^{17}$ W/cm^2 (45 fs pulse duration) for the stainless steel target if the ASE level was high enough, and only 500 keV with a low level of ASE. The deduced slope of the gamma-spectrum was as high as 255 keV compared to 115 keV with suppressed ASE and 65 keV with a femtosecond pre-pulse.

The increase in the laser pulse duration from 45 to ~350 fs was accompanied by the appreciable growth of hot electron energies, if the ASE had high level (10^{-5}). This indicates that the mechanisms of high energy electron acceleration are very sensitive not only to the intensity (that is characteristic of the ponderomotive acceleration, resonant heating, etc.), but also to the pulse duration. The latter feature may be connected with such processes as stochastic heating, quasistatic field formation, parametric instabilities, and others.

Numerical simulations with the 2D3V version of the Mandor PIC code support the experimental observations. The fast electron production comes from the complex interplay between self-focusing, plasma wake excitation and direct laser acceleration. Further numerical analysis, including 3D3V modeling, is underway.

The approach based on ASE enhanced electron acceleration may find a lot of applications if higher (10^{19} – 10^{22} W/cm^2) intensities are used to couple laser energy into a hot electron and gamma rays. The optimized pre-plasma scale length and density should be deduced from PIC simulations at given intensity and duration of the pulse. The desired level of the ASE ~10^{12} W/cm^2 is natural for modern PW and sub-PW lasers without special pulse cleaning measures.

Our study also justifies the importance and utility of plasma jet formation on the surface of a liquid gallium target for X-ray generation. We used two femtosecond laser pulses: the main interaction pulse and the weak prepulse producing jets. We observed an increase of 3 to 4 times in the mean hot-electron energy and nearly two orders of magnitude enhancement in both bremsstrahlung (above 5 keV) and line (Ga K) plasma emission compared with the case of a single high-contrast pulse with the same intensity.

From 3D3V PIC laser-target interaction simulations, we deduced that a properly delayed intense (above 10^{16} W/cm^2) femtosecond laser pulse acting on these prepulse-produced jets provides efficient electron heating and acceleration along the jet surface. Such electron generation is sensitive to the jet diameter and direction with respect to the laser beam axis. The numerical simulations support the experimental findings. A significant enhancement in both the hard X-ray yield and the mean hot-electron energy observed for the prepulse contrast below 100 is certainly attributable to efficient microjet production. At a contrast below 30, the jet diameter is comparable to the focal spot size, and the electron acceleration efficiency decreases.

Our explanation of the microjet generation is related to an inhomogeneous laser energy deposition at the target surface. The energy deposition in the form of two or more neighboring hot spots or in the form of an intense central core and a weaker annular ring may be a source of converging flows. After the prepulse irradiation, the heated material is vaporized from the surface, while shock waves are launched from the irradiated areas. These shock waves propagating along the liquid metal surface intersect with each other, thus creating the pressure maxima beneath the liquid surface. These zones are the origins of the jet ejections from the target surface. This hypothesis explains why the liquid target is better suited for the jet formation and why similar jets were created in the cases of focused and slightly defocused laser beams. Moreover, the observations of the focal spot with the microscope objective reported in the previous section, confirm a strongly inhomogeneous laser energy deposition in the focal spot in our experiments.

References

1. K. Ivanov et al., *Contributions to Plasma Physics,* 2013, **53,** 116.
2. K.A. Ivanov, submitted to *Phys. Plasmas,* 2014.
3. D.S. Uryupina et al., *Phys. Plasmas,* 2012, **19**, 013104.
4. A. Lar'kin et al., submitted to *Phys. Plasmas,* 2014.

ANALYTICAL MODEL FOR GAMMA-RAY GENERATION IN LASER-IRRADIATED PLASMA

D.A. Serebryakov[1,2], **E.N Nerush**[1,2], and **I.Yu. Kostyukov**[1,2]

[1]Institute of Applied Physics RAS, Nizhny Novgorod, Russia, dmserebr@gmail.com
[2]Nizhny Novgorod State University, Nizhny Novgorod, Russia

Abstract. Based on PIC-simulation results, we propose a model for gamma-ray emission from a plasma layer irradiated by an ultra-short high-intensity laser pulse. The radiation characteristics obtained from the model are in a good agreement with 3D PIC simulations for a range of parameters.

Gamma-rays are currently in a widespread use in numerous applications from medicine to nuclear physics. The majority of the existing non-radioactive gamma-ray sources require high-energy electron bunches as an input so they are available only at large facilities. The proposed alternative source of gamma-rays is plasma irradiated by a high-intensity laser pulse. In strong fields electrons in plasma begin to move with ultra-relativistic velocities and emit hard photons due to the synchrotron radiation mechanism.

The interaction of a normally and obliquely incident laser pulse with solid targets (foils) has been widely investigated through last years. The theoretical researches in the area have shown that electrons in the target form a thin electron layer which acts as a relativistic mirror and can result in efficient coherent high-harmonics generation. This phenomenon was studied in [1, 2]. However, we focus on incoherent radiation from the moving electron layer; in PIC 3D simulations it was shown that at intensities of the order of 10^{24} W/cm^2 the efficiency of incoherent gamma-ray generation can reach 30 % [3].

Electron layer dynamics model

In the current work, we propose an analytical model for gamma-ray radiation from a thin foil irradiated by a normally incident high-intensity laser pulse. The model assumes that radiation pressure pushes the electrons towards the laser pulse and they form an infinitely thin layer and its radiation almost compensates the laser field behind the layer (so we neglect plasma density perturbations behind the layer). Also we consider ions to be immobile (this assumption is justified for ultra-short laser pulses). After calculating the field emitted by the electron layer we can write a system of equations of motion for the layer, which considers its motion in an aggregated field of laser, self-generated field and charge separation field from the ions.

Solution to these equations gives a trajectory of the electron layer. A typical trajectory of the layer is shown in Fig. 1 (left), where color represents relativistic Lorentz factor of the layer. It is known that in case of ultra-relativistic velocities synchrotron radiation formula can be used. This gives a possibility to build a radiation pattern of gamma-rays (see Fig. 1, right).

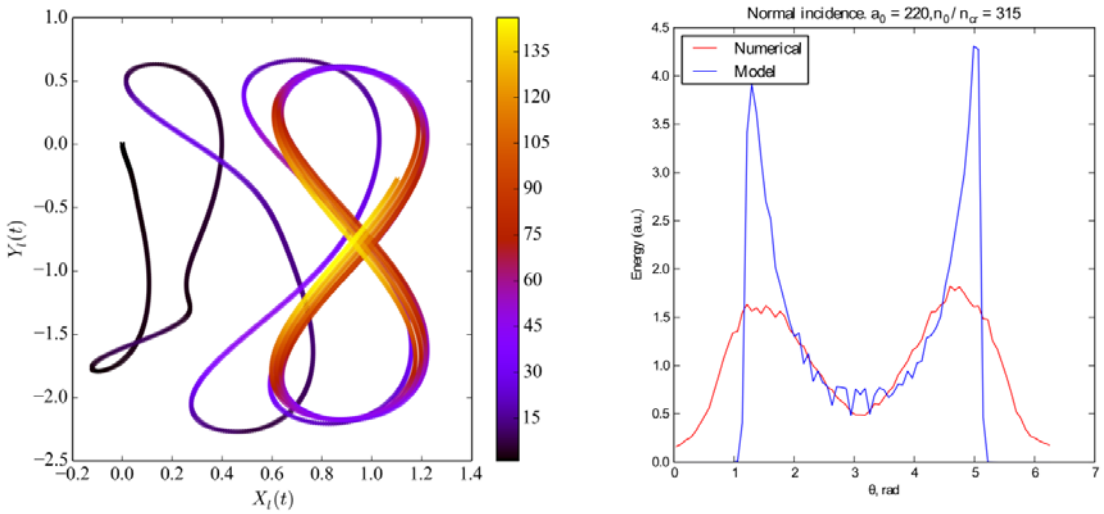

Fig. 1. (*left*) Model trajectory of electron layer (color represents relativistic Lorentz-factor); (*right*) radiation pattern for normal incident laser pulse obtained from model and from numerical experiments. Parameters: a_0 = 220, n_0/n_{cr} = 315

We compared the model with the previous “simple model” that was described in [3] (it demands that the electric field behind the layer exactly turns to zero). In case of high dimensionless laser field amplitude a_0 (500–1000) the two models suit each other well, in the opposite case the trajectories slightly differ. This means that with small a_0 values, laser field doesn’t completely vanish behind the layer so the model is seen to be applicable for strong enough fields.

The radiation pattern from the model is consistent with what was obtained from PIC 3D simulations (Fig. 1, right). The sharp peaks from the model curve can’t be observed in the simulations because plasma particles always have velocity spread and they can’t move as a single electron layer in the same direction.

PIC 3D numerical simulations

We have performed a number of PIC+Monte-Carlo 3D simulations of a normally and obliquely incident laser pulse interacting with a thin foil. An example of the simulation with oblique incidence is shown in Fig. 2.

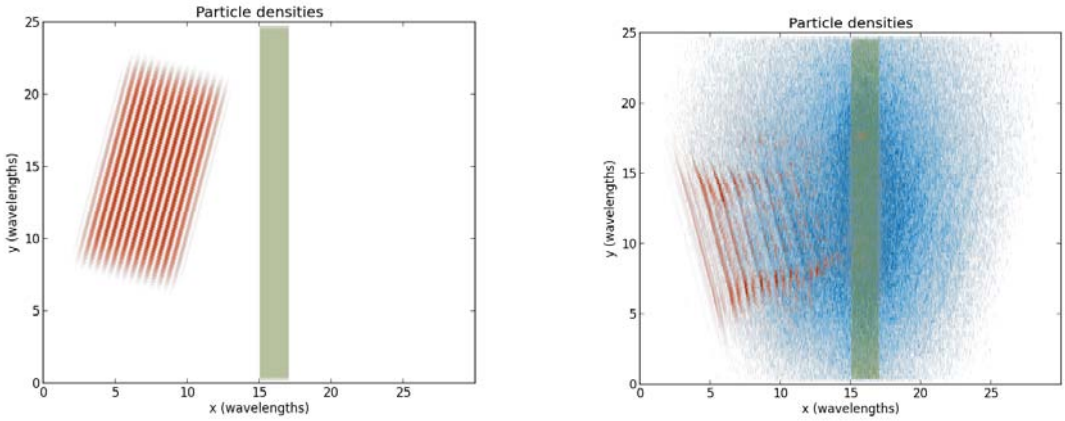

Fig. 2. PIC 3D simulation of gamma-quanta (blue) generation from a plasma layer (green) irradiated by an oblique 15° laser pulse (red). Configuration of plasma and laser pulse before (*left*) and after (*right*) interaction. Parameters: $a_0 = 220$, $n_0/n_{cr} = 210$

Simulations for a normally incident laser pulse show that numerical electron layer dynamics and gamma-ray radiation patterns are in good agreement with the analytical model for relatively high densities (n_0/n_{cr} = 200 and higher), for lower densities we observe that the laser pulse penetrates through the electron layer and its position strongly disagrees with the model. For the oblique incidence, we see that the gamma-ray radiation pattern has higher directivity than in the case of the normal incidence, so it appears to be a more promising configuration for practical applications.

Acknowledgements

This work was supported in part by the Government of the Russian Federation (Project No. 14.B25.31.0008), and by the Russian Foundation for Basic Research (Grants Nos. 14-02-31496, 13-02-00886 and 13-02-00372).

References

1. A.A. Gonoskov, A.V. Korzhimanov, A.V. Kim et al., *Phys. Rev. E*, 2011, **84**, 046403.
2. S.V. Bulanov et al., *Phys. Plasmas*, 2013, **20**, 123114.
3. E.N. Nerush, I.Yu. Kostyukov et al., *Phys. Plasmas*, 2014, **21**, 013109.

Invited

ION ACCELERATION FROM RELATIVISTIC LASER PLASMA

S. Ter-Avetisyan

Center for Relativistic Laser Science, Institute for Basic Science (IBS)
Department of Physics and Photon Science, GIST

Abstract. New perspectives have been opened up in the field of laser–matter interactions due to recent advances in laser technology, leading to laser systems of high contrast and extreme intensity values, where the frontier of maximum intensity is pushed now to about 10^{22} W/cm^2. Many striking phenomena such as laser-acceleration of electrons up to the GeV level, fast moving ions with kinetic energies of several 10 s of MeV, as well as nuclear physics experiments have already actuated a broad variety of theoretical as well as experimental studies. Also highly relativistic effects like laser induced electron-positron pair production are under discussion. All these activities have considerably stimulated the progress in understanding the underlying physical processes and possible applications. This article reviews recent advances in the experimental techniques as well as the associated plasma dynamics studies at relativistic intensities.

Introduction

Recent achievements in laser technology have led to laser systems with high contrast and extreme intensity values, which have opened up new perspectives in the field of laser–matter interaction and particle acceleration [1]. Nowadays accessible intensities, well beyond 10^{20} W/cm^2, have provided for the first time the opportunity to extend scaling laws for the known acceleration process in the ultra-short regime, and to access new ion acceleration scenarios.

In most laser-driven ion acceleration studies carried out to date, ions were accelerated by sheath fields established by relativistic electrons at target surfaces, via the so-called Target Normal Sheath Acceleration (TNSA). A separate mechanism, Radiation Pressure Acceleration (RPA), has attracted extensive theoretical attention in recent years. Radiation pressure is exerted via laser ponderomotive force on a foil surface, which results in local electron-ion displacement, and ion acceleration via the ensuing space-charge field. This regime of acceleration is predicted to lead to high acceleration efficiencies, and to energetic, narrow band ion beams if ultrathin targets are used. The recently obtained experimental results where evidences of the transition to this “new” regime of ion acceleration, the so-called RPA regime, have shown also more favorable ion energy scaling with the laser intensity as predicted by PIC simulations.

It should be notes that TNSA and RPA scenarios are not mutually exclusive. Their relative contributions depend strongly upon the particular target and laser parameters and can contribute to the generation of hot electrons and, in turn, to ion acceleration mechanisms. In both mechanisms the ions still will be accelerated in the field arising due to charge separation. Here the laser pulse contrast has a profound effect on accelerated ions and their cut-off energy.

These developments open new perspectives for many proposed applications of laser driven ion beams which includes e.g., isochoric heating of matter, fusion energy (“fast ignitors” electron- or proton-driven), injection into conventional accelerators, cancer therapy, production of isotopes for PET (positron emission tomography), industrial applications (implantation, lithography), nuclear/particle physics applications.

Although, these applications require performances exceeding present capabilities in terms of maximum energy and particle density, as peak laser intensities continue to rise it is expected that the near future will be characterized by a significant enhancement of the proton/ion cut off energy generated under tightly controlled interaction conditions. This will have an impact on many foreseen applications and will encourage further activities for the optimization of laser plasma-based accelerators. Additionally, laser pulse parameters, including temporal, spatial, and intensity contrast and target conditions need to be carefully characterized. Therefore, more advanced diagnostics needs to be developed which may lead to measuring plasma effects not even thought of today. Development of comprehensive on-line diagnostic systems for simultaneous measurements of different plasma parameters (visible- and XUV-light, X-rays, Gamma-rays, ion and electrons) with high temporal, spectral and spatial resolution together with laser pulse parameters are essential. This requirement is especially important because of both: shot-to-shot fluctuations of laser pulse parameters and inherent shot-to-shot variations in the local target parameters, which can derogate the whole plasma dynamics.

Current progress

Figure 1 shows measurements and simulation results of maximum proton energy at different laser pulse parameters. Two different scalings of increase of accelerated proton energy with increasing laser intensity at different pulse durations are clearly visible. Obviously, short-pulse laser interaction with the target has advantageously faster scaling.

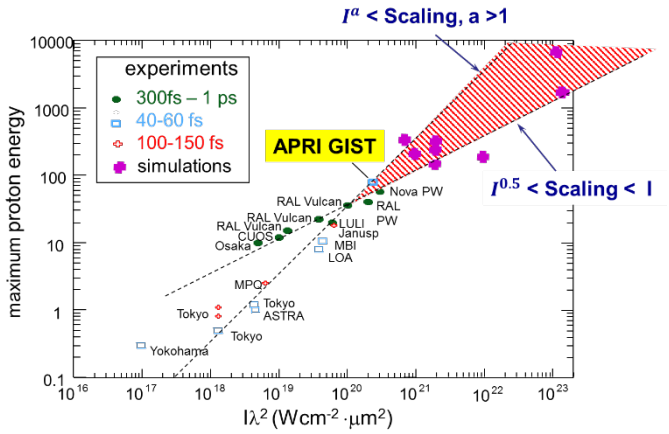

Fig.1. Maximum proton energies dependent on laser intensity: measurements and simulations. Also shown (shaded surface) what will be laser development allow in near future

Additionally, optimized laser-target interaction concept can pave a way to increase proton energies [2, 3]. This includes target design and laser pulse characteristics. Particle in cell simulations and the analytical model, with appropriately chosen interaction conditions, allow accelerating protons to the energies exceeding 200 MeV with 20 J laser pulses.

It was found, that in spite of various acceleration mechanisms, optimization of different types of targets, solid state foils, near-critical targets, or under-dense targets results in almost the same maximum proton energy for a given laser pulse energy, and that the maximum energy of protons accelerated from thin foils with an optimal areal density increases almost linearly with the laser pulse field amplitude, a_0, in agreement with figure 1.

This is accomplished by developing advanced diagnostics which allows making detailed measurements of plasma properties across wide ranges of plasma temperature and density parameters for an extensive and thorough research of relevant laser-plasma processes and can provide essential information on their complex dynamics. With that specific requirements of different acceleration mechanisms and interaction concepts can be realized.

Conclusion

Our study shows a potential for efficient proton acceleration with high intensity compact laser systems. As peak laser intensities continue to rise, proof of principle experiments will continue to highlight potential new applications of laser accelerated ion beams.

References

1. A. Macchi, et al., *Rev. Mod. Phys*., 2013, **85**, 751.
2. E. d'Humie`res, et al., *Phys. Plasmas*, 2013, **20**, 023103.
3. A.A. Andreev, et al., *Phys. Plasmas*, 2013, **20**, 03311.

NONLINEAR THOMSON SCATTERING OF A TIGHTLY FOCUSED LINEARLY POLARIZED ULTRASHORT LASER PULSE

O. Vais[1,2], S.G. Bochkarev[1], V.Yu. Bychenkov[1], and **A.B. Savel'ev[2]**

[1] Lebedev Physical Institute of the Russian Academy of Sciences, Moscow, Russia, bochkar@lebedev.ru
[2] Lomonosov Moscow State University, Moscow, Russia

Current femtosecond pulse petawatt (PW) technologies enable reaching a very high concentration of laser energy in a tight focal spot with focal intensity up to 10^{22} W/cm^2. Laser-plasma interaction with ultra-short powerful laser pulses is a unique source of high energy electrons, ions and secondary radiation, including ultrashort X-ray and gamma pulses [1, 2]. In comparison with high-order harmonic generation in gas jets, where the flux and photon energy of X-rays are limited [3], a superintense laser pulse – plasma interaction is free of such limitation since a very strong EM field is applied to electrons in a plasma. Bright attosecond X-rays can be generated in relativistic laser-overdense plasma interactions [4], or through an inverse Compton backscattering source driven by ultrarelativistic electron beam and nonlinear Thomson scattering of laser pulse by free electrons from laser focus [5]. Such X-ray pulses have many applications in atomic and molecular physics, chemistry, and also in life science [1–3].

In the present work, we investigate the nonlinear Thomson scattering of a tightly focused laser pulse. The interaction between tightly focused laser fields and plasma electrons is determined by a peculiar topology of the laser field in the focal spot. It is important for the case when a laser pulse interacts with nanotargets, i.e. ultrathin solid dense foils or other more complicated nanotargets with a size much less than λ, where λ is laser wavelength. The investigation addresses namely the regime where the focal spot size, D_F, may be comparable to the laser wavelength. For description of EM fields of a tightly focused laser pulse beyond the paraxial approximation we use an exact solution of the vector Helmholtz equation in the form of Stratton-Chu diffraction integrals and the angular spectrum representation method. This approach allows one to take into account correctly all 6 components of the laser EM field, including a longitudinal component of electric field, which strongly affects electron acceleration [6, 7].

Let us first consider radiation of a single electron initially located at a tight focus of a 30 fs, 800 nm, 120 TW linearly polarized Gaussian laser pulse. To describe characteristics of the radiation we calculated the angular spectral energy radiated by the electron

$$\frac{d^2W}{d\omega d\Omega} = \frac{e^2\omega^2}{4\pi^2 c}\left|\int_{-\infty}^{\infty} dt\,[\,\vec{n}\times\vec{\beta}]e^{i\omega(t-\vec{R}\cdot\vec{n}/c)}\right|^2, \qquad (1)$$

where $\vec{R}(t)$ and $\vec{\beta}(t)$ define the position and dimensionless velocity of the electron. Equation (1) gives the energy radiated in the direction of the unit vector $\vec{n}$ per unit solid angle Ω and per unit frequency ω.The trajectory $\vec{R}(t)$ and dimensionless velocity $\vec{\beta}(t)$ of the test electron are calculated by integrating the relativistic motion equation of the particle in given laser fields when the radiation friction impact on electron dynamics and radiation spectra is neglected. The calculations of the spectral function (1) were made for different focal spot diameters of the laser energy. The results were compared with those obtained from paraxial formulas for laser fields taking into account the longitudinal laser field component. In both cases radiation is emitted mostly in the polarization plane (*X, Z)* at the angle $\pm\theta_{\max}$ with respect to the laser propagation direction (*Z*). One can see in Fig. 1a,b, where the angular spectral energy distributions are shown for the exact (a) and paraxial (b) laser fields for different polar angles θ, that using the paraxial approximation for tight focusing, $D_F \approx \lambda$ $(I_F \approx 10^{22} W/cm^2)$, overestimates peak angular spectral energy. Also, as compared to paraxial spectra, there is a shift in the spectral functions to low photon energies. At the same time, in comparison with paraxial radiation fields, the isolated attosecond pulses are generated. It is easy to explain such radiation characteristics when considering the electron dynamics in nonparaxial fields where electrons very quickly, on the scale of order Rayleigh length, escape from the tight laser focus in radial direction and cannot radiate energy anymore. For the paraxial case, the electrons are not expelled so fast, as a result, the electron stays longer within the laser focus and with high probability will experience stronger acceleration and radiate more energy. Note that an optimal angle $\theta_{\max}$ for paraxial fields is less than for nonparaxial fields.

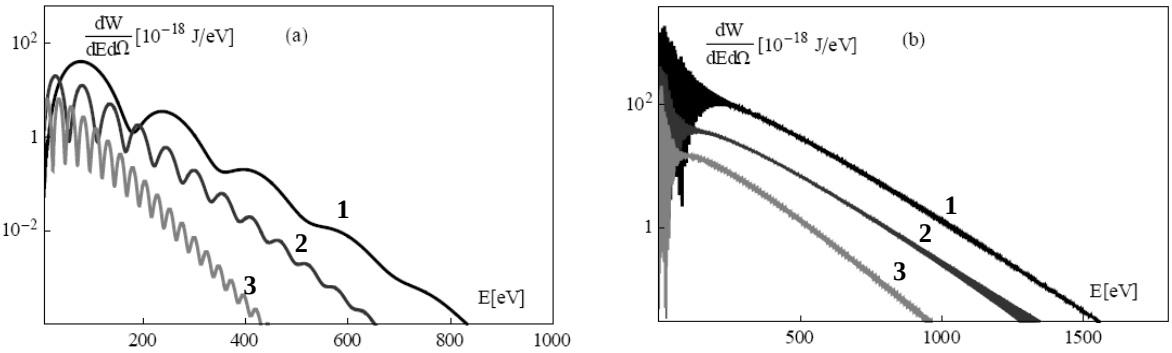

Fig. 1. Angular spectral energy radiated by test electron for exact (a) and paraxial fields (b). Curve 1 corresponds to angles $\theta = \theta_{\max}$, curves 2 and 3 to angles $\theta_{1,2}$, where $\theta_{\max} < \theta_1 < \theta_2$, $\theta_1 \approx 1.2\,\theta_{\max}$ and $\theta_2 \approx 1.5\,\theta_{\max}$

We have also studied radiation for higher D_F values, including the case, where paraxial approximation should work well enough. The radiated power reaches maximum value at $D_F \approx 10\lambda$ (see Fig. 2). In fact, the electron radiates noticeably higher in the case of smoother focusing than at very tight focusing at the same laser energy. However, for a wider focal spot the peak radiated power decreases.

It is important that the paraxial approximation describes radiation characteristics incorrectly for $D_F < 10\lambda$. That is why it is necessary to revise the nonlinear Thomson scattering theory for typical experimental conditions. Study of the radiation by the test electron initially located not exactly at the focal plane ($z_0 = z_F$) shows that the maximum of the radiated power corresponds to the initial electron position before the focal plane ($z_0 < z_F$) at a distance of order Rayleigh length and can be increased.

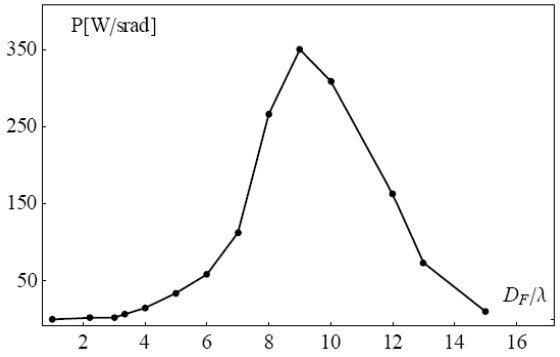

Fig. 2. The peak radiated power at the optimal angle $\theta_{\max}$ as a function of focal spot size

Thus, in the case of a tightly focused laser pulse ($D_F \sim \lambda$), isolated attosecond X-ray pulses are generated.There is an optimal focal spot size for which radiation power reaches its maximum.

Acknowledgements

This work was supported by the Russian Foundation for Basic Research (Grants Nos. 12-02-00231-a, 13-02-00426-a, 14-02-31407-mol-a, 14-02-00849-a), the Program for Supporting Leading Scientific Schools of the Russian Federation (Grant No. NSh-1424.2014.2), and the Russian Scientific Foundation (grant # 14-12-00194).

References

1. K. Lee, S.-Y. Chung, and D.-E. Kim, *in book: Advances in Solid-State Lasers*, INTECH, 2010, 509-538.
2. S. Corde,K. Ta Phuoc, G. Lambert et al., *Rev. Mod. Phys.*, 2013, **85**, 1-48.
3. F. Krausz and M. Ivanov, *Rev. Mod. Phys.*, 2009, **81**, 163-234.
4. T. Baeva, S. Gordienko, and A. Pukhov, *Phys. Rev. E*, 2006, **74**, 046406, 1-11.
5. J. Koga, T.Zh. Esirkepov, and S.V. Bulanov, *Phys. Plasmas*, 2005, **12**, 093106, 1-8.
6. K.I. Popov, V.Yu. Bychenkov, W. Rozmus, and R.D. Sydora, *Phys.Plasmas*, 2008,**15**, 013108.
7. S.G. Bochkarev, V.Yu. Bychenkov, *Quantum Electron.*, 2007, **37**(3)**,** 273-284.

International Symposium

TOPICAL PROBLEMS OF NONLINEAR WAVE PHYSICS

SCHOOL FOR YOUNG SCIENTISTS

ELECTRON TRAPPING IN LASER FIELD DUE TO RADIATION REACTION

L.L. Ji[1,2], A. Pukhov[1,4], I.Yu. Kostyukov[3,4], B.F. Shen[2], and **K. Akli[5]**

[1]Institut für Theoretische Physik I, Heinrich-Heine-Universität Düsseldorf, 40225 Düsseldorf, Germany
[2]Shanghai Institute of Optics and Fine Mechanics, Chinese Academy of Sciences, Shanghai 201800, China
[3]Institute of Applied Physics of the Russian Academy of Sciences, 603950 Nizhny Novgorod, Russia
[4]Lobachevsky National Research University of Nizhni Novgorod, 603950, Nizhny Novgorod, Russia
[5]The Ohio State University, Columbus, Ohio 43210, USA

Abstract. A radiation trapping effect of electrons (RTE) [1] is revealed in the near-QED regime of laser-plasma interaction. Electrons quivering in laser pulse experience radiation reaction (RR) recoil force by radiating photons. When the laser field reaches the threshold, the RR force becomes significant enough to compensate for the expelling laser ponderomotive force. Then, electrons are trapped inside the laser pulse instead of being scattered off transversely and form a dense plasma bunch. The mechanism is demonstrated both by full three-dimensional (3D) particle-in-cell (PIC) simulations using QED photonic approach and numerical test-particle modeling based on the classical Landau-Lifshitz formula of RR force. Furthermore, the proposed analysis shows that the threshold of laser field amplitude for RTE is approximately the cubic root of laser wavelength over classical electron radius. Due to the pinching effect of the trapped electron bunch, the required laser intensity for RTE can be further reduced.

Laser intensities up to 10^{22}W/cm^2 have been demonstrated [2] and are expected to surpass 10^{23}W/cm^2 in the course of several ongoing projects and initiatives [3, 4]. At this intensity level, the laser-plasma interaction will be prompted to the exotic near-QED regime [5–10]. One of the most foreseeable effects is that electrons lose a considerable amount of energy by emitting photons in the laser field, namely the radiation reaction (RR) effect [11]. Particle-in-cell (PIC) simulations suggest γ-photons may become the dominant energy absorption channel and even take more energy than electrons [8]. As a result, the relativistic motion of electrons at these laser intensities is strongly modified. It leads to much lower electron energies than those one would expect neglecting RR [12–21]. It has also been noticed that free electrons can be attracted to the positions of electric field peaks in the near-QED regime, by creating a standing electromagnetic (EM) wave structure with multiple laser pulses [22–24].

In this work, we investigate laser-plasma interaction in the near-QED regime via full 3D PIC simulations. We found the radiation trapping effect (RTE) of a dense electron bunch inside the laser pulse. When a sufficiently intense laser propagates in plasma, we observe a new regime, where the RR force can compensate for the ponderomotive force. Unlike in the non-QED regime, electrons can be transversely trapped by the laser field instead of being pushed away. Different from the standing EM wave cases [22–24], where free electrons are mostly confined in a small volume of the laser wavelength, we consider a traveling EM wave. The spatial period and the oscillation amplitude are typically large as compared with the laser wavelength. As we will see later, the RR reduces oscillation amplitude leading to concentration of electrons in the high intensity region and forming a dense bunch. Since the electron bunch becomes ultra-relativistic quickly and co-propagates with the laser pulse, the electric part of the transverse Lorentz force is almost compensated by the magnetic part. The required laser amplitude for RTE is then greatly reduced. The RTE changes the laser-plasma interaction significantly. Furthermore, a large part of the laser energy is converted into high-energy photons providing a bright source of MeV γ-rays.

The new effect is observed with the 3D code VLPL [25]. A QED model is implemented to describe the RR and electron-positron pair creation [26]. The new RTE effect stems from RR and electrons are transversely trapped by the laser pulse when the RR force is comparable to the laser ponderomotive force. The underlying mechanism is shown in Fig. 2 (a). Electrons quivering in the highly relativistic laser field emit photons along their propagation directions, causing a recoil force oppositely directed to the instantaneous momentum [26]. The tendency of the laser ponderomotive force to push electrons forward and aside is compensated by the recoil force. In the limit of strong RR, the recoil can be so strong that instead of being expelled away, electrons gradually fall into the high-laser-intensity region and are trapped there.

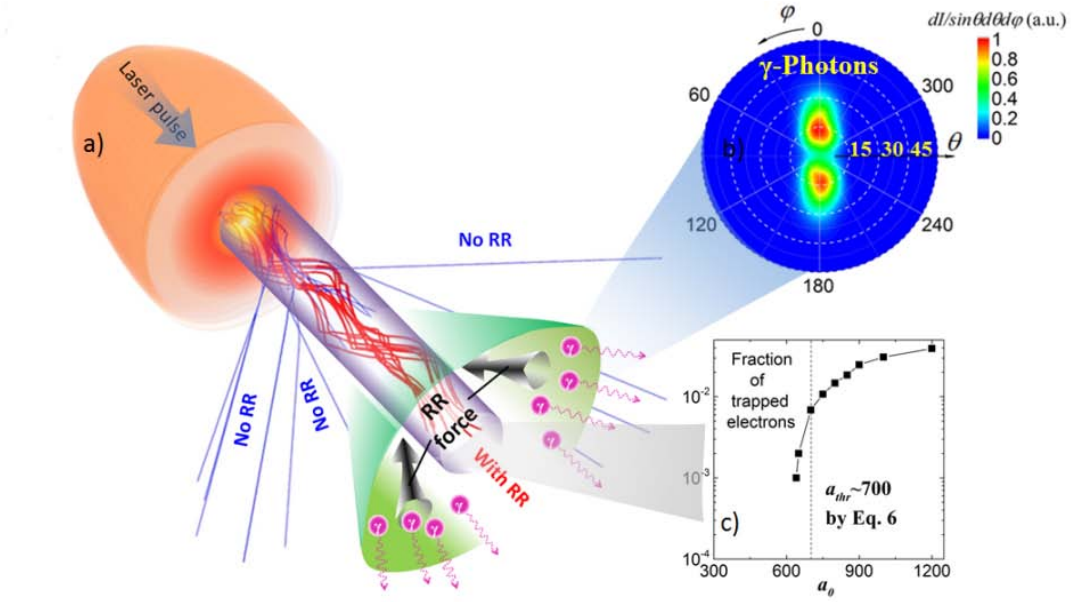

Fig. 1. Sketch of laser-plasma interaction in the regime of RTE.
(a) Trajectories of test electrons numerically calculated according to Eq. (1) either neglecting (blue solid lines), or including RR (red solid lines). Electrons are trapped in the high-laser-intensity region through the RR force (black arrow) induced by the emitted photons (wavy arrows). (b) The typical angular distribution of γ-photons from 3D PIC simulations. (c) The relative fraction of trapped test electrons versus laser amplitude

Acknowledgements

This work was supported by the Government of the Russian Federation (Project No. 14.B25.31.0008) and by the Russian Foundation for Basic Research (Grants No. 13-02-00886, 13-02-97025), by DFG TR18 (Germany) and by EU FP7 Eucard-2.

References

1. L.L. Ji, A. Pukhov, I.Y. Kostyukov, B.F. Shen, K. Akli, *Physical review letters*, 2014, **112** (14), 145003.
2. V. Yanovsky *et al*., *Opt. Express*, 2008, **16**, 2109.
3. Extreme Light Infrastructure European Project (www.extreme-light-infrastructure.eu).
4. Exawatt Center for Extreme Light Studies (www.xcels.iapras.ru).
5. A.M. Fedotov et al., *Phys. Rev. Lett*., 2010, **105**, 080402.
6. A. Di Piazza et al., *Rev. Mod. Phys*., 2012, **84**, 1177.
7. I.V. Sokolov et al., *Phys. Rev. E*, 2010, **81**, 036412.
8. C.P. Ridgers et al., *Physics of Plasmas*, 2013, **20**, 056701.
9. E.N. Nerush et al., arXiv:1309.1648 .
10. E.N. Nerush et al., *Phys. Rev. Lett*., 2011, **106**, 035001.
11. Ya.B. Zel'dovich, *Sov. Phys. Usp*., 1975, **18**, 79.
12. A. Zhidkov et al., *Phys.Rev. Lett*., 2002, **88**, 185002.
13. A. Di Piazza et al., *Phys.Rev. Lett*., 2009, **102**, 254802.
14. M. Tamburini et al., *Phys. Rev. E*, 2012, **85**, 016407.
15. R. Capdessus et al., Phys. Rev. E, 2012, **86**, 036401.
16. S.V. Bulanov et al., arXiv:1304.6519v1.
17. M. Chen et al., *Plasma Phys. Control. Fusion*, 2011, **53**, 014004.
18. I.V. Sokolov et al., *Phys.Plasmas*, 2009, **16**, 093115.
19. N. Naumova et al., *Phys. Rev. Lett*., 2009, **102**, 025002.
20. I. Kostyukov et al., *Phys. Plasmas*, 2003, **10**, 4818.
21. R. Capdessus et al., *Phys. Rev. Lett*., 2013, **110**, 215003.
22. G. Lehmann et al., *Phys. Rev. E*, 2012, **85**, 056412.
23. J. G. Kirk et al., *Plasma Phys. Control.Fusion*, 2009, 51, 085008.
24. A. Gonoskov et al., arXiv:1306.5734v2.
25. A. Pukhov, *J. Plasma Phys*., 1999, **61**, 425.
26. A.M. Pukhov, I.Yu. Kostyukov, *Problems of Atomic Science and Technology*, 2013, **4**(86), 245.

ELECTRON ACCELERATION IN LASER-PLASMA BUBBLES

A. Pukhov, O. Jansen, T. Tückmantel, J. Thomas, and **I. Yu. Kostyukov**

University of Dusseldorf, 40225 Germany, pukhov@tp1.uni-duesseldorf.de
Lobachevsky University of Nizhny Novgorod, Russia

Abstract. Electron acceleration in the laser-plasma bubble proved to be the most successful regime of laser wake field acceleration in the last decade. The laser technology became mature enough to generate short and relativistically intense pulses required to reach the bubble regime naturally delivering quasi-monoenergetic bunches of relativistic electrons. The upcoming laser technology projects are promising short pulses with many times more energy than the existing ones. The natural question is how the bubble regime will scale with the available laser energy. We present here a parametric study of laser-plasma acceleration in the bubble regime using full three dimensional particle-in-cell simulations and compare numerical results with the analytical scalings from the relativistic laser-plasma similarity theory.

Brilliant bunches of high energy electrons have a number of applications. As a source of tunable short wavelength radiation [1–2] they can be used to investigate the structure of matter [3]. With the use of free-electron lasers (FEL) [4] they become a source of coherent X-rays. Thus, there is a quest for a compact and tunable source of high energy electrons. Due to radio-frequency-cavity electrical breakdown, electrical fields in classical accelerators are restricted to 20–100 MV/m. This leads to large, expensive accelerator facilities. Wakefield acceleration [5] has been a promising field for the generation of fast electrons and hard X-rays. Various accelerating schemes employing different kind of driver beams have been suggested in the last decades [6–9].

A topic of particular interest in the field of laser-wakefield acceleration is the bubble regime [10]. This highly relativistic regime became available for applications with the invention of the Chirped Pulse Amplification (CPA) technology [11] that resulted in relativistically intense femtosecond short [12] laser pulses. The bubble regime has the potential to accelerate electrons in the range of several hundred MeV to GeV energies on cm-scales [13–14]. In the bubble regime, the laser pulse creates a cavity called the bubble, which is free from thermal background electrons. During the formation of the bubble, electrons get trapped from the background plasma and accelerated in electric fields 3–4 orders of magnitude stronger than in classical electron accelerators, easily exceeding 100GV/m [15]. The bubble regime involves strongly non-linear fields as well as wave-breaking of the plasma wave following the laser pulse. Analytical wave-breaking is well understood in 1D. However, in more dimensions numerical approaches are necessary. Therefore, we are using results from 3D particle-in-cell (PIC) simulations from the VLPL-code [16].

Acknowledgements

This work was supported by the Government of the Russian Federation (Project No. 14.B25.31.0008) and by the Russian Foundation for Basic Research (Grants No. 13-02-00886, 13-02-97025), by DFG TR18 (Germany) and by EU FP7 Eucard-2.

References

1. H. Motz, "Applications of the Radiation from Fast Electron Beams", *J. Appl. Phys*., 1951, **22**, 527.
2. P. Luchini, H. Motz, *Undulators and Free-electron Lasers Oxford University Press*,1990.
3. H. Chapman et al., "Femtosecond diffractive imaging with a soft-X-ray free-electron laser", *Nature Physics*, 2006, **2**, 839-843.
4. Ayvazyan et al., "First operation of a free-electron laser generating GW power radiation at 32 nm wavelength", *EPJ D*, 2006, **37**, 2, 297-303.
5. J. Tajima, T. Dawson, "Laser Electron Accelerator", *Phys. Rev. Let.*, 1979, **43**, 4, 267-270.
6. E. Esarey, P. Sprangle, J. Krall, A. Ting, "Overview of Plasma-Based Accelerator Concepts", *IEEE transactions on Plasma Science*, 1996, **24**, 252-288.
7. A. Pukhov, "Strong field interaction of laser radiation", *IEEE transactions on Plasma Science*, 2003, **66**, 47-101.
8. V. Malka, "Laser Plasma Accelerators", in *Laser-Plasma Interactions and Applications, Scottish Graduate Series*, 2013, 281-301.
9. E. Esarey, C.B. Schroeder, W.P. Leemans, "Physics of laser-driven plasma-based electron accelerators", *Reviews of Modern Physics*, 2009, **81**(3), 1229-1285.
10. A. Pukhov, J. Meyer-ter-Vehn, "Laser wake field acceleration: the highly non-linear broken-wave regime", *Applied Physics B*, 2002, **74**(4-5), 355-361.

11. D. Strickland, G. Mourou, "Compression of amplified chirped optical pulses", *Optics Communications*, 1985, **56**(3), 219-221.
12. Extreme Light Infrastructure European Project (www.extreme-light-infrastructure.eu).
13. B. Hidding, K.-U. Amthor, B. Liesfeld, H. Schwoerer, S. Karsch, M. Geissler, L. Veisz, K. Schmid, J.G. Gallacher, S.P. Jamison, D. Jaroszynski, G. Pretzler, and R. Sauerbrey, "Generation of Quasi monoenergetic Electron Bunches with 80-fs Laser Pulses", PRL, 2006, **96**, 105004.
14. W.P. Leemans, B. Nagler, A.J. Gonsalves, Cs. Toth, K. Nakamura, C.G.R. Geddes, E. Esarey, C.B. Schroeder, S.M. Hooker, "GeV electron beams from a centimetre-scale accelerator", *Nature Physics*, 2006, **2**, 696-699.
15. I. Kostyukov, E. Nerush, E. Nerush, A. Pukhov, V. Seredov, "Electron self-injection in multidimensional relativistic plasma wake fields", *Physical Review Letters*, 2009, **103**(17), 175003.
16. A. Pukhov, "Particle-in-cell code VLPL (Virtual Laser Plasma Lab)", *Journal of Plasma Physics*, 1999, **61**, 425-433.

ADAPTIVE OPTICS AND POWERFUL LASERS

F.A. Starikov

Russian Federal Nuclear Center – VNIIEF, Institute of Laser Physics Research
Mira ave. 37, Sarov, Nizhni Novgorod Reg. 607200, Russia

The lecture is devoted to the methods for correction of powerful laser beams by means of the adaptive optics. Adaptive optics is generally related to the controllable action of an optical system on the radiation field accommodating it to the required conditions.Adaptive optics, having famous employment in astronomy in the ground-based large-aperture space telescopes, during last time have resulted in considerable advances in ophthalmology and laser technologies.

The purpose of adaptive optics application to powerful lasers is to minimize the inevitable phase distortions of laser beam or to transform the phase front (and, if possible, amplitude distribution) so that to obtain the needed intensity distribution in a given plane. The operation of adaptive optical system can be realized using the nonlinear as well as linear optical effects, so it is possible to say about nonlinear adaptive optics or linear adaptive optics. But usually nonlinear adaptive optics is referred to as nonlinear optics whereas linear adaptive optics is referred to as adaptive optics.It is widely meant now terminologically that adaptive optics is connected with regulated changing of phase front (wavefront) of the radiation beam by means of controllable optical elements (as a rule, reflectance of this beam from the mirror with deformable optical surface).

In the lecture the conventional principles and methods of nonlinear (by example of phase conjugation at SBS) and linear (deformable mirrors) adaptive optics as well as the general conditions for their practical application are considered. The examples of correction of optical aberrations of laser beams are given in the case of pulsed and cw powerful laser radiation using SBS and deformable mirrors.Besides, the problem of coherent beam combining (phase locking) of the cw multi-channel powerful lasers is discussed in terms of an adaptive optical procedure and some experimental results are demonstrated.

INDEX OF AUTHORS

International Symposium

TOPICAL PROBLEMS OF NONLINEAR WAVE PHYSICS

SPONSORS

The Government of the Russian Federation supports organization of the NWP-2014 Symposium under the program of mega-grants designed to support research projects implemented under the supervision of the world's leading scientists at Russian institutions of higher learning and research

Mega-grant No. 14.Z50.31.0007

"Laboratory and numerical investigation of plasma phenomena in extreme astrophysical objects"

Leading Scientist – Julien Fuchs

Mega-grant No. 14.Z50.31.0033

"New approaches to investigating climatic processes and forcasting extreme phenomena

Leading Scientist – Juergen Kurths

Mega-grant No. 14.B25.31.0024

"Laboratory of the novel optical materials for advanced lasers"

Leading Scientist – Ken-ichi Ueda

Mega-grant No. 14.B25.31.0023

"Lightning and thunderstorms: physics and effects"

Leading Scientist – Vladimir Rakov

Amplitude TECHNOLOGIES

The ultimate laser systems

PULSAR for particle acceleration

- High peak power >1 PW
- High temporal contrast down to 10^{-12}
- Ultra-short pulse duration (sub-20 fs)
- Dedicated Man-Machine Interface
- Unique spatial and temporal real-time metrology and diagnostics

AURORA for ultrafast science

- High power CEP stabilized laser (> 20 W at 1-10 kHz)
- Ultra-short pulse duration down to 15 fs
- CEP single-shot measurement and control

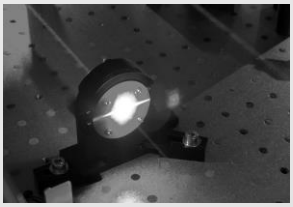

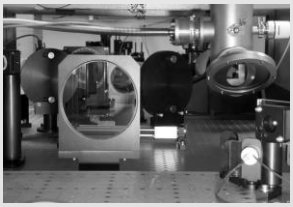

nothing but ultrafast

AMPLITUDE TECHNOLOGIES
2-4, rue du Bois Chaland – CE 2926 Lisses
91029 EVRY Cedex – France
info@amplitude-technologies.com
www.amplitude-technologies.com

Amplitude TECHNOLOGIES

The ultimate laser systems

PULSAR for particle acceleration

- High peak power >1 PW
- High temporal contrast down to 10^{-12}
- Ultra-short pulse duration (sub-20 fs)
- Dedicated Man-Machine Interface
- Unique spatial and temporal real-time metrology and diagnostics

Particles generation

X-ray generation

Accelerator physics

nothing but ultrafast

AMPLITUDE TECHNOLOGIES
2-4, rue du Bois Chaland – CE 2926 Lisses
91029 EVRY Cedex – France
info@amplitude-technologies.com
www.amplitude-technologies.com

Amplitude TECHNOLOGIES

The ultimate laser systems

AURORA for ultrafast science

High power CEP stabilized laser (> 20 W at 1-10 kHz)

Ultra-short pulse duration down to 15 fs

CEP single-shot measurement and control

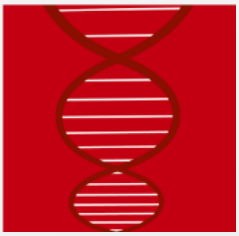

Attoscience

New light sources

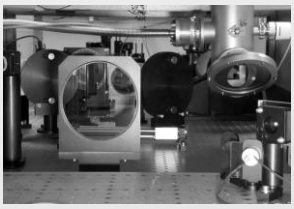

nothing but ultrafast

AMPLITUDE TECHNOLOGIES
2-4, rue du Bois Chaland – CE 2926 Lisses
91029 EVRY Cedex – France
info@amplitude-technologies.com
www.amplitude-technologies.com

Corning Incorporated is the world leader in specialty glass and ceramics. We create and make keystone components that enable high-technology systems for consumer electronics, mobile emission control, telecommunications, and life sciences. We succeed through our sustained investment in R&D, more that 160 years of material science and process engineering knowledge, and a distinctive, collaborative culture. We work closely with our customers to solve complex problems that others can't, or won't solve. Time and again, our breakthrough, life-changing innovations have proven that, if it is possible, Corning will make it real.

From creating glass windows for space shuttles to developing optical components for high-tech industries, Corning develops solutions for virtually any glass-based challenge.

Corning is one of the very few manufacturers with deep capabilities in materials science, optical design, shaping, coating, finishing, and assembly. Our optical materials cover the entire spectrum, from extreme ultraviolet (EUV) to infrared, and from refractive to reflective. These capabilities position the company to meet the needs of a broad array of markets including display, semiconductor, aerospace/defense, astronomy, vision care, lithography, industrial/commercial, metrology and telecommunications.

Photonic Materials

Products such as Polarcor™ glass polarizers and specialty optical fibers (e.g. bend insensitive, polarizing or polarization maintaining) play an important role in optical modules and components from telecommunication to instruments, sensors or gyroscopes.

Technical glasses and glass ceramics

The rich portfolio of technical glasses and glass ceramics reflects Corning's innovations potential in glass technology. It ranges from Eagle XG™ Industrial Grade Substrate, used as an optical substrate for a variety of micro display components including small LCD displays, to Corning's new Gorilla™ Glass, a scratch resistant, durable, optical quality glass optimized for high-end portable devices and touch screens.

Zero Expansion Glass

Not only EUV optics or astronomical mirrors, but also reference scales or etalons are typical applications of ULE®. Its virtual zero expansion coefficient sets the standard and can be certified non-destructively to less than 10 ppb/K. Due to the specific properties of ULE®, it allows the manufacture of light weight structures with a weight reduction up to 95%.

Synthetic Fused Silica

Corning HPFS® synthetic fused silica is of the highest purity. With excellent optical, thermal and mechanical properties, it is used for challenging applications from DUV microlithography to high-energy lasers and space shuttle windows.

Optical Crystals: CaF_2, MgF_2

High transmission in the UV and excellent laser resistance are the reason why Corning's fluoride crystals are used for industrial and laser optics in industry, medicine and lithography.

Corning Fairport Precision Optics

Corning Tropel is a leading company for development and manufacturing of customer specific optical subsystems (modules), mainly used in the DUV.



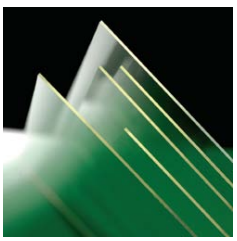

CORNING

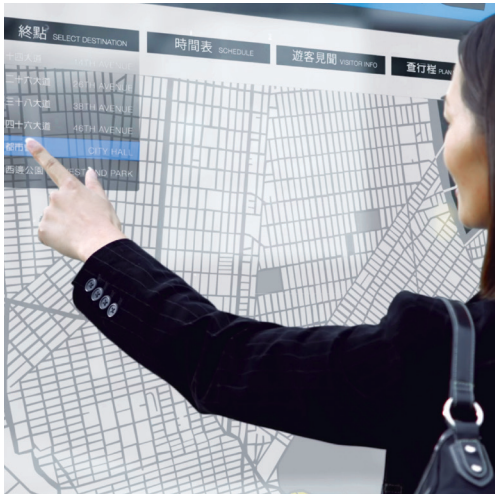

At A Glance

About Corning

As the world leader in specialty glass and ceramics, Corning invents, makes, and sells keystone components that enable high-technology systems for consumer electronics, mobile emissions control, optical communications, and life sciences.

Corning succeeds through sustained investment in R&D, more than 160 years of materials science and process engineering knowledge, and a distinctive collaborative culture.

We work closely with customers to understand their toughest challenges. Corning's passion for science helps solve those problems with life-enhancing technologies.

Research & Development

Corning's commitment to research and development drives our ability to turn possibilities into breakthrough realities.

Our renowned laboratory and research facilities attract and enable the world's best scientific minds. Corning's state-of-the-art resources, multi-disciplined materials expertise, and dedicated technology leadership help foster our collaborative culture at every innovation phase.

Cross-functional teams and a broad portfolio of capabilities allow our researchers to leverage existing technologies across multiple product lines, enabling faster discovery of practical solutions.

Corning's sustained investment and unwavering commitment to R&D will ensure the next wave of technological advancements.

What's Next?

Beginning with a track record of more than 160 years, Corning's vision for the future is full of cutting-edge and life-enhancing technologies that deliver extraordinary benefits to everyday products.

Across our business segments and around the globe, Corning is constantly driving the next wave of innovations powered by specialty glass and ceramics.

Our Values

Quality. Integrity. Performance. Leadership. Innovation. Independence. The Individual.

Corning's visionary leadership remains steadfast to these enduring Values that guide us in everything we do. Our Values define our relationships with employees, customers, and the communities in which we operate in around the globe.

Equity Companies

Corning maintains successful alliances with other leading organizations in key markets, including the following equity companies: Cormetech, Inc.; Dow Corning Corporation; Eurokera, S.N.C.; and Samsung Corning Advanced Glass, LLC.

Want to learn more? Visit: Corning.com/AboutUs

Display Technologies

Corning's glass substrates enable the thin, high-resolution, multi-function displays consumers demand.

Our environmentally friendly glass compositions and technological innovations help advance the display industry, creating the foundation for a range of scalable and durable electronic devices used at work, home, and on the go.

As vivid organic light-emitting diode (OLED) displays and next-generation liquid crystal displays (LCDs) evolve, Corning will drive the advanced glass technologies required by display manufacturers.

Corning.com/DisplayTechnologies

Environmental Technologies

Our materials and process expertise in ceramic substrates have made Corning a key contributor in the campaign for cleaner air for 40 years.

We develop emissions-control products for the world's major manufacturers of gasoline- and diesel-powered engines and vehicles. Our advanced ceramic substrates and diesel particulate filters set the standard for catalytic converters and help control pollution around the world.

As the global concern for clean air intensifies, Corning's technologies continue to advance emissions-control solutions.

Corning.com/EnvironmentalTechnologies

Optical Communications

Corning keeps pace with the world's insatiable demand for bandwidth by providing optical communications solutions that put all the information you need right at your fingertips.

Our innovative optical connectivity solutions deliver high-quality broadband capabilities for the Enterprise, Carrier, and Wireless markets, as well as the expanding frontier of consumer electronic devices.

Corning's optical communications products and services are uniquely positioned to meet tomorrow's bandwidth demands for mobile devices, the increasing need for constant connectivity, and the growing volume of data being transmitted around the globe.

Corning.com/Products_Services/Telecommunications

Life Sciences

Corning helps scientists bring life-saving medicines to market through a comprehensive line of glass and plastic labware, as well as label-free technology, media, and reagents for cell culture, genomics, and bioprocessing applications.

By supplying high-quality tools and research technologies, we support life science advancements and help drive efficiencies for researchers and lab technicians seeking to compress costs and timelines during drug discovery.

Our industry-leading products help create the next wave of possibilities in healthcare.

Corning.com/LifeSciences

Specialty Materials

From cover glass for consumer electronics to advanced optics for high-technology industries, Corning develops customer-driven solutions for some of the toughest material-based challenges.

Our unmatched expertise in fundamental glass science and our hundreds of material formulations for glass, glass ceramics, and fluoride crystals makes this possible, along with our deep knowledge of thin films and our ability to process other materials.

Corning is changing the way the world thinks about glass while inspiring new possibilities and design applications for tomorrow.

Corning.com/SpecialtyMaterials

© 2012–14 Corning Incorporated. All Rights Reserved.

LASER COMPONENTS

For more than 8 years our company "Laser components" has supplied kinds of productions for lasers with different applications, also for optics, which manufacturers in China, Italy and USA.

Our company is the official distributor of such companies as: the manufacturer of optical glass "DGM Glass" (China), manufacturers of measuring instruments of laser radiation parameters "LaserPoint" (Italy) and "Duma Optronics" (Israel).

We also have cooperation with leading enterprises, as well as Shanghai Institute of Optics and Fine Mechanics (Chinese Academy of Sciences, CAS), Chinese Electronics Technology Group Corporation (CETC), and China North Industries Group Corporation (NORINCO GROUP). We can supply large size optics with high requirements of processing and coating. Our partners are large Russian industrial companies and academic institutes, working in different sectors of development and production.

Principles that our partners when choosing our company "Laser components" are transparent and professional approach to cooperation, high quality work and quick order.

The multi-national colleague in our company "Laser components" assure to contact the producers without language barriers, as well as to perform quality control at the factory.

«Laser components» +7 495 258-10-58; +7 495 212-16-58,
olga@lasercomponens.ru
2/2, Balaklavskiy av., Moscow, Russia

"GEORGIY ZHNUKOV"

"Георгий Жуков"

DECK MAP

SUN DECK

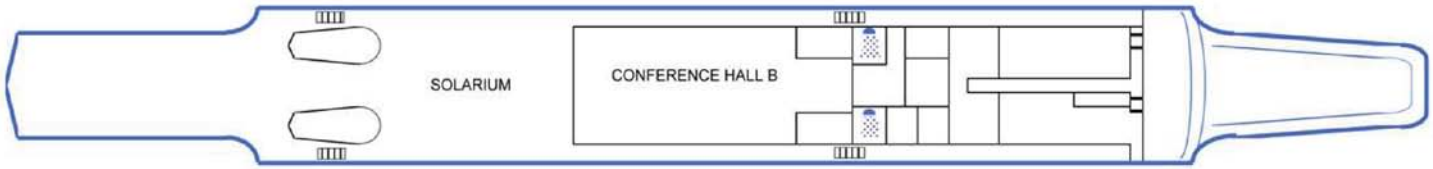

BOAT DECK

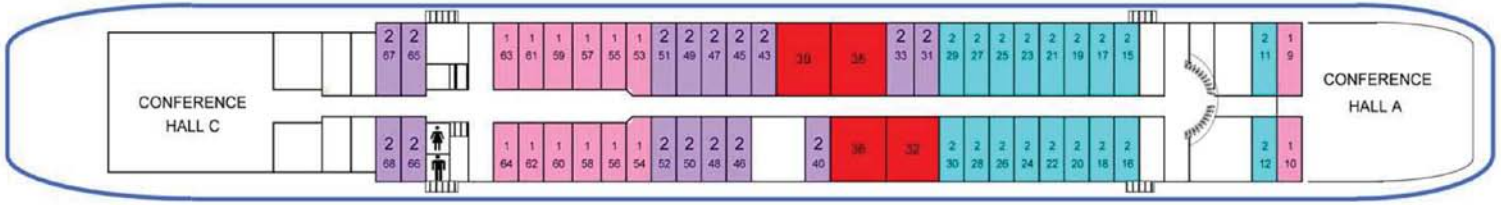

PROMENADE DECK

MAIN DECK

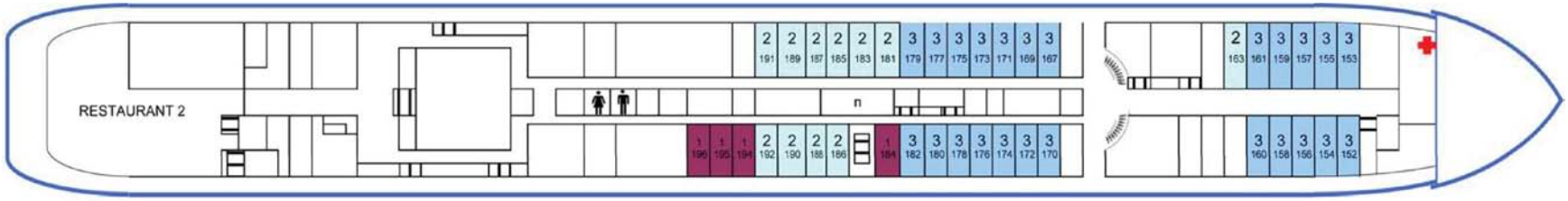

International Symposium
TOPICAL PROBLEMS OF NONLINEAR WAVE PHYSICS
NWP-2014

PROCEEDINGS